Photonic Terahertz Emitters and Receivers

Michele Natrella

A thesis submitted to University College London
for the degree of Doctor of Philosophy

Department of Electronic and Electrical Engineering

University College London

March 2015

I, Michele Natrella, confirm that the work presented in this thesis is my own. Where information has been derived from other sources, I confirm that this has been indicated in the thesis.

Abstract

The research work presented in this thesis is concerned with the design, fabrication and characterisation of Continuous Wave (CW) Photonic Terahertz (THz) Emitters employing antenna-integrated Uni-Travelling-Carrier Photodiodes (UTC-PDs), based on the Indium Phosphide (InP) materials system. The solution employing photonic techniques for the generation of sub-millimetre and THz waves, via photomixing of lasers operating at 1550 nm, is a major candidate for the realisation of tuneable, power efficient, compact and cost effective THz sources operating at room-temperature. The availability of sources endowed with such properties would make many important applications possible in this frequency range, such as ultra-broad band wireless communications, spectroscopic sensing and THz imaging.

The UTC-PDs enable high optical-to-electrical (O-E) conversion efficiency and are key components for the realisation of a photonic terahertz emitter. In this thesis the fabrication and characterisation of test vertically illuminated UTC-PDs, achieved using materials grown by Solid Source Molecular Beam Epitaxy at UCL and the fabrication of high performance waveguide UTC-PDs are reported, as milestones towards the development of a simple, repeatable and high yield fabrication process.

A comprehensive study of UTC-PD impedance and frequency photo-response, carried out using experimental techniques, circuit analysis and 3D full-wave electromagnetic modelling, is presented. The results of this investigation provide valuable new information for the optimisation of the UTC-PD-to-antenna coupling efficiency.

New THz antenna and antenna array designs, obtained by means of full-wave modelling, are also presented, and shown to be suitable for integration with both standard silicon lenses and a novel solution employing a ground plane. The accurate antenna design, along with the results of the UTC-PD impedance investigation, enables the prediction of the power radiated by antenna integrated UTC-PDs, not only in terms of trend over the frequency range but also of absolute level of emitted power.

3D full-wave modelling has also been used at optical frequencies, to address the problem of the optical fibre-to-chip coupling efficiency, which is another fundamental factor for the optimisation of a photonic THz emitter. Among other features, this analysis enables a better understanding of how the light is absorbed throughout the device structure and provides key information for future realisation of travelling-wave photodetectors.

An additional experimental tool for the analysis of THz emission, namely the sub-wavelength aperture probe, has been modelled and characterised, revealing interesting properties for the characterisation of antenna far-fields and near-fields, and hence providing a valuable tool for THz antenna analysis and design.

Acknowledgements

My admiration and respect for my supervisor Prof. Alwyn Seeds have made this PhD journey an amazing professional experience. Every suggestion and cause for reflection received during our meetings and discussions, has prompted a significant advance in my understanding of the concerned technical question and raised my scientific research maturity to a next level. Serious extra-professional problems happened to be part of my PhD journey, and for the wisdom and humanity that came as a response from my supervisor I am deeply grateful.

I would also like to thank my second supervisor Dr. Cyril Renaud, for so many insightful suggestions and important technical discussions.

I have also had the privilege to be part of the research work led by Dr. Oleg Mitrofanov, who has been a source of knowledge and has given me the opportunity to expand my research horizon and interests.

Dr. Chin-Pang Liu has been my mentor for key experimental aspects of my research work and I am really grateful for his extraordinary availability to help.

I am thankful to Dr. Chris Graham for his precious help with several experiments and for being more than happy to share his expertise at all times.

I would like to thank Dr. Martyn Fice, who has had the misfortune to sit next to my desk and has always been available to share his broad technical knowledge and willing to answer my many questions about the English culture and language of which I am fond.

This time at UCL has also given me the chance to meet Ms. (soon to be Dr.) Katarzyna Balakier, with whom I started and I have shared this PhD journey and is now one of my best friends. I am grateful to her for giving me open-hearted advice.

My beloved family in Italy always plays a role in the nice events of my life and my achievements. My adored “mamma” Sofia, sister Floriana, brother Giuseppe, sister and brother in law Lucia and Giuseppe and wonderful nieces Sara, Alice, Martina and Sofia… I love them all.

The most special thank you is for my partner Joy Emuan, whom I love immensely. Joy is the most important person in my life and my soul mate. Thank you Joy for your constant and loving care, for your wise and intelligent advice, for always encouraging me and being so patient when I am annoying. Thank you “principessa”.

List of Publications

Journals

[1] **M. Natrella**, E. Rouvalis, C.-P. Liu, H. Liu, C. C. Renaud, and A. J. Seeds, "InGaAsP-based uni-travelling carrier photodiode structure grown by solid source molecular beam epitaxy," *Optics Express*, vol. 20, no. 17. pp. 19279–19288, 2012.

[2] **M. Natrella**, O. Mitrofanov, R. Mueckstein, C. Graham, C. C. Renaud, and A. J. Seeds, "Modelling of surface waves on a THz antenna detected by a near-field probe," *Opt. Express*, vol. 20, no. 14, pp. 16023–16032, Jul. 2012.

[3] M. Navarro-Cía, **M. Natrella**, F. Dominec, J. C. Delagnes, P. Kužel, P. Mounaix, C. Graham, C. C. Renaud, A. J. Seeds, and O. Mitrofanov, "Terahertz imaging of sub-wavelength particles with Zenneck surface waves," *Appl. Phys. Lett.*, vol. 103, no. 22, pp. 221103 1 – 221103 5, 2013.

[4] A. J. Seeds, M. J. Fice, K. Balakier, **M. Natrella**, O. Mitrofanov, M. Lamponi, M. Chtioui, F. van Dijk, M. Pepper, G. Aeppli, a. G. Davies, P. Dean, E. Linfield, and C. C. Renaud, "Coherent terahertz photonics," *Opt. Express*, vol. 21, no. 19, pp. 22988–23000, Sep. 2013.

[5] R. Mueckstein, **M. Natrella**, O. Hatem, J. R. Freeman, C. S. Graham, C. C. Renaud, A. J. Seeds, E. H. Linfield, A. G. Davies, P. J. Cannard, M. J. Robertson, D. G. Moodie, and O. Mitrofanov, "Near-field analysis of terahertz pulse generation from photo-excited charge density gradients," *Terahertz Sci. Technol. IEEE Trans.*, vol. 5, no. 2, pp. 260 – 267, 2015.

Conferences

[1] A. J. Seeds, E. Rouvalis, **M. Natrella**, H. Liu, M. Chtioui, F. van Dijk, and G. Carpintero, "High efficiency THz photodetectors," *Eur. Conf. Integr. Opt. 2012*, 2012.

[2] A. J. Seeds, G. Aeppli, K. Balakier, A. G. Davies, M. Fice, E. H. Linfield, O. Mitrofanov, **M. Natrella**, M. Pepper, E. Rouvalis, and C. C. Renaud, "Coherent terahertz systems," *Microw. Photonics (MWP), 2012 Int. Top. Meet.*, pp. 278–281, 2012.

[3] O. Mitrofanov, M. Navarro-Cia, R. Mueckstein, **M. Natrella**, C. Graham, C. C. Renaud, a. J. Seeds, F. Dominec, P. Kužel, J. C. Delagnes, and P. Mounaix, "Surface plasmon waves for broad band THz spectroscopy," *SPIE Photonics West 2014-OPTO Optoelectron. Devices Mater.*, vol. 8993, pp. 89931B 1 – 89931B 6, Dec. 2014.

[4] **M. Natrella**, O. Mitrofanov, R. Mueckstein, C. Graham, C. Renaud, and A. Seeds, "Near-Field Probe Mapping of the THz Electric Field Distribution on Metallic Surfaces," *Lasers Electro-Optics (CLEO), 2013 Conf.*, pp. 1-2, 2013.

[5] R. Mueckstein, O. Hatem, **M. Natrella**, J. R. Freeman, C. S. Graham, C. C. Renaud, A. J. Seeds, E. H. Linfield, A. G. Davies, P. J. Cannard, M. J. Robertson, D. G. Moodie, and O. Mitrofanov, "Mapping the distribution of photocurrents responsible for generation of terahertz pulses at semiconductor surfaces," *Infrared, Millimeter, Terahertz waves (IRMMW-THz), 2014 39th Int. Conf.*, pp. 1 -2, 2014.

[6] M. Navarro-Cía, **M. Natrella**, F. Dominec, J.-C. Delagnes, P. Kuzel, P. Mounaix, C. Graham, C. C. Renaud, A. J. Seeds, and O. Mitrofanov, "Zenneck THz surface waves-assisted imaging of subwavelength dielectric particles," *Lasers Electro-Optics (CLEO), 2014 Conf.*, pp. 1–2, 2014.

[7] R. Mueckstein, O. Hatem, **M. Natrella**, J. R. Freeman, C. S. Graham, C. C. Renaud, A. J. Seeds, E. H. Linfield, A. G. Davies, P. J. Cannard, M. J. Robertson, D. G. Moodie, and O. Mitrofanov, "Angular distribution of terahertz radiation emitted from semiconductor surfaces," *4th EOS Top. Meet. Terahertz Sci. Technol.*, 2014.

[8] C. C. Renaud, M. J. Fice, L. Ponnampalam, **M. Natrella**, C. Graham, and A. J. Seeds, "Uni-travelling carrier photodetectors as THz detectors and emitters," *SPIE Proc.*, vol. 9370, pp. 93700B 1 – 93700B 9, Feb. 2015.

Table of Contents

Table of Figures

List of Tables

List of acronyms

ACP	Air Coplanar
BCB	Benzocyclobutene
BPM	Beam Propagation Method
BWO	Backward Wave Oscillator
CC-MUTC-PD	Charge Compensated Modified Uni-Travelling Carrier Photodiode
CPW	Coplanar Waveguide
CW	Continuous Wave
DC	Direct Current
DFG	Difference Frequency Generation
EC	External Cavity
EDFA	Erbium-Doped Fibre Amplifier
EME	Eigenmode Expansion
FA	Fibre Amplifier
FDTD	Finite Difference Time Domain
FEL	Free Electron Laser
FIT	Finite Integration Technique
FWHM	Full Width at Half Maximum
GO	Geometrical Optics
GS-MBE	Gas Source Molecular Beam Epitaxy
HBT	Heterojunction Bipolar Transistor
HEMT	High Electron Mobility Transistor
HRXRD	High-Resolution X-Ray Diffraction
ICT	Information and Communication Technology
IMPATT	Impact Avalanche Transit Time
IR	Infrared
ISS	Impedance Standard Substrate
LCA	Lightwave Component Analyser
LD	Laser Diode

LT-GaAs	Low Temperature grown GaAs
MBE	Molecular Beam Epitaxy
MFD	Mode Field Diameter
MOVPE	Metal Organic Vapour Phase Epitaxy
MUTC-PD	Modified Uni-Travelling Carrier Photodiode
NDR	Negative Differential Resistance
NEP	Noise Equivalent Power
OIP3	Third Order Output Intercept Point
OSA	Optical Spectrum Analyser
PBA	Perfect Boundary Approximation
PEC	Perfect Electric Conductor
PNA	Performance Network Analyser
PO	Physical Optics
QCL	Quantum Cascade Laser
RF	Radio Frequency
RTD	Resonant Tunnelling Diodes
SEM	Scanning Electron Microscope
SI	Semi-Insulating
SMA	Sub-Miniature type A
SMF	Single Mode Fibre
SNR	Signal to Noise Ratio
SOLT	Short-Open-Load-Through
SS-MBE	Solid Source Molecular Beam Epitaxy
TDS	Time-Domain Spectroscopy
TED	Transferred Electron Devices
TK	Thomas Keating
TST	Thin Sheet Technique
TUNNET	Tunnel Injection Transit Time
TW	Travelling Wave
UTC-PD	Uni-Travelling Carrier Photodiode
VSWR	Voltage Standing Wave Ratio
WG	Waveguide

Chapter 1 - **Introduction**

1.1 The terahertz (THz) gap

The terahertz range is often referred to as “terahertz gap” [1.1] having been only partially explored. Figure 1.1 shows a representation of the electromagnetic spectrum illustrating the “THz gap” relative to the microwave and infrared (IR) region. Despite great scientific interest since at least the 1920s [1.2], the terahertz frequency range remains one of the least tapped regions of the electromagnetic spectrum. In the last two decades though, semiconductor technology has advanced considerably and its effect on the research in this band-gap of the electromagnetic spectrum has also been noticed [1.3]. The *terahertz* term is largely employed to identify the sub-millimetre-wave energy falling in the wavelength interval between 1000 µm and 100 µm (300 GHz–3 THz) [1.4], [1.5]; below 300 GHz we enter the range of microwave and millimetre-wave bands (well delimited by the upper operating frequency of WR-3 waveguide - 330 GHz [1.4]) and some definitions extend the upper limit of the terahertz gap to 30 µm wavelength as the frequencies between 3 THz and 10 THz also belonged to a more or less unclaimed territory with few components available, until the first Quantum Cascade Laser with a photon energy less than the semiconductor optical phonon energy was demonstrated at 4.4 THz [1.6]. The border between far-IR and sub-millimetre waves is rather indistinct and the description is likely to follow the methodology (bulk or modal, photon or wave), which is dominant in the particular instrument [1.4].

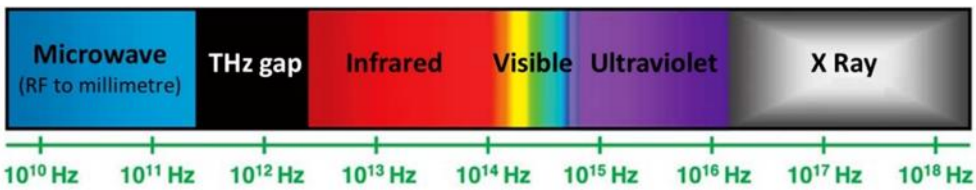

Figure 1.1: Representation of the electromagnetic spectrum illustrating the “THz gap” relative to the microwave and infrared (IR) region.

Research on sub-millimetre and terahertz (THz) waves has been an area of strong recent interest as the nature of these electromagnetic waves is suited to spectroscopic sensing, ultra-broad band wireless communications and several other attractive applications. In fields like astronomy and analytical science, research on THz radiation has been carried out for many years but recently, the number and variety of applications that could benefit from THz technology has been increasing constantly: spectroscopic sensing and ultra-broad band wireless communications [1.7]; information and communications technology (ICT); biology and medical sciences; non-destructive evaluation; quality control of food and agricultural products; global environmental monitoring; ultrafast computing [1.1]; imaging of concealed items, defence applications, basic science, semiconductor wafer inspection [1.8]. The broad application area of terahertz spectrum is due to its unique radiation characteristics [1.9], some of which have been summarized as follows [1.8]:

- Penetration: the terahertz wave can pass through different materials with different levels of the attenuation;
- Resolution: the resolution of an image increases with the decrease in the wavelength, and the resolution in the terahertz band is better than that of the microwave regime of the spectrum;
- Spectroscopy: various solid and gaseous materials exhibit terahertz signature between 0.5 THz and 3 THz;
- Non-ionising: due to the low photon energy levels, terahertz does not cause ionisation on biological tissues;
- Scattering: the scattering is inversely proportional to the wavelength, and it is low in the terahertz band in comparison with the light wave;
- Smaller divergence: collimating THz radiation is easier than microwave radiation.

The success of many of the mentioned emerging system applications utilising sub-millimetre waves, critically depends on reliable and compact continuous-wave sources with low power consumption and excellent noise performance [1.10] and indeed the major obstacle to developing practical, high performance and cost-effective systems for such applications is a lack of solid-state signal sources, rather than of detectors [1.11].

There have been several recent advances in the THz field leading to the achievement of milestones such as the development of THz time-domain spectroscopy (THz-TDS), THz imaging, and high-power THz generation by means of nonlinear effects. Photonics has led the way to the realisation of many important THz devices such as the quantum cascade laser (QCL) and the uni-travelling-carrier photodiode (UTC-PD). The QCL provides a powerful continuous-wave (CW) THz source, and the UTC-PD is a high-power and high-speed photodiode employing a photomixing technique to generate sub-THz and THz waves [1.1].

In order to accomplish the goal of the present work a few requirements need to be met at the same time: a) the design of a high performance UTC-PD; b) a simple, repeatable and high-yield fabrication process; c) a high directivity and wide-band THz antenna (band defined not only in terms of input-impedance but also radiation pattern [1.12]); d) good fibre-to-chip and chip-to-antenna coupling.

In the following section an overview of state of the art CW THz sources is presented with special attention given to photomixing techniques employing uni-travelling carrier photodiodes, which are the subject of this work.

1.2 Sources for continuous wave terahertz generation

Conventional microwave sources do not work fast enough to generate radiation efficiently at frequencies above a few hundred GHz, while diode laser sources are limited by thermal effects to the infrared and visible [1.13] and QCLs need cryogenic cooling to work efficiently in the THz range. Several approaches have been developed that enable the efficient generation and detection of terahertz waves, by means of experimental schemes that are truly commercially viable. The most mature technology employs ultra-fast pulsed laser technology, with photoconductive devices, and produces very short terahertz pulses. As a pulsed technique, with sub-picosecond timescales, the method is intrinsically broad band.

Sub-millimetre wave and THz coherent systems, based on photonic local oscillators, can enable the creation of highly coherent, thus highly sensitive, systems for frequencies ranging from 100 GHz to 5 THz, within an energy efficient integrated platform [1.14], [1.15]. Spectroscopy systems based on continuous-wave CW technology, which use monochromatic sources with an accurate frequency control capability, have attracted much attention [1.16], [1.17] as there are numerous systems and phenomena of great interest in chemistry, physics, and biology, which can be very effectively studied by high resolution spectroscopy in the THz gap; these include the determination of intermolecular potential surfaces, studies of hydrogen bond tunneling dynamics, vibrational spectroscopy of metal and covalent clusters, and studies of reactive molecular complexes [1.18]. Also, the THz range covers the energy range for molecular rotation of polar molecules and librations of macromolecules. High-resolution THz absorption spectroscopy is very appealing for chemical composition analysis since rotation spectra with many narrow characteristic lines in this frequency range represent highly selective fingerprints of molecules [1.19]-[1.21], including (large) organic molecules [1.22]-[1.24]. The CW source-based systems provide a higher signal-to-noise ratio (SNR) and spectral resolution than pulsed technology; when the frequency band of interest is targeted for the specific absorption line of the objects being tested, CW systems with the selected frequency-scan length and resolution are more practical in terms of data acquisition time as well as system cost [1.7].

Another wide field of interesting applications of CW THz radiation is related to the fact that the cosmic background radiation density peaks in the THz range [1.25]; tuneable CW THz sources can be used as local oscillators for heterodyne detection of cosmic radiation. A particular advantage results for phase-locked coherent detection within an array of antennas.

Continuous-wave (CW) terahertz sources can be divided into seven categories: electron beam sources; optically pumped far-infrared gas lasers; solid-state sources; frequency multipliers; terahertz semiconductor lasers; terahertz parametric sources; and terahertz photomixers. Sub-sections 1.2.1 to 1.2.7 provide a brief overview of these CW THz sources.

1.2.1 Electron beam sources

Gyrotrons [1.26], free electron lasers (FELs) [1.27], and backward wave oscillators (BWOs) [1.28] are electron beam sources that can generate high power signals at terahertz frequencies. The operation of these devices is based on the interaction of a high-energy electron beam with a strong magnetic field inside resonant cavities or waveguides, which results in an energy transfer between the electron beam and an electro-magnetic wave. Gyrotrons for complete CW operation mode have been designed and constructed [1.29]-[1.33]. The gyrotron is the most powerful source of coherent radiation in the millimetre wave and terahertz region of the electromagnetic spectrum; today gyrotron oscillators produce over 1 MW of average power in continuous (CW) operation at frequencies up to 170 GHz [1.34]. Since gyrotron operation is based on the cyclotron resonance interaction between electrons gyrating in external magnetic fields and electromagnetic waves, the frequency of radiation is proportional to the external magnetic field. Therefore, to realise high-power radiation at wavelengths shorter than 1 mm at the fundamental cyclotron resonance, magnetic fields must exceed 11 T [1.35]. Acceptably expensive superconducting solenoids can provide not more than 15 T, therefore, for the generation of the near-terahertz range of frequencies, operation at higher cyclotron harmonics is needed [1.35]. Optimised for the second harmonic operation of $TE_{4,12}$ at the frequency of 1013.7 GHz, gyrotrons have exhibited output powers of several hundred watts at the fundamental frequency and several tens of watts at the second harmonic operation [1.29].

The figures related to gyrotron power budgets can vary significantly. A frequency-tuneable continuous-wave (CW) 330-GHz gyrotron oscillator, operating at the second harmonic of the electron cyclotron frequency, was reported [1.36]. With a beam voltage of 10.1 kV, a beam current of 190 mA and 18 W of generated power, the corresponding efficiency was equal to 0.9%; the cavity magnetic field was 6 T. The Gyrotron FU CW VII reported in [1.33] emitted 200 W at 203.75 GHz (TE_{42} mode) and 50 W at 395.28 GHz (TE_{l6} mode), with a 9.2 T magnetic field and typical parameters of electron beam such as 10-15 kV acceleration voltage and 200-350 mA beam current. An output power of 600 kW at 170 GHz, was demonstrated in [1.37] at steady-state operation maintained for over one hour. A constant current was maintained at about 30 A, keeping the nominal $TE_{31,8}$ oscillating mode and the stable 600 kW output. An efficiency of 45% was obtained with a depressed collector of 27kV.

Gyrotrons are power hungry systems and are expensive as well as very bulky and heavy. Some reported figures of height/weight are 2.08 m/1041 kg [1.38], 2.7 m/200 kg [1.39], 3 m/800 kg [1.37].

Free-electron lasers use a beam of high-velocity bunches of electrons propagating in a vacuum through a strong, spatially varying magnetic field. The magnetic field causes the electron bunches to oscillate and emit photons. Mirrors are used to confine the photons to the electron beam line, which forms the gain medium for the laser. Such systems impose prohibitive cost and size constraints and typically require a dedicated facility [1.40], [1.41].

1.2.2 Optically pumped far-infrared gas lasers

Optically Pumped Far-Infrared Gas Lasers consist of a CO_2 pump laser radiating into a cavity filled with a gas that lases in the terahertz frequency range [1.42], [1.43]. The lasing frequency is determined by the filling gas, with one of the strongest being that of methanol at 2522.78 GHz; at this frequency an output power of 1.25 W was demonstrated by Farhoomand et al [1.44] for a CO_2 pump power of 125 Watts and a not specified input electrical power.

In general output power levels of 1-20 mW are common for 20–100 W pump laser power depending on the chosen line [1.45]. The lasing process is quite inefficient as the majority of the pump radiation is simply converted to heat [1.46]. For example the theoretical limit on efficiency for the line of methanol at 2522.78 GHz is 4%, but typical efficiency for this transition is on the order of 0.2%, and the best efficiency reported is 1% [1.44]. Also large cavities and kilowatt power supplies are typically required [1.40], such as the high voltage power supply (25 kV, 10 mA) used in [1.47]. Molecular gas lasers can emit at several thousand discrete wavelengths which sparsely cover the THz region [1.47], however these CW sources are not continuously tuneable [1.40]. Solutions to realise tuneability have been suggested in [1.48], [1.18] by mixing a tuneable microwave source with these lasers. It was found [1.49], [1.50] that the lack of tuneability of these lasers is a direct consequence of their operation at low pressure, a requirement seemingly imposed on CW systems by rather fundamental theoretical considerations; Everitt et al. [1.50] suggested that operating the lasers at pressures significantly higher than the maximum allowed by theory, could provide substantial tuneability. Table 1.1 gives a summary of the power emitted in the THz gap by some state of the art optically pumped lasers and gyrotrons oscillator, operating in CW regime.

Table 1.1: Details of the power emitted in the THz gap by state of the art gyrotrons and optically pumped lasers, operating in CW regime. The entries are ordered by type first (gyrotrons and gas lasers) and by frequency then.

Source Description	Output Power (W)	Frequency (THz)
Gyrotron oscillator [1.37]	6×10^5	0.170
Gyrotron FU CW VII [1.33]	200	0.203
Gyrotron oscillator [1.36]	18	0.330
Gyrotron FU CW VII [1.33]	50	0.395
Gyrotron FU CW III [1.29], [1.33]	> 10	1.014
Optically-pumped laser (SIFIR-50 DSW) [1.46]	0.002	0.333
Optically-pumped laser (SIFIR-50 FSW) [1.46]	> 0.1	1.760
CO_2 pumped Far-Infrared Gas Laser [1.44]	1.25	2.523

1.2.3 Solid-state sources

Solid-state sources can be categorised as two-terminal and three-terminal devices [1.51]-[1.54]. Two-terminal devices are commonly used to generate more THz power and can be used as local oscillators for THz mixers and as drivers for frequency multipliers [1.45]. Two-terminal devices include resonant tunnelling diodes (RTDs) [1.55], Gunn or transferred electron devices (TEDs) [1.56], [1.57], and transit time devices such as impact avalanche transit time (IMPATT) diodes and tunnel injection transit time (TUNNETT) diodes. All of these devices exhibit a negative differential resistance (NDR), which is the critical property for oscillation and amplification. The difference arises from how the negative differential resistance is achieved.

An RTD with a graded emitter and a 0.39 μm^2 mesa area was described in [1.58], exhibiting a 7 μW output power at 1.04 THz, for a current peak density of about 23 mA/μm^2 and a 0.8 V voltage at the current peak. In [1.59] an InP Gunn device was demonstrated, which generated 85 μW at 479 GHz for a DC power of about 920 mW. IMPATT diodes generate inevitably high level of phase noise because of the statistical nature of the avalanche process. They have anyway shown high levels of CW power up to 361 GHz. Examples are 78 mW at 185 GHz from a 21 μm diameter diode for a

12.8 V voltage and 780 A/mm^2 current density, which yields a 2.3 % efficiency [1.60]; 7.5 mW at 285 GHz from a 17 µm diameter diode for a 11.7 V voltage and 800 A/mm^2 current density (0.35 % efficiency) [1.60]; 0.2 mW at 361 GHz from a 15 µm diameter diode for 680 A/mm^2 current density and unspecified voltage [1.60].

A GaAs tunnel TUNNETT diode on a diamond heatsink yielded a CW power level of more than 140 µW at 355 GHz in third-harmonic mode for a DC power of about 670 mW [1.61]. The GaAs TUNNETT diode presented in this letter requires much lower DC input power than IMPATT diodes and offers better noise performance than a Si IMPATT diode.

Three-terminal devices have traditionally been used principally for low-noise and wideband amplifiers; progress in power amplifiers has been reported with GaN HEMT (High Electron Mobility Transistors) having achieved more than 0.5 W at 100 GHz and InP HEMTs and HBTs (Heterojunction Bipolar Transistors) having exhibited 30-50 mW around 200 GHz and 1-10-mW around 300 GHz [1.62]. The transistor-based oscillators are also showing improvements; they attain negative differential resistance (NDR) from the circuit-level property of transistor networks, instead of the device-level property exploited for two-terminal oscillators. Various types of topologies, such as LC cross-coupled, Colpitts, and ring, have been employed for THz oscillators [1.63].

1.2.4 Frequency multipliers

Frequency multipliers are nonlinear devices that generate a specific harmonic of an input sine signal and suppress undesired ones. They require a matching network at the input and output frequencies, but also at the undesired (idler) frequencies to optimize the transfer of power from the fundamental frequency to the desired harmonic [1.64] which makes the building of high order frequency multipliers difficult. The most efficient terahertz frequency multipliers are realised by series chain of frequency doublers and frequency triplers [1.4]. Multiplier chains formed with cascaded Schottky doublers and/or triplers have been broadly used in the last two decades to up-convert the signal provided by the available solid-state sources at 100-150 GHz [1.65], [1.66].

A frequency multiplier chain able to generate up to 1.4 mW of output power across the 840–900-GHz band at room temperature was demonstrated in [1.67]. These power levels were made possible by the use of in-phase power combining of frequency multiplier chips, previously proposed in [1.68], and by the advances in planar GaAs Schottky diode multipliers. The chain consists of a W-band power amplifier module that drives two cascaded frequency triplers. The driver chain of the 900-GHz in-phase power-combined frequency tripler includes a W-band synthesizer followed by a high power power-combined W-band amplifier module, and a power-combined 300-GHz frequency tripler based on [1.68]. When pumped with 330–500 mW, this tripler delivers 29-48 mW in the 276–321-GHz band. The 900-GHz tripler output power was measured in the 826–950-GHz band. The conversion efficiency is explicitly stated only for the second tripler and was calculated by dividing the power levels recorded at the output of the 900-GHz chain by the power levels recorded at the output of the driver stage; this conversion efficiency is in the range of 2.1% to 2.5% in the frequency range 849.6 GHz to 898.2 GHz, whereas decreases from 2.4% to 0.3% between 900–950 GHz. The overall efficiency of the whole chain will be significantly smaller as the efficiency of the driver section has to be included and the DC power supply should also be taken into account. The next generation of Schottky multipliers should be able to take advantage of the advances and the high power already available from driver amplifiers based on InP high electron-mobility transistors (HEMTs) [1.62].

1.2.5 Terahertz semiconductor lasers

Very promising terahertz semiconductor sources are Quantum Cascade Lasers (QCLs) [1.69]-[1.73]. A QCL is a unipolar laser, in which the conduction band or the valence band is divided into a few sub-bands. The carrier transition occurs between these discrete energy levels within the same band. The discrete energy levels are created in a semiconductor heterostructure containing several coupled quantum wells. The idea of QCLs was introduced in 1971 [1.69], however the first QCL was demonstrated at the wavelength of 4 µm (75 THz) at Bell Labs in 1994 [1.70]. The first QCL with a photon energy less than the semiconductor optical phonon energy was demonstrated at a wavelength of 67 µm (4.4 THz) by Köhler et al. [1.6] at the Scuola

Normale Superiore in Pisa, in a collaboration with Cambridge University; later in 2006 a QCL operating at 1.6 THz was also demonstrated [1.74]. Quantum Cascade Lasers are not ideal for most terahertz applications as their tuning range is limited [1.75] and, most importantly, they must operate at energy levels close to the lattice phonon to generate THz radiation, therefore requiring cryogenic cooling and in some cases the support of strong magnetic fields.

In any case the output power drops significantly as the frequency decreases across the spectral coverage 0.84 THz to 5.0 THz which has been demonstrated [1.76]. In [1.77], for a 10 K operating temperature, a 123 mW CW output power was demonstrated at 4.4 THz, with a voltage and a current of about 11.5 V and 1.9 A respectively, which yields 0.5 % efficiency; it should be noted that, once the power consumption of the cooling system is also taken into account, the wall-plug efficiency of THz QCLs systems integrated with pulsed-tube cryorefrigerators or Stirling cryocoolers can get as low as 0.001 % [1.78]. An even higher power (138 mW) was generated in the same experiment, using a QCL with a wider and shorter ridge, but the resulting efficiency was lower. Significantly smaller levels of power have been instead demonstrated, for the same 10 K operating temperature, at the low end of the demonstrated spectral coverage, e. g. 360 µW in the range 1.6 THz to 1.8 THz [1.74] and 100 µW at 1.3 THz [1.79].

A new emerging solution, employing the QCL technology to generate tuneable THz radiation at room temperature, is based on intracavity difference-frequency generation (DFG) in dual-wavelength mid-infrared quantum cascade lasers [1.78], [1.80]. Terahertz quantum cascade laser sources based on an optimised non-collinear Cherenkov difference-frequency generation scheme demonstrated a tuneable external-cavity (EC) THz QCL source, with a tuning range spanning 1.70-5.25 THz [1.78]. Devices emitting at 4 THz exhibited a mid-infrared-to-terahertz conversion efficiency greater than 0.6 mW/W^2 and generated nearly 0.12 mW of peak output power; devices emitting at 2 THz and 3 THz fabricated on the same chip displayed output powers of 12 µW and 36 µW respectively, with 0.09 mW/W^2 and 0.4 mW/W^2 mid infrared-to-terahertz conversion efficiency at room temperature. The wall-plug efficiency of these DFG-QCL systems remains less than 10^{-6}, with the maximum value of 9 x 10^{-7} obtained at 4THz.

1.2.6 Terahertz parametric sources

Parametric interaction in nonlinear crystals can generate terahertz waves via interaction of near-infrared photons and optical vibration modes inside a nonlinear optical crystal, as observed for the first time in 1969 [1.81]. In this process, the energy of an input pump photon with frequency f_P is partially depleted through parametric interaction with the optical vibration modes inside the crystal and produces a Raman-shifted Stokes photon with frequency f_S [1.82]. Consequently, the difference frequency generation (DFG) process between the pump and the Stokes photons inside the nonlinear crystal generates a terahertz signal with frequency f_T, such that $f_T = f_P - f_S$ to fulfil the law of conservation of energy.

Nonlinear crystals are also used for difference frequency mixing where narrow band THz signals can be generated by mixing two frequency detuned narrow linewidth laser beams inside the crystals [1.83]-[1.87]; in this case both input laser beams are generated outside the crystal and are coupled into the crystal for mixing purpose. Efforts to generate pure CW THz radiation have been made.

A continuous-wave optical parametric terahertz light source is presented in [1.88]. This source employs simultaneous phase matching of two nonlinear processes within one periodically-poled lithium niobate crystal, situated in an optical resonator, and coherently emits a diffraction-limited terahertz beam that is tuneable from 1.3 THz to 1.7 THz with power levels exceeding 1 µW; the linewidths of the generated THz signal-wave is estimated to be about 1 MHz, while the required optical pump power ranges from 6 W to 12 W.

Continuous-wave terahertz was demonstrated in [1.89] by laser diode (LD) pumping in non-collinear phase-matched difference frequency generation (DFG); the authors also discuss the effects of interaction length and beam spot size of the input lasers (near-IR) in GaP crystals. This system generates narrow linewidth CW THz radiation and offers quite a wide tuneability, previously demonstrated from 0.69 THz to 2.74 THz in [1.90]. The CW output power is limited, with a level of 4 nW obtained with a 20 mm long GaP crystal at 1.5 THz; the pump laser power is not given but the authors indicated having used in [1.89] two fibre amplifiers (FAs) to amplify the output power of each laser diode as the maximum pump laser power in their previous work [1.90] was below a few hundred mW.

1.2.7 Terahertz photomixers

Terahertz photomixers are coherent CW THz sources continuously tuneable over a very wide frequency range. They are among the most promising candidates for developing compact, low-power consuming, and low-cost THz spectroscopy and imaging systems operating at room temperature, for various THz applications [1.45]. To date, photoconductors based on Low-Temperature Grown GaAs (LT-GaAs) have been the prevalent types of photomixing elements. Photoconductive or electro-optic techniques have been extensively employed for coherent detection in photomixing-based terahertz systems. The success of this technology has relied mainly on the sensitivity of the detection rather than the power capability of the emitter since the exploitation of photoconductive effects can offer limited output power levels [1.91]. Recently though, Peytavit et al [1.92] have demonstrated a continuous wave output power, from a low-temperature-grown GaAs photoconductor, reaching 1.8 mW at 252 GHz for a 270 mW input optical power, a 24 mA DC photocurrent and a 3 V bias voltage; such a high level of output power was made possible by the use of a metallic mirror-based Fabry-Pérot cavity and an impedance matching circuit. An essential merit of the device discussed in [1.92] is the high level of saturation current as saturation begins to show for an optical input power of 180 mW and is attributed mainly to thermal effects; the photoconductor is believed to handle such a high thermal power thanks to the thermal management built on the thinness of the LT-GaAs layer and the high thermal conductivities of the buried gold layer and the silicon substrate.

CW terahertz systems can substantially benefit from migrating to the InP material system since many optical functions can be implemented with “off-the-shelf” cheap, compact and reliable components [1.93], [1.94]; InP has also been the enabling material for the development and mass production of optoelectronic devices that operate in the low loss window of single mode optical fibres (SMF) at 1550 nm [1.95]. The need for high speed devices with high saturation currents led to the development of the Uni-Travelling Carrier Photodiode (UTC-PD) [1.96], [1.97] whose most popular implementation based on InP materials is nowadays an established solution for CW terahertz generation via photomixing. The photo-response of the UTC-PD is dominated by the electron transport in the whole structure. This is an essential difference from the conventional pin PD, where both electrons and holes contribute to the response, and the low-velocity hole-transport dominates the performance. The velocity of electrons (3-5×10^7 cm/s) is 6-10 times higher than that of holes (5×10^6 cm/s) and in the UTC-PD, electrons exhibit velocity overshoot in the InP carrier collection layer; in addition the UTC-PD generates higher output saturation current even in the high-frequency operation due to the reduced space charge effect in the depletion layer, which also results from the high electron velocity in the depletion layer [1.98]. These properties make the UTC-PD a high speed and high output power photodiode. An output power of 0.75 W (28.8 dBm) at 15 GHz from a modified UTC (MUTC) was demonstrated in [1.99] for a saturation current greater than 180 mA and a reverse bias of 11 V. A 3 dB bandwidth of 310 GHz was demonstrated in [1.100] from an ultra-thin (30 nm) InGaAs absorption layer UTC; the bandwidth value was obtained with a pulsed measurement returning a full width at half maximum (FWHM) of 0.97 ps for a reverse bias voltage -0.5 V and an input power of 0.14 pJ/pulse. Also, a 3 dB bandwidth higher than 110 GHz and 10 mW extracted power at 110 GHz were demonstrated in [1.101], for 100 mW of optical input power (up to 36 mA of DC photocurrent) and 2 V reverse bias.

Figure 1.2 shows the state of the art of the output power generated in the frequency range 15 GHz to 5 THz by different semiconductor CW terahertz sources operating at room temperature, while Table 1.2 provides further details of such sources. This is a constantly evolving scenario where new performance records are set regularly.

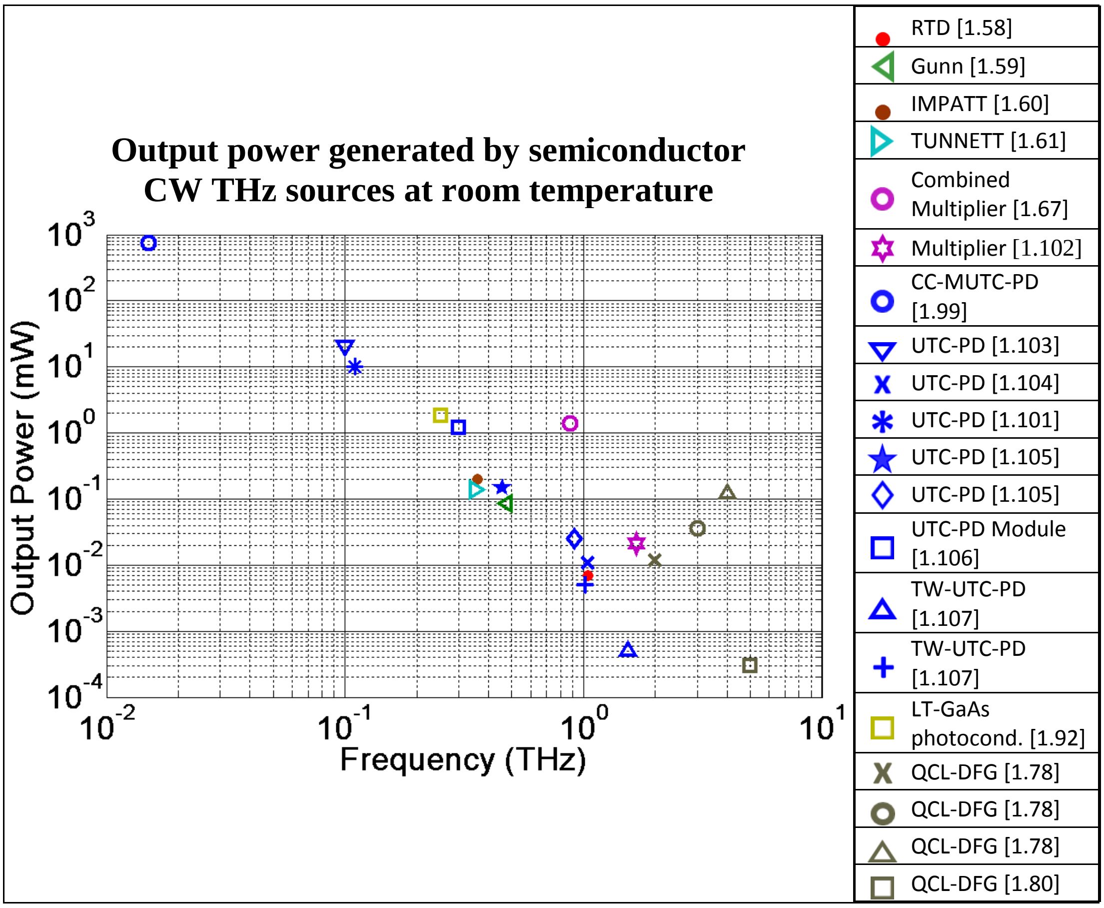

Figure 1.2: Output power generated in the frequency range 15 GHz to 5 THz by different semiconductor CW THz sources operating at room temperature.

Table 1.2: Details of state of the art semiconductor CW THz sources operating at room temperature.

Source Description	Output Power (mW)	Frequency (THz)
GaInAs/AlAs double-barrier resonant tunneling diode (**RTD**) [1.58]	7×10^{-3}	1.040
InP **Gunn** device [1.59]	85×10^{-3}	0.479
p^{+}-p^{-}-n^{+} silicon impact avalanche transit time (**IMPATT**) diode [1.60]	200×10^{-3}	0.361
GaAs tunnel injection transit-time (**TUNNETT**) diode [1.61]	140×10^{-3}	0.355
Chain of a power amplifier module driving two cascaded frequency triplers (**Combined Multiplier**) [1.67]	1.4	0.875
Fix-tuned x 2 x 3 x 3 frequency multiplier chain (**Multiplier**) [1.102]	21×10^{-3}	1.640
40-µm back-illuminated and flip-chip-bonded, charge-compensated modified uni-travelling carrier photodiode (**CC-MUTC-PD**) [1.99]	750	0.015
Double-mesa back-illuminated uni-travelling carrier photodiode (**UTC-PD**) with an absorption area of 30 µm^2 [1.103]	20.8	0.100
Double-mesa back-illuminated uni-travelling carrier photodiode (**UTC-PD**) integrating resonant narrowband dipole antennae [1.104]	10.9×10^{-3}	1.04
Edge-coupled waveguide uni-travelling carrier photodiode (**UTC-PD**) [1.101]	10	0.110
Edge-coupled waveguide uni-travelling carrier photodiode (**UTC-PD**) [1.105]	148×10^{-3}	0.457
Edge-coupled waveguide uni-travelling carrier photodiode (**UTC-PD**) [1.105]	25×10^{-3}	0.914
Uni-travelling carrier photodiode module (**UTC-PD Module**) with two identical UTC-PDs monolithically integrated along with a T-junction to combine the power from the two PDs. [1.106]	1.2	0.300
Travelling wave uni-traveling carrier photodiode employing a mode-converting waveguide (**TW-UTC-PD**) [1.107]	5×10^{-3}	1.02
Travelling wave uni-traveling carrier photodiode employing a mode-converting waveguide (**TW-UTC-PD**) [1.107]	0.5×10^{-3}	1.53
Low-temperature-grown GaAs photoconductor using a metallic mirror-based Fabry-Pérot cavity and an impedance matching circuit (**LT-GaAs photoconductor**)[1.92]	1.8	0.252
Terahertz quantum cascade laser sources based on an optimized non-collinear Cherenkov difference-frequency generation generation (**QCL-DFG**)[1.78]	12×10^{-3}	2
Terahertz quantum cascade laser sources based on an optimized non-collinear Cherenkov difference-frequency generation generation (**QCL-DFG**)[1.78]	36×10^{-3}	3
Terahertz quantum cascade laser sources based on an optimized non-collinear Cherenkov difference-frequency generation generation (**QCL-DFG**)[1.78]	0.12	4
Room temperature terahertz quantum cascade laser source based on intracavity difference-frequency generation (**QCL-DFG**) [1.80]	0.3×10^{-3}	5

As mentioned previously, the objective of this work is the realisation of high-power and room-temperature Continuous Wave (CW) Photonic Terahertz Emitters employing Antenna-Integrated Uni-Travelling-Carrier Photodiodes (UTC-PDs). The role played by the THz antenna is central to the achievement of this goal. At low microwave frequencies and below, the consolidated and systematic knowledge of antennas, both in terms of theory and practical applications, allows engineers to optimise those properties that are essential to maximise the antenna performance (e. g. matching to the driving source, radiation efficiency and far-field radiation pattern) and are strongly frequency dependent. In the author's opinion such a thorough and systematic approach is still to be extended to the world of sub-millimetre and THz waves, having often being underestimated in favour of the physics of the device employed as a source, and yet it is indispensable to understand and optimise the operation of CW THz emitters. In the next section a brief discussion is presented regarding the role and importance of planar antennas in a photonic THz emitter, while a short review of the state of the art of antennas employed in the frequency range from millimetre to THz waves will be given in Chapter 5.

1.3 Terahertz (THz) antennas

The use of high performance uni-travelling carrier photodiodes, as devices enabling high optical-to-electrical (O-E) conversion efficiency, is central to the realisation of photonic terahertz emitters. An equally important factor, to achieve high performance in such emitters, is the realisation of the best possible terahertz antenna, ideally having a wide bandwidth, both in terms of radiation pattern and the efficiency of energy coupling from the driving source, in order to exploit the tuneability of photonic THz sources. Also, succeeding in achieving such high performance from antennas with a planar geometry, would be a breakthrough because of the easy and practical on-chip integration to photodiodes.

To meet the need of high gain and directivity, several antennas with different objectives have been developed but, for instance, compatibility with communication systems of these antennas is difficult. Waveguide and planar antennas have traditionally been regarded as suitable for communication systems as they can be integrated with monolithic transceiver systems. Waveguide type antennas have extensively been studied and even used in the terahertz communication systems. On the other hand, planar antennas are attractive due to integration, low cost, and lightweight, but suffer from low directivity and radiation efficiency. For this reason, planar antenna systems have not yet found much place in sub-millimetre wave and terahertz communication systems; hence, there is the need to explore the potential of this type of antenna at terahertz frequencies [1.8].

With regards to THz wireless communication applications, the essential role played by antenna properties, such as gain and efficiency of energy coupling to the driving source, is obvious from the well-known Friis equation, first derived by Harald T. Friis at Bell Labs in 1945 [1.108] and here shown in its generalised form (1.1). The generalised Friis equation essentially allows us to calculate the fraction of the power made available to the transmitting antenna, that is ultimately delivered to the load connected to the receiving antenna (P_r/P_t), within a radio circuit made up of a transmitting antenna and a receiving antenna in free space.

$$\frac{P_r}{P_t} = G_t(\theta_t, \varphi_t)G_r(\theta_r, \varphi_r)\left(\frac{\lambda}{4\pi d}\right)^2 (1 - |\Gamma_t|^2)(1 - |\Gamma_r|^2)(PLF)e^{-\alpha d} \tag{1.1}$$

The significance of the factors on the right hand side term of (1.1) is described as follows. **1)** G_t and G_r represent the gains of the transmitting and receiving antenna respectively, and are function of the angles θ and φ in a spherical reference system. It is noted that the antenna gain comprises both the directivity and the radiation efficiency and, for instance, if part of the power delivered to the antenna from the source is lost into the antenna as heat, instead of being coupled into free space, then the radiation efficiency will be less than 1 (e. g. less than 0 dB) and the gain will be smaller than the directivity. **2)** λ is the wavelength at the operating frequency, in the propagation medium. **3)** d is the distance between the transmitting and the receiving antenna. **4)** Γ_t and Γ_r are the reflection coefficients of the voltage wave at the source/transmitting-antenna interface and at the receiving-antenna/load interface respectively. When the source impedance and the load are real then $(1 - |\Gamma_t|^2)$ and $(1 - |\Gamma_r|^2)$ represent the fraction of power provided by the source that is accepted by the transmitting antenna and the fraction of power captured by the receiving antenna that is accepted by the load, therefore minimising $|\Gamma_t|$ and $|\Gamma_r|$ is equivalent to maximising the power transfer. When the source impedance is complex, as is the case for the UTC, then the complex/conjugate matching to the antenna impedance needs to be considered. **5)** PLF is the Polarisation Loss Factor and takes into account the polarisation mismatch between the radiated electric field and the receiving antenna. **6)** α is the absorption coefficient in the transmission medium and the term $e^{-\alpha d}$ accounts for the absorption loss across the whole distance d. The absorption losses between 0.1 – 1.0 THz are mainly due to strong absorption of THz radiation by atmospheric water vapour, nevertheless windows of fairly high transmission are present, especially at the lower THz frequencies, where transmission over paths greater than 100 meters is feasible [1.109]. Figure 1.3 plots the attenuation from 0.1 THz to 1 THz, for six different atmospheric conditions, all at sea level, representing the extremes from very low atmospheric attenuation in the winter, to very high levels in tropical climates [1.110].

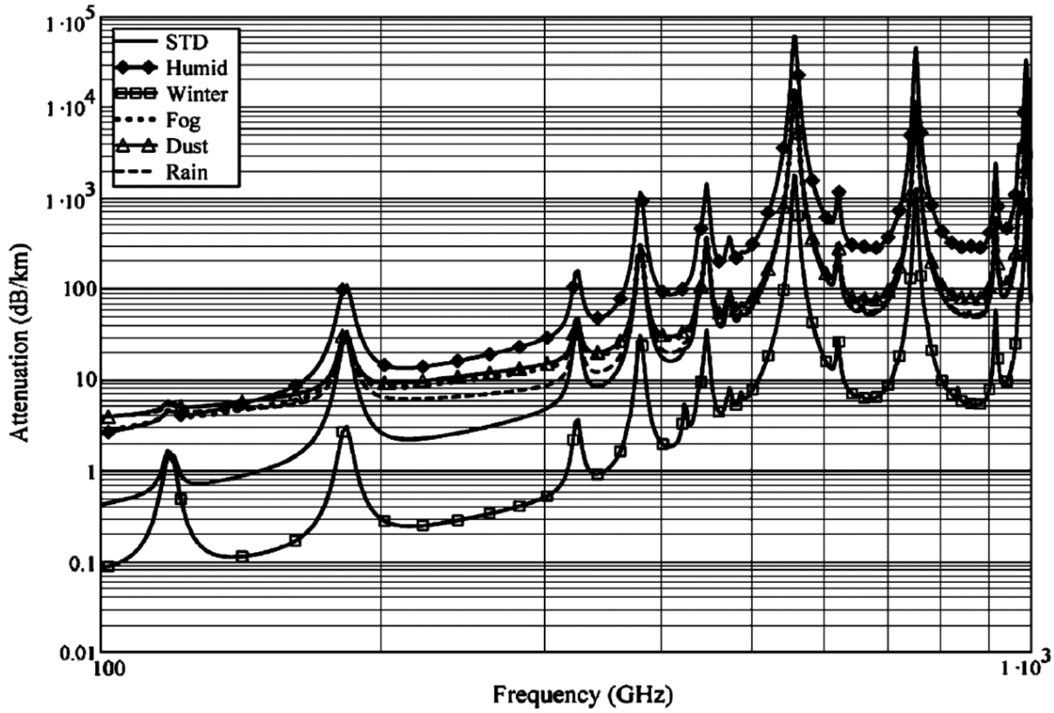

Figure 1.3: Atmospheric attenuation at sea level pressures for six different conditions of temperature, humidity, and atmospheric particulates [1.110].

Thus, if the realisation of a source capable of generating high levels of power, such as the UTC-PDs employed in the THz photonic emitters discussed in this work, is essential for the overall performance, it is evident from (1.1) how the careful design of the antenna plays an absolutely vital role in maximising the fraction of generated power ultimately delivered to the target load. The maximisation of the efficiency of energy coupling at the source/transmitting-antenna interface and at the receiving-antenna/load interface, requires the knowledge of source and load impedance, to be matched to the antenna impedance in order to achieve a maximum transfer of power in the frequency range of interest. On the other hand, directivity and radiation efficiency are intrinsic properties of antennas and their optimisation is irrespective of the driving source and the load.

Optimising the gain of an antenna in transmission will also result in the antenna being optimised as a receiver, as indicated in the principle of reciprocity in antenna theory, proposed by M. S. Neiman [1.111]. Antennas do not have distinct transmit and receive radiation patterns and if the radiation pattern in the transmit mode is known, then the pattern in the receive mode is also known. It follows that the better an antenna radiates energy the better it collects it. As a consequence, the optimisation of the antenna parameters in a photonic THz emitter will also contribute to the realisation of better THz receivers and more sensitive detectors.

The essential role played by the antenna properties, quantified in equation (1.1), is then obvious not only with regards to wireless communication applications, but for all THz applications employing antenna integrated devices such as, among others, spectroscopy sensing and imaging. In effect, the first THz antennas to be developed were intended for applications other than wireless communications which had not yet been considered [1.3], [1.112].

1.4 Organisation of the thesis and key novel contributions

Chapter 2 discusses the first ever reported InGaAsP-based uni-travelling carrier photodiodes fabricated from a structure grown by Solid Source Molecular Beam Epitaxy (SS-MBE). The use of Solid Source Molecular Beam Epitaxy enables the major issue associated with the unintentional diffusion of zinc in Metal Organic Vapour Phase Epitaxy to be overcome and gives the benefit of the superior control provided by MBE growth techniques without the costs and the risks of handling toxic gases of Gas Source Molecular Beam Epitaxy. Large area vertically illuminated test UTCs were fabricated and characterised. Material growth, device fabrication and characterisation were all carried out at UCL; this achievement is a milestone towards the development of a simple, repeatable and high yield fabrication process enabling the realisation of high performance UTCs, from material growth to device fabrication. The next step is the fabrication of edge-coupled waveguide UTC, also reported in this chapter; an outline of the fabrication process and some results obtained from the first devices which have been fabricated are shown.

Chapter 3 reports the experimental characterisation and circuit analysis of waveguide UTCs. The device impedance and S_{11} have been measured up to 110 GHz and the frequency photo-response up to 67 GHz. A detailed analysis is performed to find out why the classical diode circuit model, based on the junction-capacitance/series-resistance concept, cannot explain the experimental data. A new circuit model is proposed, to explain the observations, that achieves very good agreement with the measurements and a link is suggested between the additional energy storage circuit elements present in the new circuit and quantum mechanical effects taking place between the UTC absorption and collection layers. An evaluation of the quasi-field generated in the absorber of the analysed UTCs by the graded doping profile is also carried out, in order to take the transit time limited response into account.

Chapter 4 presents the 3D full-wave modelling and simulation of the UTC structure at sub-millimetre wave frequencies and at optical frequencies. Building on the results obtained in the previous chapter, the full-wave modelling allows the device S_{11} and impedance to be calculated and refined up to 400 GHz; the UTC frequency photo-response is also modelled. The results obtained enable the question regarding the UTC-to-antenna coupling efficiency to be more thoroughly understood. This chapter also presents 3D full-wave optical modelling and simulation, aiming to better understand and improve the optical power coupling between lensed fibre and UTC optical waveguide. The coupling between an incident Gaussian beam and the UTC optical waveguide is also analysed.

Chapter 5 describes new THz antenna designs, obtained by means of full-wave electromagnetic modelling, which prove to be suitable for integration with both standard silicon lenses and a novel solution employing a ground plane. Realising accurate alignment between silicon lens and antenna chip is essential to optimise the radiation pattern and yet is a challenging task to accomplish; antennas integrated with ground planes do not require such alignment. The effect of misalignment between antenna chip and substrate lens on the radiation pattern is shown. The ground plane solution can offer advantages in terms of heat dissipation, as it is more suitable for the realisation of efficient heat sinks. In this chapter the case study of a large bow-tie antenna is also presented and the comparison between modelled and measured radiated power is discussed; it is shown that the knowledge about the UTC impedance achieved in Chapter 3 and 4 enables the radiated power to be predicted with satisfactory accuracy while the radiated power calculated based on the classical junction-capacitance/series-resistance concept is in substantial disagreement with the measurements.

Chapter 6 presents a detailed analysis regarding the use of a sub-wavelength aperture probe to investigate THz emission, particularly in antenna near- and far-fields. Thanks to its excellent properties as a near-field detector, the probe enables the reconstruction of the electric field in the vicinity of antennas and can be employed as a tool to assist the realisation of the optimum terahertz antenna via experimental analysis of the antennas designed numerically. The achieved full understanding of the near-field probe response and its limited invasiveness allow the distribution of the electric field, and hence surface currents, to be extracted, providing important information about THz antenna operation. The probe also exhibits properties enabling accurate detection of far-fields and the experimental system incorporating the probe is suited to map antenna far-field radiation patterns; therefore the sub-wavelength aperture probe can be a valid tool to measure the far-field radiation pattern of antenna integrated photodetectors at sub-millimetre wave and THz frequencies, where this type of measurement is challenging and no standard experimental arrangements are available.

Chapter 7 reports three different designs to realise UTC PDs monolithically integrated with THz antenna arrays with ground planes and substrate lenses. A 2 x 2 antenna array with a ground plane exhibits good performance in terms of radiation pattern and radiation efficiency although requiring a challenging fabrication process to separate the antenna elements and eliminate the mutual coupling. A second 2 x 2 antenna array design with a ground plane overcomes the mutual coupling problem without requiring difficult fabrication and is suitable for realisation of large arrays, but exhibits a narrower bandwidth. The modelling of a 2 x 2 antenna array with a silicon lens shows that substrate lenses are not suited to antenna arrays. This is due to the fact that the alignment between a substrate lens and the emitter is essential to obtain a good radiation pattern; when a lens is integrated with an array, each antenna element is inevitably misaligned with the lens.

Chapter 8 gives a summary of the thesis, draws conclusions about the presented work and indicates ideas for follow up and future work. In the next section a list is provided of the key novel results achieved by the research work presented in this thesis. Parts of these novel contributions have already been published on peer reviewed journals and presented at peer reviewed conferences; a list of publications can be found before the table of contents. Additional papers are in preparation.

1.4.1 Key novel contributions

- First reported InGaAsP based Uni-Travelling Carrier Photodiodes from a structure grown by Solid Source Molecular Beam Epitaxy. Large area vertically illuminated test devices and broad band edge-coupled waveguide devices have been realised.
- Semi analytical study of waveguide UTC impedance, S_{11} and photo-response up to 400 GHz, supported with experimental data taken up to 110 GHz and circuit analysis.
- 3D full-wave electromagnetic modelling of a waveguide UTC structure, allowing a further refinement of the UTC impedance knowledge to be achieved and enabling, for the first time, an in depth understanding of the UTC to antenna coupling efficiency question.
- Use of the UTC impedance knowledge to calculate, by means of full-wave modelling, the power radiated by an antenna integrated UTC and comparison with the experimental measurements, not only in terms of trend over the

frequency range but even in terms of absolute level of emitted power. Good agreement is obtained.

- Design of high radiation efficiency and high directivity sub-millimetre wave planar antennas with ground planes on electrically thick substrates. High radiation efficiency and high directivity sub-millimetre wave planar antennas have been previously designed only on substrate lenses and thin membranes.
- Improved antenna design to bring the ground plane close to the antenna. This solution is suited to antenna array realisation, as the substrate modes are suppressed and the deleterious mutual coupling between antenna elements is greatly reduced.
- The first 3D full-wave modelling of an antenna array on a hyper-hemispherical silicon lens at sub-millimetre wave frequencies.
- Evaluation of the effect of misalignments between substrate lens and antenna chip by means of 3D full-wave modelling.
- The first in-depth study of the response of a sub wavelength aperture probe and its use as an additional experimental tool for the analysis of antenna near- and far-field properties.
- The first design of sub-millimetre wave UTC antenna arrays with ground planes on electrically thick substrates and novel design with a ground plane close to the antenna elements.

1.5 References

[1.1] M. Tonouchi, "Cutting-edge terahertz technology," *Nature Photonics*, vol. 1, no. 2. Nature Publishing Group, pp. 97–105, 2007.

[1.2] E. J. Nichols and J. D. Tear, "Joining the infrared and electric wave spectra," *Astrophys. J.*, vol. 61, pp. 17–37, 1925.

[1.3] K. R. Jha and G. Singh, "Terahertz planar antennas for future wireless communication: A technical review," *Infrared Physics and Technology*, vol. 60. pp. 71–80, 2013.

[1.4] P. H. Siegel, "Terahertz technology," *IEEE Trans. Microw. Theory Tech.*, vol. 50, no. 3, pp. 910–928, 2002.

[1.5] P. Mukherjee and B. Gupta, "Terahertz (THz) Frequency Sources and Antennas - A Brief Review," *Int. J. Infrared Millimeter Waves*, vol. 29, no. 12, pp. 1091–1102, Sep. 2008.

[1.6] R. Kohler, A. Tredicucci, F. Beltram, H. Beere, E. Linfield, G. Davies, D. Ritchie, R. Iotti, and F. Rossi, "Terahertz-semiconductor-heterostructure laser," *Nature*, vol. 171, no. 6885, pp. 156–159, May 2002.

[1.7] T. Nagatsuma, "Generating millimeter and terahertz waves," *Microw. Magazine IEEE*, vol. 10, no. 4, pp. 64–74, 2009.

[1.8] K. R. Jha and G. Singh, *Terahertz Planar Antennas for Next Generation Communication*. Cham: Springer International Publishing, 2014.

[1.9] D. L. Woolard, E. R. Brown, M. Pepper, and M. Kemp, "Terahertz frequency sensing and imaging: A time of reckoning future applications?," *Proc. IEEE*, vol. 93, no. 10, pp. 1722–1743, Oct. 2005.

[1.10] H. Eisele, "State of the art and future of electronic sources at terahertz frequencies," *Electronics Letters*, vol. 46, no. 26. pp. s8 – s11, 2010.

[1.11] C. Mann, "Practical challenges for the commercialisation of terahertz electronics," *IEEE MTT-S Int. Microw. Symp. Dig.*, pp. 1705–1708, Jun. 2007.

[1.12] J. D. Kraus and R. J. Marhefka, *Antenna for all applications*, 3rd ed. Boston: Tata McGraw-Hill, 2002.

[1.13] W. R. Tribe, "Hidden object detection: security applications of terahertz technology," *Proc. SPIE*, vol. 5354, pp. 168–176, 2004.

[1.14] A. J. Seeds, M. J. Fice, K. Balakier, M. Natrella, O. Mitrofanov, M. Lamponi, M. Chtioui, F. van Dijk, M. Pepper, G. Aeppli, a. G. Davies, P. Dean, E. Linfield, and C. C. Renaud, “Coherent terahertz photonics,” *Opt. Express*, vol. 21, no. 19, pp. 22988–23000, Sep. 2013.

[1.15] A. J. Seeds, G. Aeppli, K. Balakier, A. G. Davies, M. Fice, E. H. Linfield, O. Mitrofanov, M. Natrella, M. Pepper, E. Rouvalis, and C. C. Renaud, “Coherent terahertz systems,” *Microw. Photonics (MWP), 2012 Int. Top. Meet.*, pp. 278–281, 2012.

[1.16] J. R. Demers, R. T. Logan, and E. R. Brown, “An optically integrated coherent frequency-domain THz spectrometer with signal-to-noise ratio up to 80 dB,” *Microw. Photonics, 2007 IEEE Int. Top. Meet.*, pp. 92–95, 2007.

[1.17] H. J. Song, N. Shimizu, T. Furuta, K. Suizu, H. Ito, and T. Nagatsuma, “Broad band-frequency-tunable sub-terahertz wave generation using an optical comb, AWGs, optical switches, and a uni-traveling carrier photodiode for spectroscopic applications,” *J. Light. Technol.*, vol. 26, no. 15, pp. 2521–2530, 2008.

[1.18] G. A. Blake, K. B. Laughlin, R. C. Cohen, K. L. Busarow, D. H. Gwo, C. A. Schmuttenmaer, D. W. Steyert, and R. J. Saykally, “Tunable far infrared laser spectrometers,” *Rev. Sci. Instrum.*, vol. 62, no. 7, pp. 1693–1700, 1991.

[1.19] G. Carelli, A. Moretti, D. Pereira, and F. Strumina, “Heterodyne frequency measurements of FIR laser lines around 1.2 and 1.6 THz,” *IEEE J. Quantum Electron.*, vol. 31, no. 1, pp. 144–147, 1995.

[1.20] A. S. Pine, R. D. Suenram, E. R. Brown, and K. A. Mcintosh, “A Terahertz Photomixing Spectrometer : Application to SO2 Self Broadening,” *Baseline*, vol. 47, no. 1, pp. 37–47, 1996.

[1.21] D. M. Mittleman, R. H. Jacobsen, R. Neelamani, R. G. Baraniuk, and M. C. Nuss, “Gas sensing using terahertz time-domain spectroscopy,” *Appl. Phys. B-Lasers Opt.*, vol. 67, no. 3, pp. 379–390, 1998.

[1.22] D. F. Plusquellic, K. Siegrist, E. J. Heilweil, and O. Esenturk, “Applications of terahertz spectroscopy in biosystems,” *ChemPhysChem*, vol. 8, no. 17, pp. 2412–2431, Dec. 2007.

[1.23] B. M. Fischer, H. Helm, and P. U. Jepsen, “T-ray spectroscopy of biomolecules: from chemical recognition toward biochip analysis-horizons and hurdles,” *Proc. SPIE 6038, Photonics Des. Technol. Packag. II*, vol. 6038, pp. 603809 1 – 603809 13, Dec. 2006.

[1.24] M. Nagel, P. Haring Bolivar, M. Brucherseifer, H. Kurz, A. Bosserhoff, and R. Büttner, “Integrated THz technology for label-free genetic diagnostics,” *Appl. Phys. Lett.*, vol. 80, no. 1, pp. 154–156, 2002.

[1.25] "The Atacama Large Millimeter/submillimeter Array (ALMA)." [Online]. Available: http://almaobservatory.org/en/home. [Accessed: 10-Mar-2015].

[1.26] K. L. Felch, B. G. Danly, H. R. Jory, K. E. Kreischer, W. Lawson, B. Levush, and R. J. Temkin, "Characteristics and applications of fast-wave gyrodevices," *Proc. IEEE*, vol. 87, no. 5, pp. 752–781, 1999.

[1.27] S. Krishnagopal and V. Kumar, "Free-electron lasers," *Radiat. Phys. Chem.*, vol. 70, no. 4–5, pp. 559–569, Jul. 2004.

[1.28] R. Kompfner and N. Williams, "Backward-Wave Tubes," *Proc. IRE*, vol. 41, no. 11, pp. 1602–1611, 1953.

[1.29] T. Idehara, I. Ogawa, and H. Mori, "A THz Gyrotron FU CW III with a 20T superconducting magnet," *J. Plasma Fusion Res. Ser.*, vol. 8, pp. 1508–1511, 2009.

[1.30] T. Idehara, I. Ogawa, H. Mori, S. I. Kobayashi, S. Mitsudo, and T. Saito, "A THz gyrotron FU CW III with a 20T superconducting magnet," *33rd Int. Conf. Infrared Millim. Waves 16th Int. Conf. Terahertz Electron. 2008, IRMMW-THz 2008*, pp. 1–2, 2008.

[1.31] A. C. Torrezan, S. T. Han, I. Mastovsky, M. a Shapiro, J. R. Sirigiri, R. J. Temkin, A. B. Barnes, and R. G. Griffin, "Continuous-wave operation of a frequency-tunable 460-GHz second-harmonic gyrotron for enhanced nuclear magnetic resonance," *IEEE Trans. Plasma Sci.*, vol. 38, no. 6 part 1, pp. 1150–1159, Jun. 2010.

[1.32] L. Agusu, T. Idehara, H. Mori, T. Saito, I. Ogawa, and S. Mitsudo, "Design of a CW 1 THz gyrotron (gyrotron Fu Cw III) using a 20 T superconducting magnet," *Int. J. Infrared Millimeter Waves*, vol. 28, no. 5, pp. 315–328, 2007.

[1.33] T. Idehara, T. Saito, I. Ogawa, and Y. Tatematsu, "High power THz technologies opened by high power radiation sources - Gyrotrons," *2010 Int. Kharkov Symp. Phys. Eng. Microwaves, Millim. Submillim. Waves, MSMW'2010*, pp. 1–6, 2010.

[1.34] R. Temkin, "High power gyrotrons and their appplications," *Plasma Sci. (ICOPS), 2013 Abstr. IEEE Int. Conf.*, p. 1, 2013.

[1.35] R. Pu, G. S. Nusinovich, O. V. Sinitsyn, and T. M. Antonsen, "Numerical study of efficiency for a 670 GHz gyrotron," *Phys. Plasmas*, vol. 18, no. 2, pp. 023107 1 - 023107 5, Feb. 2011.

[1.36] A. C. Torrezan, M. A. Shapiro, J. R. Sirigiri, R. J. Temkin, and R. G. Griffin, "Operation of a continuously frequency-tunable for dynamic nuclear polarization," *IEEE Trans. Electron Devices*, vol. 58, no. 8, pp. 2777–2783, 2011.

[1.37] A. Kasugai, K. Sakamoto, K. Takahashi, K. Kajiwara, and N. Kobayashi, "Steady-state operation of 170 GHz–1 MW gyrotron for ITER," *Nucl. Fusion*, vol. 48, no. 5, pp. 054009 1- 054009 6, May 2008.

[1.38] S. Cauffman, M. Blank, K. Felch, P. Borchard, P. Cahalan, and H. Jory, "Initial testing of a 95 GHz, 2.5 MW gyrotron," *Infrared Millim. Waves 2007, 2007 15th Int. Conf. Terahertz Electron. IRMMW-THz. Jt. 32nd Int. Conf.*, pp. 94–95, 2007.

[1.39] A. G. Litvak, G. G. Denisov, M. V. Agapova, V. E. Myasnikov, L. G. Popov, E. M. Tai, S. V. Usachev, V. E. Zapevalov, A. V. Chirkov, V. I. Ilin, A. N. Kuftin, V. I. Malygin, E. V. Sokolov, and E. A. Soluyanova, "Development in Russia of 170 GHz gyrotron for ITER," *Infrared, Millim. Terahertz Waves (IRMMW-THz), 2011 36th Int. Conf.*, pp. 1–3, 2011.

[1.40] B. Ferguson and X.-C. Zhang, "Materials for terahertz science and technology.," *Nat. Mater.*, vol. 1, no. 1, pp. 26–33, 2002.

[1.41] S. Jacobsson, "Optically pumped far infrared lasers," *Infrared Physics*, vol. 29, no. 5. pp. 853–874, 1989.

[1.42] T. Chang and T. Bridges, "Laser action at 452, 496, and 541 µm in optically pumped CH3F," *Optics Communications*, vol. 1, no. 9. pp. 423–426, 1970.

[1.43] M. Inguscio, G. Moruzzi, K. M. Evenson, and D. A. Jennings, "A review of frequency measurements of optically pumped lasers from 0.1 to 8 THz," *J. Appl. Phys.*, vol. 60, no. 12, pp. R161–R192, 1986.

[1.44] J. Farhoomand and H. M. Pickett, "Stable 1.25 watts CW far infrared laser radiation at the 119 µm methanol line," *Int. J. Infrared Millimeter Waves*, vol. 8, no. 5, pp. 441–447, 1987.

[1.45] D. Saeedkia and S. Safavi-Naeini, "Terahertz photonics: Optoelectronic techniques for generation and detection of Terahertz waves," *J. Light. Technol.*, vol. 26, no. 15, pp. 2409–2423, 2008.

[1.46] E. R. Mueller, "Optically-pumped THz laser technology," *Coherent-DEOS Product Note*, 2001. [Online]. Available: https://www.coherent.com/downloads/OpticallyPumpedLaser.pdf. [Accessed: 10-Mar-2015].

[1.47] F. C. Cruz, G. T. Nogueira, L. F. L. Costa, N. C. Frateschi, R. C. Viscovini, and D. Pereira, "Continuous and pulsed THz generation with molecular gas lasers and photoconductive antennas gated by femtosecond pulses," *SBMO/IEEE MTT-S Int. Microw. Optoelectron. Conf. Proc.*, pp. 446–449, 2007.

[1.48] D. D. Bićanić, B. F. J. Zuidberg, and A. Dymanus, "Generation of continuously tunable laser sidebands in the submillimeter region," *Appl. Phys. Lett.*, vol. 32, no. 6, pp. 367–369, 1978.

[1.49] M. S. Tobin, "A review of optically pumped NMMW lasers," *Proc. IEEE*, vol. 73, no. 1, pp. 61–85, 1985.

[1.50] H. O. Everitt, D. D. Skatrud, and F. C. DeLucia, "Dynamics and tunability of a small optically pumped cw far-infrared laser," *Appl. Phys. Lett.*, vol. 49, no. 16, pp. 995–997, 1986.

[1.51] H. Eisele, "Superlattice and other negative-differential-resistance devices: Current status," in *Terahertz Frequency Detection and Identification of Materials and Objects*, R. E. Miles, X.-C. Zhang, H. Eisele, and A. Krotkus, Eds. Dordrecht: Springer Netherlands, 2007.

[1.52] G. Haddad and R. Trew, "Microwave solid-state active devices," *MMicrowave Theory Tech. IEEE Trans.*, vol. 50, no. 3, pp. 760–779, 2002.

[1.53] H. Eisele, A. Rydberg, and G. I. Haddad, "Recent advances in the performance of InP gunn devices and GaAs TUNNETT diodes for the 100-300-GHz frequency range and above," *IEEE Trans. Microw. Theory Tech.*, vol. 48, no. 4 part 2, pp. 626–631, 2000.

[1.54] H. Eisele and G. Haddad, "Two-terminal millimeter-wave sources," *Microw. Theory Tech. IEEE Trans.*, vol. 46, no. 6, pp. 739-746, 1998.

[1.55] E. R. Brown and C. D. Parker, "Resonant tunnel diodes as sub-millimetre-wave sources," *Philosophical Transactions of the Royal Society A: Mathematical, Physical and Engineering Sciences*, vol. 354, no. 1717. pp. 2365–2381, 15-Oct-1996.

[1.56] H. Eisele and R. Kamoua, "Submillimeter-wave InP Gunn devices," *IEEE Trans. Microw. Theory Tech.*, vol. 52, no. 10, pp. 2371–2378, Oct. 2004.

[1.57] L. Wandinger, "mm-wave InP Gunn devices-Status and trends," *Microw. J.*, vol. 24, pp. 71, 75–78, 1981.

[1.58] S. Suzuki, M. Asada, A. Teranishi, H. Sugiyama, and H. Yokoyama, "Fundamental oscillation of resonant tunneling diodes above 1 THz at room temperature," *Appl. Phys. Lett.*, vol. 97, no. 24, pp. 242102 1 - 202102 3, 2010.

[1.59] H. Eisele, "480 GHz oscillator with an InP Gunn device," *Electron. Lett.*, vol. 46, no. 6, pp. 422-423, 2010.

[1.60] M. Ino, T. Ishibashi, and M. Ohmori, “C.W. oscillation with p+-p-n+ silicon IMPATT diodes in 200 GHz and 300 GHz bands,” *Electronics Letters*, vol. 12, no. 6. pp. 148-149, 1976.

[1.61] H. Eisele, “355 GHz oscillator with GaAs TUNNETT diode,” *Electron. Lett.*, vol. 41, no. 6, pp. 329-331, 2005.

[1.62] L. A. Samoska, “An overview of solid-state integrated circuit amplifiers in the submillimeter-wave and THz regime,” *IEEE Trans. Terahertz Sci. Technol.*, vol. 1, no. 1, pp. 9–24, 2011.

[1.63] J. Rieh, D. Yoon, and J. Yun, “An overview of solid-state electronic sources and detectors for Terahertz imaging,” *Solid-State Integr. Circuit Technol. (ICSICT), 2014 12th IEEE Int. Conf.*, pp. 1–4, 2014.

[1.64] A. Maestrini, B. Thomas, H. Wang, C. Jung, J. Treuttel, Y. Jin, G. Chattopadhyay, I. Mehdi, and G. Beaudin, “Schottky diode-based terahertz frequency multipliers and mixers,” *Comptes Rendus Phys.*, vol. 11, no. 7–8, pp. 480–495, 2010.

[1.65] I. Mehdi, G. Chattopadhyay, E. Schlecht, J. Ward, J. Gill, F. Maiwald, and A. Maestrini, “Terahertz multiplier circuits,” *IEEE MTT-S Int. Microw. Symp. Dig.*, pp. 341–344, 2006.

[1.66] E. Schlecht, G. Chattopadhyay, A. Maestrini, A. Fung, S. Martin, D. Pukala, J. Bruston, and I. Mehdi, “200, 400 and 800 GHz Schottky Diode ‘Substrateless’. Multipliers: Design and Results,” *2001 IEEE MTT-S Int. Microw. Sympsoium Dig. (Cat. No.01CH37157)*, vol. 3, pp. 2–5, 2001.

[1.67] A. Maestrini, J. S. Ward, J. J. Gill, C. Lee, B. Thomas, R. H. Lin, G. Chattopadhyay, and I. Mehdi, “A frequency-multiplied source with more than 1 mW of power across the 840-900-GHz band,” *IEEE Trans. Microw. Theory Tech.*, vol. 58, no. 7 part 2, pp. 1925–1932, 2010.

[1.68] A. Maestrini, J. S. Ward, C. Tripon-Canseliet, J. J. Gill, C. Lee, H. Javadi, G. Chattopadhyay, and I. Mehdi, “In-phase power-combined frequency triplers at 300 GHz,” *IEEE Microw. Wirel. Components Lett.*, vol. 18, no. 3, pp. 218–220, 2008.

[1.69] R. F. Kazarinov and R. A. Suris, “Possibility of the amplification of electromagnetic waves in a semiconductor with a superlattice,” *Sov. Phys. - Semicond.*, vol. 5, no. 4, pp. 707–709, 1971.

[1.70] J. Faist, F. Capasso, D. L. Sivco, and C. Sirtori, “Quantum cascade laser,” *Science (80-.).*, vol. 264, no. 5158, pp. 553 – 556, Oct. 1994.

[1.71] F. Capasso, J. Faist, C. Sirtori, D. L. Sivco, J. N. Baillargeon, a. L. Hutchinson, and a. Y. Cho, “Quantum Cascade Lasers: New Resonant Tunnelling Light

Sources for the Mid-Infrared," *Philos. Trans. R. Soc. A Math. Phys. Eng. Sci.*, vol. 354, no. 1717, pp. 2463–2467, Oct. 1996.

[1.72] F. Capasso, R. Paiella, R. Martini, R. Colombelli, C. Gmachl, T. L. Myers, M. S. Taubman, R. M. Williams, C. G. Bethea, K. Unterrainer, H. Y. Hwang, D. L. Sivco, A. Y. Cho, A. M. Sergent, H. C. Liu, and E. A. Whittaker, "Quantum cascade lasers: Ultrahigh-speed operation, optical wireless communication, narrow linewidth, and far-infrared emission," *IEEE J. Quantum Electron.*, vol. 38, no. 6, pp. 511–532, 2002.

[1.73] J. Faist, D. Hofstetter, M. Beck, T. Aellen, M. Rochat, and S. Blaser, "Bound-to-continuum and two-phonon resonance quantum-cascade lasers for high duty cycle, high-temperature operation," *IEEE J. Quantum Electron.*, vol. 38, no. 6, pp. 533–546, Jun. 2002.

[1.74] C. Walther, G. Scalari, J. Faist, H. Beere, and D. Ritchie, "Low frequency terahertz quantum cascade laser operating from 1.6 to 1.8 THz," *Appl. Phys. Lett.*, vol. 89, no. 23, pp. 231121 1 - 231121 3, 2006.

[1.75] Q. Qin, J. L. Reno, and Q. Hu, "MEMS-based tunable terahertz wire-laser over 330 GHz," *Opt. Lett.*, vol. 36, no. 5, pp. 692–694, Mar. 2011.

[1.76] B. S. Williams, "Terahertz quantum-cascade lasers," *Nature Photonics*, vol. 1, no. 9. pp. 517–525, Sep-2007.

[1.77] B. Williams, S. Kumar, Q. Hu, and J. Reno, "High-power terahertz quantum-cascade lasers," *Electron. Lett.*, vol. 42, no. 2, pp. 89–91, 2006.

[1.78] K. Vijayraghavan, Y. Jiang, M. Jang, A. Jiang, K. Choutagunta, A. Vizbaras, F. Demmerle, G. Boehm, M. C. Amann, and M. a Belkin, "Broadly tunable terahertz generation in mid-infrared quantum cascade lasers," *Nat. Commun.*, vol. 4, no. 2021, pp. 1–7, Jan. 2013.

[1.79] G. Scalari, C. Walther, M. Fischer, R. Terazzi, H. Beere, D. Ritchie, and J. Faist, "THz and sub-THz quantum cascade lasers," *Laser Photonics Rev.*, vol. 3, no. 1–2, pp. 45–66, Feb. 2009.

[1.80] M. A. Belkin, F. Capasso, F. Xie, A. Belyanin, M. Fischer, A. Wittmann, and J. Faist, "Room temperature terahertz quantum cascade laser source based on intracavity difference-frequency generation," *Appl. Phys. Lett.*, vol. 92, no. 20, pp. 201101 1 - 201101 3, 2008.

[1.81] J. M. Yarborough, S. S. Sussman, H. E. Purhoff, R. H. Pantell, and B. C. Johnson, "Efficient, tunable optical emission from LiNbO3 without a resonator," *Appl. Phys. Lett.*, vol. 15, no. 3, pp. 102–105, 1969.

[1.82] H. E. Puthoff, R. H. Pantell, B. G. Huth, and M. A. Chacon, "Near-forward Raman scattering in $LiNbO_3$," *J. Appl. Phys.*, vol. 39, no. 4, pp. 2144–2146, 1968.

[1.83] F. Zernike and P. Berman, "Generation of far infrared as a difference frequency," *Phys. Rev. Lett.*, vol. 15, no. 26, pp. 999–1001, 1965.

[1.84] D. W. Faries, K. A. Gehring, P. L. Richards, and Y. R. Shen, "Tunable far-infrared radiation generated from the difference frequency between two ruby lasers," *Phys. Rev.*, vol. 180, no. 2, pp. 363–365, 1969.

[1.85] T. J. Bridges and A. R. Strnad, "Submillimeter wave generation by difference-frequency mixing in GaAs," *Appl. Phys. Lett.*, vol. 20, no. 10, pp. 382–384, 1972.

[1.86] B. Lax, R. L. Aggarwal, and G. Favrot, "Far-infrared step-tunable coherent radiation source: 70 µm to 2 mm," *Appl. Phys. Lett.*, vol. 23, no. 12, pp. 679–681, 1973.

[1.87] Y. J. Ding, "High-power tunable terahertz sources based on parametric processes and applications," *IEEE J. Sel. Top. Quantum Electron.*, vol. 13, no. 3, pp. 705–720, 2007.

[1.88] R. Sowade, I. Breunig, I. Cámara Mayorga, J. Kiessling, C. Tulea, V. Dierolf, and K. Buse, "Continuous-wave optical parametric terahertz source," *Opt. Express*, vol. 17, no. 25, pp. 22303–22310, 2009.

[1.89] S. Ragam, T. Tanabe, K. Saito, Y. Oyama, and J. I. Nishizawa, "Enhancement of CW THz wave power under noncollinear phase-matching conditions in difference frequency generation," *J. Light. Technol.*, vol. 27, no. 15, pp. 3057–3061, 2009.

[1.90] J. I. Nishizawa, T. Tanabe, K. Suto, Y. Watanabe, T. Sasaki, and Y. Oyama, "Continuous-wave frequency-tunable terahertz-wave generation from GaP," *IEEE Photonics Technol. Lett.*, vol. 18, no. 19, pp. 2008–2010, 2006.

[1.91] S. Verghese, K. A. McIntosh, S. Calawa, W. F. Dinatale, E. K. Duerr, and K. A. Molvar, "Generation and detection of coherent terahertz waves using two photomixers," *Appl. Phys. Lett.*, vol. 73, no. 26, pp. 3824–3826, 1998.

[1.92] E. Peytavit, P. Latzel, F. Pavanello, G. Ducournau, and J. F. Lampin, "Milliwatt output power generated in the J-Band by a GaAs photomixer," *Int. Conf. Infrared, Millimeter, Terahertz Waves, IRMMW-THz*, pp. 8–10, 2013.

[1.93] M. Koch, *Terahertz Frequency Detection and Identification of Materials and Objects*. Dordrecht, Netherlands: Springer Science and Business Media, 2007.

[1.94] A. J. Seeds, C. C. Renaud, M. Pantouvaki, M. Robertson, I. Lealman, D. Rogers, R. Firth, P. J. Cannard, R. Moore, and R. Gwilliam, “Photonic synthesis of THz signals,” *Microw. Conf. 2006. 36th Eur.*, pp. 1107–1110, 2006.

[1.95] O. Wada and H. Hasegawa, *InP-based materials and devices: physics and technology*. New York: Wiley-Interscience, 1999.

[1.96] T. Ishibashi, S. Kodama, N. Shimizu, and T. Furuta, “High-speed response of uni-traveling-carrier photodiodes,” *Japanese J. Appl. Physics, Part 1 Regul. Pap. Short Notes Rev. Pap.*, vol. 36, no. 10, pp. 6263–6268, 1997.

[1.97] H. Ito, S. Kodama, Y. Muramoto, T. Furuta, T. Nagatsuma, and T. Ishibashi, “High-speed and high-output InP-InGaAs unitraveling-carrier photodiodes,” *IEEE J. Sel. Top. Quantum Electron.*, vol. 10, no. 4, pp. 709–727, 2004.

[1.98] T. Nagatsuma, H. Ito, and T. Ishibashi, “High-power RF photodiodes and their applications,” *Laser Photonics Rev.*, vol. 3, no. 1–2, pp. 123–137, 2009.

[1.99] A. Beling, Z. Li, Y. Fu, H. Pan, and J. C. Campbell, “High-power and high-linearity photodiodes,” *IEEE Photonic Soc. 24th Annu. Meet. PHO 2011*, vol. 1, pp. 19–20, Oct. 2011.

[1.100] H. Ito, T. Furuta, S. Kodama, and T. Ishibashi, “InP/InGaAs uni-travelling-carrier photodiode with 310 GHz bandwidth,” *Electronics Letters*, vol. 36, no. 21. pp. 1809–1810, 2000.

[1.101] C. C. Renaud, D. Moodie, M. Robertson, and A. J. Seeds, “High output power at 110 GHz with a waveguide Uni-travelling carrier photodiode,” *Conf. Proc. - Lasers Electro-Optics Soc. Annu. Meet.*, pp. 782–783, 2007.

[1.102] A. Maestrini, J. S. Ward, H. Javadi, C. Tripon-Canseliet, J. Gill, G. Chattopadhyay, E. Schlecht, and I. Mehdi, “Local oscillator chain for 1.55 to 1.75 THz with 100-µW peak power,” *IEEE Microw. Wirel. Components Lett.*, vol. 15, no. 12, pp. 871–873, 2005.

[1.103] H. Ito, T. Nagatsuma, A. Hirata, T. Minotani, A. Sasaki, Y. Hirota, and T. Ishibashi, “High-power photonic millimetre wave generation at 100 GHz using matching-circuit-integrated uni-travelling-carrier photodiodes,” *Optoelectron. IEE Proc.*, vol. 150, no. 2, pp. 138–142, 2003.

[1.104] H. Ito, F. Nakajima, T. Furuta, and T. Ishibashi, “Continuous THz-wave generation using antenna-integrated uni-travelling-carrier photodiodes,” *Semiconductor Science and Technology*, vol. 20, no. 7. pp. S191–S198, 01-Jul-2005.

[1.105] C. Renaud, M. Robertson, D. Rogers, R. Firth, P. Cannard, R. Moore, and A. Seeds, “A high responsivity, broad band waveguide uni-travelling carrier photodiode,” *Proc. SPIE*, vol. 6194, no. 1, pp. C1940–C1940, 2006.

[1.106] H. J. Song, K. Ajito, Y. Muramoto, A. Wakatsuki, T. Nagatsuma, and N. Kukutsu, "Uni-travelling-carrier photodiode module generating 300 GHz power greater than 1 mW," *IEEE Microw. Wirel. Components Lett.*, vol. 22, no. 7, pp. 363–365, 2012.

[1.107] E. Rouvalis, C. C. Renaud, D. G. Moodie, M. J. Robertson, and A. J. Seeds, "Continuous wave terahertz generation from ultra-fast InP-based photodiodes," *IEEE Trans. Microw. Theory Tech.*, vol. 60, no. 3 part 1, pp. 509–517, 2012.

[1.108] H. T. Friis, "A note on a simple transmission formula," *Proc. IRE Waves Electrons*, vol. 34, pp. 254–256, 1946.

[1.109] J. S. Melinger, Y. Yang, M. Mandeghar, A. Shutler, and D. Grischkowsky, "THz detection of small molecule vapors over long paths in the atmospheric transmission windows," *Opt. Express*, vol. 20, no. 6, pp. 6788–6807, Mar. 2012.

[1.110] R. Appleby and H. B. Wallace, "Standoff detection of weapons and contraband in the 100 GHz to 1 THz region," *Antennas Propagation, IEEE Trans.*, vol. 55, no. 11, pp. 2944–2956, 2007.

[1.111] M. Neiman, "The principle of reciprocity in antenna theory," *Proc. IRE*, vol. 31, no. 12, pp. 666–671, 1943.

[1.112] G. M. Rebeiz, "Millimeter-wave and terahertz integrated circuit antennas," *Proc. IEEE*, vol. 80, no. 11, pp. 1748–1770, 1992.

Chapter 2 - InGaAsP-based UTCs from materials grown by solid source MBE

The fabrication of high performance uni-travelling carrier photodiodes, as devices enabling high optical-to-electrical (O-E) conversion efficiency, is central to the realisation of a photonic terahertz emitter; on the other hand the development of a simple, repeatable and high yield manufacturing process, from material growth to device fabrication, can also allow specifications such as low cost and market suitability to be met. The first section of this chapter reports the first InGaAsP-based uni-travelling carrier photodiodes fabricated from a structure grown by Solid Source Molecular Beam Epitaxy (SS-MBE) [2.1]; the material contains layers of InGaAsP as thick as 300 nm and a 120 nm thick InGaAs absorber. Material growth was carried out by Prof Huiyun Liu at UCL, device fabrication and characterisation were carried out at by the thesis author, also at UCL. Large area vertically illuminated test UTCs were fabricated and characterised; the devices exhibited 0.1 A/W responsivity at 1550 nm, 12.5 GHz -3 dB bandwidth and -5.8 dBm output power at 10 GHz for a photocurrent of 4.8 mA. The use of Solid Source Molecular Beam Epitaxy enables the major issue associated with the unintentional diffusion of zinc in Metal Organic Vapour Phase Epitaxy to be overcome and gives the benefit of the superior control provided by MBE growth techniques without the costs and the risks of handling toxic gases of Gas Source Molecular Beam Epitaxy.

The second section of this chapter outlines the fabrication in progress at UCL of edge-coupled waveguide UTCs, using the SS-MBE materials also grown at UCL. Waveguide UTCs have shown, since their invention [2.2], superior performance in terms of responsivity-bandwidth trade-off and will be in the future integrated with THz planar antennas.

2.1 Overview

As previously mentioned, a major obstacle to developing applications of sub-millimetre and terahertz (THz) waves is the lack of compact solid-state signal sources capable of generating high output power and operating at room temperature. For the generation of sub-millimetre and terahertz waves, photonic techniques are considered to be superior to conventional electronic techniques with respect to maximum frequency and tuneability [2.3]. Furthermore, the use of optical fibres enables the distribution of such high-frequency signals over long distances. In such a system, achieving high optical-to-electrical (O-E) conversion efficiency plays a critical role. The devices intended to accomplish this conversion (photodiodes) should operate at long optical wavelengths (1.3 µm - 1.55 µm) for compatibility with telecommunications wavelength optical sources and optical amplifiers, must be able to generate high output current and operate at high speed (high power and broad band devices). Among various types of long-wavelength photodiode technologies, the uni-travelling carrier photodiode (UTC-PD) and its derivatives have exhibited the highest output powers at frequencies from 100 GHz to 1.5 THz [2.3], [2.4] and very high output RF power [2.5], [2.6], with steady improvement in layer and device structures since their debut in 1997.

All the UTC-PDs exhibiting record breaking performance in terms of bandwidth and output power, for operation at 1.55 µm wavelength, have been fabricated on Al-free InGaAsP based materials: record-high output power of 0.75 W (28.8 dBm) at 15 GHz and a third order output intercept point (OIP3) up to 59 dBm [2.5]; 3 dB bandwidth of 310 GHz and a pulse width (FWHM) of 0.97 ps [2.7]; 5 µW at 1.02 THz [2.4]; maximum saturation output power of 20.8 mW at 100 GHz [2.8]; resonant peak exhibiting a maximum (detected) output power of 10.9 µW at 1.04 THz [2.9]; 3 dB bandwidth higher than 110 GHz, up to 36 mA photocurrent and a record breaking 10 dBm extracted power at 110 GHz [2.10]; record breaking emission of up to 148 µW at 457 GHz and 25 µW at 914 GHz [2.11]; record levels of Terahertz figure of merit (P_{THz}/P_{opt}^2 in W^{-1}) ranging from 1 W^{-1} at 110 GHz to 0.0024 W^{-1} at 914 GHz [2.12]. A summary of such state of the art performance, from UTC-PDs fabricated on Al-free InGaAsP based materials, is given in Table 2.1.

Table 2.1: Summary of UTC-PDs fabricated on InGaAsP based materials, exhibiting state of the art performance in terms of bandwidth and output power, for operation at 1.55 µm wavelength. The entries are ordered by decreasing values of DC photocurrent, where applicable.

Source Description	Output Power (mW)	FWHM (ps)	3 dB bandwidth (GHz)	DC photocurrent (mA)	DC responsivity (A/W)
Charge-compensated modified uni-travelling carrier photodiode (**CC-MUTC-PD**) [2.5]	750 (at 15 GHz)	--	--	> 180	0.67
Waveguide uni-travelling carrier PD (**UTC-PD**) [2.10]	10 (at 110 GHz)	--	> 110	36	--
Waveguide uni-travelling carrier PD (**UTC-PD**) [2.11]	0.148 (at 457 GHz) 0.025 (at 914 GHz)	--	> 107	28	0.2
Double-mesa back-illuminated uni-travelling carrier photodiode (**UTC-PD**) [2.8]	20.8 (at 100 GHz)	--	--	25	--
Double-mesa back-illuminated uni-travelling carrier PD (**UTC-PD**) [2.9]	10.9×10^{-3} (at 1.04 THz)	--	--	14	--
Travelling wave uni-traveling carrier PD with a mode-converting waveguide (**TW-UTC-PD**) [2.4]	5×10^{-3} (at 1.02 THz)	--	108	12	0.53
UTC-PD [2.7]	--	0.97	310	--	--

Lattice-matched compounds of InGaAsP allow for composition of absorptive and transparent layers; InGaAsP/InP properties include band-gap variation between 1.65 µm and 0.92 µm depending on the InGaAsP composition and absorption constant for $In_{0.53}Ga_{0.47}As$ of approximately 7,000 cm^{-1} at 1.55 µm [2.13]. This material system is also desirable because many types of devices can be constructed without the use of aluminium, an advantage as aluminium containing devices can have reduced life-time due to aluminium oxidation [2.14].

Metal Organic Vapour Phase Epitaxy (MOVPE) and Gas Source Molecular Beam Epitaxy (GS-MBE) have long been the predominant growth techniques for the production of high quality InGaAsP material [2.15]. Until the early 1990s, advanced phosphide epitaxy was only possible by means of these two techniques due to the problems associated with the high vapour pressure of white phosphorus, which is unfavourable for conventional Knudsen-type Solid Source Molecular Beam Epitaxy (SS-MBE) furnaces [2.16]. In MOVPE and GS-MBE, arsenic and phosphorus are supplied from arsine and phosphine gas; however, because of the high toxicity of arsine and phosphine, special and expensive safety precautions must be taken [2.15], [2.17]; besides, phosphine is not ideal because it may also introduce water vapour into the reactor chamber [2.16]. Furthermore zinc is the most frequently used acceptor dopant in InP based compounds grown by MOVPE but it has been shown that very rapid Zn diffusion and other redistribution effects occur at Zn concentrations exceeding the mid 10^{18} cm^{-3} range making Zn doping profiles difficult to control in this concentration regime [2.18]; displacements of pn-junctions can occur with deleterious impact on initial device characteristics [2.18], [2.19].

SS-MBE is an attractive technique since material quality comparable with GS-MBE can be obtained without the cost and difficulty of handling toxic gases [2.20]. For SS-MBE arsenic and phosphorus are supplied by subliming solid arsenic and phosphorus, since toxic solids are inherently easier to control than toxic gases, the safety hazards and costs of solid group V sources are considerably less than those of gas group V sources [2.15]. Growth of InGaAsP by SS-MBE began in the 1970s but did not progress far due to difficulties related to the growth of arsenide phosphide materials [2.21]. It was not until the introduction of group V valved cracker sources, arsenic [2.22] in 1990 and phosphorus [2.23] in 1991, that SS-MBE research for InGaAsP moved forward once again. After 1991 a number of growth experiments on phosphide epitaxy by SS-MBE were reported and high quality InGaAsP materials were achieved [2.14] but results on optoelectronic devices were scarce in the literature and device characterisation data only became available in mid 1990s. The first SS-MBE grown InGaAsP high quality laser was demonstrated in 1995 for a wavelength of 1.35 μm [2.24] followed by other lasers emitting at λ = 0.98 μm, 0.68 μm and 1.5 μm. SS-MBE is an attractive growth technique for UTC devices, since the p-contact layer can be doped using beryllium at 500 ^{o}C for a phosphorus-based UTC, without the drawbacks caused by the use of zinc. In addition, SS-MBE allows realisation of doping profiles that would be more difficult to achieve by MOVPE and above all offers an extremely high degree of control over the local composition, nearly on an atomic layer scale, making it possible to realise experimentally almost any band diagram that can be drawn. To the best of the author's knowledge the first work on InGaAsP-based UTC devices grown by SS-MBE has been reported by Natrella et al. in [2.1].

The next section reports SS-MBE growth, device fabrication and characterisation of larger-area vertically-illuminated test InGaAsP-based UTC-PDs.; this part of the work is intended to be the first stage towards combining and optimising the merits of SS-MBE (no zinc diffusion issues, monolayer control, safe & cost effective) and the proven high potential of InGaAsP based materials for UTC-PD fabrication. Section 2.3 describes the fabrication in progress at UCL, of high performance edge-coupled waveguide UTCs using the same material structures grown by SS-MBE, also at UCL.

2.2 Growth fabrication and characterisation of vertically-illuminated test InGaAsP-based UTC-PDs

2.2.1 Structure growth experiment

The UTC-PD epitaxial structure grown by SS-MBE within our department for this work was first proposed by Dr. Efthymios Rouvalis. This epitaxial structure is similar to that reported previously [2.12] (grown by MOVPE), but is intended to achieve band-gap engineering improvements (more accurately localised transitions) and more precise doping profiles. The detailed epitaxy diagram is shown in Table 2.2. The cap layer consists of a thick (200 nm) layer of InGaAsP (λg = 1.3 µm) functioning as both diffusion block and p-contact. For the absorption layer, we have tried to exploit the superior growth control of the MBE by splitting it into 5 different levels with a graded doping concentration, aimed at achieving further electron acceleration. Two 10 nm spacer layers of InGaAsP (λg = 1.3 µm and λg = 1.1 µm) were inserted between the absorber and the 300 nm thick InP carrier collection layer. Although in this chapter results for simple, vertically illuminated, test devices are presented, the main goal of the future research is the realisation of edge-coupled waveguide photodiodes, as these have shown superior performance [2.4], [2.10]-[2.12]; for this reason the structure also includes a waveguide layer consisting of another thick (300 nm) layer of InGaAsP (λg = 1.3) grown on the 700 nm thick InP n-contact layer.

Table 2.2: Detailed UTC layer structure grown by SS-MBE. The structure was proposed by Dr. Efthymios Rouvalis and grown by Prof. Huiyun Liu.

UTC-PD Epitaxy			
Doping(cm^{-3})	**Material**	**Function**	**Thickness (nm)**
>1 x 10^{19}	p^{++} - $Q_{1.3}$	Barrier & p-contact	200
2.5 x 10^{18}	p^{+} - $In_{0.53}Ga_{0.47}As$	Absorber	20
1 x 10^{18}	p^{+} - $In_{0.53}Ga_{0.47}As$	Absorber	30
5 x 10^{17}	p - $In_{0.53}Ga_{0.47}As$	Absorber	30
2.5 x 10^{17}	p - $In_{0.53}Ga_{0.47}As$	Absorber	30
u.i.d	u – InGaAs	Spacer/Absorber	10
u.i.d	u – $Q_{1.3}$	Spacer	10
u.i.d	u – $Q_{1.1}$	Spacer	10
1 x 10^{16}	n - InP	Carrier Collection	300
2.5 x 10^{18}	n^{+} – $Q_{1.3}$	Waveguide	300
>1 x 10^{19}	n^{++} - InP	n – contact	700
Fe	SI - InP	Substrate	--

The phosphorus-based UTC was grown on an Fe-doped SI (100) InP substrate at 490 ^{o}C by a Veeco Gen930 solid-source MBE system, which includes Veeco SUMO cells for Indium, Gallium and Aluminium as well as valved cracker cells for Phosphorus and Arsenic. P_2 and As_4 were used as sources for the growth. An in-situ 15 keV RHEED system was used to monitor the growth process and the substrate temperature was measured by a pyrometer. Under P_2 rich conditions, the InP substrate was heated to a temperature of 530 ^{o}C to deoxidise the surface. Si and Be sources were used for n-type and p-type doping respectively.

The lattice matched quaternary InGaAsP layers require accurate control of the flux ratio for As/P. To calibrate the thickness and composition of the InGaAsP layers, a 300 nm thick InGaAsP layer and subsequent 7-period (10-nm InGaAsP/10-nm InP) superlattice were checked by high-resolution X-ray diffraction (HRXRD). All structures were characterised by HRXRD with lattice mismatch below 10^{-3}, such as the HRXRD diagram (rocking curve) of InGaAsP (λg = 1.3 μm) shown in Figure 2.1, provided by Prof. Huiyun Liu. The rocking curve of a superlattice exhibits diffraction peaks of increasing order, called satellite peaks, as well as the substrate peak, as shown in Figure 2.1. The position of the zeroth order satellite peak is determined by the average lattice constant of the superlattice and its angular separation from the substrate peak is employed to quantify the lattice mismatch between the structure and the substrate. The angular position of the higher order satellite peaks is related to the superlattice period while their relative amplitude and absence of appreciable broadening indicate a regular superlattice with little interdiffusion.

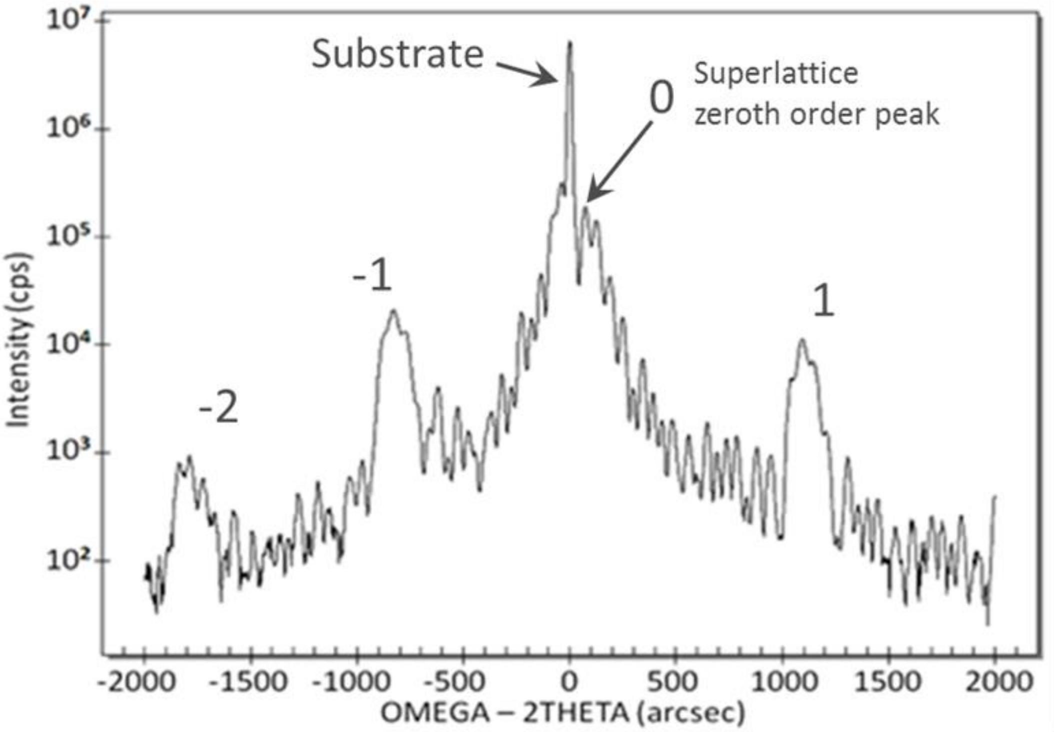

Figure 2.1: High-resolution X-ray diffraction diagram (rocking curve), provided by Prof. Huiyun Liu, of 300 nm thick InGaAsP layer and subsequent 7-period (10-nm InGaAsP/10-nm InP) superlattice grown on InP substrate by SS-MBE. The position of the zeroth order satellite peak is determined by the average lattice constant of the superlattice and its angular separation from the substrate peak is employed to quantify the lattice mismatch between the structure and the substrate. The angular position of the higher order satellite peaks is related to the superlattice period while their relative amplitude and absence of appreciable broadening indicate a regular superlattice with little interdiffusion.

2.2.2 Test-device fabrication

Large area vertically-illuminated test devices were fabricated to characterise the new material. To the best of the author's knowledge these are the first UTC-PDs fabricated from an InGaAsP-based structure grown by solid source MBE. The fabricated device is shown in Figure 2.2 (a), while Figure 2.2 (b) gives a schematic cross-section of the structure.

The fabrication process and the masks used, were devised and designed by Dr. Chin-Pang Liu at UCL, and were previously employed to realise Multiple-Quantum-Well Asymmetric Fabry-Perot Modulators [2.25]. Some changes in processing the UTC-PDs are required due to differences in the layer structure.

The p-contact pads, the 5 µm wide air bridges and the 5 µm wide mesa-rings marking out the 20 µm diameter optical window, were obtained by standard photolithography, metal evaporation (20 nm of chromium and 300 nm of gold) and lift-off technique with acetone. The complete removal of excess metal from the optical window is essential for efficient device operation. Therefore two slots were included in the mesa-rings to favour a successful lift-off that would otherwise be extremely difficult inside closed rings.

Prior to metal evaporation (20 nm of chromium and 300 nm of gold) to make the n-contact pads, the n-contact area was etched 940 nm down to the n^{++}-InP layer (n-contact layer). The non-selective etching employed in [2.25] was not considered a suitable option for this case because of the relatively limited thickness of this layer (700 nm); very precise control of the etch rate and the etched profile would have been necessary to obtain a floor entirely inside the n-contact layer. Instead, three successive selective etchants were employed as follows: 1) H_2SO_4:H_2O_2:H_2O (1:1:8) for preferential etching of InGaAsP + InGaAs (340nm) on InP [2.26], [2.27]; 2) HCl:H_3PO_4 (1:1) for preferential etching of InP (300 nm) on InGaAsP [2.26], [2.28]; 3) H_2SO_4:H_2O_2:H_2O (1:1:8) for preferential etching of InGaAsP (300 nm) on InP. This selective procedure made it possible to stop precisely on the n-contact layer and provided a flat floor for the n-contact pad metal deposition. The drawback found was the significant undercut of the sulphuric acid solution on InGaAs.

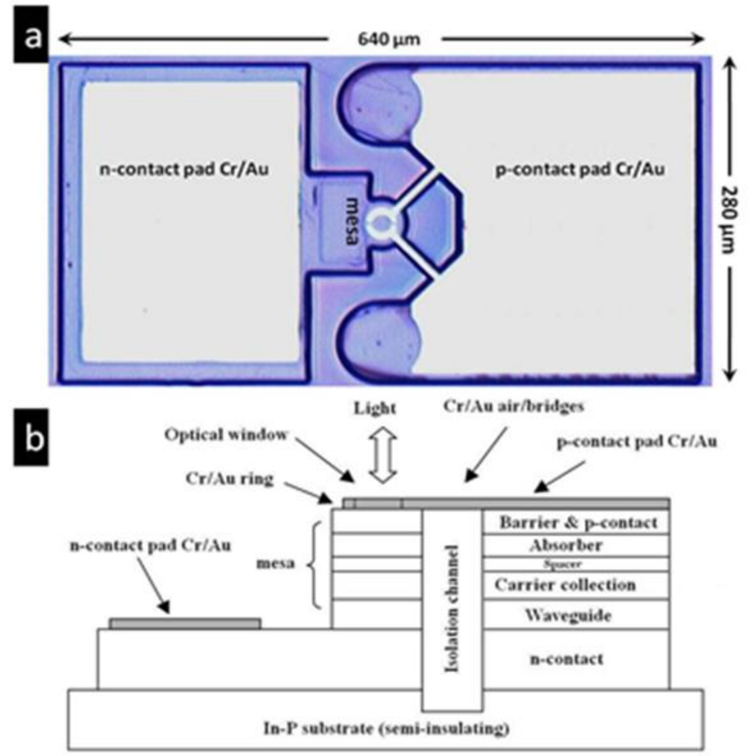

Figure 2.2: (a) Top microscopic view of an entire air-bridged normal incidence UTC-PD. (b) Schematic cross-section of the air-bridged normal incidence UTC.

The rectangular area between the mesa-ring and the n-contact pad, shown in Figure 2.2 (a), was then etched down to the same depth as the n-contact area with the same selective process. This step opened up part of the mesa side-wall.

In the last stage of the fabrication process the two contact pads, the bridges and the 30 µm diameter mesa area (containing the mesa-rings and 20 µm diameter optical window) were protected by resist and a deep etch was carried out down to the semi-insulating InP substrate with a non-selective Adachi etch $HBr:CH_3COOH:K_2Cr_2O_7$ (1:1:1) [2.29]. This etching step was long enough to allow the undercutting action of Adachi to completely clear the material underneath the bridges and thus form air-bridges. Individual UTCs were electrically isolated and the remaining mesa sidewalls were opened up.

2.2.3 Device characterisation

The photodiode I-V and C-V characteristics, measured with a KEITHLEY 4200 probe station, are displayed in Figure 2.3 and Figure 2.4. The device exhibited 70 mA of current under 3 V of forward bias, 24 Ω series resistance, 23 nA of dark current under a reverse bias of 5 V and a capacitance of 200 fF. The theoretical capacitance calculated considering that the whole mesa area (radius ≈ 15 µm) contributes to the junction capacitance and including the effect of the undoped spacers, is equal to about 240 fF; the smaller value of the measured capacitance may be due to the undercutting action of the wet etchants which may have shrunk the mesa area. Transmission line model measurements were performed and returned relatively high values of specific contact resistance (about 15 Ω), which account for the high value (24 Ω) of series resistance shown by the photodiode; the high value of measured series resistance may have also been affected by a mesa shrinkage caused by the undercutting action of the wet etchants employed for the device fabrication.

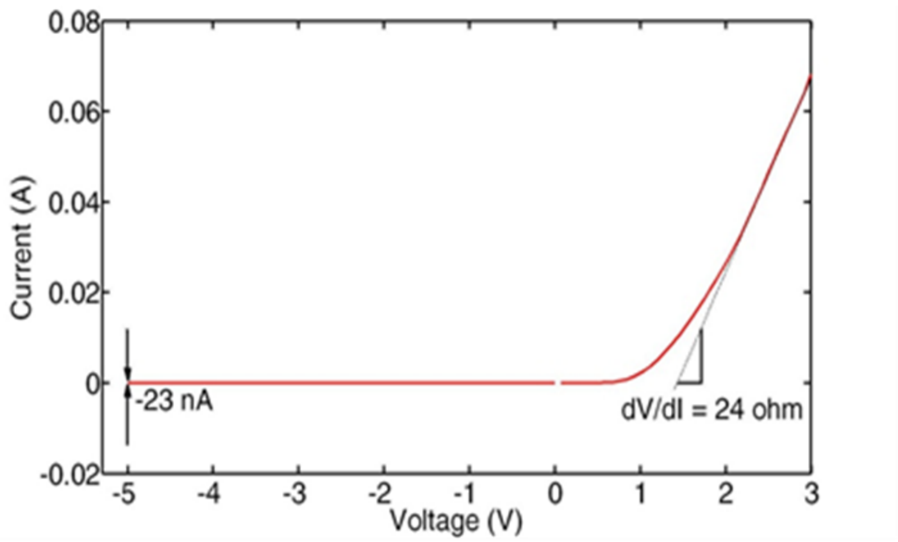

Figure 2.3: I-V characteristic of the device showing 70 mA current for a 3 V forward bias and 23 nA of dark current for a reverse bias of -5 V. The 24 Ω value of series resistance shown by the photodiode is due to non-optimal ohmic contacts.

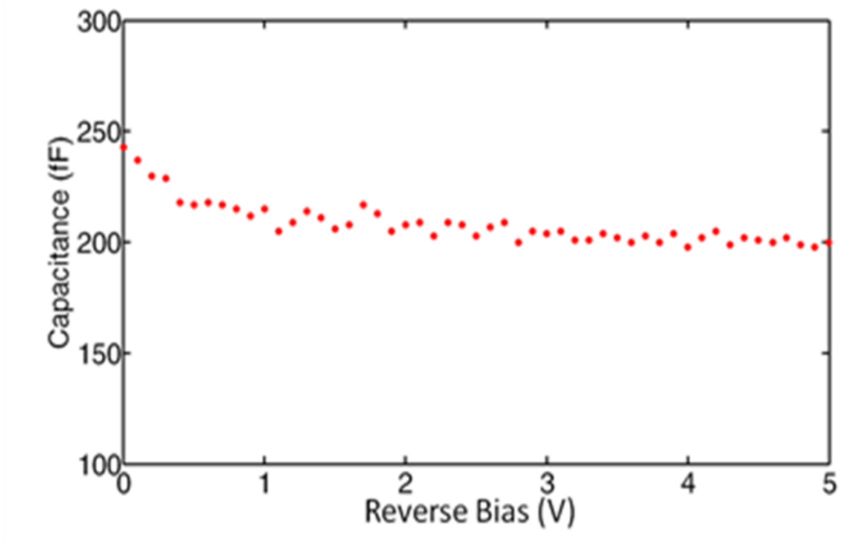

Figure 2.4: C-V measurement displaying a capacitance of approximately 200 fF when biased at -5 V.

The device was then mounted on a temperature controlled brass block (maintained at 22 ^{o}C) and illuminated with a 10^{O} lensed fibre for all the following measurements; the 10^{O} angle relates the mode diameter inside the fibre and the working distance (e.g. focal length). Uniform illumination of the optical window can minimise the space charge effect by reducing the density of the photo-generated carriers. It was demonstrated [2.30], [2.31] that the 1 dB compression current can double for the same applied voltage if the Gaussian beam is expanded so that 5-10 % of the light misses a circular absorbing region; the 1 dB compression current is the DC photocurrent at which the RF responsivity decreases by 1 dB. The measurements discussed in this section were made without carrying out such expansion of the optical beam to further optimise the coupling efficiency between the lensed fibre and the device 20 µm diameter optical window, delimited by the 5 µm wide mesa-rings on the 30 µm diameter mesa.

Silver epoxy was employed to connect the n-contact pad to the block, which acted as the signal ground, and the p-contact pad to the centre of a 2 cm long 50 Ω characteristic impedance microstrip transmission line. SMA connectors were then attached to both ends of the microstrip line with one end matched in a 50 Ω termination through a bias-T blocking the DC and the other connected to the measuring instrument (lightwave component analyser or electrical spectrum analyser) and the ammeter, through a second bias-T. This microstrip mount was employed because the contact geometry of the fabricated test device was not suitable for direct measurement with a ground-signal-ground probe. For RF power measurements a Mach-Zehnder modulator was used for the external modulation of the optical power; Figure 2.5 shows the experimental arrangement employed to measure the UTC RF output power over the frequency range. For the device relative frequency response measurement, a lightwave component analyser (LCA) was employed, in which case the laser source was provided by the LCA and the UTC RF output power was also measured by the LCA, instead of the electrical spectrum analyser.

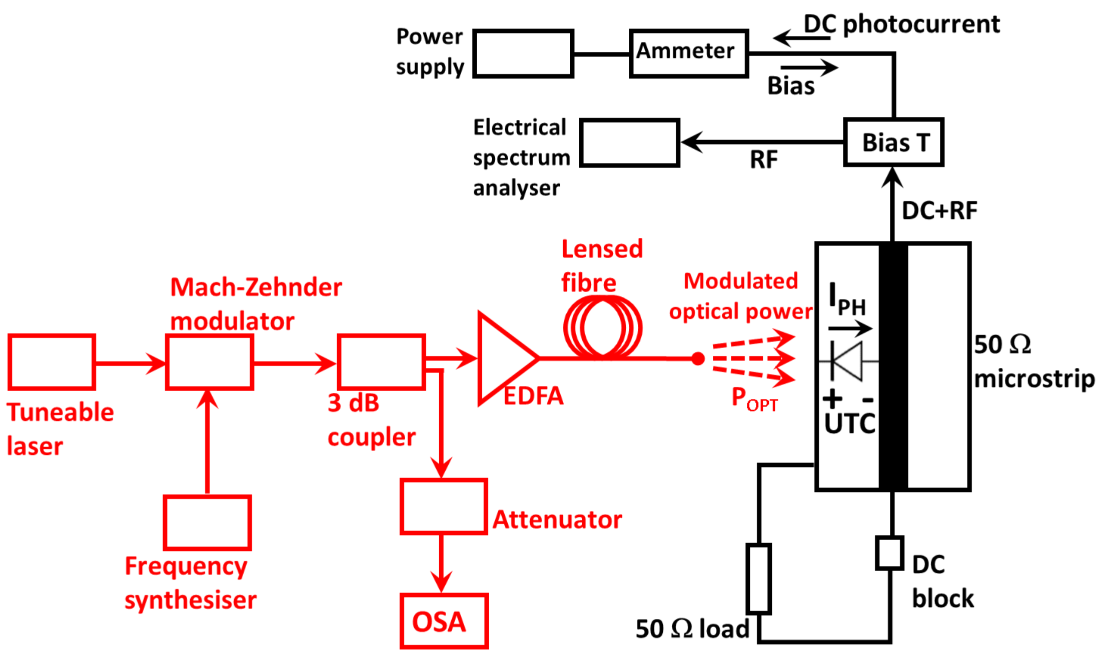

Figure 2.5: Experimental arrangement employed to measure the UTC RF output power over the frequency range. I_{PH} is the photocurrent through the UTC. The labels "plus" and "minus" highlight the reverse bias across the UTC.

Figure 2.6 shows the photocurrent versus the optical power under different values of applied bias. For 50 mW input optical power and a reverse bias of 2 V the photodiode exhibits a responsivity of 0.1 A/W at 1.55 μm. This value of responsivity can be considered a reasonable estimate of the internal responsivity if we ignore the optical power reflected at the air/InGaAsP p-contact layer interface and consider that, for vertically illuminated photodiodes with an optical window noticeably larger than the beam spot size, essentially no fraction of the incident light misses the absorbing window; the photodiodes under investigation have a 20 µm diameter optical window, while the beam spot size is less than 10 µm. The theoretical internal responsivity ρ_{int} at 1.55 µm can also be evaluated as $\rho_{int} = \eta_{int}\, q/(hf)$ where q is the electron charge (1.602 x 10^{-19} C), h is Planck constant (6.626 x 10^{-34} Js) and f the frequency (193.548 THz). The internal quantum efficiency η_{int} can be estimated as $\eta_{int} = 1 - e^{-\alpha t}$, where α is the absorption constant for $In_{0.53}Ga_{0.47}As$ (approximately 7,000 cm^{-1} at 1.55 µm) and t is the absorption layer thickness (120 nm); the reflections of unabsorbed light within the $In_{0.53}Ga_{0.47}As$ layer are negligible as the adjacent layers have very similar electrical permittivity. The calculated theoretical value of responsivity equals 0.10072, which is remarkably close to the measured value.

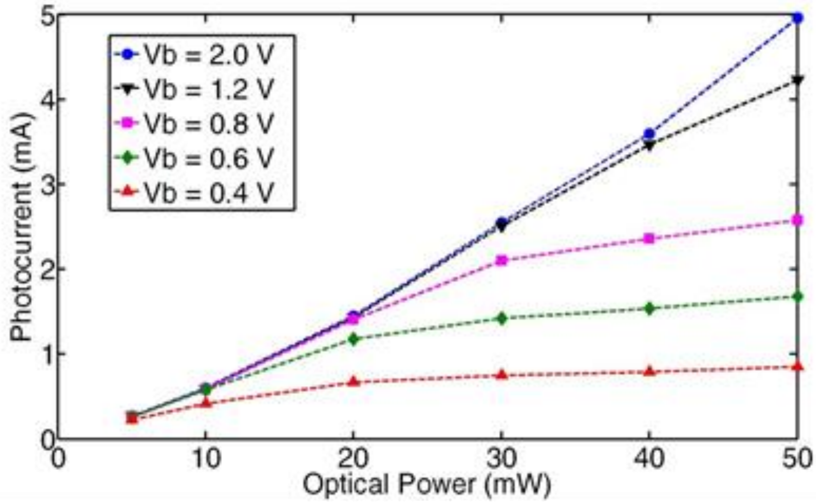

Figure 2.6: Responsivity measurements.

The device relative frequency response, measured with the lightwave component analyser calibrated to an open, a short and a 50 Ω load, is shown in Figure 2.7; the photodiode exhibits a 3dB bandwidth of approximately 12.5 GHz at a bias of -2.4 V.

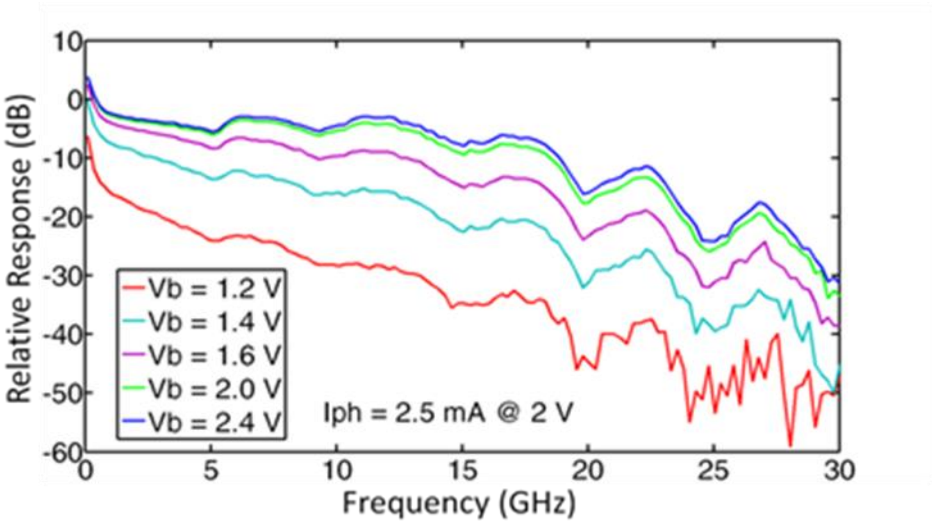

Figure 2.7: Relative frequency response measured with the Lightwave component analyser for bias values ranging from -1.2 to -2.4 V. The photodiode exhibits a 3 dB bandwidth of approximately 12.5 GHz. The minima visible at 10 GHz, 15 GHz and 20 GHz are due to the microstrip mount.

The output RF power delivered over the frequency range is shown in Figure 2.8. The effective load connected to the photodiode is 25 Ω, that is the parallel connection of two 50 Ω loads (the termination and the measuring instrument), because of the mount employed for these measurements. The RF power plotted in Figure 2.8 is the power delivered to this effective 25 Ω load. The local minima of power at 10 GHz, 15 GHz and 20 GHz visible in Figure 2.8 and consistently also present in Figure 2.7, are due to discontinuities at the connections between the mount and the loads. The RC limited bandwidth, given the photodiode 200 fF capacitance and 24 Ω resistance, and the 25 Ω load, is $1/2\pi RC \approx 16$ GHz.

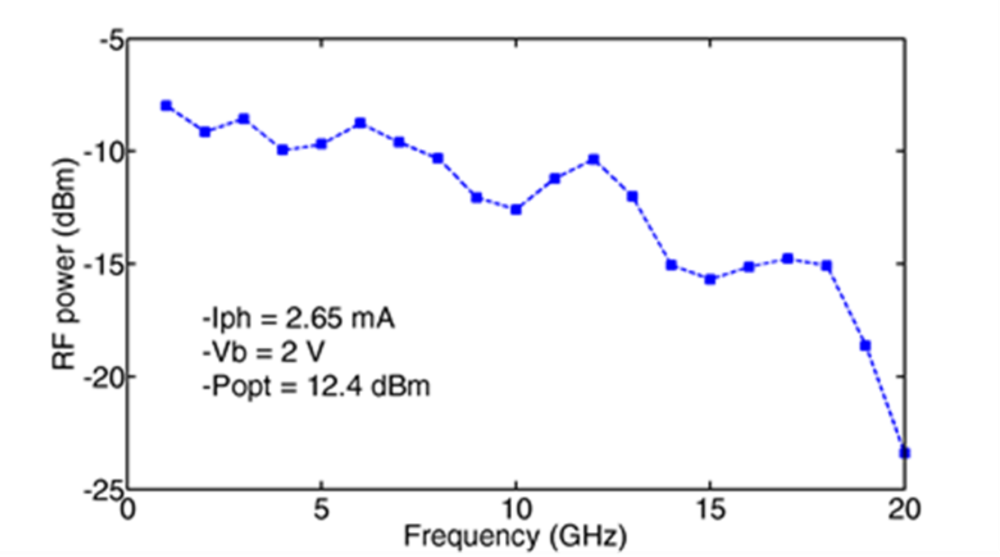

Figure 2.8: RF power over the frequency range delivered by the device to the effective 25 Ω load. In agreement with the relative frequency response measurements, ripples are visible due to the microstrip mount.

The maximum output RF power delivered by the photodiode to the effective 25 Ω load at 10 GHz, for a -4 V bias and a 13.7 dBm input optical power, was -5.8 dBm; in these conditions the device exhibited a photocurrent of 4.8 mA. This measurement was performed at 10 GHz, falling in the frequency response local minimum observable at the same frequency. This RF power is comparable to the output power generated by other large area (from 25 µm to 40 µm diameter) normal incidence UTCs for similar values of photocurrent [2.32]-[2.34]; these referenced UTCs show very high photocurrent and responsivity, having been fabricated from epitaxial layers optimised for vertical coupling with absorption layer thicknesses ranging from 450 nm to 1.5 µm. The maximum DC photocurrent generated by our normal incidence test devices was 7.5 mA for -6 V bias and 17 dBm input optical power; for these conditions the output RF power was -10 dBm (at 10 GHz). The main factor limiting the photocurrent of the devices is that the layer structure grown by SS-MBE is optimised for edge-coupled waveguide devices and is not suited to the fabrication of high performance vertically illuminated devices; the absorption layer is thin (120 nm) and provides limited responsivity under vertical illumination since it is optimised for the edge-coupled waveguide devices. The second factor is related to the fact that no optimisation was performed of the laser spot size on the optical window; as explained in the above referenced papers [2.30], [2.31], this optimisation plays an important role when coupling light into large area vertically illuminated devices. Other secondary factors may have played a role, such as the high series resistance and the significant undercut of sulphuric acid on InGaAs which may have shrunk the absorption layer in the mesa.

2.3 Fabrication of waveguide InGaAsP-based UTCs

In Section 2.2 the fabrication of vertically illuminated test devices employing InGaAsP based materials grown by solid source MBE has been presented; the discussed layer structure is optimised for edge-coupled waveguide devices and includes a waveguide layer consisting of a thick (300 nm) layer of InGaAsP ($\lambda g = 1.3$). The waveguide design for UTCs, where the light is coupled into the photodiode through an optical waveguide, adds more flexibility to the optimisation process aiming to find the best trade-off between DC responsivity and bandwidth. This section provides an outline of the design and fabrication of coplanar waveguide (CPW) integrated edge-coupled waveguide UTCs.

2.3.1 Device details

In Figure 2.9 and Figure 2.10 schematic diagrams of the edge-coupled waveguide UTCs are illustrated. The layer structure is the same employed for the fabrication described in Section 2.2, with the addition of an approximately 2 µm thick layer of silicon oxynitride (SiO_xN_y) deposited on top of the fabricated UTC for passivation purposes and for realisation of a smoother and more planar surface on which to evaporate gold coplanar waveguides (CPWs) or antennas; BCB (Benzocyclobutene) based polymer dielectrics can also be used for this purpose. Vias need to be etched through this layer in order to expose the UTC metal contacts and allow the connection between UTC and coplanar waveguide (CPW) or antenna to be realised.

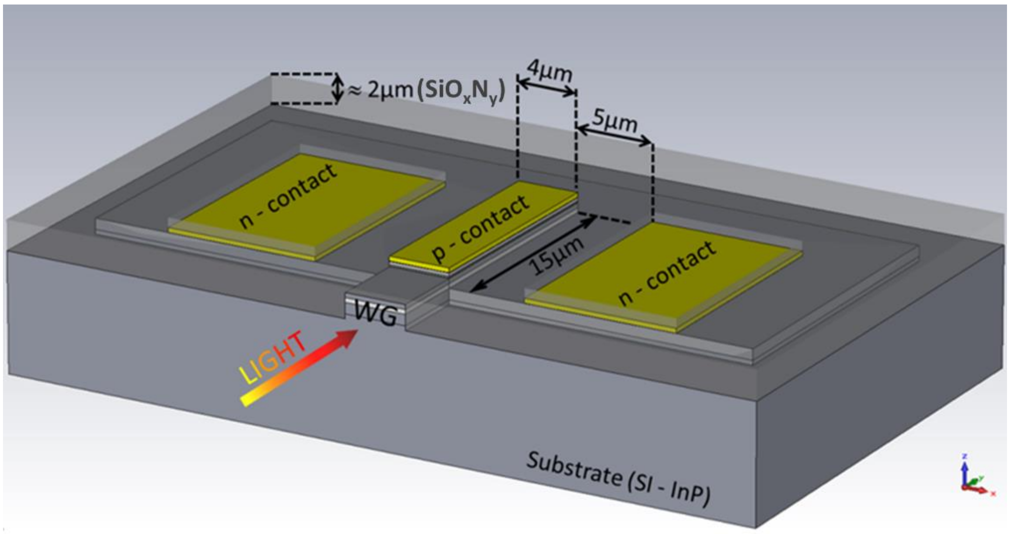

Figure 2.9: Schematic diagram of the edge-coupled waveguide UTC structure. The light coming from a lensed fibre is coupled into the chip through a passive waveguide (WG). The length of the waveguide is depicted much smaller than in reality. The approximately 2 µm thick layer of silicon oxynitride (SiO_xN_y) deposited on top of the fabricated UTC is also visible.

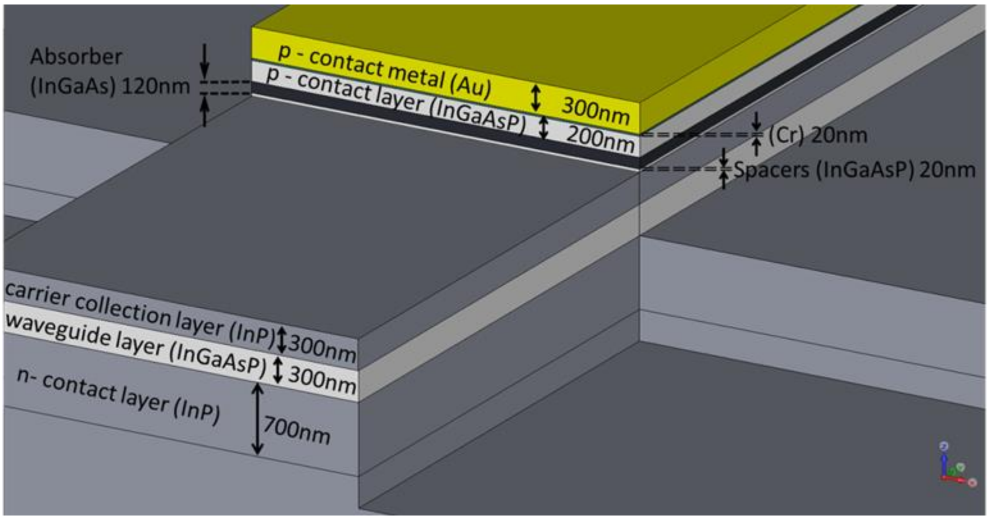

Figure 2.10: Enlarged view showing details of the layers making up the p-contact ridge and the waveguide.

The dimensions of the geometrical details shown in Figure 2.9 are only indicative and will be optimised in successive fabrication runs. Even the thickness of some of the layers highlighted in Figure 2.10 will be varied and optimised. As shown in Figure 2.10, Chromium was employed in the first fabrication runs, as an adhesion promoter layer for gold and as metallurgical solution for the ohmic contact layer, however platinum and titanium have been preferred in more recent fabrication runs.

The fabrication process of such devices has been developed and the masks for the processing in the cleanroom have been designed and realised. The earliest version of the fabrication process consisted of 6 main steps associated with the 6 layers making up the mask set, whose superimposition in an enlarged area is displayed in Figure 2.11. While only wet etching was used for the fabrication of the vertically illuminated UTCs, described in Section 2.2, a combination of wet and dry etching is needed for the fabrication of waveguide UTCs, where accurate realisation of small features such as optical waveguide and p-contact ridge is challenging.

As shown in Figure 2.11 the realisation of these UTCs also includes the integration of coplanar waveguides (CPW) allowing the RF power to be extracted and measured by means of air coplanar ground-signal-ground probes. The masks contain different options for the size of the UTCs; the majority of the CPWs on the masks are optimised for 120 µm pitch probes, having 60 µm gap and signal line widths; however the smallest UTCs are integrated with 50 µm gap and signal line width CPWs to be used with a 100 µm pitch probe up to 220 GHz. All the gold CPWs are deposited on the silicon oxynitride (SiO_xN_y) layer.

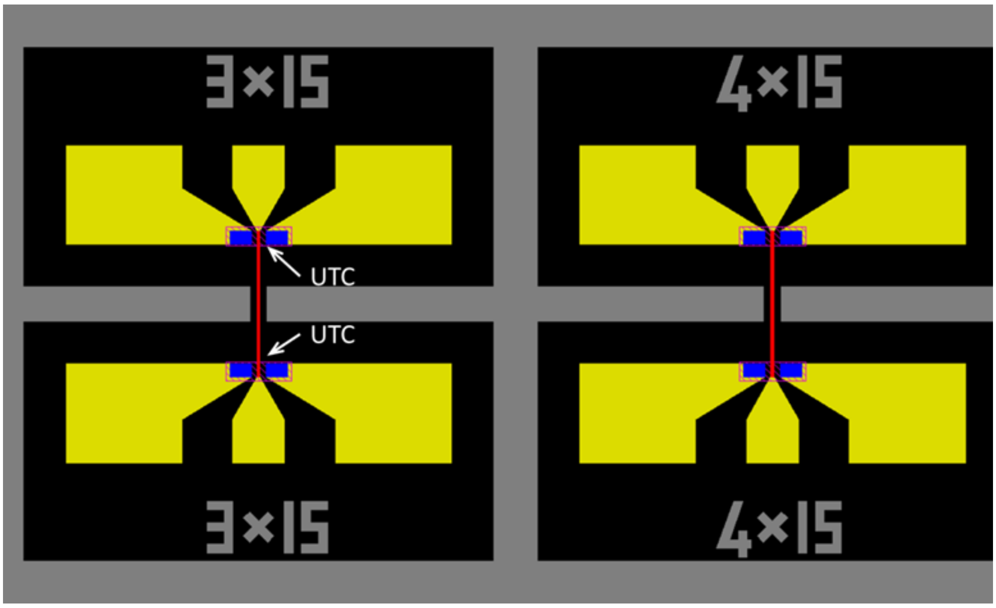

Figure 2.11: Superimposition of the fabrication mask set in an enlarged area. The numbers in grey refer to the UTC p-contact area. The grey strips are tranches etched through the SiO_xN_y layer in order to favour the separation of single devices by cleaving.

Some preliminary characterisation has been carried out on the waveguide UTCs fabricated in the first runs. Figure 2.12 shows the experimental arrangement employed to measure the waveguide UTC output power up to 50 GHz; the device was probed using a Cascade air coplanar (ACP) probe with coaxial electrical connection and a bias-T was employed to separate DC photocurrent and RF signal. For measurements within the W-band (75 GHz to 110 GHz) the UTC was probed using a Cascade air coplanar probe with a rectangular waveguide connection (WR10/WG27) followed by an Agilent sub-harmonic mixer compatible with the spectrum analyser. The external bias-T was not necessary since this probe has a separate connector to extract the DC photocurrent and bias the device under test.

The first polarisation controller in Figure 2.12 is needed to align the field polarisation of the two tuneable lasers. The second polarisation controller, located after the erbium-doped fibre amplifier (EDFA), is employed to optimise the coupling efficiency between the lensed fibre and the optical waveguide on the UTC chip.

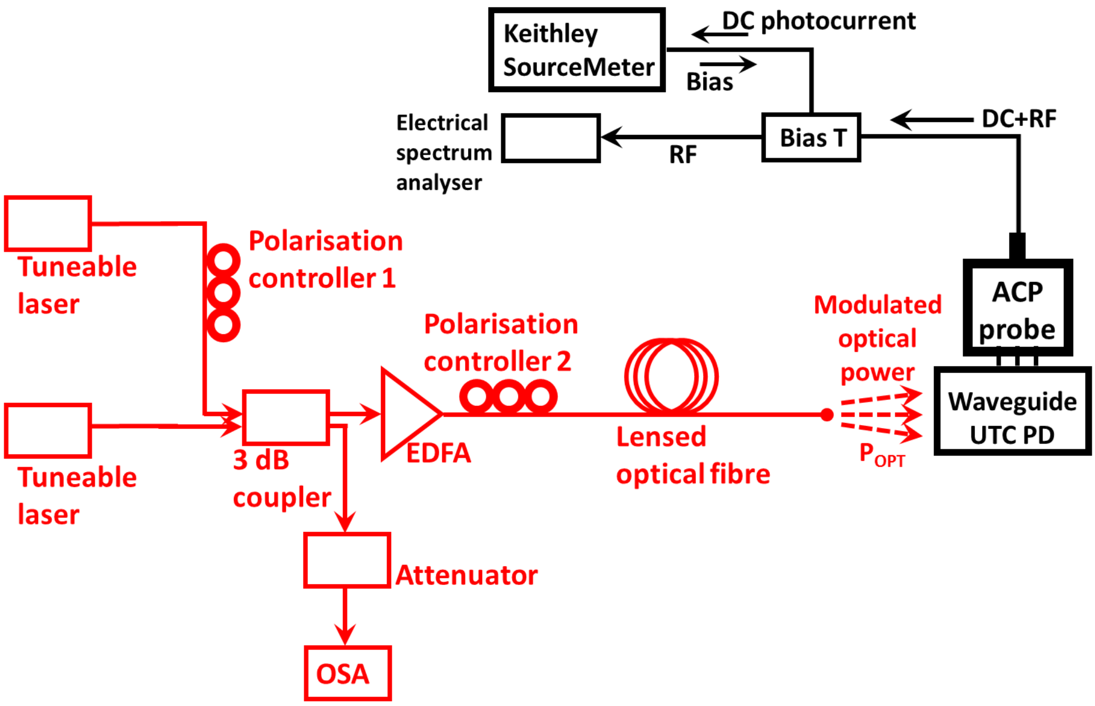

Figure 2.12: Experimental arrangement employed to measure the waveguide UTC output power up to 50 GHz. The first polarisation controller is needed to align the field polarisation of the two tuneable lasers. The second polarisation controller, located after the erbium-doped fibre amplifier (EDFA), is employed to optimise the coupling efficiency between the lensed fibre and the optical waveguide on the UTC chip. For measurements within the W-band (75 GHz to 110 GHz) the UTC was probed using a Cascade air coplanar probe with a rectangular waveguide connection (WR10/WG27) followed by an Agilent sub-harmonic mixer compatible with the spectrum analyser.

Figure 2.13 shows the RF power generated by a 7 x 15 μm^2 area UTC from 5 GHz to 110 GHz. The measured DC responsivity, at 1550 nm wavelength, was 0.035 A/W. The low DC responsivity is attributable to the challenging fabrication of the optical waveguide, whose quality is essential to maximise the fibre to chip coupling efficiency. The quite steep fall-off below 40 GHz is probably due to series resistance and/or device capacitance and modifications in the fabrication process are being made in order to address this issue.

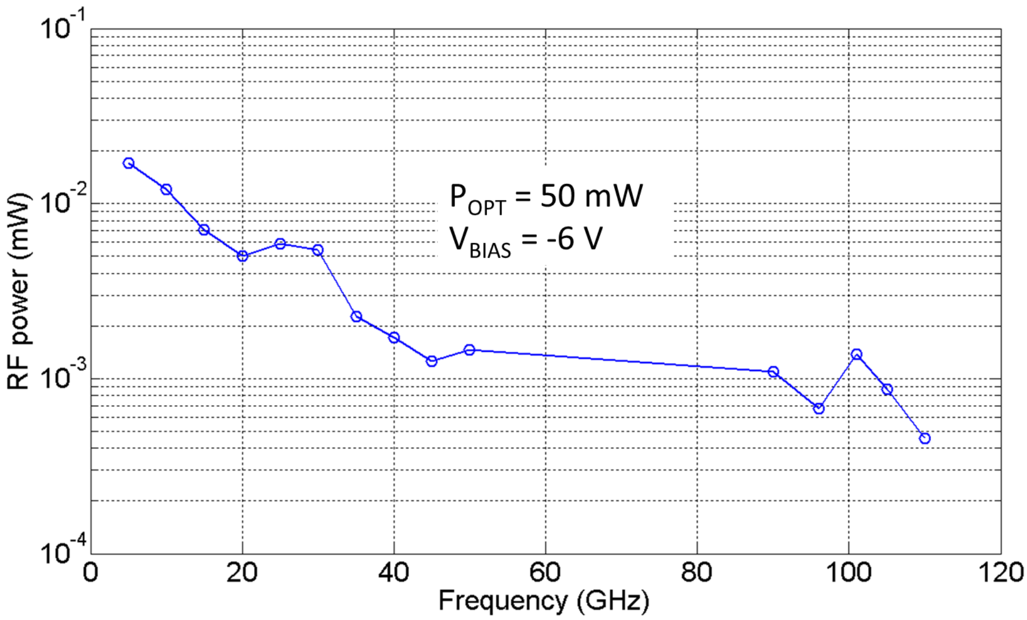

Figure 2.13: RF power generated by a 7 x 15 μm^2 area UTC from 5 GHz to 110 GHz, measured with a heterodyne experimental arrangement using two free running lasers.

2.4 Conclusions

In this chapter the first uni-travelling carrier photodiodes fabricated on InGaAsP-based material grown by solid source MBE have been reported. Large area vertically illuminated devices have been fabricated to test the material. Initial waveguide devices have also been fabricated.

This research aims to combine the merits of InGaAsP materials for the fabrication of uni-travelling carrier photodiodes with the advantages of Solid Source Molecular Beam Epitaxy. InGaAsP has been extensively employed in the literature to produce record breaking performance UTCs and is also preferred to quaternary materials containing aluminium because high optical quality aluminium compounds are difficult to grow and devices constructed with it can suffer reliability problems caused by aluminium oxidation. By using Solid Source Molecular Beam Epitaxy it is possible to solve the major problem associated with the diffusion of zinc in MOVPE and exploit the superior control provided by MBE growth techniques without the costs and the risks of handling toxic gases in Gas Source MBE.

Development of improved coplanar waveguide (CPW) integrated edge-coupled waveguide UTC-PDs is the next step; the integration of the CPW on the chip allows the microstrip mount to be removed from the measurement system, and the edge-coupled waveguide design is expected to improve significantly the device performance in terms of bandwidth and responsivity [2.4], [2.10]-[2.12]. The next chapter covers the work carried out to study and measure the output impedance of edge-coupled UTCs, which is essential to maximise the efficiency of energy coupling between the photodiode and the antenna.

2.5 References

[2.1] M. Natrella, E. Rouvalis, C.-P. Liu, H. Liu, C. C. Renaud, and A. J. Seeds, "InGaAsP-based uni-travelling carrier photodiode structure grown by solid source molecular beam epitaxy," *Optics Express*, vol. 20, no. 17. pp. 19279–19288, 2012.

[2.2] A. J. Seeds, C. Renaud, and M. Robertson, "Photodetector including multiple waveguides," US7851782 (B2), 2010.

[2.3] T. Nagatsuma, H. Ito, and T. Ishibashi, "High-power RF photodiodes and their applications," *Laser Photonics Rev.*, vol. 3, no. 1–2, pp. 123–137, 2009.

[2.4] E. Rouvalis, C. C. Renaud, D. G. Moodie, M. J. Robertson, and A. J. Seeds, "Continuous wave terahertz generation from ultra-fast InP-based photodiodes," *IEEE Trans. Microw. Theory Tech.*, vol. 60, no. 3 part 1, pp. 509–517, 2012.

[2.5] A. Beling, Z. Li, Y. Fu, H. Pan, and J. C. Campbell, "High-power and high-linearity photodiodes," *IEEE Photonic Soc. 24th Annu. Meet. PHO 2011*, vol. 1, pp. 19–20, Oct. 2011.

[2.6] X. W. X. Wang, N. D. N. Duan, H. C. H. Chen, and J. C. Campbell, "InGaAs–InP photodiodes with high responsivity and high saturation power," *IEEE Photonics Technol. Lett.*, vol. 19, no. 16, pp. 1272–1274, 2007.

[2.7] H. Ito, T. Furuta, S. Kodama, and T. Ishibashi, "InP/InGaAs uni-travelling-carrier photodiode with 310 GHz bandwidth," *Electronics Letters*, vol. 36, no. 21. pp. 1809–1810, 2000.

[2.8] H. Ito, T. Nagatsuma, A. Hirata, T. Minotani, A. Sasaki, Y. Hirota, and T. Ishibashi, "High-power photonic millimetre wave generation at 100 GHz using matching-circuit-integrated uni-travelling-carrier photodiodes," *Optoelectron. IEE Proc.*, vol. 150, no. 2, pp. 138–142, 2003.

[2.9] H. Ito, F. Nakajima, T. Furuta, and T. Ishibashi, "Continuous THz-wave generation using antenna-integrated uni-travelling-carrier photodiodes," *Semiconductor Science and Technology*, vol. 20, no. 7. pp. S191–S198, 01-Jul-2005.

[2.10] C. C. Renaud, D. Moodie, M. Robertson, and A. J. Seeds, "High output power at 110 GHz with a waveguide Uni-travelling carrier photodiode," *Conf. Proc. - Lasers Electro-Optics Soc. Annu. Meet.*, pp. 782–783, 2007.

[2.11] C. Renaud, M. Robertson, D. Rogers, R. Firth, P. Cannard, R. Moore, and A. Seeds, "A high responsivity, broad band waveguide uni-travelling carrier photodiode," *Proc. SPIE*, vol. 6194, no. 1, pp. C1940–C1940, 2006.

[2.12] E. Rouvalis, C. C. Renaud, D. G. Moodie, M. J. Robertson, and A. J. Seeds, "Traveling-wave Uni-Traveling Carrier photodiodes for continuous wave THz generation," *Opt. Express*, vol. 18, no. 11, pp. 11105–11110, 2010.

[2.13] A. Beling, J. C. Campbell, H. Pan, H. Chen, H.-G. Bach, G. G. Mekonnen, and D. Schmidt, "InP-Based High-Speed Photonic Devices InP-Based High-Speed Photonic Devices," *Opt. Fiber Commun. Fiber Opt. Eng. Conf. 2008. OFC/NFOEC 2008. Conf.*, pp. 1–27, 2008.

[2.14] J. N. Baillargeon, a. Y. Cho, F. a. Thiel, R. J. Fischer, P. J. Pearah, and K. Y. Cheng, "Reproducibility studies of lattice matched GaInAsP on (100) InP grown by molecular beam epitaxy using solid phosphorus," *Appl. Phys. Lett.*, vol. 65, no. 2, pp. 207–209, 1994.

[2.15] C. C. Wamsley, "Solid source molecular beam epitaxy of GaInAsP/InP: Growth mechanisms and machine operation," *Journal of Vacuum Science & Technology B: Microelectronics and Nanometer Structures*, vol. 14, no. 3. pp. 2322–2324, May-1996.

[2.16] M. Pessa, M. Toivonen, M. Jalonen, P. Savolainen, and A. Salokatve, "All-solid-source molecular beam epitaxy for growth of III–V compound semiconductors," *Thin Solid Films*, vol. 306, no. 2. pp. 237–243, Sep-1997.

[2.17] P. Claxton, J. Roberts, J. David, C. Sotomayor-Torres, M. Skolnick, P. Tapster, and K. Nash, "Growth and characterisation of quantum wells and selectively doped heterostructures of InP/$Ga_{0.47}In_{0.53}As$ grown by solid source MBE," *J. Cryst. Growth*, vol. 81, no. 1–4, pp. 288–295, 1987.

[2.18] E. F. Schubert, S. W. Downey, C. Pinzone, and A. B. Emerson, "Evidence of very strong inter-epitaxial-layer diffusion in Zn-doped GaInPAs/InP structures," *Appl. Phys. A Mater. Sci. Process.*, vol. 60, no. 6, pp. 525–527, 1995.

[2.19] N. Otsuka, M. Kito, M. Ishino, Y. Matsui, and F. Toujou, "Control of double diffusion front unintentionally penetrated from a Zn doped InP layer during metalorganic vapor phase epitaxy," *J. Appl. Phys.*, vol. 84, no. 8, pp. 4239–4247, 1998.

[2.20] M. Henini, "Recent developments in InP and related compounds," *III-Vs Rev.*, vol. 13, no. 2, pp. 34–44, 2000.

[2.21] M. B. Panish, "Molecular Beam Epitaxy of GaAs and InP with Gas Sources for As and P," *J. Electrochem. Soc.*, vol. 127, no. 12, pp. 2729–2733, 1980.

[2.22] D. L. Miller, S. S. Bose, and G. J. Sullivan, "Design and operation of a valved solid-source As_2 oven for molecular beam epitaxy," *J. Vac. Sci. Technol. B Microelectron. Nanom. Struct.*, vol. 8, no. 2, p. 311, 1990.

[2.23] G. W. Wicks, M. W. Koch, J. A. Varriano, F. G. Johnson, C. R. Wie, H. M. Kim, and P. Colombo, "Use of a valved, solid phosphorus source for the growth of $Ga_{0.5}In_{0.5}P$ and $Al_{0.5}In_{0.5}P$ by molecular beam epitaxy," *Appl. Phys. Lett.*, vol. 59, no. 3, pp. 342–344, 1991.

[2.24] M. Toivonen, A. Salokatve, and M. Jalonen, "All solid source molecular beam epitaxy growth of 1.35 μm wavelength strained-layer GaInAsP quantum well laser," *Electron. Lett.*, vol. 31, no. 10, pp. 797–799, 1995.

[2.25] C. P. Liu, A. Seeds, J. S. Chadha, P. N. Stavrinou, G. Parry, M. Whitehead, A. B. Krysa, and J. S. Roberts, "Design, fabrication and characterisation of normal-incidence 1.56-μm multiple-quantum-well asymmetric Fabry-Perot modulators for passive picocells," *IEICE Trans. Electron. E Ser. C*, vol. 86, no. 7, pp. 1281–1289, 2003.

[2.26] F. Fiedler, A. Schlachetzki, and G. Klein, "Material-selective etching of InP and an InGaAsP alloy," *J. Mater. Sci.*, vol. 17, no. 10, pp. 2911–2918, 1982.

[2.27] D. Pasquariello, E. S. Björlin, D. Lasaosa, Y. J. Chiu, J. Piprek, and J. E. Bowers, "Selective undercut etching of InGaAs and InGaAsP quantum wells for improved performance of long-wavelength optoelectronic devices," *J. Light. Technol.*, vol. 24, no. 3, pp. 1470–1477, 2006.

[2.28] S. Phatak and G. Kelner, "Material-Selective Chemical Etching in the System InGaAsP/ InP," *J. Electrochem. Soc.*, vol. 126, no. 2, pp. 287–292, 1979.

[2.29] S. Adachi, "Chemical Etching of InP and InGaAsP/InP," *J. Electrochem. Soc.*, vol. 129, no. 3, pp. 609–613, 1982.

[2.30] K. J. Williams and R. D. Esman, "Design considerations for high-current photodetectors," *J. Light. Technol.*, vol. 17, no. 8, pp. 1443–1454, 1999.

[2.31] G. A. Davis, R. E. Weiss, R. A. LaRue, K. J. Williams, and R. D. Esman, "A 920-1650-nm high-current photodetector," *IEEE Photonics Technol. Lett.*, vol. 8, no. 10, pp. 1373–1375, 1996.

[2.32] N. Duan, X. Wang, N. Li, H. D. Liu, and J. C. Campbell, "Thermal analysis of high-power InGaAs-InP photodiodes," *IEEE J. Quantum Electron.*, vol. 42, no. 12, pp. 1255–1258, 2006.

[2.33] M. Chtioui, D. Carpentier, S. Bernard, B. Rousseau, F. Lelarge, F. Pommereau, C. Jany, A. Enard, and M. Achouche, "Thick absorption layer uni-traveling-carrier photodiodes with high responsivity, high speed, and high saturation power," *IEEE Photonics Technol. Lett.*, vol. 21, no. 7, pp. 429–431, 2009.

[2.34] M. Chtioui, F. Lelarge, A. Enard, F. Pommereau, D. Carpentier, A. Marceaux, F. Van Dijk, and M. Achouche, "High responsivity and high power UTC and

MUTC GaInAs-InP photodiodes," *IEEE Photonics Technol. Lett.*, vol. 24, no. 4, pp. 318–320, Feb. 2012.

Chapter 3 - Characterisation and circuit analysis of waveguide UTCs

This chapter reports the experimental characterisation and circuit analysis of waveguide UTCs. Along with the 3D full-wave modelling discussed in the next chapter, this work aims to allow the question regarding the UTC-to-antenna coupling efficiency to be more thoroughly understood. To the best of the author's knowledge no in depth analysis to evaluate the UTC impedance has been attempted in the literature, with the ultimate objective to enhance the efficiency of energy coupling between photodiode and antenna. Typically, in designing or predicting the performance of antenna integrated UTC systems, the match/mismatch between the photodetector and the antenna is neglected or a simplified configuration, consisting of the estimated device capacitance and series resistance, is assumed; it will be shown that, using this simplified configuration, it is not possible to fit the measured real and imaginary part of the device impedance over the frequency range to an acceptable accuracy. Furthermore, when photodiodes and THz antennas connected through a waveguide are reported, e.g. [3.1], the waveguide-to-antenna transition and its optimisation are usually discussed but the losses of power caused by a possible mismatch between UTC and waveguide are ignored.

When the shortest electrical wavelength of the frequency range being studied is substantially greater than the UTC size, then the photodiode can be considered as a lumped element. The problem concerning the UTC-to-antenna coupling efficiency optimisation can hence be addressed as an impedance matching problem, requiring a reasonably accurate knowledge of both the antenna and UTC impedance. In Chapter 5, the design of antennas operating around 345 GHz, where there is a minimum in the atmospheric attenuation [3.2], will be presented. These antennas will be integrated with 3 x 15 μm^2 active area UTCs. At 345 GHz, the free space wavelength is 870 μm (i.e. 58 times the photodiode length) whereas the wavelength in the InGaAs absorber, which is the material with the highest relative electrical permittivity in the structure ($\varepsilon_{InGaAs} = 13.9$), is over 15 times longer than the device length.

To maximise the UTC-to-antenna coupling efficiency at higher frequencies, where the lumped element assumption ceases to stand, the development of a different analytical approach will be required, especially for longer travelling wave devices. In this scenario the UTC will have to be treated as a section of waveguide, endowed with its own characteristic impedance, and both ends of the UTC will need to “see” a load matched to the characteristic impedance in order to minimise the losses caused by the reflections at such ends; if one end of the device is left as an open circuit, whatever we connect to the other end will not “see” an impedance matched to the characteristic impedance but instead the input impedance of a section of a transmission line terminated with an open circuit. The study of the UTC-to-antenna coupling efficiency for travelling wave devices and/or short devices at very high frequencies, is not included in this thesis but is planned as part of the future work.

In Chapter 5 it will be shown how a reasonably accurate knowledge of the photodiode impedance can enable us to make a satisfactory prediction of the power radiated by an antenna integrated with such a photodiode, both in terms of absolute value and trend over the frequency range, by means of 3D full-wave simulation. It will also be noted how, the use of the simplified parallel-capacitance and series resistance configuration for the radiated power calculation, would have led to inaccurate results. This proves that a significant amount of power can be lost as rejected by the antenna and raises the possibility to enhance the radiated power by designing antennas approaching, as closely as possible, the maximum power transfer condition, realised when the load impedance is equal to the complex conjugate of the source impedance. On the other hand it is important to remember that a reflection-less impedance matching is always realised when the load impedance is equal to the source impedance. It follows that if the source impedance is real (purely resistive), then the optimum load (i.e. antenna) impedance to achieve the maximum transfer of power coincides with the optimum load impedance to achieve a reflection-less matching; in other words the minimisation of the reflection coefficient (i.e. S_{11}) leads in this case automatically to the maximisation of the real power transferred to the load. When the source impedance is complex, as is the case for the UTC, this is no longer true and the minimisation of the reflection coefficient as a criterion to maximise the real power transferred to the load cannot be employed.

While the antenna impedance is relatively easy to calculate and is established during the design stage, the modelling and evaluation of the UTC impedance is a far more challenging task. Knowing accurately the physical properties of all the semiconductor materials making up a UTC photodiode is essential to get truthful results from modelling and simulation and yet, it is a difficult knowledge to achieve. UTCs contain ternary (e.g. InGaAs) and quaternary (e.g. InGaAsP) materials, with different element concentrations and different doping levels; the values of electrical permittivity and especially electrical conductivity for these materials can only be approximately estimated. Furthermore, quantum mechanical effects governing the electron transport from the absorber to the collection layer, through the spacers' tunnel barriers due to the conduction band offsets, can affect the conduction properties in a way that, at a macroscopic scale, is reflected in changes in bulk material properties such as resistivity and electrical permittivity. For these reasons, the work regarding the study of the UTC impedance will start with the analysis of the experimental results and a circuit analysis, in this chapter, which will help assess and refine the material physical properties to employ in the full-wave modelling and simulation, presented in the next chapter. The full-wave modelling will in turn enable the S_{11} and the UTC impedance to be evaluated up to frequencies not attainable by measuring equipment.

The experimental data of the UTC frequency photo-response are also discussed in this chapter and compared with the values calculated by means of a circuit analysis adopting the results of the UTC impedance investigation.

In Chapter 2 we have discussed the epitaxial structure grown by SS-MBE at UCL, employed to fabricate test vertically illuminated UTCs; this epitaxy is similar to that reported previously in [3.3] and is the same as that being used for the fabrication of waveguide UTCs, also described in Chapter 2.

The waveguide UTCs characterised in this chapter have been provided by III-V Lab and were fabricated as part of the project iPHOS; their epitaxial layer structure [3.4] is shown in Table 3.1. The III-V Lab UTC epitaxial structure is based on that first designed at UCL [3.3], [3.5], [3.6]. The layer structure in Table 3.1 [3.4] shows some changes with respect to the UCL structure discussed in [3.3], [3.6] and in Chapter 2 [3.5], mainly due to the fact that the III-V Lab photodiodes were primarily designed and fabricated to be monolithically integrated with other components, such as lasers and semiconductor optical amplifiers. The changes are listed below:

- GaInAs is employed as p-contact layer material instead of InGaAsP ($Q_{1.3}$);
- A thick ridge layer of highly p-doped InP has been added between the p-contact and the absorber layers;
- Quaternary InGaAsP $Q_{1.17}$ is employed for the waveguide layer instead of InGaAsP $Q_{1.3}$;
- BCB was employed by III-V Lab, for passivation purposes and as a base layer to deposit the CPW pads, rather than the SiO_xN_y used in UCL structures. The BCB layer was modelled in CST employing a "loss free" polymer, from the CST material database, with an electrical permittivity of 3.5. Loss free means that no electrical conductivity or tangent delta are included in the material model.

Table 3.1: Layer structure of the UTCs provided by III-V Lab [3.4], fabricated as part of the project iPHOS. This layer structure is based on that first designed at UCL [3.3], [3.6] and then refined by Dr. Efthymios Rouvalis still at UCL [3.5].

UTC-PD Epitaxy			
Doping(cm^{-3})	**Material**	**Function**	**Thickness (nm)**
p^{++}	GaInAs	p-contact	200
p^{+}	InP	Ridge Layer	1000
p-gradual	$In_{0.53}Ga_{0.47}As$	Absorber	120
n	Q	Spacer layers	--
n	InP	Depletion	300
n^{+}	$Q_{1.17}$	Waveguide	300
n^{+}	InP	n – contact	--
Fe	SI - InP	Substrate	--

The devices were provided in different size (active area) sets. The work covered in the following sections of this chapter is focused on 3 x 15 μm^2 and 4 x 15 μm^2 active area devices. In Figure 3.1 two sample photodetectors are illustrated, with active area equal to 3 x 15 μm^2 and 4 x 15 μm^2 respectively. The device geometry is the same as the UCL waveguide UTCs described in Chapter 2. The photodiodes are integrated with coplanar waveguide contact patterns for the use of air coplanar probes. Also in Figure 3.1 the optical waveguide to couple light into the detector is highlighted; for both 3 x 15 μm^2 and 4 x 15 μm^2 area UTCs, the optical waveguide width is scaled down to less than 3 μm at the cleaved facet, where the fibre to chip coupling takes place.

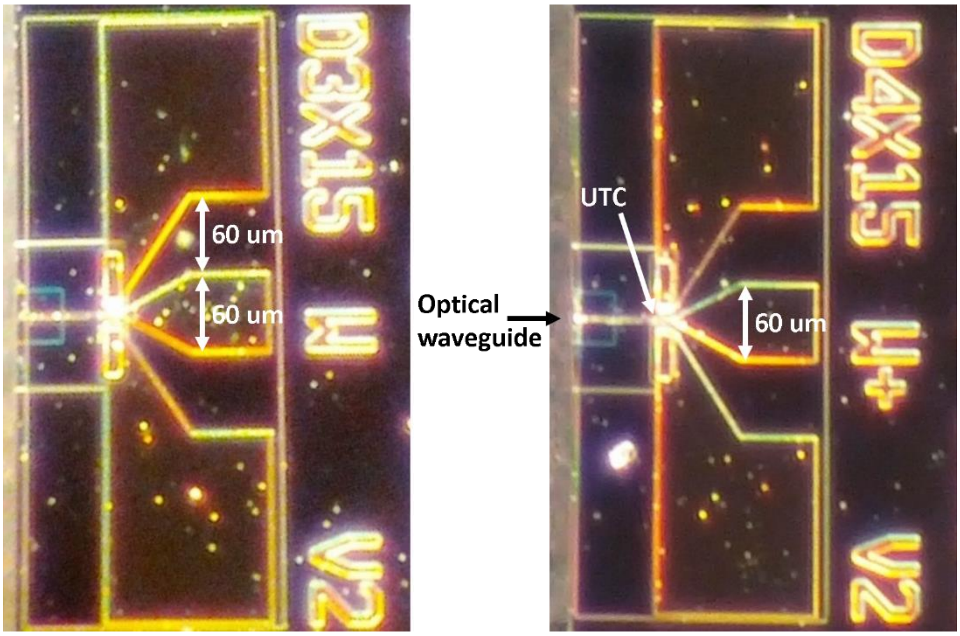

Figure 3.1: Photograph of two sample UTCs, with 3 x 15 μm^2 and 4 x 15 μm^2 area. The devices are integrated with coplanar waveguide contact pattern for the use of air coplanar probes. These UTCs have been provided by III-V Lab and were fabricated as part of the project iPHOS.

All the measurements discussed in this chapter were carried out at a constant temperature of 22 ^{o}C, maintained by means of a Peltier Cooling Module and a temperature controller.

3.1 DC characterisation

In Figure 3.2 the I-V characteristic and the resistance of two different photodiodes are displayed, measured over the voltage range -2 V to 1.5 V. The devices exhibit low dark current, of about 27 nA for a 2 V reverse bias, and somewhat high values of series resistance, e.g. 25 Ω for the 4 x 15 μm^2 area UTC and 31 Ω for the 3 x 15 μm^2 area UTC. Increased values of the device series resistance were to be expected due to the additional 1 μm thick layer of p-doped InP illustrated in Table 3.1., nevertheless, the resistance values would have decreased further for bias greater than 1.5 V, though overheating failure may also have occurred.

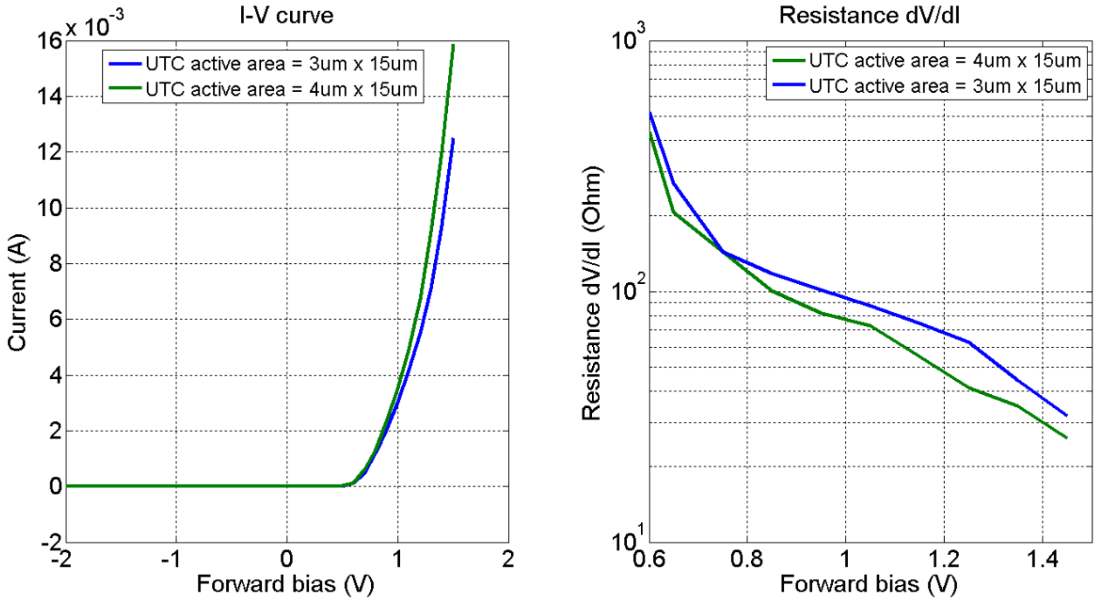

Figure 3.2: On the left, I-V curves for the two different area devices, measured over the voltage range -2 V to 1.5 V. On the right, resistance of the forward biased devices, displayed over the voltage range 0.6 V to 1.5 V.

A theoretical estimate of the series resistance can also be carried out, as long as the conductivity σ of the layers contributing to the resistance is known, since the device geometry is also known from Chapter 2. Such conductivity can be calculated as $\sigma = qn_e\mu_e + qn_h\mu_h$, where q is the electron charge (1.6022×10^{-19} C), n_e/n_h are the electron/hole concentrations and μ_e/μ_h are the electron/hole mobility. For highly doped materials, like those contributing to the UTC series resistance (namely p-contact, ridge layer, waveguide and n-contact), the majority carrier concentration can be assimilated to the donor/acceptor concentration, provided the temperature is high enough to fully activate all of the donors and acceptors. On the other hand the minority carrier concentration can be extracted from the mass action law $n_e n_h = n_i^2$, where n_i is the material intrinsic concentration; based on the doping levels shown in Table 3.1 and considering the intrinsic carrier concentrations of the materials contributing to the device series resistance (e.g. 6.3×10^{11} cm^{-3} for InGaAs, 1.3×10^{7} cm^{-3} for InP and 4.4×10^{9} cm^{-3} for $Q_{1.17}$), it appears clear that the minority carrier concentrations are several orders of magnitude smaller than the majority ones and hence their contribution to the material conductivity is negligible. It follows that the majority carrier mobility is all that is needed to have an estimate of the material conductivities and therefore the layer resistances. Displayed in Table 3.2 is a summary of the electrical conduction properties of the layers contributing to the photodetector series resistance.

Table 3.2: Electrical conduction properties of the layers contributing to the photodetector series resistance.

Layer description	**Thickness (nm)**	**Majority carrier mobility ($cm^{-2}V^{-1}s^{-1}$)**	**Electrical conductivity ($\Omega^{-1}m^{-1}$)**	**Layer resistance (Ω)**	
				3 x 15 μm² UTC	**4 x 15 μm² UTC**
p-contact GaInAs p^{++}	200	60 [3.7]	19226	0.23	0.17
Ridge Layer InP p^{+}	1000	60 [Ioffe]	1923	11.6	8.7
Waveguide $Q_{1.17}$ n^{+}	300	1600 [Ioffe]	89723	negligible	negligible
n – contact InP n^{+}	--	1500 [3.8]	96132	3	3
				Total layer resistance (Ω) 15	**Total layer resistance (Ω)** 12

The data illustrated in Table 3.2 also enable us to point out the additional resistance introduced by the thick InP ridge layer.

All the conductivities have been calculated assuming a temperature of 300 K. It is important to note that the conductivity of highly doped semiconductors is not very sensitive to temperature changes, as long as the temperature does not increase enough to trigger the transition from extrinsic to intrinsic region; in fact, in the extrinsic region, the carrier concentration is dictated by the dopant concentration and the variations of the two scattering phenomena, e.g. lattice and impurity scattering, that influence the carrier mobility, tend to cancel each other (lattice scattering increases while impurity scattering decreases as the temperature goes up) causing the mobility to remain approximately constant.

In order to obtain a more truthful value of the total device resistance, the contact resistance of the ohmic contacts formed at the interface between the metallisation (Ti/Pt/Au) and n/p-contact layers has to be taken into account. The ohmic contact resistance can be experimentally evaluated through transmission line model measurements [3.9], [3.10], though it was not possible to carry out this type of measurements on the III-V Lab UTCs as no samples with the required contact pad patterns were available.

Specific contact resistance values of 5.5×10^{-7} Ω cm^2 and 8×10^{-6} Ω cm^2 obtained by deposition of Ti/Pt/Au on Zn-doped 5×10^{18} cm^{-3} p-$In_{0.53}Ga_{0.47}As$ and S-doped 1×10^{18} cm^{-3} n-InP respectively, have been reported in the literature [3.11]. A much higher value of specific contact resistance of p-type ohmic contacts, has also been reported, i.e. 10.68×10^{-6} Ω cm^2 for Ti/Pt/Au deposited on Zn-doped 2×10^{19} cm^{-3} p-$In_{0.53}Ga_{0.47}As$, in [3.12]. Shown in Table 3.3 is the contribution to the total device resistance provided by the contact resistance of the ohmic contacts formed at the interface between the metallisation (Ti/Pt/Au) and n/p-contact layers, calculated using the specific contact resistance reported in [3.11].

Table 3.3: Contribution to the total device resistance provided by the contact resistance of the ohmic contacts formed at the interface between the metallisation (Ti/Pt/Au) and n/p-contact layers.

Contact description	**Specific contact resistance (Ω cm^2)**	**Contact resistance (Ω)**	
		3 x 15 μm^2 UTC	**4 x 15 μm^2 UTC**
Ti/Pt/Au on p^{++} GaInAs	5.5×10^{-7} [3.11]	1.22	0.92
Ti/Pt/Au on n^{+} InP	8×10^{-6} [3.11]	3.53	3.53
		Total contact resistance (Ω) 5	**Total contact resistance (Ω)** 4.5

Based on the data illustrated in Table 3.2 and Table 3.3, the total UTC series resistance is about 20 Ω for the 3 x 15 μm^2 active area device and 16 Ω for the 4 x 15 μm^2 active area device, which is, as expected, less than the lowest values shown in Figure 3.2 extracted from the I-V curve.

It has to be noted that the assessment of the contribution provided to the device series resistance by the ohmic contact on the n-InP contact layer, is not as straightforward. The area covered by the two n-metallisation pads is quite large (greater than 20 x 15 μm^2 each pad). Therefore, if the whole area was considered to calculate the n-ohmic contact resistance, then a value of only 1.3 Ω would be obtained. Actually, only a limited area of the pads is crossed by the electric current and hence the resistance offered by the ohmic contact is larger, i.e. 3.5 Ω. This analysis has been verified by means of CST MWS, as illustrated in Figure 3.3. The current flows vertically through all the ridge layers and then through the InP n-layer to reach the n-metallisation. Here the intensity of the current flowing through the n-ohmic contact decreases gradually as we move further away from the p-ridge; in practice an effective area of 7.5 x 15 μm^2 for each of the two n-ohmic contacts can be identified, which would provide the same resistance of 3.5 Ω (shown in Table 3.3) if uniformly crossed by the current. Absorber, spacer and depletion layers in the ridge have been replaced by a layer of perfect electric conductor in the CST model, as they do not contribute to the device series resistance.

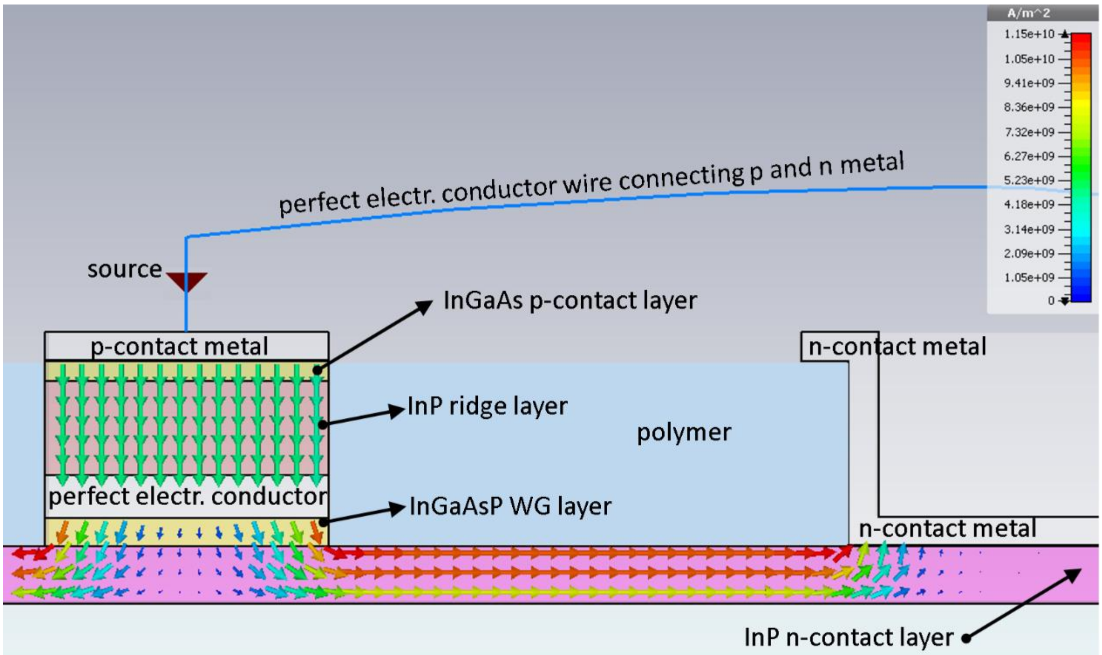

Figure 3.3: Cross section of the UTC CST model, showing the current flowing through all the ridge layers and through the InP n-layer to reach the n-metallisation. The simulation shows that only a limited area of the interface between InP n-layer and n-metallisation is actually crossed by the current. Absorber, spacer and depletion layers in the ridge have been replaced by a layer of perfect electric conductor as they do not contribute to the device series resistance.

3.2 S_{11} and impedance measurement

The UTC S_{11} and impedance measurement was performed up to 110 GHz in two steps, covering the sub-ranges 10 MHz to 67 GHz and 75 GHz to 110 GHz.

In the lower frequency range (10 MHz to 67 GHz) an Agilent performance network analyser (PNA) was employed, directly capable of operating from 10 MHz up to 67 GHz. The device was probed using a Cascade air coplanar probe with coaxial electrical connection. A one port short-open-load-through (SOLT) calibration was performed up to the probe tips, by means of a Cascade impedance standard substrate (ISS).

For measurements in the W-band (75 GHz to 110 GHz), an Agilent extender (mixer) was connected to the PNA, enabling operation between 75 GHz and 110 GHz. In this range a Cascade air coplanar probe with a waveguide electrical connection (WR10/WG27) was used. The probe and the extender were rigidly connected directly through the waveguide connections and firmly secured against any move; the 5 axis stage holding the device was then carefully controlled to ensure precise probing. In this frequency range the one port SOLT calibration was performed by means of a Cascade W-band impedance standard substrate.

The S_{11} (relative to a 50 Ω reference impedance) magnitude in dB and phase in degree are displayed in Figure 3.4, while the impedance real part (resistance) and imaginary part (reactance), both in Ohm, are given in Figure 3.5. Figure 3.6 shows the measured reflection coefficient plotted on an impedance type Smith chart. Two different size devices were measured, e.g. 3 x 15 μm^2 and 4 x 15 μm^2, and two different values of reverse voltage were applied, e.g. 0 V and 2 V.

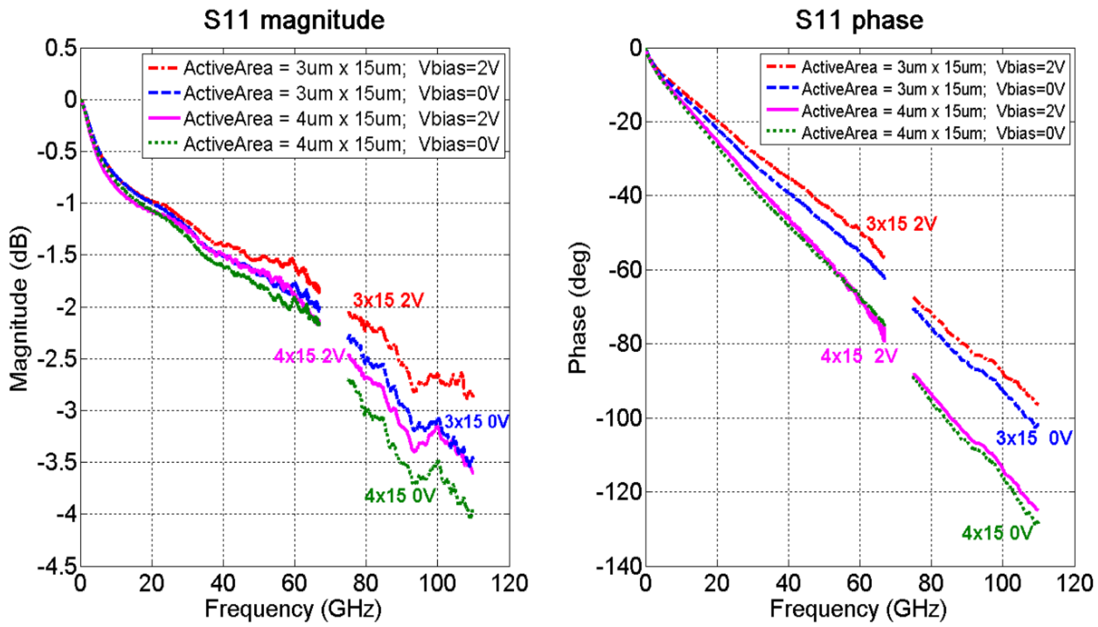

Figure 3.4: S_{11} magnitude in dB and phase in degree, measured with respect to the PNA 50 Ω impedance.

As expected, the device reactance exhibits a capacitive behaviour (i.e. is negative) within the measured frequency range and is larger (in absolute value) for smaller area devices; applied negative bias also increases the reactance absolute value. The impedance real part is visibly larger for smaller devices and appears to decrease with greater (more negative) bias in the W-band and decrease at lower frequencies.

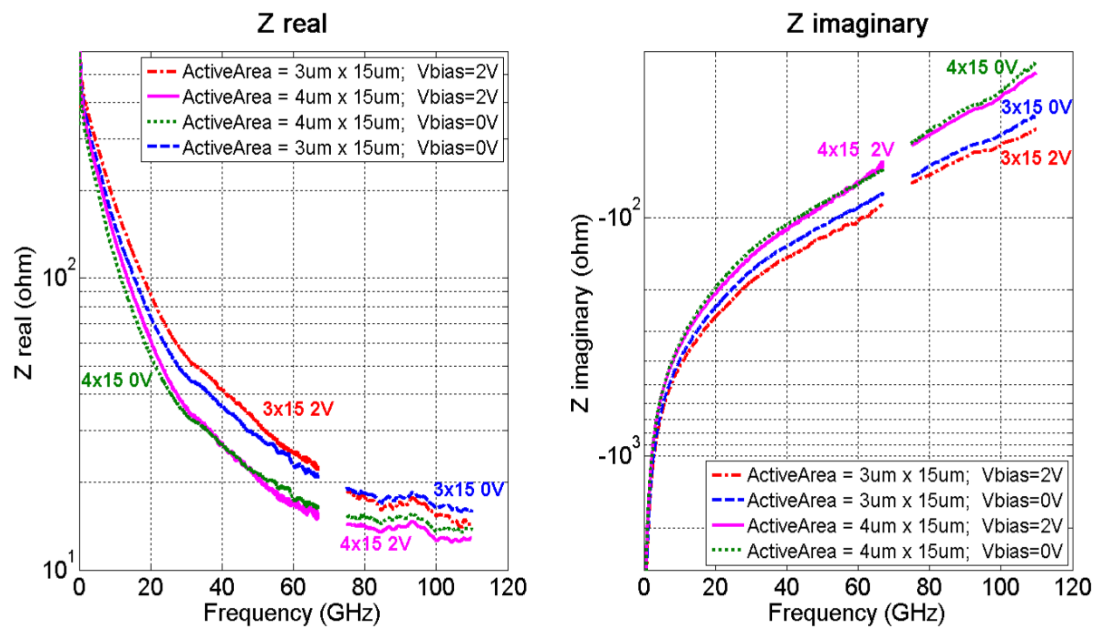

Figure 3.5: UTC impedance real part (resistance) and imaginary part (reactance).

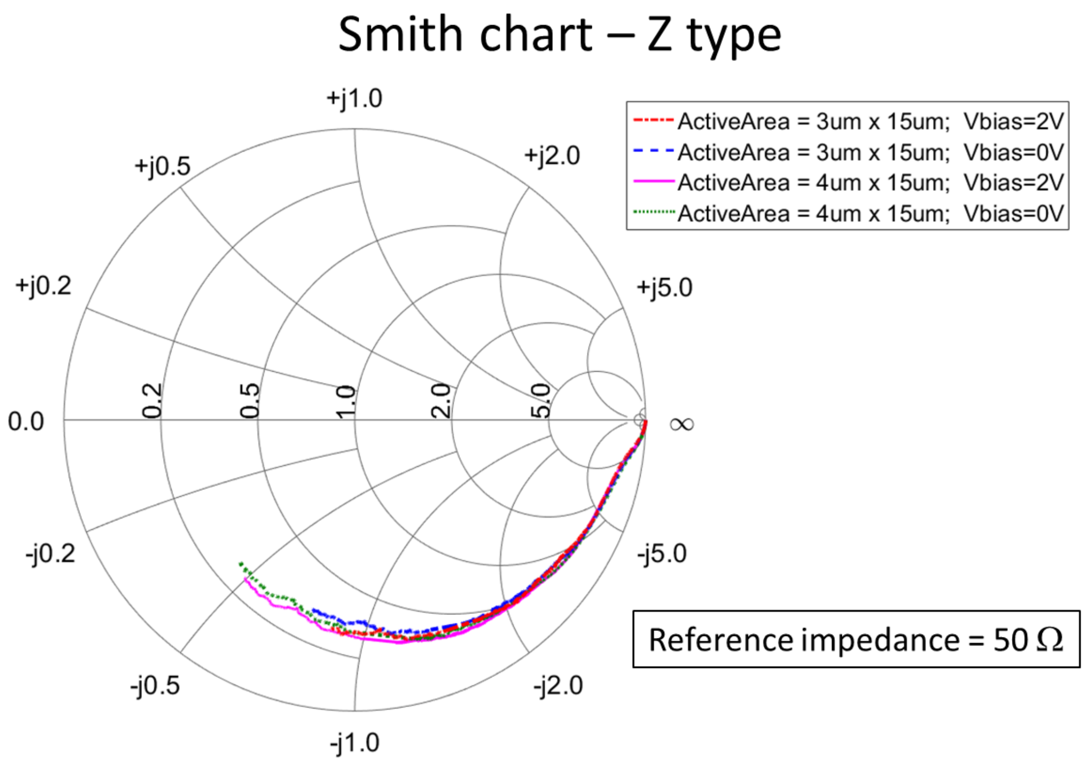

Figure 3.6: Measured reflection coefficient plotted in an impedance type Smith chart.

The theoretical capacitance for the two different area devices at zero bias, assuming the relative electrical permittivity for the depletion layer InP to be 12.5 and ignoring the effect of the two spacers, should be about 16.6 fF for the 3 x 15 μm^2 UTC and 22 fF for the 4 x 15 μm^2.

On the other hand, if we try to extract the capacitance C from the measured device reactance $X(f)$, as $C = -1/2\pi f X(f)$, we obtain the curves displayed in Figure 3.7.

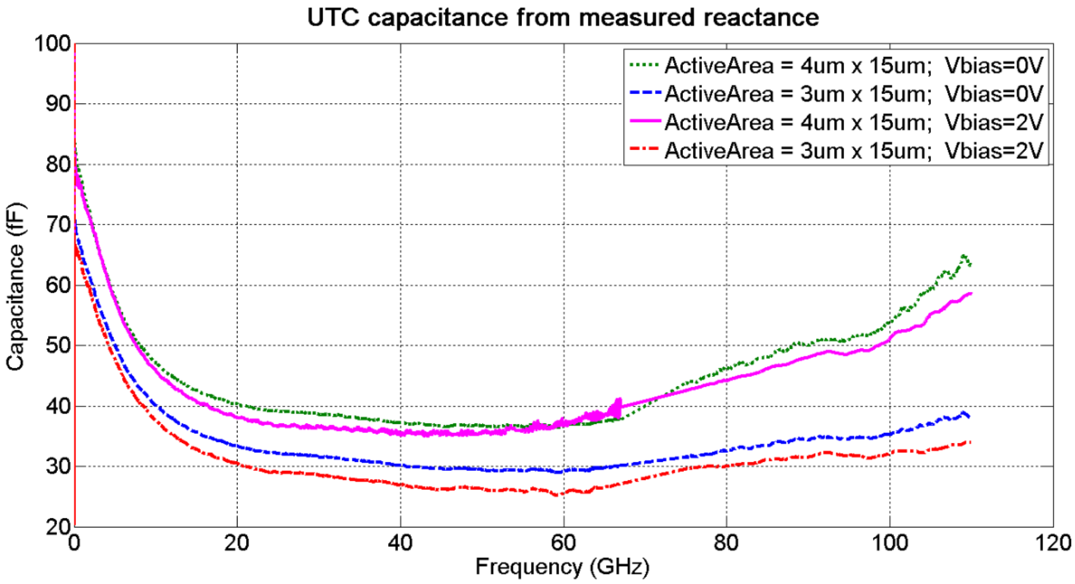

Figure 3.7: UTC capacitance derived from the measured device reactance.

The imaginary part of the impedance is in general a combination of capacitive and inductive components, however, at lower frequencies, the inductive components are much less significant unless the device equivalent inductance is very large, which is not the case for the UTCs under study. It follows that the lower the frequency the better the curves in Figure 3.7 represent the UTC total capacitance. One should expect a photodiode capacitance to be essentially frequency independent though, this does not seem to be supported by the experimental results shown thus far. The measured capacitance seems to be reasonably constant within the frequency range 20 GHz to 67 GHz. The increasing capacitance values exhibited above 75 GHz are, in the author's opinion, caused by inductive components that start to become significant or by parasitic parallel capacitances and therefore are not accurately representative of the photodetector total capacitance. To the contrary the strongly frequency dependent behaviour displayed below 20 GHz, does seem to suggest a change in the total device capacitance and indeed cannot be explained by means of the traditional single constant capacitance in parallel with the photodiode photocurrent generation, when the device is illuminated. If the device reactance actually depended only on a single capacitance or on a single capacitance in parallel with a very large resistance, then the curves in Figure 3.7 should be flat over the whole frequency range below the frequencies affected by the inductive components.

Device capacitance measurements are normally performed at a single frequency, typically below 1 MHz; as can be seen in Figure 3.7, the capacitance measured near the lowest frequency handled by the PNA (i.e. 10 MHz) ranges from about 65 fF to more than 80 fF. To verify these low frequency capacitance values, the UTC S_{11} were re-measured using an Agilent network analyser operating from 9 KHz up to 8.5 GHz; the obtained results were consistent with the PNA results (10 MHz to 67 GHz) and the capacitance measured near the lowest frequency (i.e. 9 KHz) ranged from 65 fF to 85 fF.

A simplified circuit model, shown in Figure 3.8 a), comprising the device capacitance and series resistance, is commonly recognised as an adequate model for the UTC. A slightly more accurate circuit version, illustrated in Figure 3.8 b), includes the effect of the resistance R_p, across the depletion layer, which, although very high (hundreds of KΩ), is not infinite and also the effect of parasitic capacitance C_p and inductance L_p, whose effect become relevant only at very high frequencies. The arrow in the circle, displayed in the left hand side of both circuits in Figure 3.8, is a current source which is only active when the device is illuminated, otherwise it is an open as in the case of the S_{11}/impedance measurement discussed in this section.

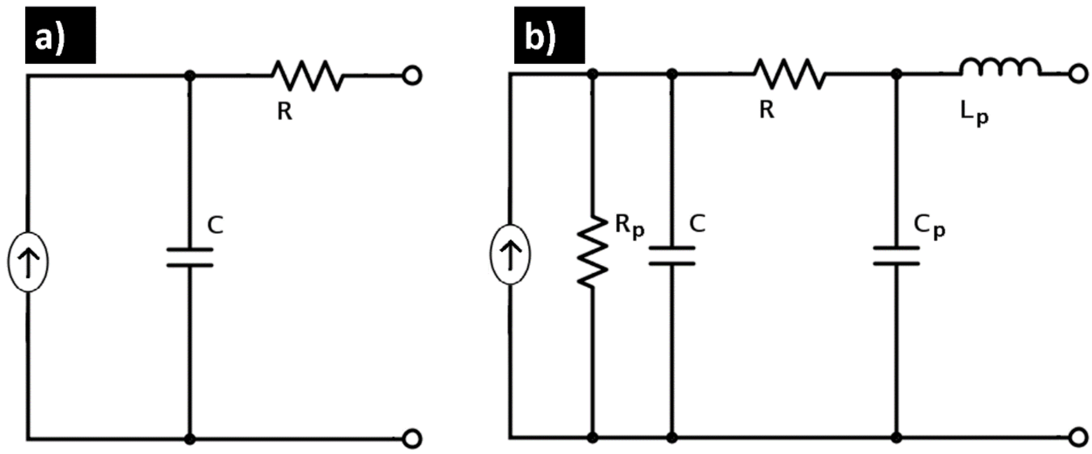

Figure 3.8: a) Simplified circuit model for a photodetector; b) simplified circuit model including the resistance R_P, across the depletion layer, which, although very high (hundreds of KΩ), is not infinite and also the effect of parasitic capacitance C_P and inductance L_P.

Interestingly, regardless of what values are assigned to the resistance R and the capacitance C, the measured device S_{11} and impedance, shown in Figure 3.4 and

Figure 3.5, cannot be explained by either of the circuits illustrated in Figure 3.8. In order to support this assertion, in Figure 3.9 the measured S_{11}/impedance, for the 3 x 15 μm^2 UTC at zero bias, is compared with the S_{11}/impedance obtained from the simplified circuit for two different values of device capacitance, e.g. 16.6 fF (theoretical value) and 68 fF (measured value at very low frequency); the parasitic capacitance C_p and inductance L_p are neglected since their effect only starts to become relevant at very high frequency, while the resistance R_p across the depletion layer is taken into account with a value of 300 KΩ because, considering its value as infinite would cause the real part of the impedance to be just a constant straight line over the whole frequency range. The results shown in Figure 3.9 strongly suggest that the difference between measured and calculated response is substantial and this is particularly noticeable in the trend of the impedance real part up to 50-60 GHz and the S_{11} magnitude up to 20-30 GHz. As a confirmation, a parameter optimisation to fit the experimental results, was also attempted numerically, sweeping a vast range of set of values of R, R_p, C and even including C_p and L_p (whose effect, as anticipated, is only perceptible above 75 GHz), however the discrepancy is substantial and no set of values can provide a satisfactory matching.

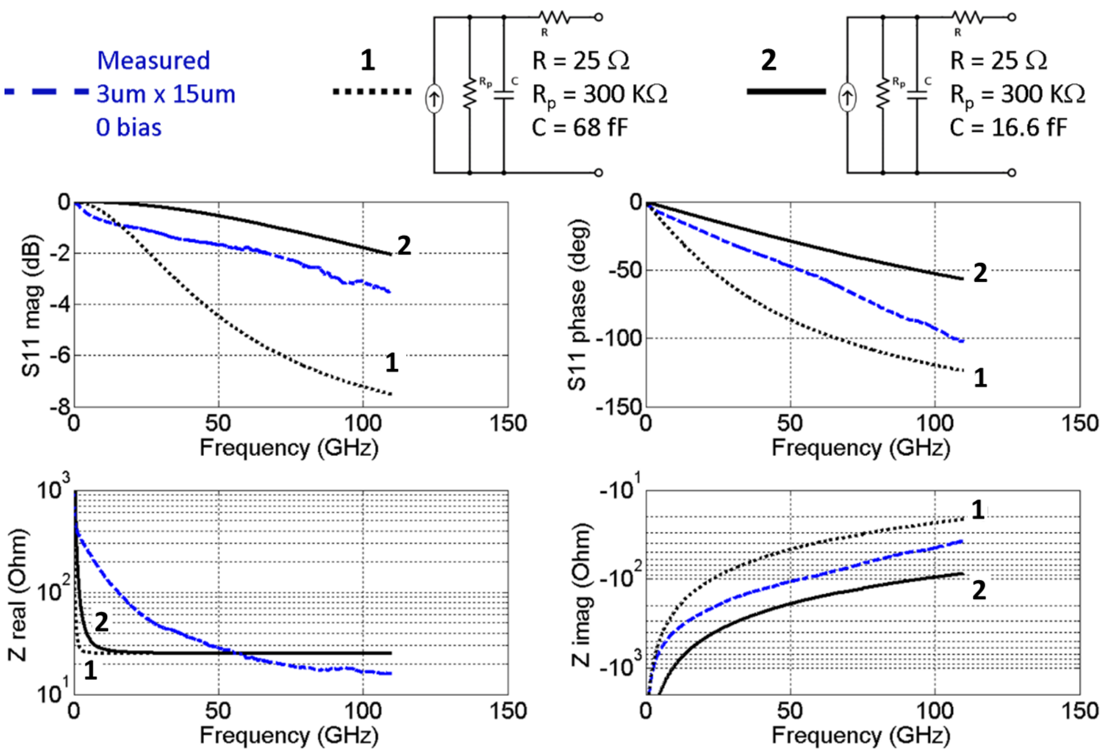

Figure 3.9: Comparison between measured S_{11}/impedance of a 3 x 15 μm² area UTC and S_{11}/impedance obtained from the simplified equivalent circuit for two different values of device capacitance.

A qualitative mathematical explanation of this discrepancy can be attempted by considering the analytical expression of the reflection coefficient S_{11} for the basic Circuit 1 and Circuit 2 illustrated in Figure 3.9; if we consider such reflection coefficient as a function (or frequency response) in the complex variable $s = \sigma + j2\pi f$ (where $j = \sqrt{-1}$ is the imaginary unit and f is the frequency) we obtain the expression (3.1):

$$S_{11}(s) = \frac{(R - R_0)\left(s + \dfrac{R + R_p - R_0}{(R - R_0)R_pC}\right)}{(R + R_0)\left(s + \dfrac{R + R_p + R_0}{(R + R_0)R_pC}\right)} \tag{3.1}$$

where R_0 is the 50 Ω reference impedance. Equation (3.1) shows that the reflection coefficient is endowed with one pole and one zero, both of the first order. The pole $s_{pole} = -\frac{R+R_p+R_0}{(R+R_0)R_pC}$ is real and negative and corresponds, at steady state, to a frequency of 31.2 GHz for Circuit 1 and 127.9 GHz for Circuit 2; the zero $s_{zero} =$

$-\frac{R+R_p-R_0}{(R-R_0)R_pC}$ is real and positive and corresponds to a frequency of 93.6 GHz for Circuit 1 and 383.5 GHz for Circuit 2. As known from circuit theory and control theory, the asymptotic effect of a negative pole of the first order is to produce a 20dB/decade magnitude falloff and a 90^o phase decrease, while a positive zero generates a 20dB/decade magnitude increase but still a 90^o phase decrease. It follows that both Circuit 1 and 2 would settle, asymptotically, on a flat magnitude and a -180^o phase. The S_{11} of Circuit 1 and 2 is hence shaped by s_{pole} and s_{zero}. Circuit 2 magnitude starts flatter than Circuit 1 reflecting the fact that the former has a pole corresponding frequency four times larger than the latter. In Circuit 1 the pole is located at quite a low frequency (31.2 GHz) and its effect on the magnitude decrease (which asymptotically would lead to a 20 dB/decade falloff) is already observable, followed by the effect of the zero, at 93.6 GHz, which tends to counterbalance the pole effect and would restore, asymptotically, the magnitude to a flat trend. The measured S_{11} magnitude, plotted in Figure 3.9 as blue line, exhibits an early decrease, even more pronounced than Circuit 1 however, unlike Circuit 1, it is soon restored to a less steep slope maintaining which it reaches -3.5 dB at 110 GHz; the measured S_{11} phase decreases virtually in a linear fashion down to -100^o at 110 GHz.

The only way for the magnitude of a one-pole-one-zero function, such as the S_{11} of Circuit 1 and 2, to fit the measured S_{11} magnitude within the low frequency range (i.e. 0 GH to 25 GHz), would be to have the pole located at a very low frequency (less than the 31.2 GHz shown for Circuit 1) and the zero closely following the pole at a slightly higher frequency, like the plot in Figure 3.10. Firstly, it has to be noted that, in order to have the pole and the zero located in this way, an unrealistically large capacitance $C = 550\,fF$ and an unlikely small resistance $R = 3\Omega$ have to be employed. Secondly, having the pole and the zero both located at such low frequencies, causes the superposition of their asymptotic effects to be already nearly noticeable below 110 GHz, with the S_{11} magnitude settling on a constant value of about -1dB and the phase on -180^o; as a consequence the discrepancy between circuit and measured magnitude becomes more and more considerable above circa 25 GHz, while the discrepancy between circuit and measured phase is substantial over the whole frequency range.

It seems reasonable to infer and conclude that more poles and zeroes, i.e. a higher order circuit, are necessary in $S_{11}(s)$ to achieve a satisfactory agreement between the measured S_{11} and the circuit-model response.

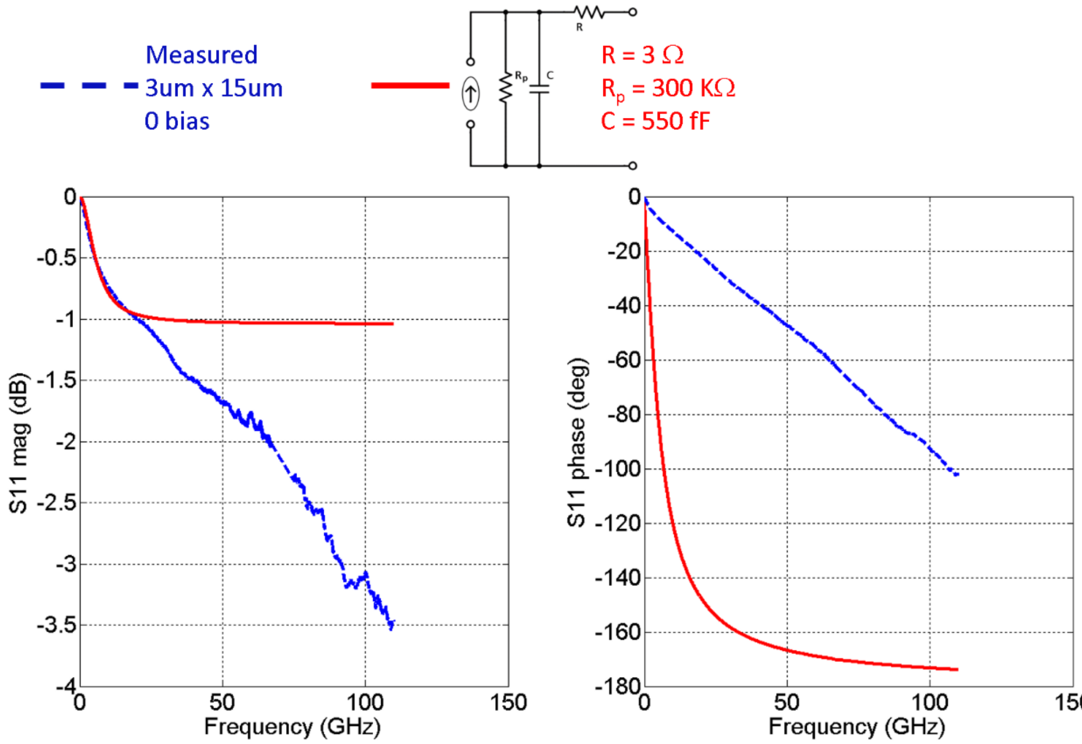

Figure 3.10: Example of a one-pole-one-zero function, such as the S_{11} of Circuit 1 and 2, fitting the measured S_{11} magnitude within the low frequency range (i.e. 0 GH to 25 GHz). In order to have the pole and the zero located in this way, an unrealistically large capacitance *C = 550 fF* and an unlikely small resistance *R = 3 Ω* have to be employed.

For the circuit $S_{11}(s)$ transfer function to have more poles and zeroes (i.e. the circuit order to increase), additional independent energy storage elements, such as capacitors and/or inductors, must be introduced; the presence of these new elements though, needs to be justified and a reasonable connection to the device structure and physics has to be suggested.

The capacitance C and the resistance R_p in the simplified circuit described in Figure 3.9 and Figure 3.10, essentially account for the effect of the depletion layer, modelled as an appropriate capacitance in parallel with a very large resistance; the rest of the device structure is simply taken into account by the resistance R which includes the resistive effect of the ohmic contacts and the doped layers contributing to the device series resistance.

The spacer layers, grown between the absorber and the carrier collection layer, have the function of alleviating the conduction band discontinuity generated at the heterojunction between the narrow band-gap p-doped InGaAs and the wide band-gap lightly n-doped InP. The electrons move by diffusion within the p-doped absorber layer and, once injected into the carrier collection layer, drift towards the cathode layer with overshoot velocity; the conduction band discontinuity tends to hinder the electron injection into the depletion layer and hence acts as a barrier for the electron transport. A comprehensive description of the UTC dynamic (non-equilibrium) behaviour, may have to include an in depth analysis of the role played by the spacer layers and the conduction band discontinuities, in the device response.

The issue concerning the presence of an offset in the conduction band edge was identified for Heterostructure Bipolar Transistors (HBT) where, such a discontinuity gave rise to a barrier impeding the injection of electrons from the emitter into the base region [3.13], [3.14]; a description was proposed, for the electron transport across this barrier, using a thermionic model discussed by Anderson [3.15]. A study regarding the effect of graded layers and tunnelling on the performance of AlGaAs/GaAs heterojunction bipolar transistors was presented by Grinberg et al [3.16]. Here HBTs with an abrupt emitter-base junction and graded HBTs were modelled, using a thermionic-diffusion model, and the electron current density across the heterointerface was calculated together with the electron concentrations at each side of the heterointerface; it was found that the values of the common emitter current gain in HBT's with an abrupt emitter-base junction are smaller than graded HBT because the electron injection is limited by the interface spike barrier. Grinberg also proposed a new thermionic field-diffusion model including the effect of electron tunnelling near the peak of the interface spike; when the effect of tunnelling is included, a multiplicative term is introduced in the expression of the electron current density across the heterointerface, which accounts for the barrier transparency. It turned out that tunnelling effects play an essential role in HBTs with abrupt spikes, while are less important in HBTs with graded junctions and become negligible for grading lengths larger than 30 nm. The transit-time effect of the electrons injected from the channel into the gate layer, in a heterostructure similar to a high-electron mobility transistor, was studied theoretically in [3.17] to explain the plasma instability in the structure. As well as the temperature and the applied voltage, the electron injection depended on the band offset at the heterointerface and occurred via either tunnelling through the top of the barrier or thermionic emission over the barrier.

To the best of the author's knowledge, a thorough study about the effect of spacer layers and conduction band discontinuities on the dynamic (non-equilibrium) operation of UTCs, has not been carried out. The topic is certainly of great interest for future research, however we introduce here a model for the observed effects.

Based on the above mentioned studies [3.13]-[3.17] it arises that tunnelling and thermionic emission are the phenomena governing the electron transport across conduction band offsets. As seen in [3.16], such electron transport is associated with different charge concentrations at each side of the barriers and with possible impediment to the electron passage (i.e. current decrease) caused by the potential barrier. Here we suggest the hypothesis that these effects may be reflected, at a macroscopic scale, in a way that can be interpreted as capacitive and resistive effects on the UTC frequency behaviour. In the new Circuit 3, illustrated in Figure 3.11, the two spacers have been modelled as two RC parallel circuits (R_2C_2 and R_3C_3), which provide the required additional poles/zeroes in the $S_{11}(s)$ transfer function; the neutral region of the heavily p-doped 120 nm thick absorber is ignored as it would only provide a negligible resistive effect. The R_4C_4 parallel represents the carrier collection layer, while R_1 takes into account the resistive effects of doped materials and ohmic contacts. The parasitic capacitance and inductance C_p and L_p only have the function to refine the agreement with the experimental data above 75 GHz. It will be shown in the next section, where the experimental data is compared with 3D full-wave simulation results, that most of the L_p value is not due to the UTC itself but to the inductive effect introduced by the coplanar waveguide contact pads, deposited to enable the use of air coplanar probes, which becomes observable in the W-band. The value of C_p is very small and can be associated to capacitive coupling between the n- and p-contact metal pads; an additional parasitic capacitive coupling takes place between the side walls of the thick heavily p-doped ridge layer and the underlying heavily n-doped n-contact and waveguide layers, enhanced by the polymer electrical permittivity.

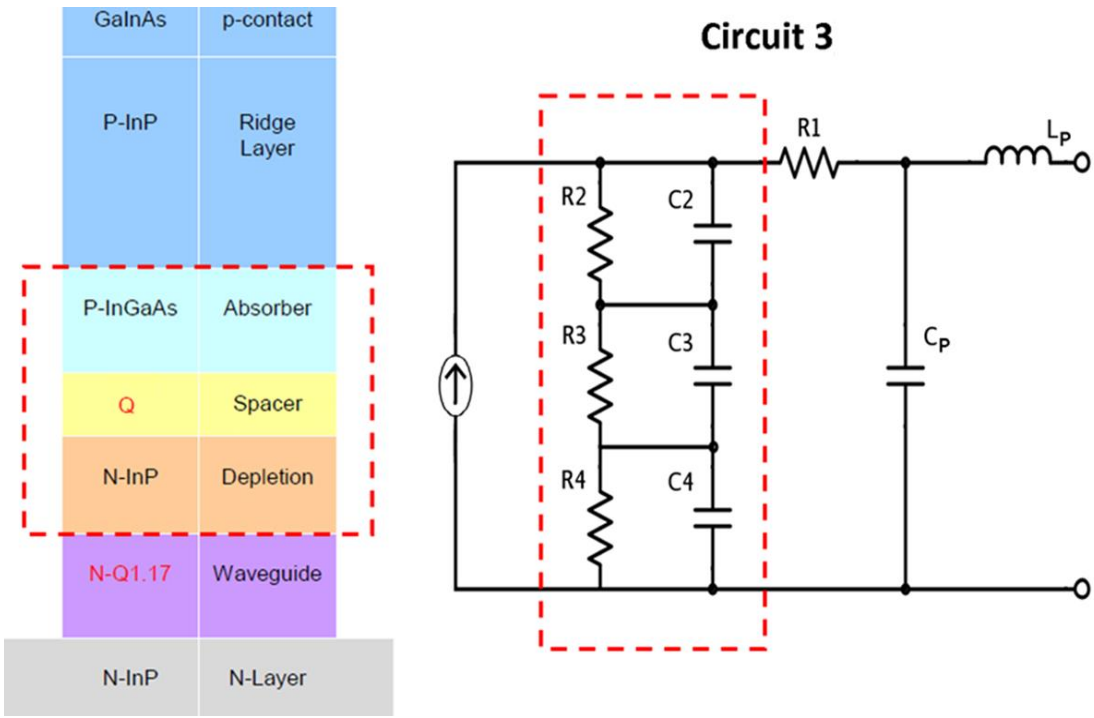

Figure 3.11: Relation between the new equivalent circuit and the UTC structure.

Figure 3.12 shows the comparison between S_{11}/impedance of the new circuit illustrated in Figure 3.11 and S_{11}/impedance of a III-V Lab 3 x 15 µm^2 area UTC measured at zero bias; all of Circuit 3 elements have been optimised to match the response of the 3 x 15 µm^2 area UTC and their optimum values are also displayed in Figure 3.12. The agreement between Circuit 3 and experimental results is excellent and supports the hypothesis proposed above, regarding the role played by spacer layers and conduction band discontinuities in the photodiode frequency response.

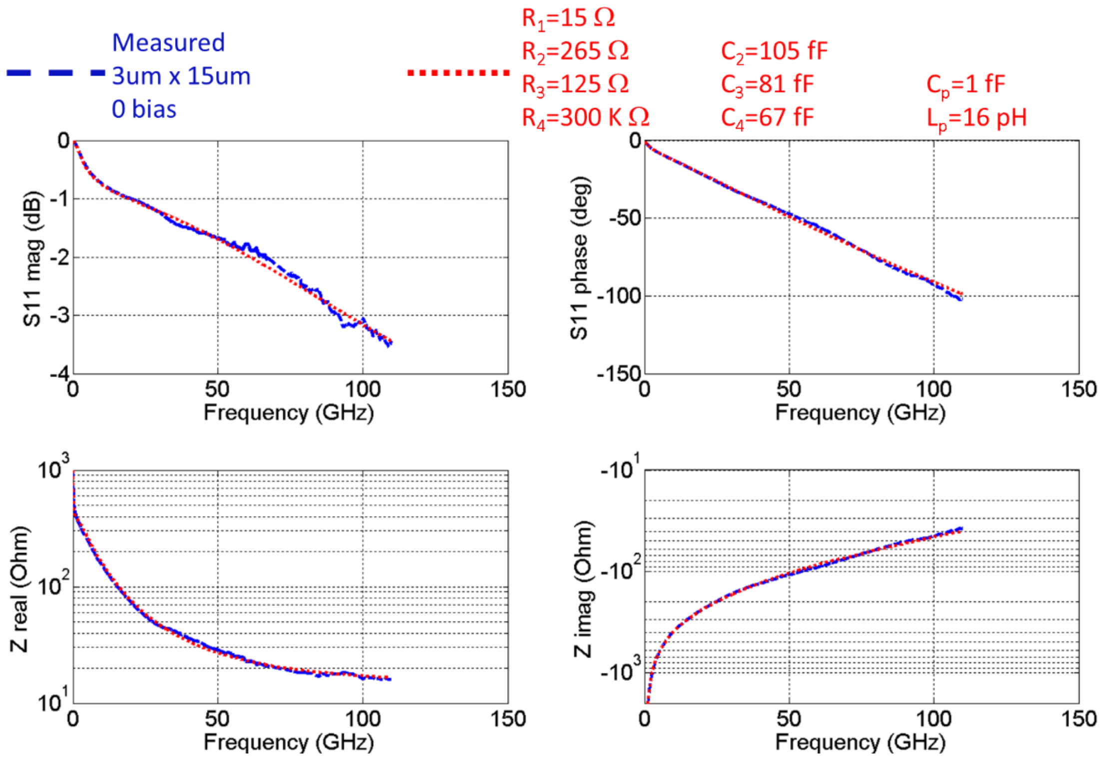

Figure 3.12: Comparison between measured S_{11}/impedance of a 3 x 15 µm² area UTC at 0 V bias (dashed blue line), and S_{11}/impedance obtained from Circuit 3 which models the proposed effect of spacer layers and conduction band discontinuities (dotted red line).

Remarkably, to obtain a good agreement between Circuit 3 and the measured S_{11}/impedance of a 4 x 15 µm² area UTC (still at zero bias) it is not necessary to repeat an optimisation process, but is sufficient to scale down the optimum resistances of the 3 x 15 µm² UTC by a factor 3/4 and scale up the capacitances by a factor 4/3; this comparison is shown in Figure 3.13.

In order to match the experimental results of the 3 x 15 µm² area UTC measured at 2 V reverse bias, the values of the capacitances C_2, C_3, and C_4, associated with the spacers and the depletion layer, have been adjusted, while all the resistances are unchanged with respect to the 0 V bias case; in particular this is consistent with the fact that the applied voltage does not influence the device series resistance. The agreement is good and depicted in Figure 3.14.

As in the zero bias case, for the measurements taken at 2 V reverse bias, it is sufficient to scale the optimum resistances and capacitances found for the 3 x 15 µm² UTC, in order to obtain a good match between Circuit 3 and S_{11}/impedance of the 4 x 15 µm² area UTC, as illustrated in Figure 3.15.

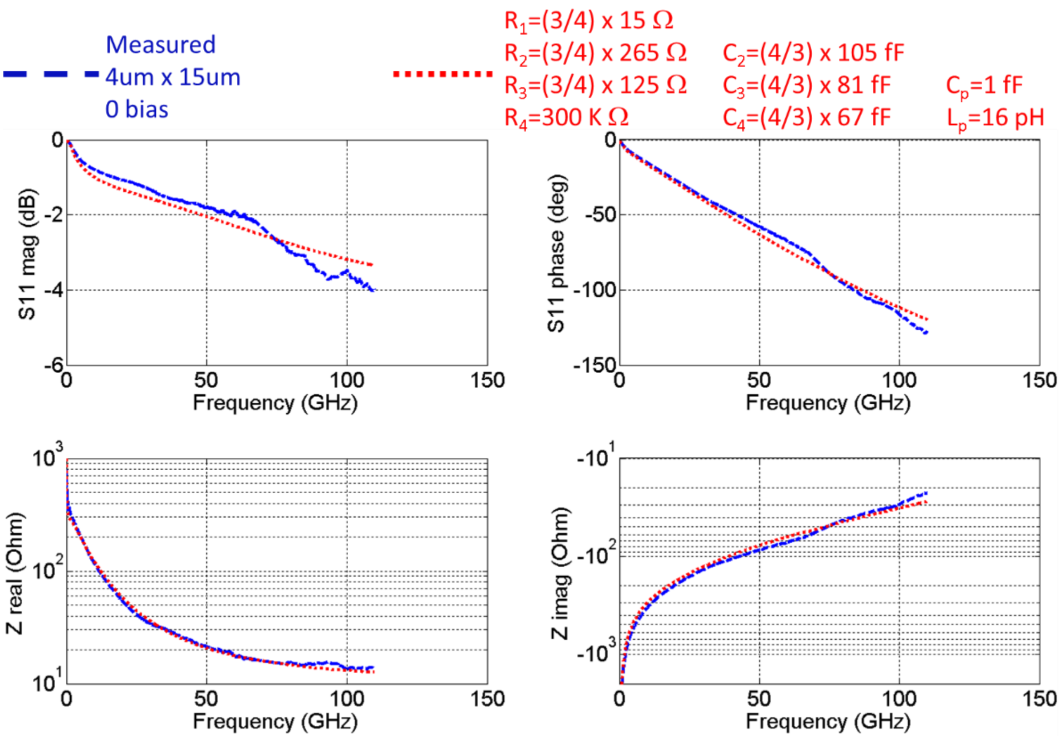

Figure 3.13: Comparison between measured S_{11}/impedance of a 4 x 15 μm^2 area UTC at 0 V bias (dashed blue line), and S_{11}/impedance obtained from Circuit 3 (dotted red line). The optimum resistance and capacitance values are obtained by scaling the optimum values found for the 3 x 15 μm^2 area UTC at 0 V.

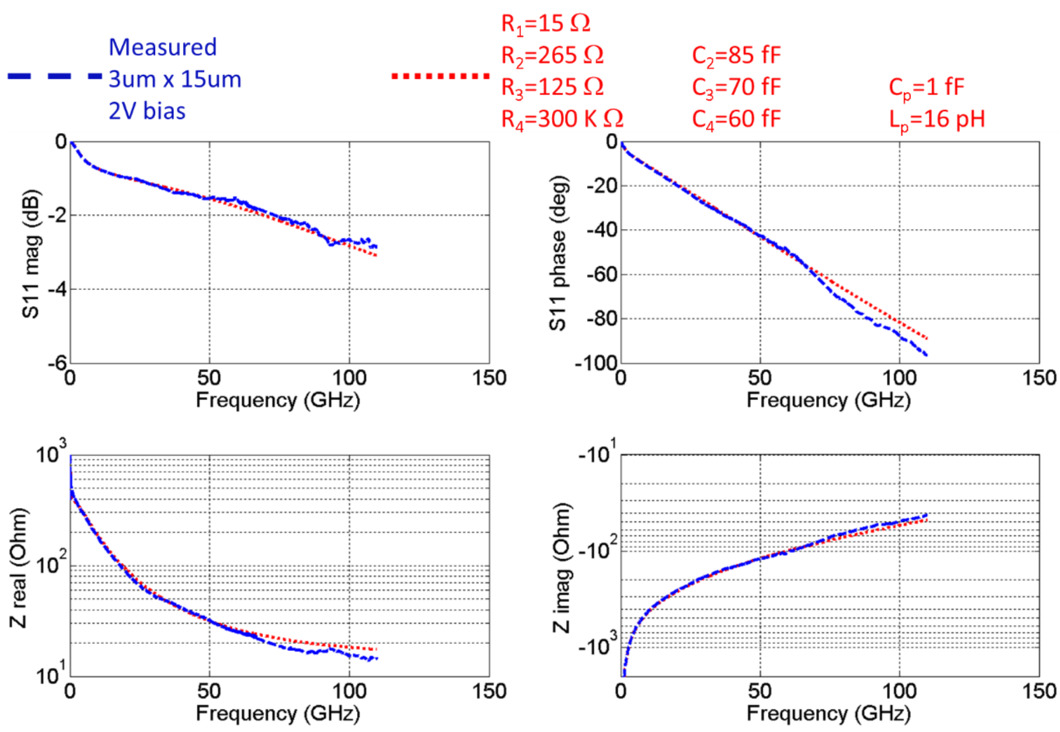

Figure 3.14: Comparison between measured S_{11}/impedance of a 3 x 15 μm^2 area UTC at 2 V reverse bias (dashed blue line), and S_{11}/impedance obtained from Circuit 3 (dotted red line). The capacitances C_2, C_3 and C_4, associated with the spacers and the depletion layer, have been adjusted, while all the resistances are unchanged with respect to the 0 V bias case.

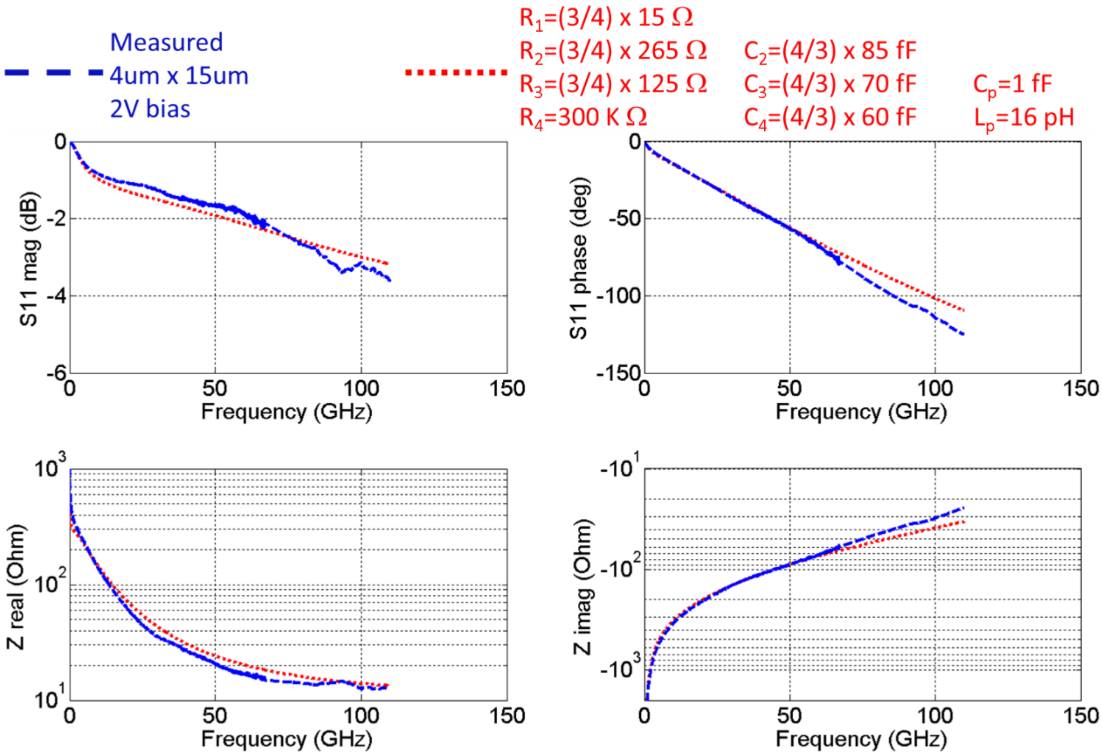

Figure 3.15: Comparison between measured S11/impedance of a 4 x 15 μm² area UTC at 2 V reverse bias (dashed blue line), and S11/impedance obtained from Circuit 3 (dotted red line). The optimum resistance and capacitance values are obtained by scaling the optimum values found for the 3 x 15 μm² area UTC at 2 V reverse.

The values of the resistance R_1 in Circuit 3, deduced from the S parameter measurements, is 15 Ω for the 3 x 15 μm² area UTCs and (3/4) x 15 Ω for the 4 x 15 μm². It is noted that this values are about 5 Ω smaller than the series resistance estimates presented in Section 3.1. It seems reasonable to place this discrepancy within the error tolerance in the evaluation of the materials carrier mobility and the ohmic contact contributions. In this chapter preamble, it was indeed said, that the experimental work discussion would precede the 3D full-wave modelling and simulation, in order to refine the knowledge of the material physical properties to employ in such modelling. It is also noted that the full-wave modelling discussed in the next section will show that the optimum value for the series resistance R_1 of the 4 x 15 μm² area UTCs is in reality slightly larger than (3/4) x 15 Ω, which is consistent with the fact that only the contributions to the series resistance due to the materials in the ridge actually do scale down by a factor (3/4), but the contribution due to n-contact layer and n-ohmic contact do not.

The values of Circuit 3 optimum parameters, found in this section, will be hence employed in Chapter 4 to set the appropriate material properties in the 3D full-wave modelling.

In the next section the measured photodiode frequency photo-response is discussed and it is shown how the results obtained for Circuit 3 can be employed to predict such photo-response.

3.3 Frequency photo-response measurement

The UTC frequency photo-response was measured from 10 MHz to 67 GHz by means of an Agilent lightwave component analyser (LCA), based on the performance network analyser (PNA) used for the S_{11} measurements. The device was probed using a Cascade Air Coplanar (ACP) probe with coaxial electrical connection and lensed fibres with a spot size ranging from 4 µm to 10 µm were used to couple the light into the device optical waveguide. A Scanning Electron Microscope (SEM) photograph of a packaged 3 x 15 µm^2 area UTC is shown in Figure 3.16, with details regarding the position of photodiode, optical waveguide and lensed fibre; as shown in the inset, the optical waveguide width is less than 3 µm at the cleaved facet, which gives an idea of the challenge related to the optimisation of the fibre-to-waveguide alignment, essential to maximise the optical responsivity.

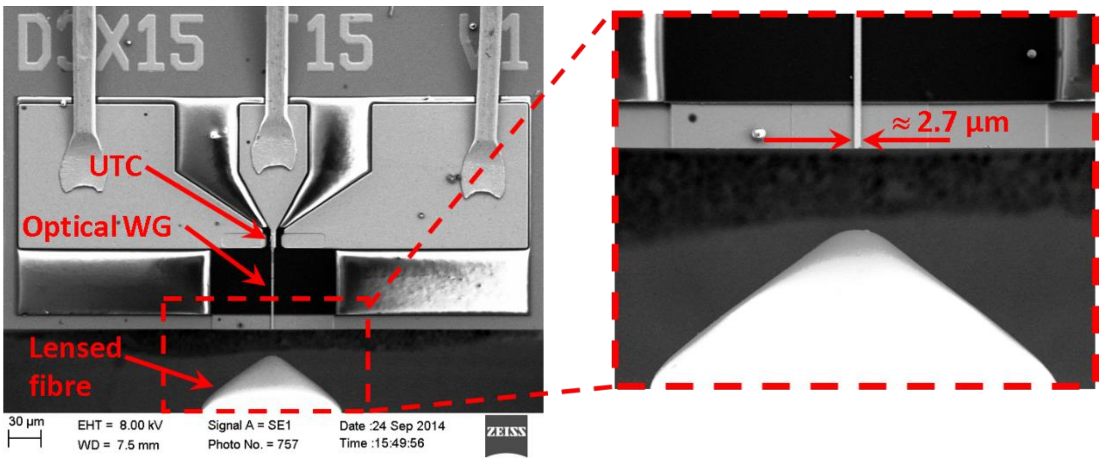

Figure 3.16: SEM image of a packaged 3 x 15 µm^2 area UTC. The position of photodiode, optical waveguide and lensed fibre is indicated with red arrows. The inset highlights the optical waveguide width.

The experimental arrangement used for the frequency photo-response measurement is shown in Figure 3.17. The optical section of the LCA contains a 1550 nm laser source and a Mach-Zehnder modulator which is driven by an RF signal provided by the electrical section of the LCA. The modulated laser is transmitted via an optical fibre and then coupled to the UTC optical waveguide through a lensed optical fibre.

A Keithley source-meter, which operates as both power supply and digital multimeter, was connected to the electrical section of the LCA. The RF and DC photocurrent generated by the UTC and extracted through the ACP, are received by the LCA, whose internal bias-T enables the RF power and the DC photocurrent to be measured separately by the LCA and the Keithley respectively. The source-meter also provides the bias for the UTC through the Cascade ACP.

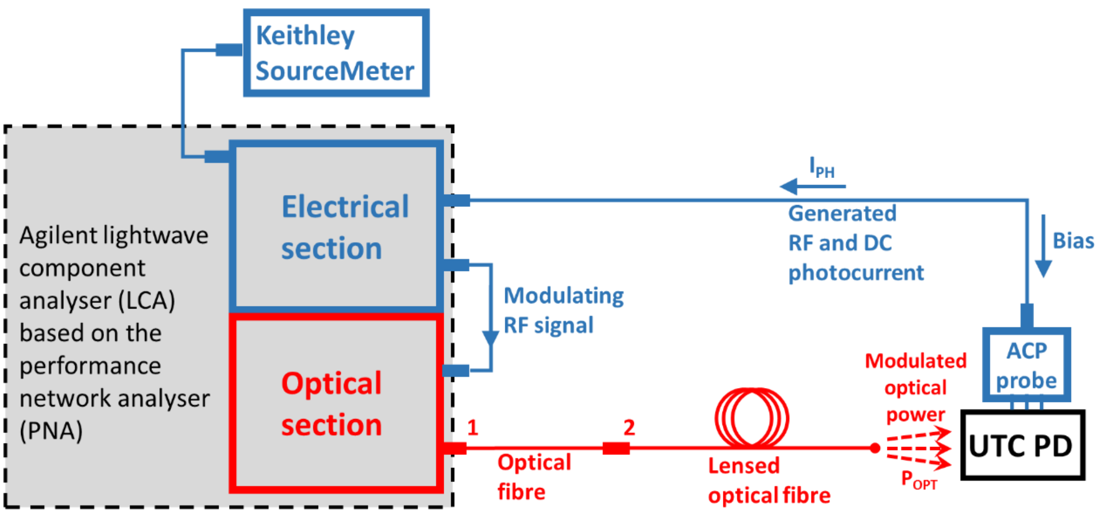

Figure 3.17: Experimental arrangement used for the measurement of the UTC frequency photo-response.

The measured frequency response returned by the LCA consists of the responsivity $\rho(f)$ normalised to 1 A/W, in dB, as in (3.2).

$$\rho(f)_{dB} = 20\log_{10}\left[\frac{|I_{PH}(A)|}{P_{OPT}(W)} / \left(1\frac{A}{W}\right)\right] \tag{3.2}$$

The measured frequency photo-response normalised to 0 dB of a 3 x 15 μm^2 area photodiode and a 4 x 15 μm^2 area photodiode are plotted in Figure 3.18 and Figure 3.19 respectively, with a continuous black line. In the two figures the response has been plotted both with a linear abscissa a) and a logarithmic abscissa b) as the former enables the curve trend below 30 GHz (similar to the S_{11} trend) to be noticed, while the latter highlights the curve knees, above which the response will tend to settle on the high frequency roll-off, determined by the combined effects of transit-time limited and RC limited response. For non-travelling wave devices, like those studied in this work, the asymptotic roll-off of the RC limited response is equal to -20 dB/decade if the parasitic capacitance and inductance are ignored, otherwise is -60 dB/decade. For travelling wave photodiodes (TW-PDs), the RC bandwidth limitation is eased as it depends on the velocity mismatch between optical and electrical waves, rather than the total device area [3.18]; the high frequency roll-off for travelling-wave photodetectors can be better than -10 dB/decade [3.19], ignoring additional parasitic effects. The asymptotic roll-off contribution due to the transit-time limited response is -20 dB/decade for both lumped and travelling-wave devices.

The optical power set in the LCA was 6 dBm, though a 0.4 dB loss through the optical fibre was measured with a power meter at point 2 in Figure 3.17; the optical power was also measured at the output of the lensed fibre and showed no additional loss with respect to point 2. The measured optical power leaving the lensed fibre was therefore 5.6 dBm ($\approx$ 3.6 mW).

The measured DC photocurrent was very similar for both devices, namely 460 μA for the 3 x 15 μm^2 UTC and 490 μA for the 4 x 15 μm^2 UTC, which therefore exhibited DC responsivities of 0.127 A/W and 0.135 A/W respectively, at a 1.55 μm wavelength. It is noted that the DC responsivity was improved by almost 10 % when a polarisation controller was inserted between the optical fibre and the lensed fibre, as this allowed the coupling into the UTC optical waveguide to be further optimised; nevertheless, due to some losses through the polarisation controller, the actual optical power reaching the photodiode dropped of a couple of dB, causing the measured frequency photo-response to be noisy. The frequency response was hence measured without the use of the polarisation controller.

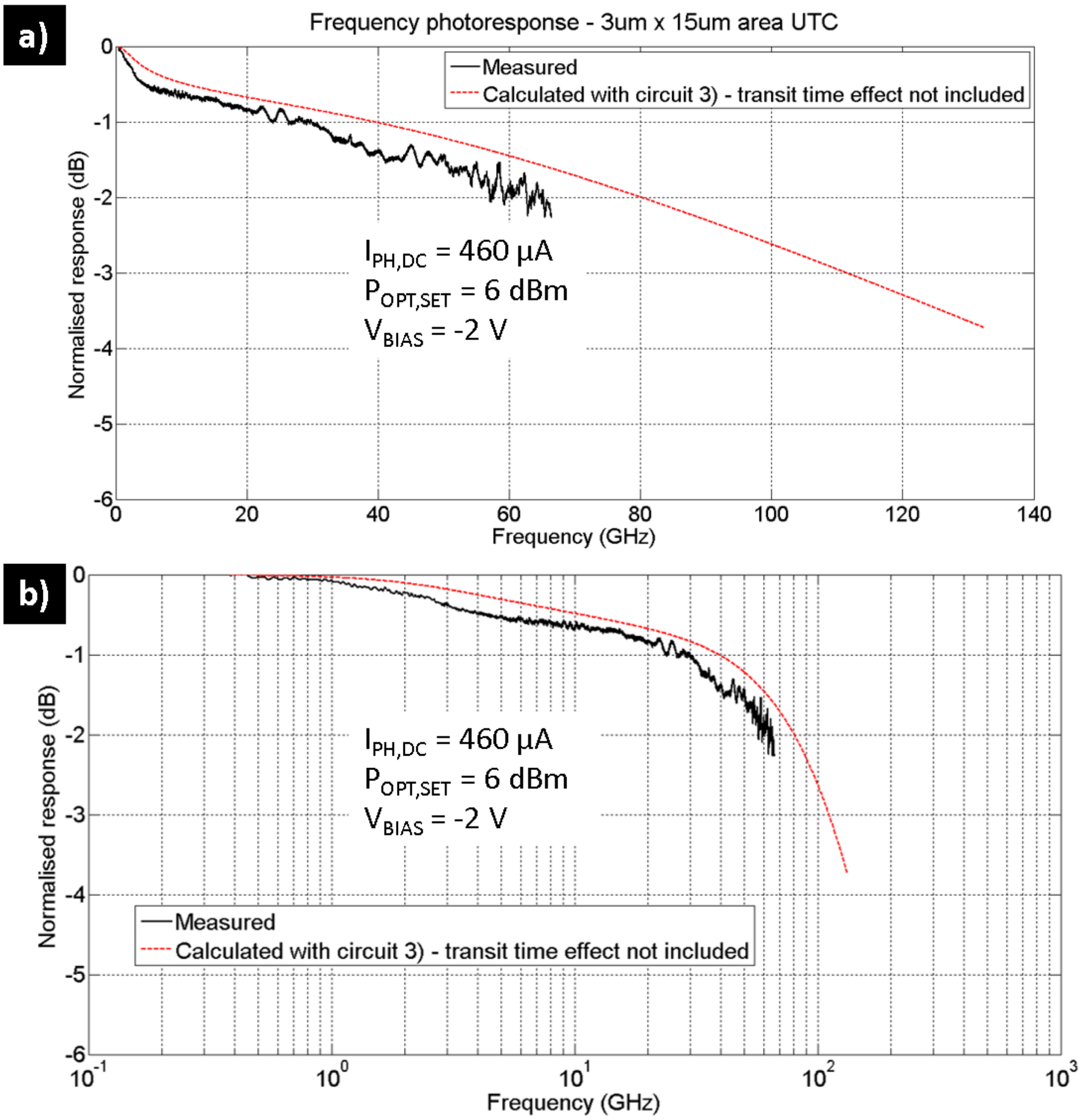

Figure 3.18: Measured (continuous black line) photo-response and calculated RC limited photo-response (dashed red line) of a 3 x 15 µm^2 area UTC, displayed with a linear abscissa in a) and a logarithmic abscissa in b).

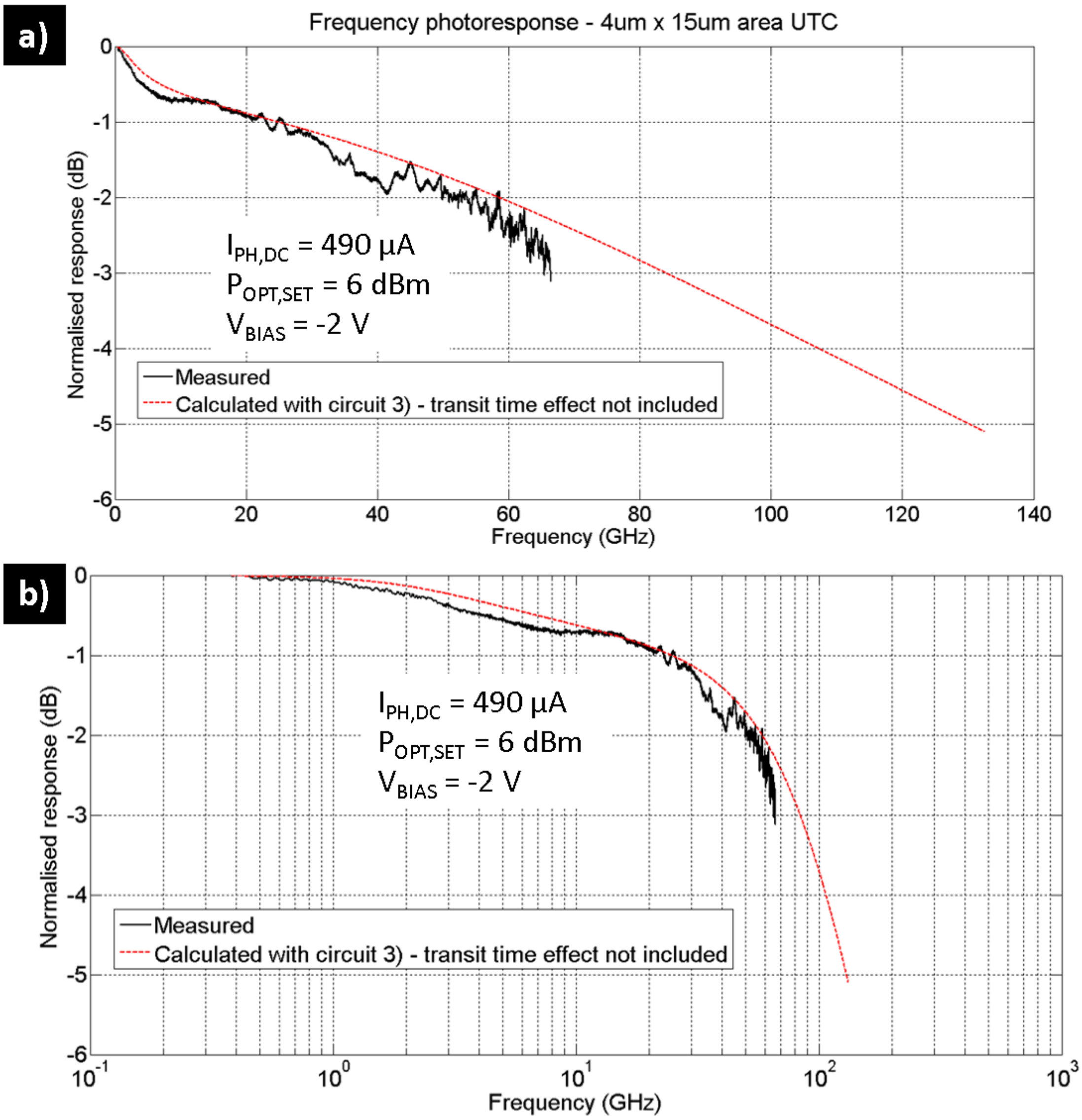

Figure 3.19: Measured (continuous black line) photo-response and calculated RC-limited photo-response (dashed red line) of 4 x 15 μm^2 area UTC, displayed with a linear abscissa in a) and a logarithmic abscissa in b).

Circuit 3, discussed in the previous section with its optimum parameters, was employed to predict the frequency response of the two different area UTCs and make a comparison with the measured photo-response. For this purpose, the current generator of Circuit 3, that was an open-circuit for the S_{11}/impedance evaluation, is now active and accounts for the photocurrent I_{PH} generated by the incident optical power, as shown in Figure 3.20; also, the terminals at which the S_{11} and the impedance were evaluated, are now terminated in a 50 Ω load R_L representing the LCA input impedance, to which the RF power generated by the UTC is delivered.

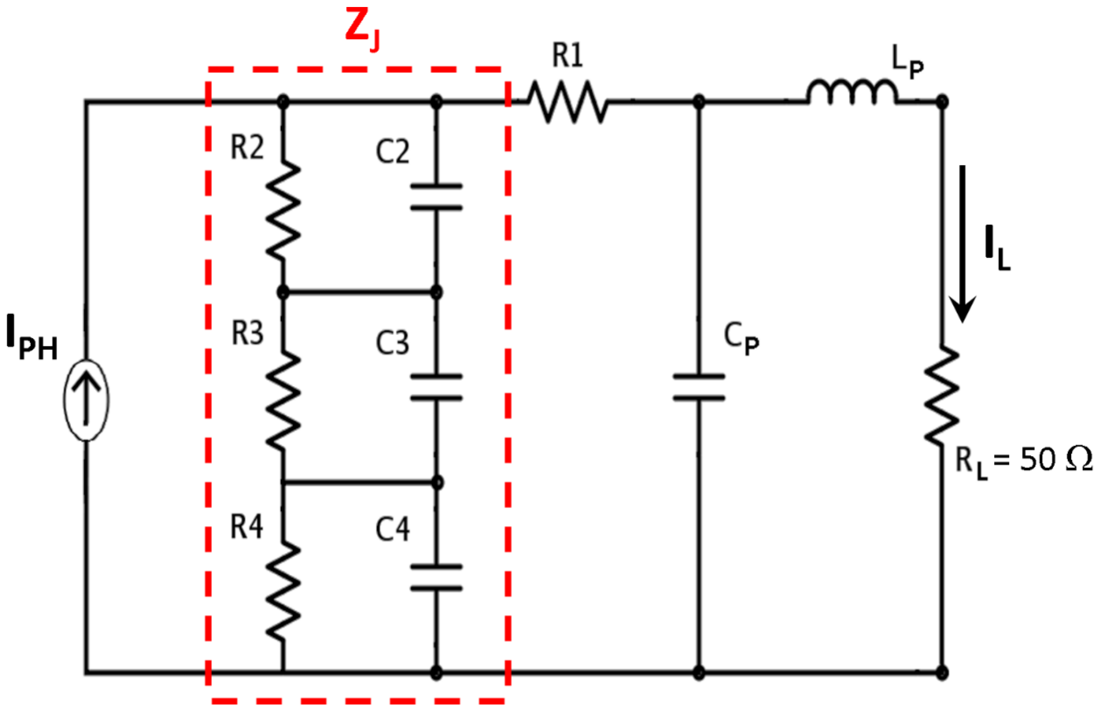

Figure 3.20: Circuit 3 for the evaluation of the frequency photo-response. I_{PH}, which was zero for the S_{11}/impedance evaluation, is now active and accounts for the photocurrent generated by the incident optical power. R_L is the LCA input impedance and $\frac{1}{2}R_L|I_L|^2$ is the RF power delivered to the LCA.

If we indicate with Z_J the total impedance associated with absorber, spacers and depletion layer, given by (3.3)

$$Z_J = \frac{R_2}{1 + j2\pi f R_2 C_2} + \frac{R_3}{1 + j2\pi f R_3 C_3} + \frac{R_4}{1 + j2\pi f R_4 C_4} \tag{3.3}$$

then we can quantify the relationship between I_{PH} and I_L as in (3.4)

$$I_L = I_{PH} \frac{Z_J}{(Z_J + R_1)(1 - 4\pi^2 f^2 L_P C_P + j2\pi f R_L C_P) + j2\pi f L_P + R_L} \tag{3.4}$$

If the transit-time effect is ignored and only the RC limited response is considered, the amplitude of the current I_{PH} can be regarded as constant over the frequency range and the calculated UTC photo-response corresponds to the dashed red lines plotted in Figure 3.18 and Figure 3.19. These curves represent the squared modulus of $I_L(f)$ normalised to the DC squared modulus of I_L, in dB, i.e.

$10log_{10}(|I_L(f)|^2_{norm})$; the optimum circuit parameters, found in the previous section for the 3 x 15 µm^2 UTC and the 4 x 15 µm^2 UTC at -2 V bias, have been employed. As can be noticed in Figure 3.18 and Figure 3.19, the two different size photodiodes exhibit RC-limited response 3 dB bandwidths of 111 GHz and 84 GHz respectively; the full-wave modelling results of the next chapter will show that the RC limited 3 dB bandwidth values have been here overestimated due to the too large value of inductance L_P considered for Circuit 3 in Figure 3.20, whose effect is to slightly raise the frequency response curves.

For a comprehensive calculation of the device photo-response, the transit-time effect must be taken into account. The amplitude of the current I_{PH} is not constant over the frequency range but suffers from a decrease caused by the electron transit time across absorber and depletion region.

In depth studies of InP/InGaAs heterojunction bipolar transistors (HBT) have demonstrated that electrons can drift at overshoot velocities, as high as 4 x 10^7 cm/s [3.20]; for the 300 nm thick InP collection layer of the UTCs characterised in this chapter, such velocity yields a 0.75 ps transit time. If this transit time τ_C across the collection region was the only reason for I_{PH} to decrease over the frequency range, then $|I_{PH}|^2$ would drop as $\sin^2(\pi f \tau_C)\,/(\pi f \tau_C)^2$, as is the case for PIN photodiodes [3.21], [3.22], and the 3dB transit time limited bandwidth would be $f_{TT} = 0.443/\tau_C = 590\ GHz$. Actually, in a UTC structure, for reasonable values of the depletion layer thickness, the transit time across the collection layer is shorter than across the absorber and therefore, the device transit time limited 3 dB bandwidth is mainly determined by the response in the absorption layer.

The expression for I_{PH} was calculated in [3.23]-[3.24] and is shown in (3.5):

$$I_{PH}(f) = \frac{1}{W}\int_0^{W_A} I_{e,inj}(W_A,f)\left[1 - \frac{j2\pi f\tau_R}{1+j2\pi f\tau_R}\left(1 - \frac{I_e(x,f)}{I_{e,inj}(W_A,f)}\right)\right]dx + \\ + \frac{W_C}{W} I_{e,inj}(W_A,f)\left[\frac{\sin(\pi f\tau_C)}{\pi f\tau_C}\right]e^{-j\pi f\tau_c} \tag{3.5}$$

where W_A is the absorber thickness, W_C is the collector thickness, $W = W_A + W_C$, $I_{e,inj}(W_A, f)$ is the electron injection current at the absorber/collector interface, x is the coordinate along the layer thickness, $I_e(x, f)$ is the electron current across the absorber, τ_R is the absorber dielectric relaxation time, τ_c is the electron transit time across the depletion layer. The first term in equation (3.5), i.e. the integral, represents the contribution to the total photocurrent I_{PH} provided by the absorption layer, while the second represents the collection layer contribution.

When the doping in the absorber is adequately high (> mid $10^{17}/cm^3$) [3.23]-[3.24], a quasi-neutral condition is preserved in this region and the hole drift current, generated by the background holes, is largely predominant against the hole diffusion current, produced by the excess holes, which becomes negligible. Equivalently, it can be said that the holes respond within the dielectric relaxation time $\tau_R = \varepsilon/\sigma$ (where ε and σ are the material electrical permittivity and conductivity respectively) which for p-InGaAs 10^{18} cm^{-3} can be as short as 33 fs [3.23]. Under these conditions, the influence of the absorber holes on the UTC bandwidth can be ignored and the device transit-time limited response will only depend on the electron injection current at the absorber/depletion interface and on the transfer function through the collection layer. Essentially, the term within square brackets inside the integral in (3.5) approaches 1 and equation (3.5) can be simplified as in (3.6):

$$I_{PH}(f) = I_{e,inj}(W_A, f)\left\{\frac{W_A}{W} + \frac{W_C}{W}\left[\frac{\sin(\pi f \tau_C)}{\pi f \tau_C}\right]e^{-j\pi f \tau_c}\right\} \tag{3.6}$$

where the term between curly brackets represents the transfer function through the collection layer.

If no quasi field is present in the absorber, the minority electrons within this layer only move by diffusion and, despite the high mobility of the minority electrons (greater than 4000 cm^2/Vs for p-InGaAs 10^{18} cm^{-3}), the transit time across the absorption layer can still be longer than the hole transit time across an equally thick depletion layer in a PIN photodiode [3.23]. As shown in [3.24], in this pure diffusion scenario the analytical expression of the electron injection current $I_{e,inj}(W_A, f)$ at the absorber/depletion layer interface, can be more easily calculated and is given by (3.7):

$$\frac{I_{e,inj}(W_A, f)}{I_0} = \frac{\left(\frac{1}{W_A}\right)\frac{D_e\tau_{rec}}{1+j2\pi f\tau_{rec}}v_{TH}tanh\left(\frac{W_A}{\sqrt{\frac{D_e\tau_{rec}}{1+j2\pi f\tau_{rec}}}}\right)}{D_e tanh\left(\frac{W_A}{\sqrt{\frac{D_e\tau_{rec}}{1+j2\pi f\tau_{rec}}}}\right)+v_{TH}\sqrt{\frac{D_e\tau_{rec}}{1+j2\pi f\tau_{rec}}}} \tag{3.7}$$

where I_0 is the DC injection current (i.e. the equation right hand side term is 1 when $f = 0$), D_e is the electron diffusion coefficient in the absorber, τ_{rec} is the carrier recombination lifetime and v_{TH} is the electron thermionic emission velocity.

It was shown [3.23], [3.25] that the effect of a quasi-field within the absorption layer can be significant when high-mobility InGaAs is used and the transit time limited frequency response can be improved substantially, since the quasi-field helps the electrons to be swept out from the layer. A quasi-field can be generated either via band-gap grading or doping grading, the latter being the case for the III-V Lab UTCs characterised in this chapter, as can be seen from the epitaxy structure in Table 3.1. An enhancement of the intrinsic 3 dB bandwidth can also be seen at a high excitation level (high photocurrent) as the electron transport changes from diffusive to mixed drift/diffusive due to the effect of a self-induced field [3.24]. To calculate the transit-time frequency response of the III-V Lab UTCs, the contribution of the quasi-electric field generated by the graded doping shown in Table 3.1 needs to be estimated. The quasi-electric field concept was first discussed by H. Kroemer in [3.26] and it was shown that, unlike “ordinary” electric fields, quasi-electric fields do not exert forces equal in magnitude and opposite in direction upon electrons and holes and therefore represent a new degree of freedom for the device designer to obtain effects impossible to obtain with ordinary electric fields. The generation of a quasi-electric field is a complex phenomenon which occurs, as mentioned above, in compositionally non-uniform semiconductor materials and materials with graded doping. An analytical study of quasi-electric fields generated in such scenarios can be found in [3.27]; the quasi-electric field E_{QN} acting on the electrons is due to the spatial variation of the electron affinity χ as in (3.8):

$$E_{QN} = -\frac{1}{q}\frac{d\chi}{dx} \tag{3.8}$$

whereas that acting on holes is due to the spatial variation of both electron affinity and band-gap energy as in (3.9):

$$E_{QP} = -\frac{1}{q}\frac{d(\chi + E_G)}{dx} \tag{3.9}$$

The graded doping in the p-type UTC absorption layer yields a potential gradient, and hence a quasi-field, which effectively accelerates electrons in the direction of decreasing doping levels. Therefore, the graded doping realised in the absorber of the III-V lab UTCs, shown in Table 3.1, produces a quasi-field that effectively accelerates the minority electrons from the absorption towards the collection layer. Although the overall effect of this doping profile is favourable to a faster device response, it also generates a secondary effect which tends to slow down the minority electrons; this effect is due to the effective band-gap narrowing associated to high doping levels.

While the spatial variation of the band-gap energy in a compositionally non-uniform semiconductor is clearly due to the graded composition, the band-gap narrowing occurring as a consequence of doping is not as obvious. When the semiconductor is lightly doped, the conduction and valence bands are parabolic with sharply defined band edges. As the doping density increases, the localized impurity states broaden into an impurity band and the fluctuating potential associated with the dopants located on randomly situated lattice sites produces tails in the conduction and valence bands and, as the doping level increases, the impurity band merges with the conduction band and an effective shrinkage of the band-gap results [3.27]. An assessment of the band-gap shrinkage versus doping levels in p-type $In_{0.53}Ga_{0.47}As$ was presented in [3.28]; based on such results the difference of band-gap narrowing produced by the doping levels equal to the upper and lower bounds of the graded doping profile in the III-V Lab UTC absorber, can be estimated to be about 10 meV. For minority electron transport in a quasi-neutral region, as is the case for the III-V Lab UTC absorber, the effective band-gap shrinkage can be entirely attributed to the conduction band (i.e. the effective asymmetry factor discussed in [3.27] equals 1), while the valence band remains flat, as also shown in [3.23]. It follows that the estimated band-gap narrowing (about 10 meV) also coincides with an effective electron affinity variation that generates, as in (3.8), a quasi-electric field E_{QN} acting on electrons. Therefore, the corresponding potential is about 10 mV, and its effect slows down the electron travelling towards the collection layer. The results discussed in [3.25] show that a quasi-field equivalent to a 50 mV potential can increase the 3 dB bandwidth of a UTC with 120 nm thick absorption and depletion layers, from 160 GHz (diffusion only) to almost 400 GHz; the III-V Lab UTCs have a 120 nm thick absorber and a 300 nm thick depletion layer, hence their transit time limited 3 dB bandwidth would increase from almost 160 GHz (diffusion only) to over 300 GHz under the effect of the same 50 mV potential. The overall potential generated by the graded doping in Table 3.1 will be favourable to a faster device response and will dominate the adverse secondary effect due to the effective band-gap narrowing. It appears reasonable to suppose that the overall potential generated in the III-V Lab UTCs by the graded doping in Table 3.1, will be in the range 10 mV to 20 mV and will therefore increase the transit-time limited bandwidth to between 200 GHz and 300 GHz.

Figure 3.21 illustrates the transit time limited response of a UTC with a 120 nm thick InGaAs absorber and a 300 nm thick InP collection layer, calculated using equations (3.6) and (3.7) and the estimated quasi-field contribution, for five different scenarios. The continuous red line represents the response due only to the transfer function through the collector, i.e. the squared modulus of the term between curly brackets in equation (3.6) in dB, which shows a 3 dB bandwidth of over 500 GHz. The dotted blue line is the transit-time limited response, i.e. $10\log_{10}(|I_{PH}(f)|^2_{norm})$, for the pure diffusion case, when no quasi-field is present, and exhibits a 3 dB bandwidth of 152 GHz. The three dashed green lines 1, 2 and 3 represent three possible transit-time limited responses obtained with the contribution of the estimated overall potential (between 10 mV and 20 mV) generated by the doping grading shown in Table 3.1, and have 3 dB bandwidths of about 200 GHz, 235 GHz and 270 GHz respectively. A summary of the parameters in equations (3.6) and (3.7), employed to calculate the responses in Figure 3.21, is given in Table 3.4; the electron diffusive constant was calculated using the Einstein relation for the diffusion of charged particles.

Table 3.4: Summary of the parameters in equations (3.6) and (3.7), employed to calculate the responses in Figure 3.21.

Parameter	**Description**	**Value**
W_A	Absorption layer thickness	120 nm
W_C	Collection layer thickness	300 nm
τ_C	Electron transit time across the collection layer, calculated assuming an overshoot velocity of 4 x 10^7 cm/s [3.20]	0.75 ps
D_e	Diffusion constant of electrons in the absorber calculated for an electron mobility of 4000 $cm^2/(Vs)$ [3.23], [3.25]	103 cm^2/s
v_{TH}	Thermionic emission velocity used as a boundary condition at the absorption/collection layer interface	2.5 x 10^7 cm/s [3.25], [3.24]
τ_{rec}	Carrier recombination lifetime in the absorber	2 ns [3.29]

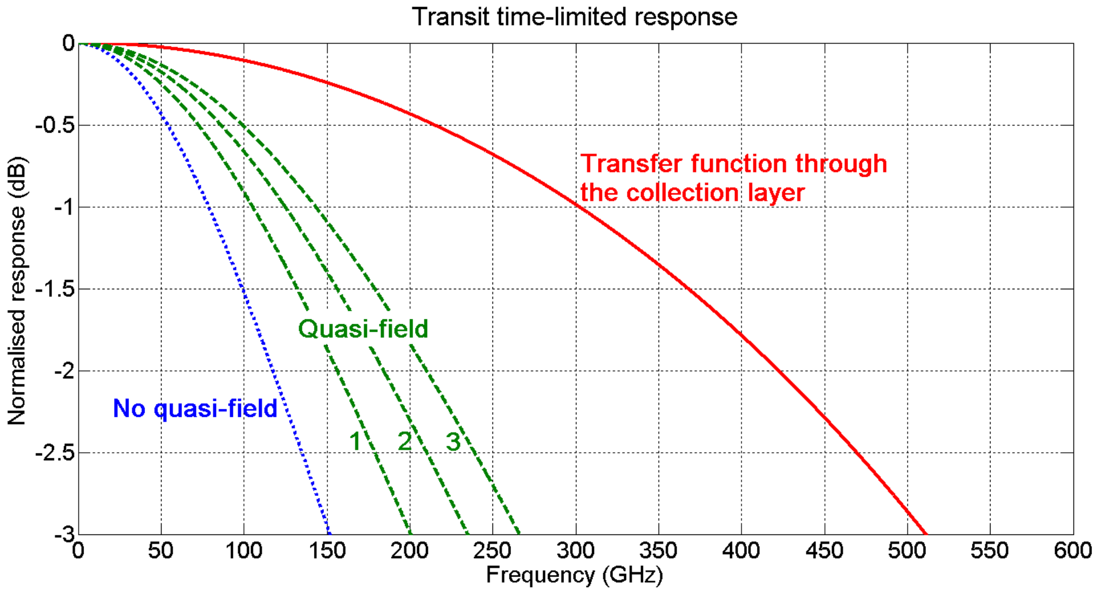

Figure 3.21: Transit-time limited response of a UTC with a 120 nm thick InGaAs absorber and a 300 nm thick InP collection layer. The continuous red line represents the decrease due only to the transfer function through the collector. The dotted blue line is the transit-time limited response for the pure diffusion case, when no quasi-field is present. The three dashed green lines 1, 2 and 3 represent three possible transit-time limited responses obtained with the contribution of the estimated potential (between 10 mV and 20 mV) generated by the doping grading shown in Table 3.1.

The RC-limited frequency response has previously been calculated in equation (3.4) using Circuit 3 in Figure 3.20 and considering the current source I_{PH} as ideal (i.e. constant over the frequency range). The transit-time limited responses plotted in Figure 3.21 can now be used to assess the overall III-V Lab UTC photo-response, incorporating both the RC-limited and transit-time limited contributions; essentially the ideal current source I_{PH} in equation (3.4) can now be replaced with a current source whose squared modulus decreases over the frequency range following the responses plotted in Figure 3.21. The total frequency response of the 3 x 15 μm^2 and the 4 x 15 μm^2 III-V Lab UTCs, for diffusion only and the three different quasi-field scenarios shown in Figure 3.21, is plotted in Figure 3.22 and Figure 3.23 respectively and compared with the measured photo-response.

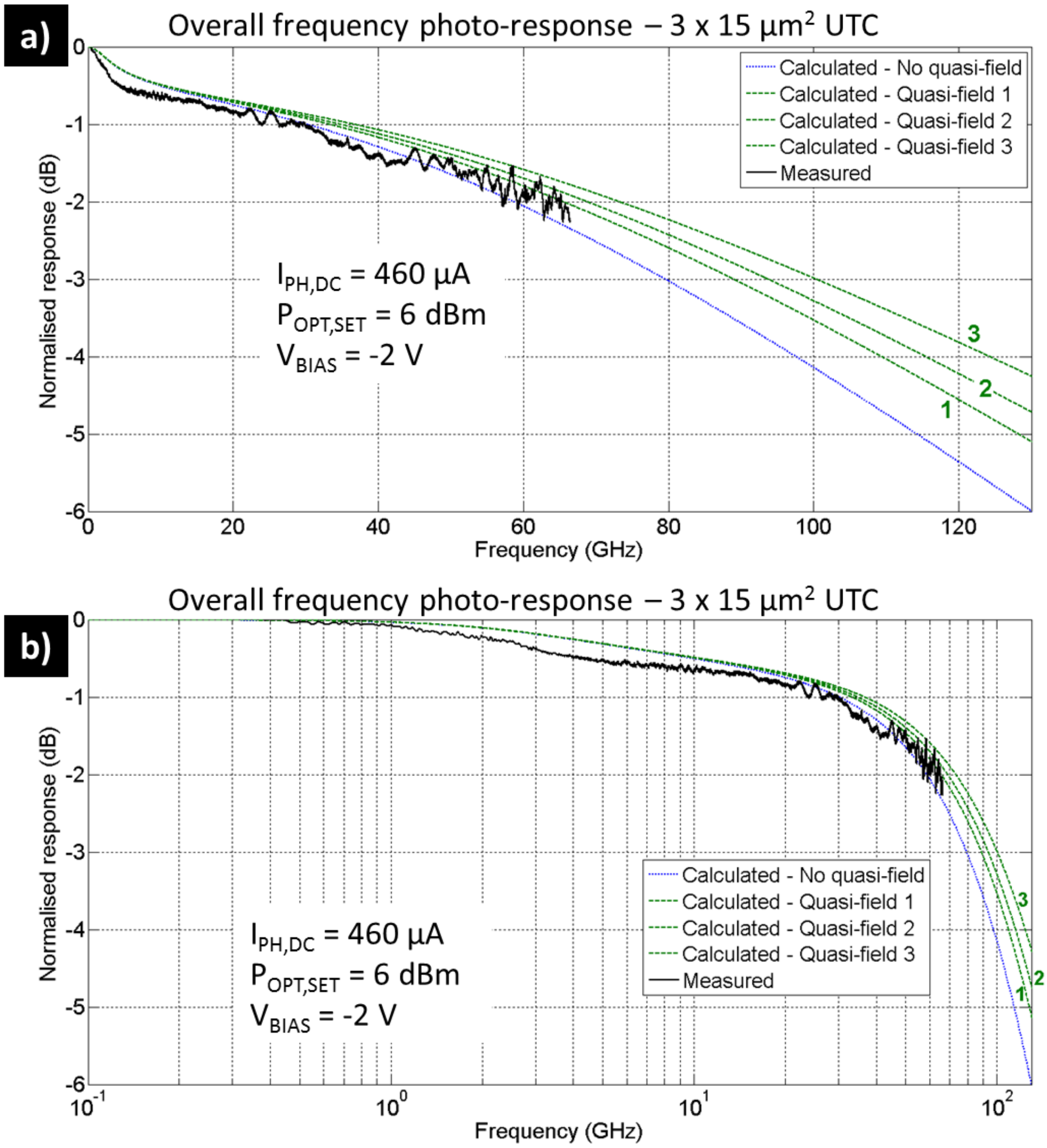

Figure 3.22: Overall frequency response of the 3 x 15 µm² III-V Lab UTCs, for the diffusion only scenario (dotted blue line) and the three different quasi-field scenarios (dashed green lines) depicted in Figure 3.21, compared with the measured response (continuous black line).

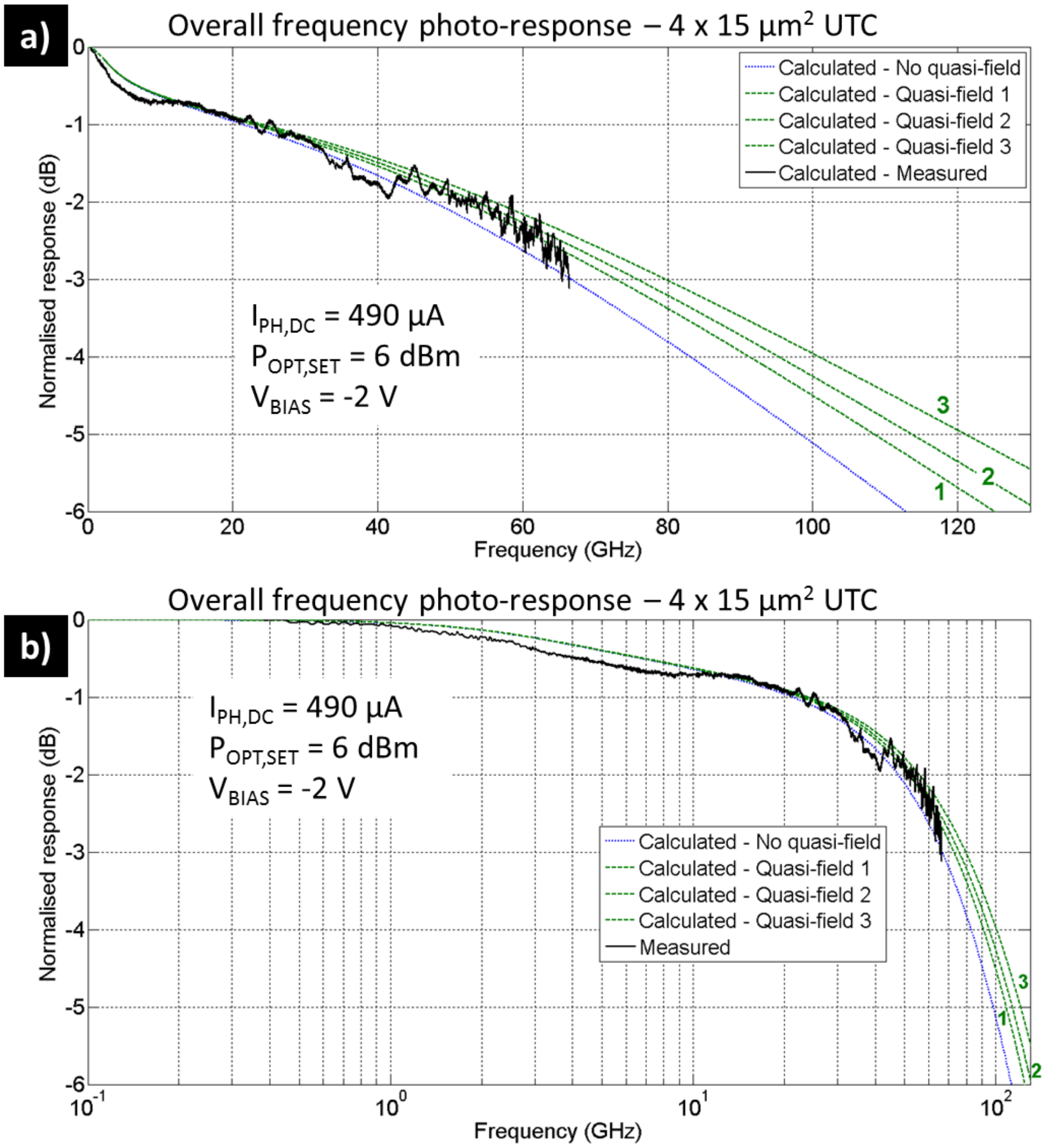

Figure 3.23: Overall frequency response of the 4 x 15 μm² III-V Lab UTCs, for the diffusion only scenario (dotted blue line) and the three different quasi-field scenarios (dashed green lines) depicted in Figure 3.21, compared with the measured response (continuous black line).

The overall frequency responses calculated including the estimated quasi-field contribution (dashed green lines in Figure 3.22 and Figure 3.23) show wider bandwidths than the experimental data. On the other hand, the frequency response calculated ignoring the quasi-field in the absorber (dotted blue line in Figure 3.22 and Figure 3.23) appears to decrease just slightly faster than the measured photo-response. This seems to suggest that the effect of the quasi-field generated by the graded doping should be rather modest, in order to match the experimental data, contradicting the quasi-field enhancement expected on the basis of the analysis presented in [3.23] and [3.24]. The reason for this disagreement is that, as already mentioned previously, the calculated RC-limited 3 dB bandwidth has been here overestimated due to the too large value (16 pH) assigned to L_P in Circuit 3 in Figure 3.20. The CST full-wave modelling, discussed in the next section, will show that the actual inductive component of the UTC is in reality smaller, i.e. 6.5 pH, which causes a reduction of the RC-limited 3dB bandwidth and therefore requires, in order to match the experimental data, a quasi-field enhancement in line with the calculation shown in Figure 3.21. The reason why a greater value of inductance L_P provides a better power transfer to the 50 Ω R_L within the considered frequency range (i.e. a broader 3 dB bandwidth), is that the UTC reactance is clearly capacitive (i.e. negative) in such frequency range. The higher value of inductance L_P (16 pH) tunes the UTC capacitive reactance more efficiently than the smaller value (6.5 pH), within the considered frequency range, and hence yields a wider RC-limited 3 dB bandwidth.

3.4 Conclusions

In this chapter the III-V Lab UTC impedance and frequency photo-response have been studied in depth using experimental data, circuit analysis and some theoretical investigation. The UTC S_{11} and impedance were measured up to 110 GHz and the experimental results were employed to carry out a circuit analysis of the devices. It was found that the circuit model typically used to describe the photodetector response, which attributes the UTC reactance to one energy storage element only (junction capacitance), cannot describe the experimental results with acceptable accuracy, no matter what values are considered for the junction capacitance and the series resistance. In order to describe the observations a novel model was introduced, suggesting that the spacer layers and the conduction band discontinuities at their interfaces may play a not negligible role in shaping the UTC impedance and frequency response. An investigation of the UTC transit-time limited frequency response has also been carried out, including an assessment of the quasi-field generated by the graded doping profile in the absorption later. The results obtained in this chapter will be employed to set the material properties in the 3D full-wave modelling work discussed in the next section.

3.5 References

[3.1] J. Lampin and E. Peytavit, "High efficiency optoelectronic terahertz sources," *Proc. SPIE 7763, Terahertz Emit. Receiv. Appl.*, vol. 7763, pp. 77630A1–77630A7, Aug. 2010.

[3.2] R. Appleby and H. B. Wallace, "Standoff detection of weapons and contraband in the 100 GHz to 1 THz region," *Antennas Propagation, IEEE Trans.*, vol. 55, no. 11, pp. 2944–2956, 2007.

[3.3] E. Rouvalis, C. C. Renaud, D. G. Moodie, M. J. Robertson, and A. J. Seeds, "Traveling-wave uni-traveling carrier photodiodes for continuous wave THz generation.," *Opt. Express*, vol. 18, no. 11, pp. 11105–11110, 2010.

[3.4] E. Rouvalis, M. Chtioui, M. Tran, F. van Dijk, M. Fice, C. Renaud, G. Carpintero, and A. Seeds, "High-speed uni-travelling carrier photodiodes for InP photonic integrated circuits," *Opt. Express*, vol. 20, no. 8, pp. 9172–9177, 2012.

[3.5] M. Natrella, E. Rouvalis, C.-P. Liu, H. Liu, C. C. Renaud, and A. J. Seeds, "InGaAsP-based uni-travelling carrier photodiode structure grown by solid source molecular beam epitaxy," *Optics Express*, vol. 20, no. 17. pp. 19279–19288, 2012.

[3.6] A. J. Seeds, C. Renaud, and M. Robertson, "Photodetector including multiple waveguides," US7851782 (B2), 2010.

[3.7] T. Pearsall and J. Hirtz, "The carrier mobilities in $Ga_{0.47}In_{0.53}As$ grown by organo-metalic CVD and liquid-phase epitaxy," *J. Cryst. Growth*, vol. 54, no. 1, pp. 127–131, 1981.

[3.8] C. Kopf, G. Kaiblinger-Grujin, H. Kosina, and S. Selberherr, "Influence of dopant species on electron mobility in InP," *Conf. Proceedings. 1997 Int. Conf. Indium Phosphide Relat. Mater.*, pp. 280 – 283, 1997.

[3.9] G. Reeves and H. Harrison, "Obtaining the specific contact resistance from transmission line model measurements," *IEEE Electron Device Lett.*, vol. 3, no. 5, pp. 111–113, 1982.

[3.10] H. Berger, "Models for contacts to planar devices," *Solid. State. Electron.*, vol. 15, no. 2, pp. 145–158, 1972.

[3.11] A. Katz, B. E. Weir, and W. C. Dautremont-Smith, "Au/Pt/Ti contacts to p-$In_{0.53}Ga_{0.47}As$ and n-InP layers formed by a single metallization common step and rapid thermal processing," *J. Appl. Phys.*, vol. 68, no. 3, pp. 1123–1128, 1990.

[3.12] L. Shantharama and H. Schumacher, “Evaluation of single ohmic metallisations for contacting both p-and n-type GaInAs,” *Electron. Lett.*, vol. 26, no. 15, pp. 1127–1129, 1990.

[3.13] H. Kroemer, “Heterostructure bipolar transistors and integrated circuits,” *Proc. IEEE*, vol. 70, no. 1, pp. 13–25, 1982.

[3.14] H. Kroemer, “Heterostructure bipolar transistors: What should we build?,” *J. Vac. Sci. Technol. B Microelectron. Nanom. Struct.*, vol. 1, no. 2, pp. 126–130, 1983.

[3.15] R. L. Anderson, “Experiments on Ge-GaAs heterojunctions,” *Solid. State. Electron.*, vol. 5, no. 5, pp. 341–351, 1962.

[3.16] A. A. Grinberg, M. S. Shur, R. J. Fischer, and H. Morkoc, “An investigation of the effect of graded layers and tunneling on the performance of AlGaAs/GaAs heterojunction bipolar transistors,” *Electron Devices, IEEE Trans.*, vol. 31, no. 12, pp. 1758–1765, 1984.

[3.17] V. Ryzhii and M. Shur, “Tunnelling- and barrier-injection transit-time mechanisms of terahertz plasma instability in high-electron mobility transistors,” *Semicond. Sci. Technol.*, vol. 17, no. 11, pp. 1168–1171, 2002.

[3.18] K. Giboney, “Traveling-wave photodetectors,” *Photonics Technol. Lett. IEEE*, vol. 4, no. 12, pp. 1363–1365, 1992.

[3.19] E. Rouvalis and C. C. Renaud, “Indium phosphide based photodiodes for continuous wave terahertz generation,” University College London, 2011.

[3.20] K. Kurishima and H. Nakajima, “Fabrication and characterization of high-performance InP/InGaAs double-heterojunction bipolar transistors,” *Electron Devices, IEEE Trans.*, vol. 41, no. 8, pp. 1319–1326, 1994.

[3.21] J. Liu, *Photonic Devices*. Cambridge: Cambridge University Press, 2005.

[3.22] B. E. A. Saleh and M. C. Teich, *Fundamentals of photonics*, 2. New York: Wiley, 2007.

[3.23] T. Ishibashi, S. Kodama, N. Shimizu, and T. Furuta, “High-speed response of uni-traveling-carrier photodiodes,” *Japanese J. Appl. Physics, Part 1 Regul. Pap. Short Notes Rev. Pap.*, vol. 36, no. 10, pp. 6263–6268, 1997.

[3.24] T. Ishibashi, T. Furuta, H. Fushimi, and H. Ito, “Photoresponse characteristics of uni-traveling-carrier photodiodes,” *Proc. SPIE 4283, Phys. Simul. Optoelectron. Devices IX*, vol. 4283, pp. 469–479, 2001.

[3.25] T. Ishibashi, N. Shimizu, and S. Kodama, “Uni-traveling-carrier photodiodes,” *Tech. Dig. Ultrafast Electron. Optoelectron.*, vol. 13, pp. 83–87, 1997.

[3.26] H. Kroemer, "Quasi-electric and quasi-magnetic fields in nonuniform semiconductors," *RCA Rev.*, vol. 18, pp. 332–342, 1957.

[3.27] M. Lundstrom, "ECE 612 Lecture 31: Heterostructure Fundamentals," 2006. [Online]. Available: http://nanohub.org/resources/2082. [Accessed: 10-Mar-2015].

[3.28] S. C. Jain, J. M. McGregor, and D. J. Roulston, "Band-gap narrowing in novel III-V semiconductors," *J. Appl. Phys.*, vol. 68, no. 7, pp. 3747–3749, 1990.

[3.29] R. K. Ahrenkiel, R. Ellingson, S. Johnston, and M. Wanlass, "Recombination lifetime of $In_{0.53}Ga_{0.47}As$ as a function of doping density," *Appl. Phys. Lett.*, vol. 72, no. 26, pp. 3470–3472, 1998.

Chapter 4 - 3D full-wave modelling of waveguide UTCs

This chapter presents the 3D full-wave modelling work (performed in CST STUDIO SUITE), carried out to allow the question regarding the UTC-to-antenna coupling efficiency to be more thoroughly understood. To the best of the author's knowledge no 3D full-wave modelling to analyse the UTC impedance has been reported. A brief description of the CST equations and numerical methods will be provided in Section 4.3.

As mentioned previously we will show, in the next chapter, how a reasonably accurate knowledge of the photodiode impedance can enable us to make a satisfactory prediction, both in terms of absolute value and trend over the frequency range, of the power radiated by an antenna integrated with that photodiode. The modelling of the UTC frequency photo-response has also been carried out in this chapter. To model the frequency response the results of the impedance analysis have been adopted. We also present in this chapter the results of 3D full-wave optical modelling and simulation, aiming to better understand and improve the optical power coupling between lensed fibre and UTC optical waveguide.

As reference source for the material electrical and optical properties, the CST STUDIO SUITE material database was employed together with the information available in [4.1]-[4.3] and in the on-line electronic archive of the Ioffe Physico-Technical Institute. The full-wave modelling will allow the device S_{11} and impedance to be calculated up to 400 GHz. The value of the photodiode impedance will then be used in Chapter 5 to determine the power radiated by antenna integrated UTCs, properly taking into account the UTC to antenna coupling efficiency.

4.1 S_{11} and impedance 3D full-wave modelling

The optimised parameters of Circuit 3 found in Section 3.2 and their relation with the device structure, illustrated in Figure 3.11, can be employed to set the material properties, i.e. conductivity and relative electrical permittivity, in CST. The series resistance R_1 obtained for the 3 x 15 μm^2 UTC, at both 0V and 2V reverse bias, is equal to 15 Ω, therefore the conductivities of the layers contributing to the UTC series resistance (namely p-contact, ridge layer, waveguide and n-contact) need to be adjusted, starting from the values shown in Table 3.2, in order to produce a total device series resistance equal to 15 Ω, including the effects of n- and p-ohmic contacts, for the 3 x 15 μm^2 model; the obtained conductivity values are summarised in Table 4.1.

Table 4.1: Conductivities used in the full-wave modelling for the layers contributing to the UTC series resistance. The relative electrical permittivity values are also shown, although they play a very marginal role for these layers.

Layer description	**Thickness (nm)**	**Electrical conductivity ($\Omega^{-1}m^{-1}$)**	**Relative electrical permittivity**
p-contact	200	19226	13.91
Ridge Layer	1000	3600	12.5
Waveguide	300	95000	13.12
n – contact	--	103000	12.5

As mentioned previously, the calculation of the n-contact layer and n-ohmic contact contributions to the series resistance is not a trivial geometrical problem hence a simplified CST model, as in Figure 3.3, has been used to verify that the conductivities given in Table 4.1 and the specific contact resistances shown in Table 3.3 actually produce a total device resistance of 15 Ω. The p- and n-ohmic contact resistances have been taken into account in the CST model by inserting thin layers of appropriate conductivity between the n/p-contact layers and the gold pads. This simplified CST model has also been used to verify whether the device series resistance actually scales down by a factor 3/4 for the 4 x 15 μm^2 UTC; it was found that the 4 x 15 μm^2 UTC series resistance is 12.7 Ω which is slightly larger than (3/4) x 15 Ω (=11.2 Ω) and this is consistent with the fact that in reality only the resistance of the layers making up the ridge scales down by (3/4) while that of n-contact layer and n-ohmic contact does not.

The properties of the two spacers and the collection layer are dictated by the optimised circuit elements R_2, C_2, R_3, C_3, R_4 and C_4 of Circuit 3 in Figure 3.11, which were discussed in Section 3.2, and are summarised in Table 4.2. It is important to bear in mind that these properties are not intended to represent the actual bulk properties of the materials making up the layers concerned (i.e. InGaAsP and InP) but are the results of the model we have introduced in Section 3.2 to explain the effects observed in the experimental data. As can be seen in Table 4.2, the relative electrical permittivity of the layers, except the absorption layer, is slightly different for the two different bias values (0 V and -2 V) which takes into account the capacitance change introduced by the applied reverse voltage; although the changes in capacitance are generally due to variations of the depletion region thickness, we have preferred to maintain the model geometry unchanged and account for the effect by means of an equivalent permittivity variation. Since the absorption layer only provides a marginal resistive contribution, its permittivity was not changed.

Table 4.2: Material properties of the two spacers and the collection layer derived by the optimised circuit elements R_2, C_2, R_3, C_3, R_4 and C_4 of Circuit 3. The absorber properties are also shown, although this layer only provides a marginal resistive contribution.

Layer description	**Thickness (nm)**	**Electrical conductivity ($\Omega^{-1}m^{-1}$)**	**Relative electrical permittivity (0 V bias)**	**Relative electrical permittivity (-2 V bias)**
Absorption layer	120	4005	13.91	13.91
Spacer Q	--	1.26	3.95	3.20
Spacer Q	--	2.67	3.05	2.63
Collection layer	300	0.02	50.45	45.18

As mentioned previously, the BCB layer was modelled in CST employing a “loss free” polymer, from the CST material database, with an electrical permittivity of 3.5. The substrate was modelled with standard loss free 12.5 permittivity indium phosphide (InP) while for the metal pads the default CST gold model (conductivity of 4.561×10^7 $(\Omega m)^{-1}$) was employed. The III-V Lab UTCs also contain very thin layers of platinum (conductivity of 9.52×10^6 $(\Omega m)^{-1}$) and titanium (conductivity of 2.015×10^6 $(\Omega m)^{-1}$) whose exact thickness was unknown; these two layers were included in the model between the polymer and the CPW gold, with typical thickness values of 10 nm (Pt) and 5 nm (Ti), while were not inserted between the UTC n/p- contact layers (InGaAs/InP) and the gold because at this locations, as mentioned previously, ad-hoc layers were introduced to take the ohmic contact resistances into account.

A model including the whole of the cleaved chip and the CPW pads is illustrated in Figure 4.1. Figure 4.2 shows additional details of the area near the UTC, including the n-contact layer mesa and the optical waveguide, while a further magnified cross section view is given in Figure 4.3, showing details of the layers making up the ridge. Since the chip was placed on a brass mount during the measurement, a perfect electric conductor (PEC) plane was used as boundary condition underneath the InP substrate (Z_{min}), while all the other boundaries were surrounded by vacuum. The excitation source, highlighted in red in Figure 4.1, was placed on the CPW signal pad and connected to the ground pads through ideal one-dimensional PEC wires (blue lines in Figure 4.1) which introduced no parasitic capacitance; to reduce the current loop inductance introduced by the wires, the loop areas were kept as small as possible. The excitation source is a CST “discrete port”, essentially representing a Norton (or Thevenin) equivalent with a 50 Ω impedance. It is noted that CST also provides a different type of excitation source, called “waveguide port”, which has a planar geometry and basically acts as a special kind of boundary condition of the calculation domain, enabling the stimulation as well as the absorption of energy; the waveguide port is generally preferred over the discrete port, in terms of accuracy, for the S parameter calculation of waveguide and microstrip structures. In the author’s opinion though, the use of the waveguide port could not have represented the actual connections and geometry of the experimental arrangement with acceptable accuracy. The use of the discrete port with the connections shown in Figure 4.1 was hence preferred, as it was considered to be better representative of the way the air coplanar probes are brought in contact with the CPW pads. The CST discrete ports provide accurate results when their size is much smaller than the wavelength; in our model the discrete port is 1 µm long.

It should also be noted that the hardware used for this work enabled the simulation of very large models, up to a few hundred million mesh cells, containing geometrical features extremely small compared to the bounding box size.

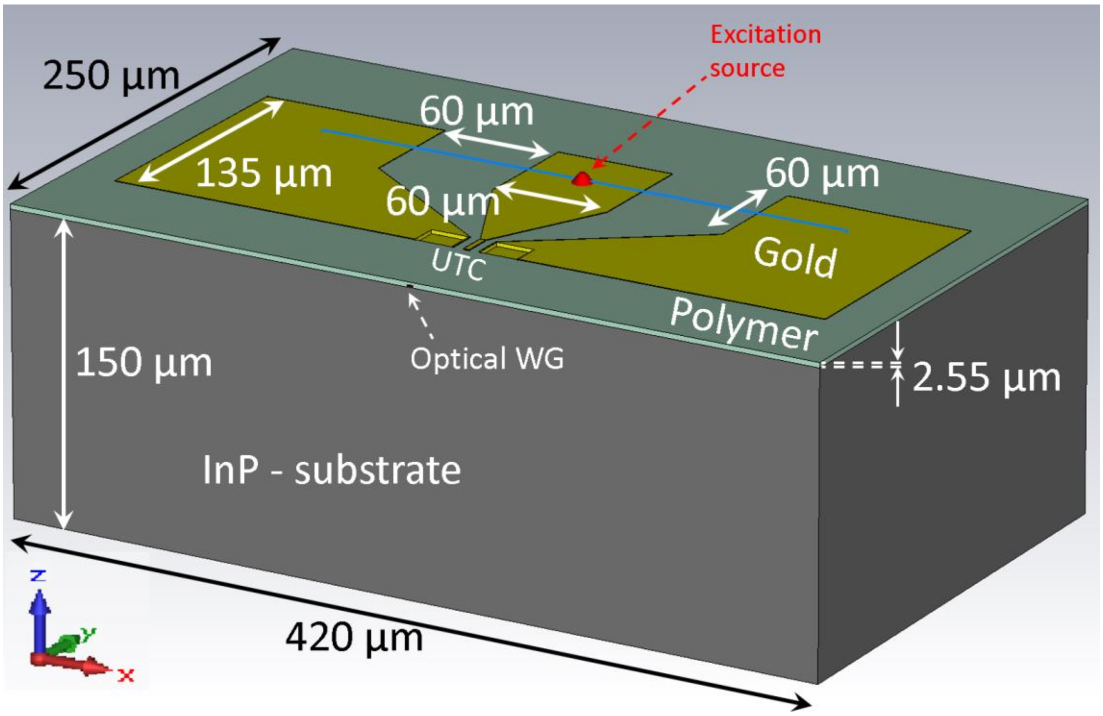

Figure 4.1: CST model including the whole of the cleaved chip and the CPW pads.

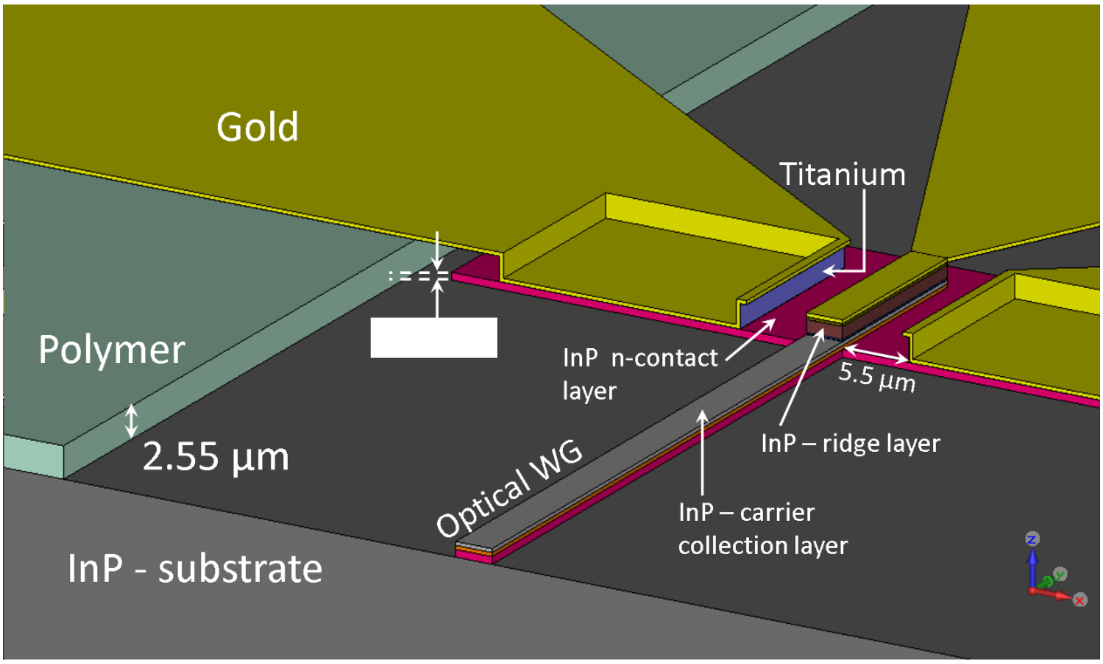

Figure 4.2: Model details of the area near the UTC, including the n-contact layer mesa and the optical waveguide.

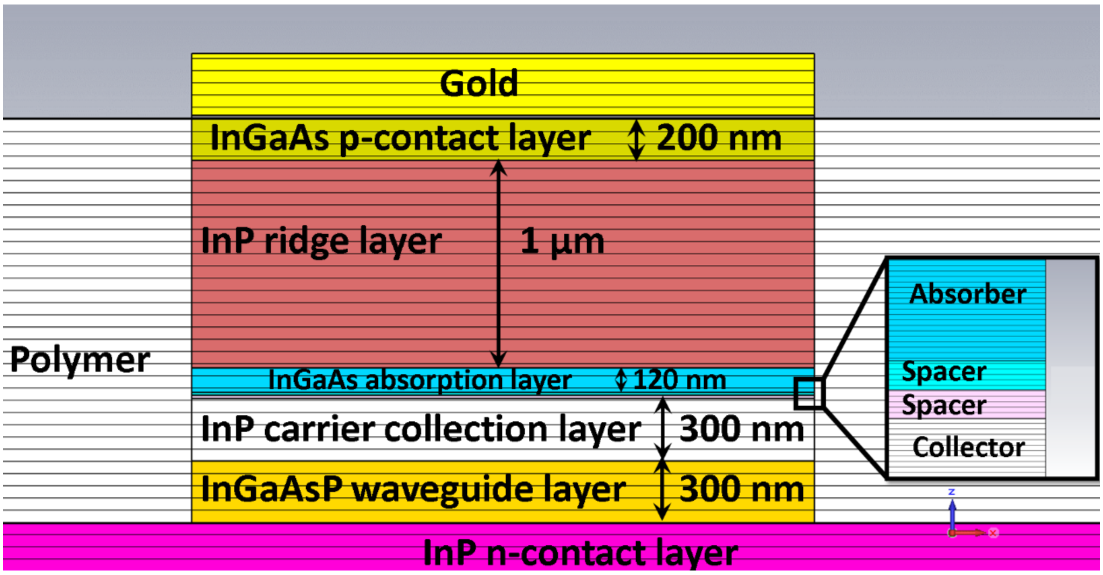

Figure 4.3: Magnified cross section view showing details of the layers making up the UTC ridge.

The first simulations were carried out on the model shown in Figure 4.1, which includes the whole of the chip with the CPW pads. Because the frequency range of interest extends up to 400 GHz, it is essential to assess and de-embed the effect of the CPW as this would affect dramatically the calculated S_{11}/impedance values at such high frequencies; we are interested in the S_{11}/impedance of the UTC alone, which will help us evaluate and improve the efficiency of energy coupling with antennas.

It was found during the laboratory experiment that varying the ACP contact position along the CPW had very little effect on the measured S_{11} below 67 GHz, while introducing some change in the W-band. The same test was performed numerically on the model in Figure 4.1 and yielded different results, showing a noticeable effect, particularly on the S_{11} phase, at all frequencies. As the excitation source position in the model was moved further away from the UTC, a progressively steeper quasi-linear phase decrease was observed in the frequency range below circa 200 GHz. Also when the excitation source in the model was brought close to the UTC, near the CPW angles, a phase decrease steeper than the measurement was still observed. As for the S_{11} magnitude, the agreement with the measurement was good from 0 GHz up to 67 GHz when the source was brought close to the UTC, but remained good only up to 35 GHz when the source was moved further away from the UTC. Figure 4.4 shows the comparison, for the case of a 3 x 15 µm^2 area UTC at -2 V bias, between the measured S_{11} and the S_{11} calculated with the model in Figure 4.1, when the source is placed near the end of the CPW pads, as in Figure 4.1. The numerical phase decrease is also slightly affected by the small inductance introduced by the PEC wires (blue lines in Figure 4.1), however this contribution is not nearly enough to explain the discrepancy with the measurement.

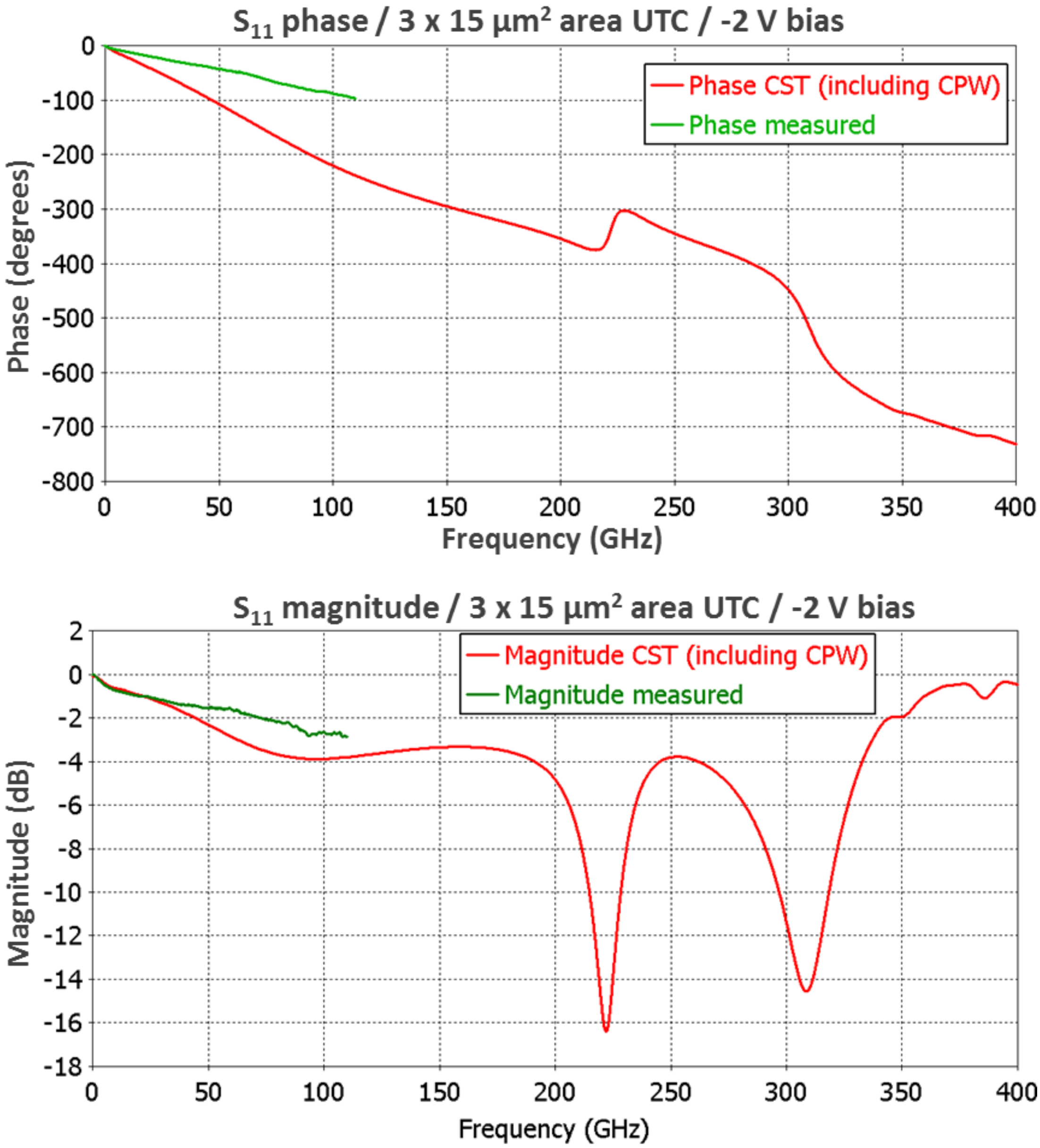

Figure 4.4: Comparison, for the case of a 3 x 15 µm² area UTC at -2 V bias, between the measured S_{11} and the S_{11} calculated with the model in Figure 4.1 when the source is placed near the end of the CPW pads.

To test whether the discrepancy was actually caused by the properties assigned to the UTC being incorrect, a range of different UTC material properties for the model in Figure 4.1 were tested. The result of this test suggested that when the complete model including the CPW pads, i.e. Figure 4.1, is simulated, the more gently sloping phase decrease obtained from the measurement cannot be even approached. It seems reasonable to consider the possibility that the CPW pads in the measurement did not have, especially below 67 GHz, the same relevant effect they have on the CST model in Figure 4.1 excited by the discrete port. Since a likely effect introduced by the CPW is an additional parasitic inductance (and possibly capacitance) increase, Circuit 3 was also used, with its optimised values in Figure 3.14, as starting point to assess the influence of L_p and C_p; remarkably it was found that when L_p is increased above 80 pH and C_p above 4 fF, the S_{11} phase and magnitude, below about 120 GHz, become very similar to the S_{11} shown in Figure 4.4, obtained by simulating the model in Figure 4.1. As a final test, the UTC in the model in Figure 4.1, was replaced with a second discrete port and the CPW was analysed as a 2 port network, by calculating the full 2 port S parameters; such 2 port S parameters were then employed to add the CPW effect to the measured S_{11} and the result was in very good agreement with the S_{11} obtained with the model in Figure 4.1, shown in Figure 4.4.

A possible explanation of why the CPW response does not appear to be present in the measured S_{11}, particularly below 67 GHz, is that the inductive and capacitive effects associated with the CPW pads may be similar to those measured on the impedance standard substrate (ISS) during the calibration and are hence corrected during the calibration. The cascade ISS standards are fabricated on a 625 µm thick alumina substrate, with electrical permittivity of 9.9. As a very elementary test, we modelled the short standard (not enough information about the load standard is available), which consists of a 50 µm x 500 µm rectangular metal pad, and calculated the S_{11} using the same discrete port and set of ideal wires shown in Figure 4.1; we found that such S_{11} exhibits a phase decrease over the frequency range which is comparable, below about 100 GHz, with that obtained by simulating the model in Figure 4.1 when the UTC is replaced with a short and the excitation source is brought closer to the UTC location, i.e. at the CPW pad angles.

All the modelling work was then continued excluding the CPW pads and performing the simulation on the model shown in Figure 4.5, which is identical to the model in Figure 4.1 in terms of geometrical details and material properties. Only a portion of substrate around the UTC was considered in this model, with perfect boundary absorption in all directions except Z_{max}, because it was verified that when the UTC alone (with no CPW) is simulated, the S_{11} is not influenced by the conditions set at the boundary of the whole of the chip in Figure 4.1.

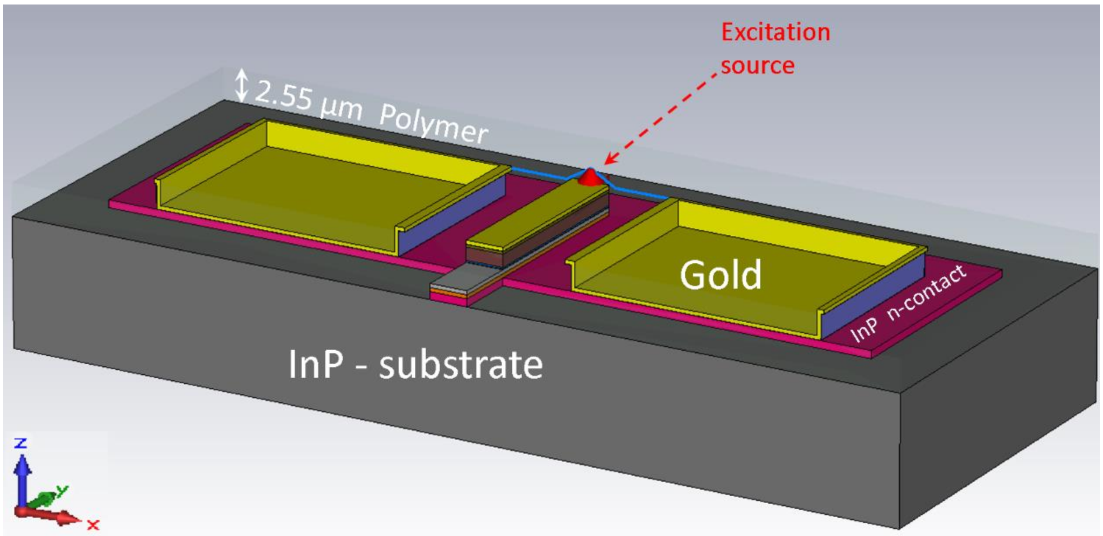

Figure 4.5: UTC model without CPW pads.

The S_{11} and impedance of the 3 x 15 μm^2 area UTC at 2 V reverse bias, calculated using the CST model in Figure 4.5, are shown in Figure 4.6 and compared with the experimental data and with the results obtained using Circuit 3 with its optimised values in Figure 3.14. The magnitudes of the measured S_{11} and the S_{11} obtained with CST and Circuit 3 are all in excellent agreement up to 90 GHz and good agreement between 90 GHz and 110 GHz; the phases are all in excellent agreement up to 67 GHz, then measurement and Circuit 3 phases maintain good agreement up to 110 GHz, while CST phase begins to depart. Above 110 GHz the disagreement between Circuit 3 and CST S_{11} becomes more and more significant. Such disagreement is entirely due to the value of the inductance L_p in Circuit 3 which is too high (16 pH), as can be seen clearly from the reactance in Figure 4.6 which switches from capacitive (i.e. < 0) to inductive (i.e. > 0) at 255 GHz for Circuit 3 while it is still slightly capacitive at 400 GHz for the CST result; notably, if L_p is reduced to 6.5 pH, the S_{11} and impedance obtained with CST and Circuit 3 are identical up to 400 GHz for the case of both 3 x 15 μm^2 and 4 x 15 μm^2 area UTC at both 0 V and -2 V bias. The influence of L_p on Circuit 3 S_{11} was minor below 67 GHz while becoming noticeable in the W-band; the value of 16 pH for L_p essentially resulted from the need to force the Circuit 3 S_{11}, particularly its phase, to match the S_{11} measured between 75 GHz and 110 GHz. Despite being simple and broad band, the SOLT calibration is still considered challenging at high frequencies [4.4]; it requires very well-defined standards and provides lower accuracy at high frequency, particularly on wafer [4.5]. For the SOLT calibration on wafer, the probe placement accuracy is of critical importance [4.6] and all standards must be accurately contacted physically, since the inductance values are very dependent on probe placement on the standard [4.7], especially in the W-band. As is particularly visible in Figure 3.4 and Figure 3.5, all the values of phase/reactance measured from 75 GHz to 110 GHz show a small offset downward/upward compared to those measured from 10 MHz to 67 GHz. In summary, also considering that, as mentioned previously, the values measured in the W-band were found to be sensitive to the probe placement on the CPW pad, it is probable that the values measured within the W-band (mainly phase and reactance) are to some extent affected by an inductive error which may have originated from an imperfect calibration and/or the CPW inductance that is more significant at such frequencies. The 6.5 pH inductance, which provides an excellent agreement between Circuit 3 and CST results up to 400 GHz, is hence accepted to be correct and the impedance values calculated with the full-wave modelling will be employed in the antenna analysis and design presented in the next chapter.

The S_{11} and impedance of the 3 x 15 μm^2 UTC at 0 V, 4 x 15 μm^2 UTC at 0 V and 4 x 15 μm^2 UTC at -2 V are shown in Figure 4.7, Figure 4.8 and Figure 4.9 respectively. It is important to bear in mind that also for these three scenarios, as for the result in Figure 4.6, the amended 6.5 pH inductance would provide excellent agreement between Circuit 3 and CST results up to 400 GHz.

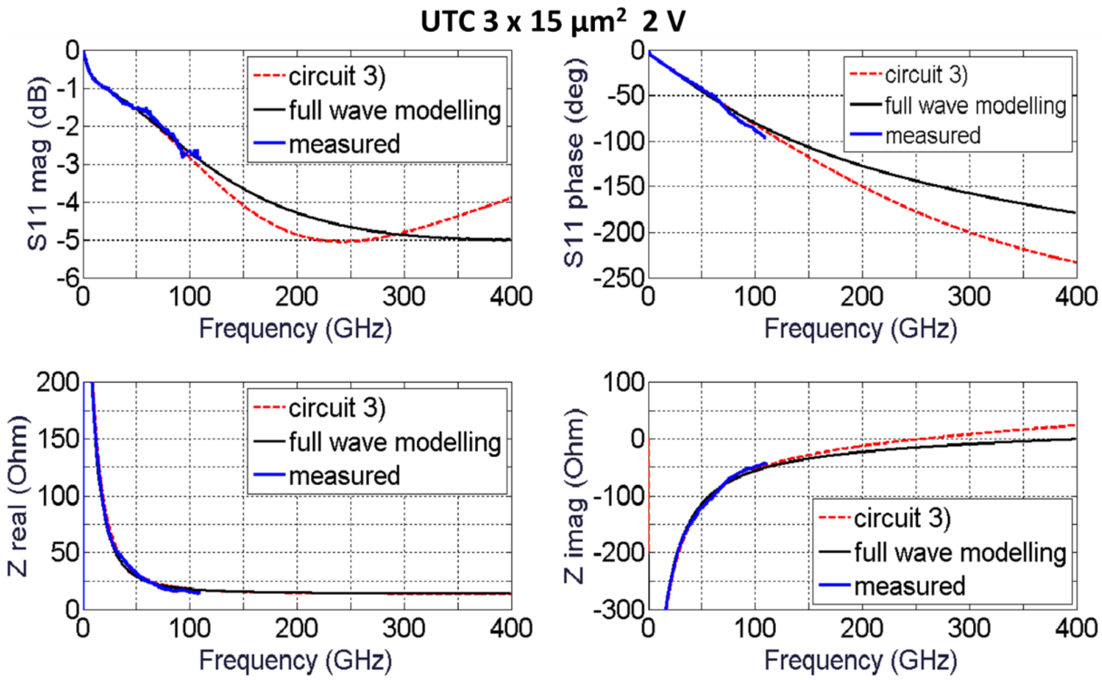

Figure 4.6: S_{11} and impedance of the 3 x 15 µm² area UTC at 2 V reverse bias, calculated using the CST model in Figure 4.5, compared with the experimental data and with the results obtained using Circuit 3 with its optimised values in Figure 3.14, which include the value of 16 pH for the parasitic inductance L_p. The amended value of 6.5 pH for L_p in Circuit 3 would provide excellent agreement between Circuit 3 and CST results up to 400 GHz.

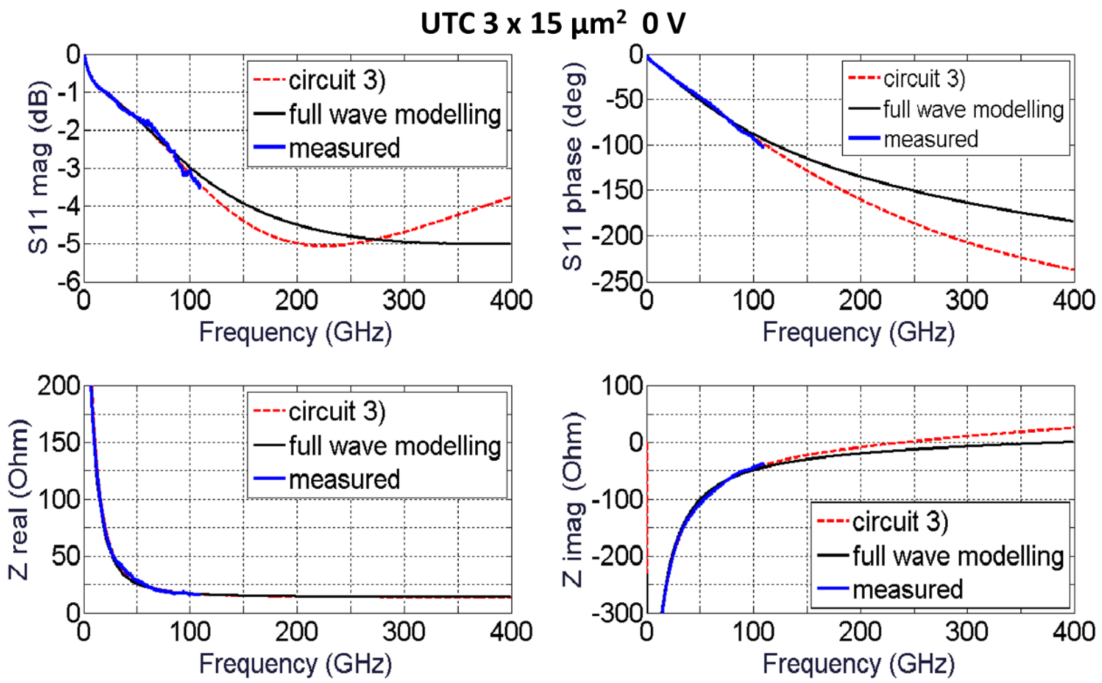

Figure 4.7: S_{11} and impedance of the 3 x 15 µm² area UTC at 0 V bias, calculated using the CST model in Figure 4.5, compared with the experimental data and with the results obtained using Circuit 3 with its optimised values in Figure 3.12, which include the value of 16 pH for the parasitic inductance L_p. The amended value of 6.5 pH for L_p in Circuit 3 would provide excellent agreement between Circuit 3 and CST results up to 400 GHz.

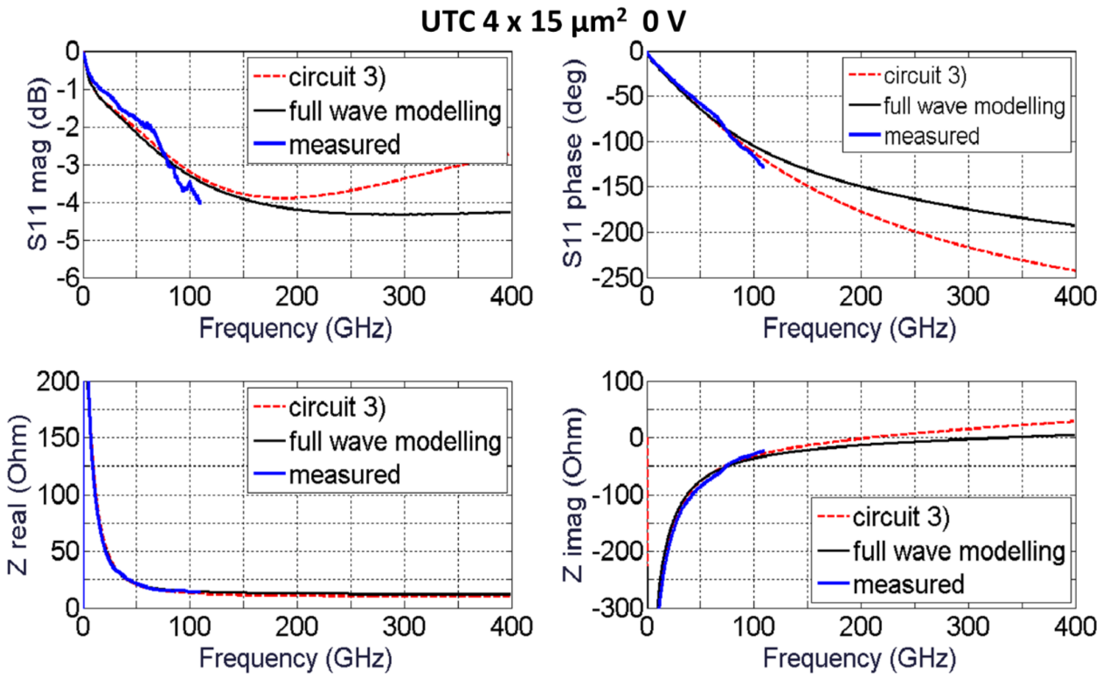

Figure 4.8: S_{11} and impedance of the 4 x 15 µm^2 area UTC at 0 V bias, calculated using the CST model in Figure 4.5, compared with the experimental data and with the results obtained using Circuit 3 with its optimised values in Figure 3.13, which include the value of 16 pH for the parasitic inductance L_p. The amended value of 6.5 pH for L_p in Circuit 3 would provide excellent agreement between Circuit 3 and CST results up to 400 GHz.

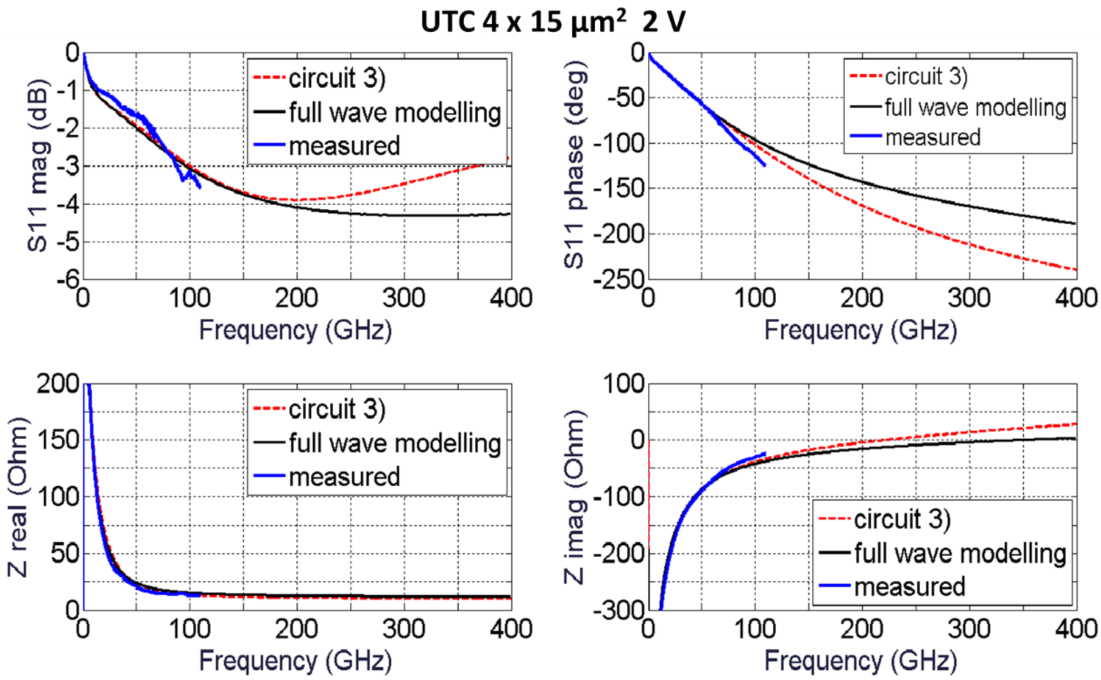

Figure 4.9: S_{11} and impedance of the 4 x 15 µm^2 area UTC at 2 V reverse bias, calculated using the CST model in Figure 4.5, compared with the experimental data and with the results obtained using Circuit 3 with its optimised values in Figure 3.15, which include the value of 16 pH for the parasitic inductance L_p. The amended value of 6.5 pH for L_p in Circuit 3 would provide excellent agreement between Circuit 3 and CST results up to 400 GHz.

In the next section the RC limited frequency photo-response is calculated in CST using the model in Figure 4.5 and compared with that calculated with Circuit 3 and with the measurement. Then the transit-time limited response discussed in Section 3.3 is included to calculate the overall frequency response.

4.2 Frequency photo-response 3D full-wave modelling

The structure shown in Figure 4.5 was also employed to calculate the UTC frequency response. The frequency response calculated in CST only represents the RC-limited response; the transit-time limited response contribution will then be incorporated using the results shown in Figure 3.21. As shown in Figure 4.10, the discrete port used as excitation source for the S_{11} calculation was replaced with a 50 Ω load, representing the LCA input impedance to which the RF power generated by the UTC is delivered; also, an ideal current source was placed across collection layer, spacers and absorber, connecting the heavily doped waveguide and ridge layers. The model in Figure 4.10 reflects the connections discussed for Circuit 3 shown in Figure 3.20, employed to calculate the photodiode frequency response.

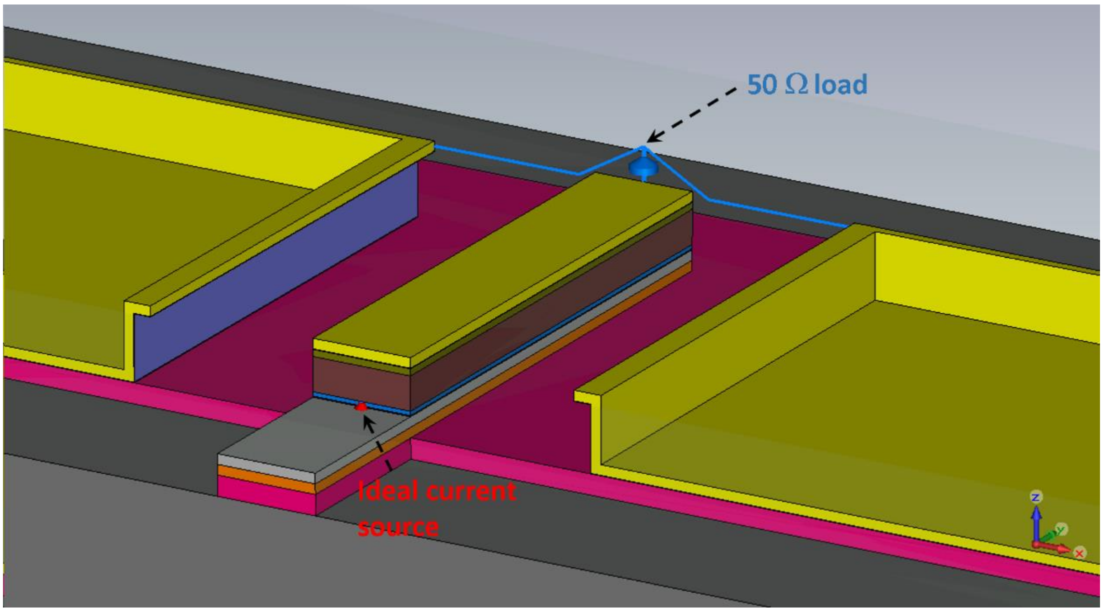

Figure 4.10: CST model used for the frequency response full-wave modelling.

The relevance of the current source position along the ridge was analysed and, as expected, was found to slightly influence the response only at high frequency, above circa 300 GHz; in fact the 15 µm long devices can be treated as a lumped element up to 400 GHz with reasonable accuracy. For future work on longer devices and at higher frequencies, modelling of distributed excitation along the ridge will be investigated, benefiting from the optical full-wave modelling result, discussed in the next section, which enable a better understanding of how the light is absorbed throughout the absorption layer. It is interesting to note that an alternative way to model the frequency response would be to use the same discrete port employed for the S_{11} calculation (50 Ω port), positioned at the same location as for the S_{11} calculation, and record the voltage between the heavily doped waveguide and ridge layers, across absorber, spacers and collection layer. It is in fact easy to demonstrate that, because the model equivalent network contains only passive elements and all the materials are isotropic, the current flowing in the 50 Ω load in Figure 4.10 is proportional to the voltage between waveguide and ridge layers in Figure 4.5. For the calculation of the frequency response discussed in this section, the ideal current source as shown in Figure 4.10 was used.

As was concluded in Section 3.3, based on the RC-limited frequency responses calculated by means of Circuit 3 in Figure 3.20 and its optimised parameters in Figure 3.14 and Figure 3.15, the effect of the graded-doping-induced quasi-field, required to match the experimental data, turns out to be rather modest, contradicting the bandwidth enhancement expected on the basis of the analysis presented in [4.8]-[4.10]. In fact the overall responses calculated combining the RC-limited response of Circuit 3 and the transit-time limited responses 1, 2 and 3 (which are in line with the analysis in [4.8], [4.9], [4.10]) are faster than the measured responses, as shown in Figure 3.22 and Figure 3.23. As was anticipated, the reason for the disagreement lies in the fact that the RC-limited 3 dB bandwidth, calculated by means of Circuit 3, was overestimated due to the too large value (16 pH) assigned to L_P in Circuit 3. The RC-limited response calculated with full-wave simulation, using the model in Figure 4.10, is plotted in Figure 4.11 and compared with the experimental data and with Circuit 3 RC-limited response for both the original value of parasitic inductance ($L_p = 16\ pH$) and the amended value ($L_p = 6.5\ pH$). Exactly as for the case of S_{11} and impedance calculation, the too high initial value of the inductance L_p

(16 pH) is entirely responsible for the disagreement between Circuit 3 and CST results. Remarkably, as for S_{11} and impedance, the amended value of 6.5 pH for L_p also provides a very good agreement between Circuit 3 and CST RC-limited frequency response up to 400 GHz, as also shown in Figure 4.11.

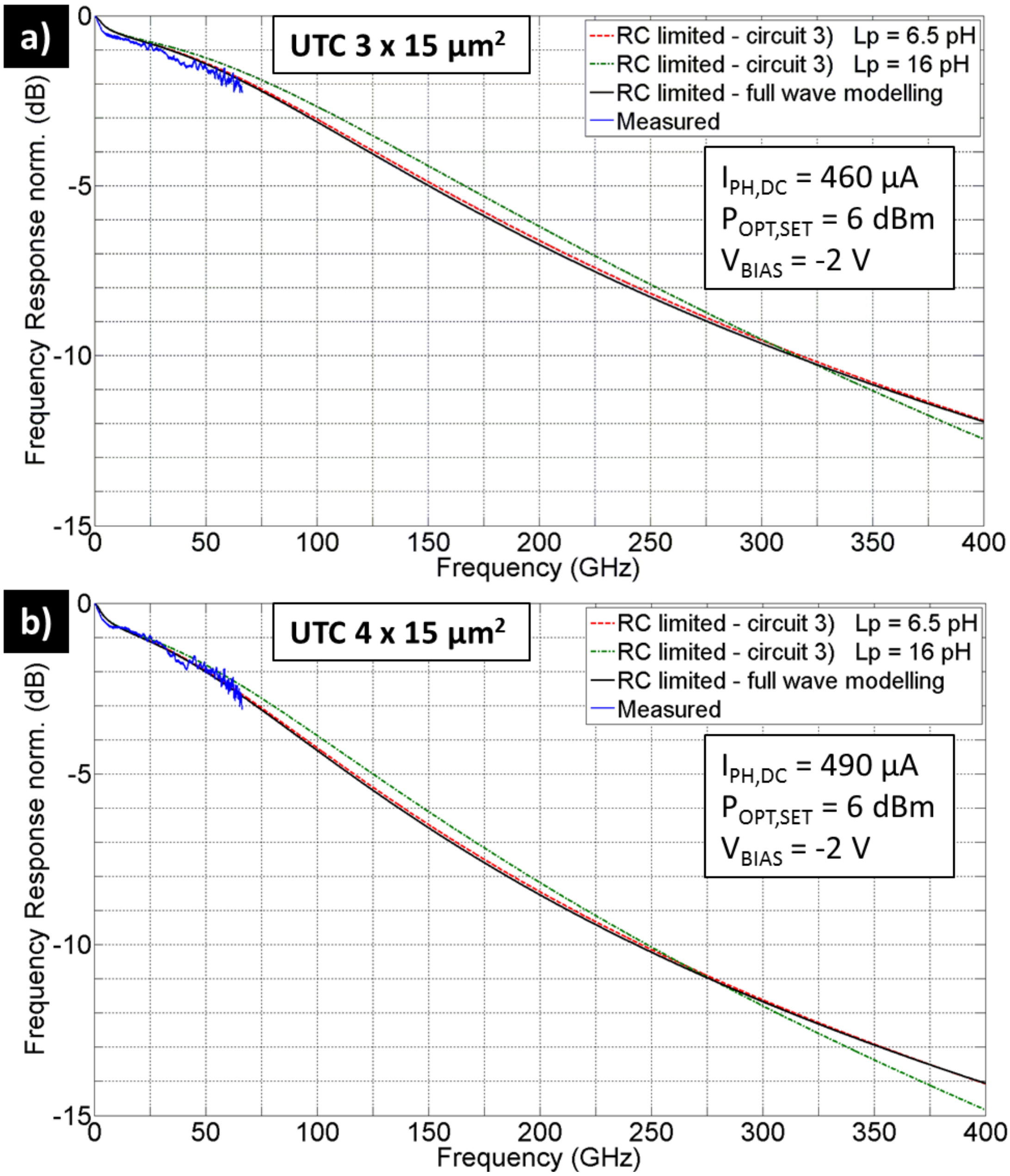

Figure 4.11: Comparison between RC-limited response calculated with full-wave simulation using the model in Figure 4.10 (continuous black line) and experimental data (continuous blue line). The RC-limited response calculated with Circuit 3 using both the initial value of parasitic capacitance L_P = 16 pH (dash-dot green line) and the amended value 6.5 pH (dashed red line) are also shown.

If we now use the CST RC-limited response to calculate the overall UTC frequency response, by incorporating the transit-time limited responses 1, 2 and 3 in Figure 3.21, we obtain the results shown in Figure 4.12 and Figure 4.13 for the 3 x 15 μm^2 and 4 x 15 μm^2 UTCs respectively. The agreement between numerical and measured results is now good. In particular the results obtained by incorporating the transit-time limited response 2, which exhibited a 235 GHz 3 dB bandwidth, appears to provide a good agreement with the experimental data for both 3 x 15 μm^2 and 4 x 15 μm^2 UTCs. The insets in Figure 4.12 a) and Figure 4.13 a) are a magnified view of the responses in the frequency range 0 GHz to 80 GHz and are intended to provide a clearer comparison between numerical and experimental data.

For the 3 x 15 μm^2 area device, the responses 1, 2 and 3 exhibit 3 dB bandwidth of 82 GHz, 86 GHz and 88 GHz respectively. For the 4 x 15 μm^2 area device, the responses 1, 2 and 3 exhibit 3 dB bandwidth of 65 GHz, 67 GHz and 69 GHz respectively.

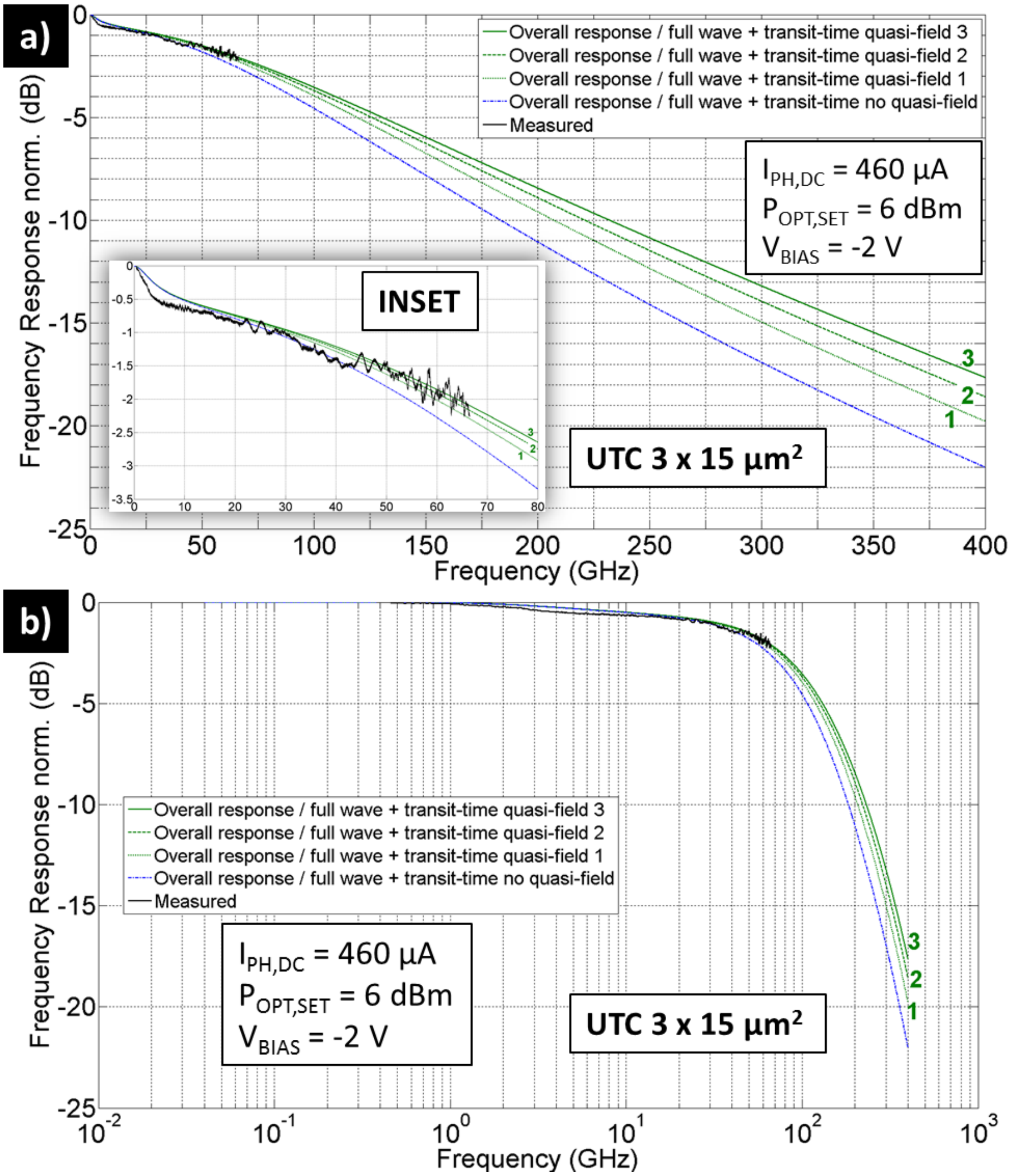

Figure 4.12: Comparison between measured frequency photo-response and overall frequency photo-response calculated combining the full-wave modelling RC-limited response with the transit-time limited responses in Figure 3.21, for the case of a 3 x 15 µm^2 area UTC. The inset in Figure 4.12 a) is a magnified view of the responses in the frequency range 0 GHz to 80 GHz and enables a clearer comparison between numerical and experimental data.

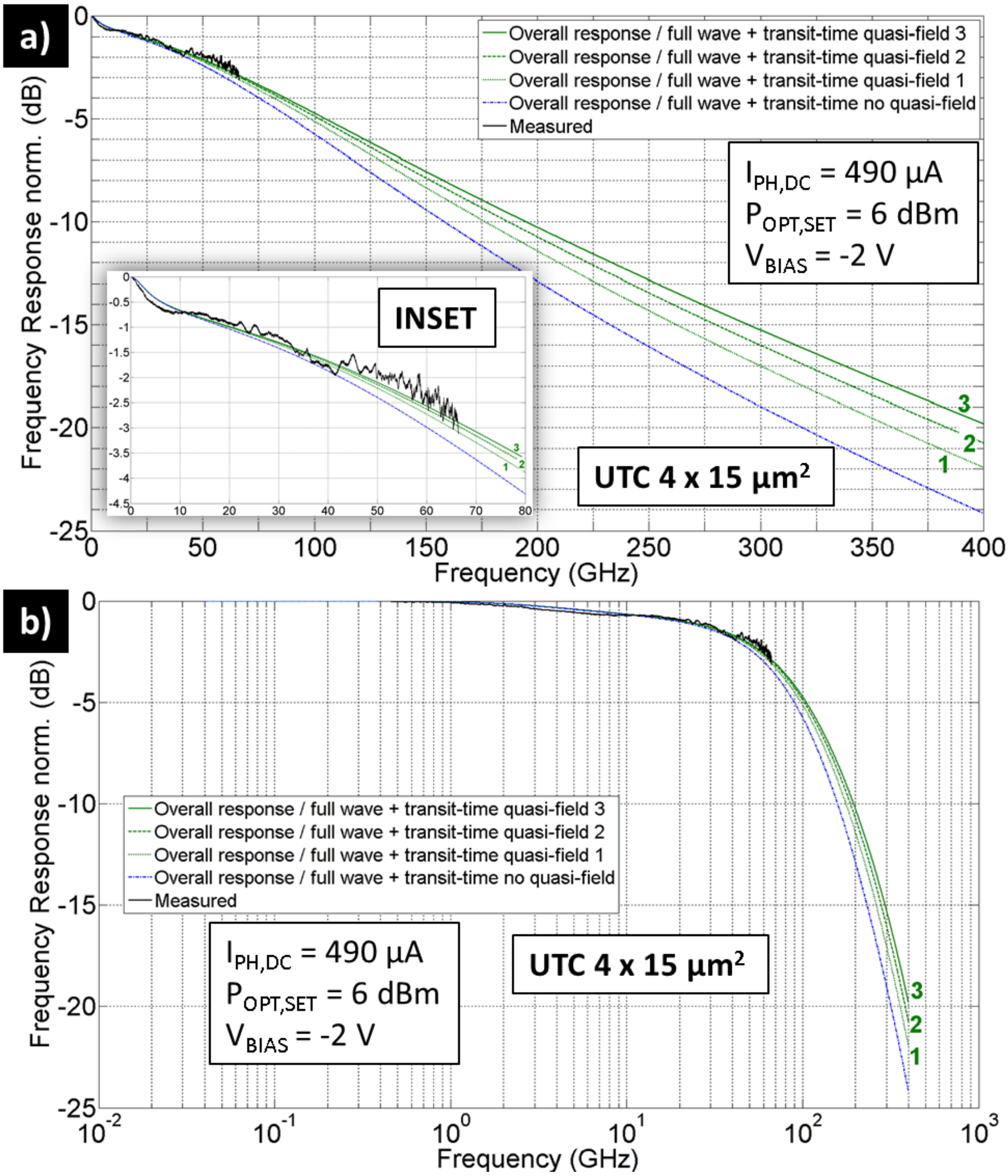

Figure 4.13: Comparison between measured frequency photo-response and overall frequency photo-response calculated combining the full-wave modelling RC-limited response with the transit-time limited responses in Figure 3.21, for the case of a 4 x 15 μm² area UTC. The inset in Figure 4.13 a) is a magnified view of the responses in the frequency range 0 GHz to 80 GHz and enables a clearer comparison between numerical and experimental data.

4.3 Fibre to chip coupling optical 3D full-wave modelling

In this section the optical 3D-full-wave modelling of the III-V Lab waveguide UTCs is presented. A wide variety of algorithms have been developed for the simulation of passive photonic devices, though only a few have made it to mainstream use, such as Beam Propagation Method (BPM), Eigenmode Expansion Method (EME) and Finite Difference Time Domain (FDTD) [4.11].

The BPM method is an approximation technique for simulating the propagation of light in slowly varying optical waveguides; BPM struggles with handling structures containing material with significantly different refractive index, cannot deal with metals and reflections, and has problems modelling non-rectangular structure.

The EME method is a linear frequency-domain method which relies on the decomposition of the electromagnetic fields into a basis set of local eigenmodes that exists in the cross section of the device; although unable to deal with non-linearities, it provides a rigorous solution to Maxwell's equations, the main approximation being the number of modes used. It should be noted though, that not all problems can be solved by considering only a modest number of modes. Furthermore, the choice of the modes to be considered to simulate a device is still an assumption to be made by the user while, for devices like the waveguide UTCs, the type of propagation excited within the device by an optical beam incident externally, is one of the unknown to calculate and a major question that we want to investigate. Also, the EME cannot provide information such as external responsivity and effect of the misalignment between incident beam and waveguide.

The FDTD method is a finite-difference discretisation of Maxwell's equation in time and space and in principle can model virtually anything, provided enough computing power. The Finite Integration technique (FIT), employed in CST Studio Suite is a spatial discretisation scheme to numerically solve electromagnetic field problems in time and frequency domain. It preserves basic topological properties of the continuous equations such as conservation of charge and energy and covers the full range of electromagnetics (from static up to high frequency) and optic applications. The FIT method applies the Maxwell equations in integral form to a set of staggered grids and stands out due to high flexibility in geometric modelling and boundary handling as well as incorporation of arbitrary material distributions and material properties such as anisotropy, non-linearity and dispersion. The CST Transient solver is based on the Finite Integration Technique (FIT) and applies some highly advanced numerical techniques like the Perfect Boundary Approximation (PBA) in combination with the Thin Sheet Technique (TST) to allow accurate modelling of small and curved structures without the need for an extreme refinement of the mesh at these locations. With the optical full-wave modelling performed in CST, we will be able to simulate very realistic scenarios in which the excitation source is a Gaussian beam, which is a good approximation of the light coupled from the lensed optical fibre into the waveguide. In this way it is possible to calculate, among other things, the external responsivity, the effect of the misalignment between Gaussian beam and waveguide, the type of propagation excited within the waveguide (single- or multi-mode) and the way the light actually propagates and is absorbed throughout the UTC structure.

The material properties used to model the UTC at 1550 nm free space wavelength (193.548 THz) are shown in Table 4.3. In particular, the gold metallisation was characterised with the CST default gold optical model with dispersive permittivity, derived from [4.12].

Table 4.3: Material optical properties at 1550 nm wavelength, i.e. 193.548 THz.

Layer description	**Thickness (nm)**	**Relative electrical permittivity**	**Tangent delta**
p-contact GaInAs	200	12.88	--
Ridge layer InP	1000	10.11	--
Absorption layer $In_{0.53}Ga_{0.47}As$	120	12.88	0.0446
Spacer Q	--	11.49	--
Collection layer InP	300	10.11	--
Waveguide $Q_{1.17}$	300	11.49	--
n-contact layer InP	--	10.11	--
Substrate InP	--	10.11	--

4.3.1 Waveguide port source

The optical analysis has been carried out at 193.548 THz (e.g. 1550 nm wavelength) on the 3 x 15 μm^2 device. The geometrical details of the initial UTC optical model are illustrated in Figure 4.14; as can be noticed, the scaling of the waveguide width has been here taken into account since its effect at optical frequencies cannot be ignored, while it was irrelevant for the S_{11} calculation below 400 GHz.

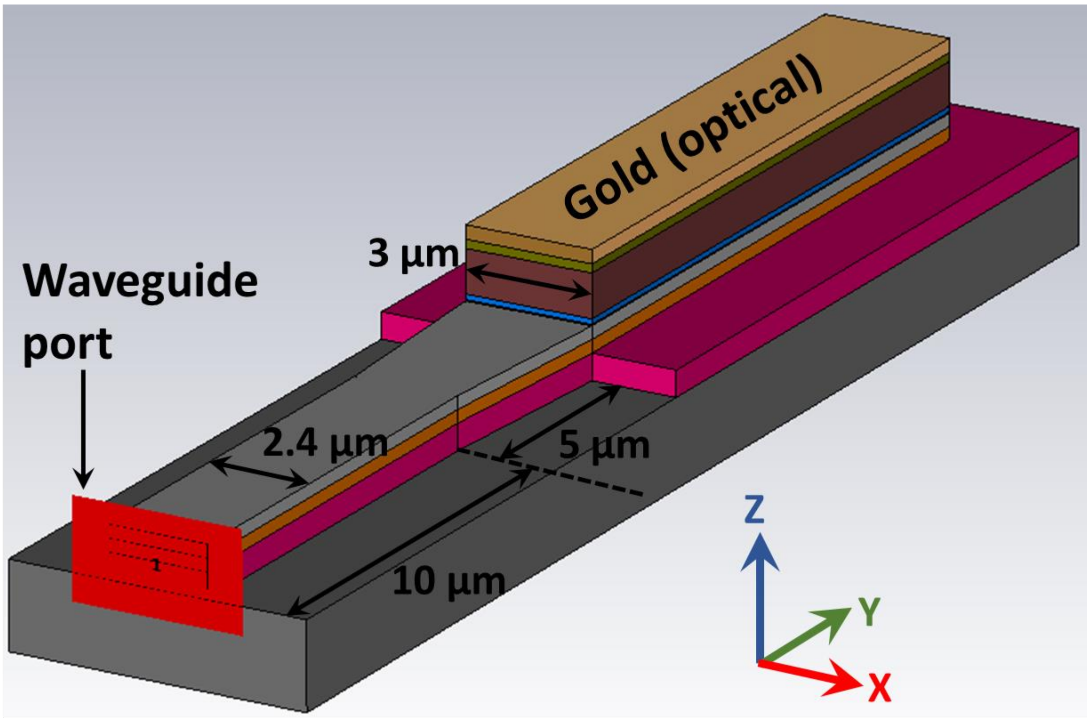

Figure 4.14: Geometrical details of the initial UTC model used for the optical full-wave simulations. The gold metallisation was characterised with the CST default gold optical model with dispersive permittivity, derived from [4.12].

For this first optical analysis a CST waveguide port was employed as excitation source. As explained in Section 4.1, the waveguide ports represent a special kind of boundary condition of the calculation domain which enables the stimulation as well as the absorption of energy and allows the calculation of the waveguide modes; the electric field distribution, the power flow and absorption, generated by each mode, can be computed among other things.

The power flow pattern along the Y direction and the propagation constant β of the two main modes is shown in Figure 4.15. The optical waveguide does not support any transverse mode as both mode 1 and mode 2 are hybrid. The X component of the electric field is the dominant component for mode 1 which is similar to a TE_{01} mode, while the X component of the magnetic field is the dominant component for mode 2 which is similar to a TM_{01} mode.

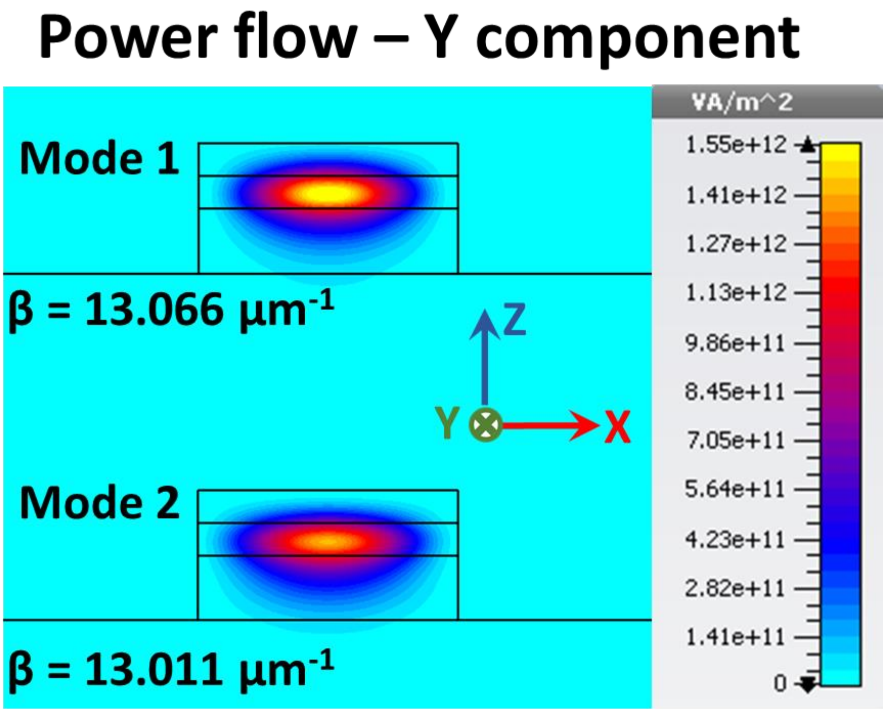

Figure 4.15: Power flow pattern along the Y direction and the propagation constant β of the two main modes. Both mode 1 and mode 2 are hybrid. The X component of the electric field is the dominant component for mode 1 which is similar to a TE_{01} mode, while the X component of the magnetic field is the dominant component for mode 2 which is similar to a TM_{01} mode.

A side cross section of the power flow along the structure is given in Figure 4.16, showing in particular the power coupling between the waveguide layer and the absorption layer in the ridge; the fact that some power is coming out from the absorber at the end of the ridge suggests that the $In_{0.53}Ga_{0.47}As$ layer is not long enough to absorb the whole power coupled in it.

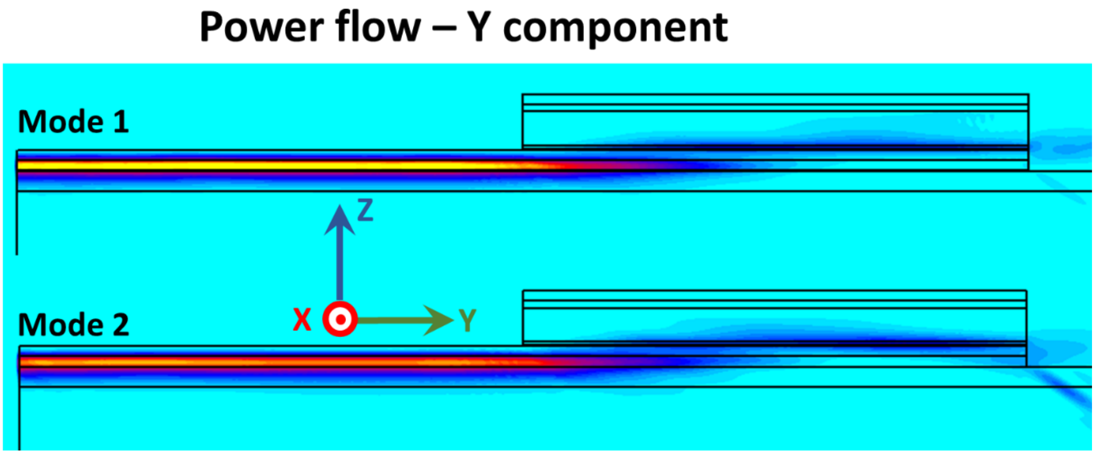

Figure 4.16: Side cross section of the power flow along the structure, showing the power coupling between the waveguide layer and the absorption layer in the ridge.

Figure 4.17 shows a horizontal cross section cutting through the waveguide layer; specifically it can be noticed how, because of the single mode propagation, the intensity pattern does not change along the Y direction within the waveguide.

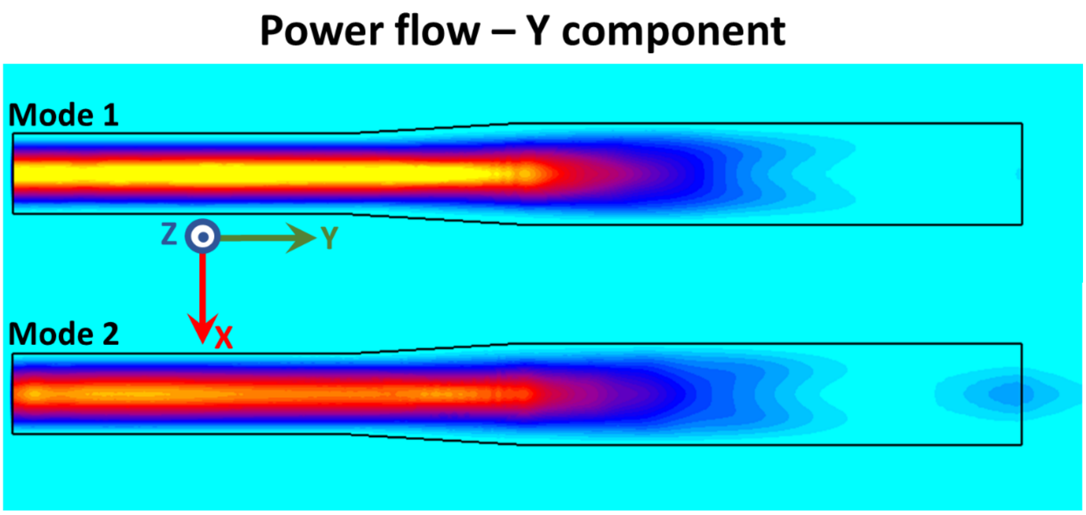

Figure 4.17: Horizontal cross section cutting through the waveguide layer, showing the power flow along the Y direction.

In Figure 4.18 a horizontal cross section cutting through the absorber is displayed, showing the way the light is absorbed along the layer. It is noted that the power simulated by the waveguide port was equal to 0.5 W and that, at the frequency of interest (193.548 THz), the power coupled into the waveguide was virtually 100 %, i.e. 0.4997 W for mode 1 and 0.4984 W for mode 2. It follows that, by considering the ratio between the power absorbed in $In_{0.53}Ga_{0.47}As$ (0.3683 W for mode 1 and 0.2995 W for mode 2) and the power accepted, the internal quantum efficiency η_{int}, given in Figure 4.18, can be calculated; the internal responsivity can also be evaluated as $\rho_{int} = \eta_{int}\, q/(hf)$ where q is the electron charge (1.602 x 10^{-19} C), h the Plank constant (6.626 x 10^{-34} Js) and f the frequency (193.548 THz). The value of 0.921 A/W can hence be looked upon as the maximum theoretical responsivity attainable for the structure discussed in this section, ideally achievable if 100 % of the optical power coming out of the lensed fibre is coupled into the waveguide and propagates as mode 1. This scenario is far from being realisable because, as discussed in the next section, firstly only a fraction of the incident optical power will be successfully coupled into the waveguide, even if the optical beam leaving the lensed fibre is perfectly aligned with the waveguide, and secondly because the concerned waveguide is multi-mode at 1550 nm free space wavelength. It is noted that when mode 1 and mode 2 were simulated simultaneously for the model in Figure 4.14, the quantum efficiency was equal to 0.669, between that obtained for mode 1 and mode 2.

The power absorption pattern in Figure 4.18 suggests that the single modes travelling through the input waveguide excite multimode propagation in the waveguide represented by the UTC ridge structure, principally because of the greater width of that waveguide; the absorption pattern though, is also slightly determined by the power that is not entirely absorbed and is reflected back into the layer. A test simulation was run with mode 1, to check the absorption pattern when the UTC ridge has the same width as the input waveguide. The obtained pattern was still not truly single mode but more uniform along Y in the first two thirds of the ridge length; interestingly, despite the smaller absorber size, compared to Figure 4.18, the power lost in the absorber was slightly greater, i.e. 0.3713 W, for equal power coupled in the input waveguide. This is because the scaled up width, at the transition between input waveguide and UTC ridge, reduces the coupling efficiency between the two.

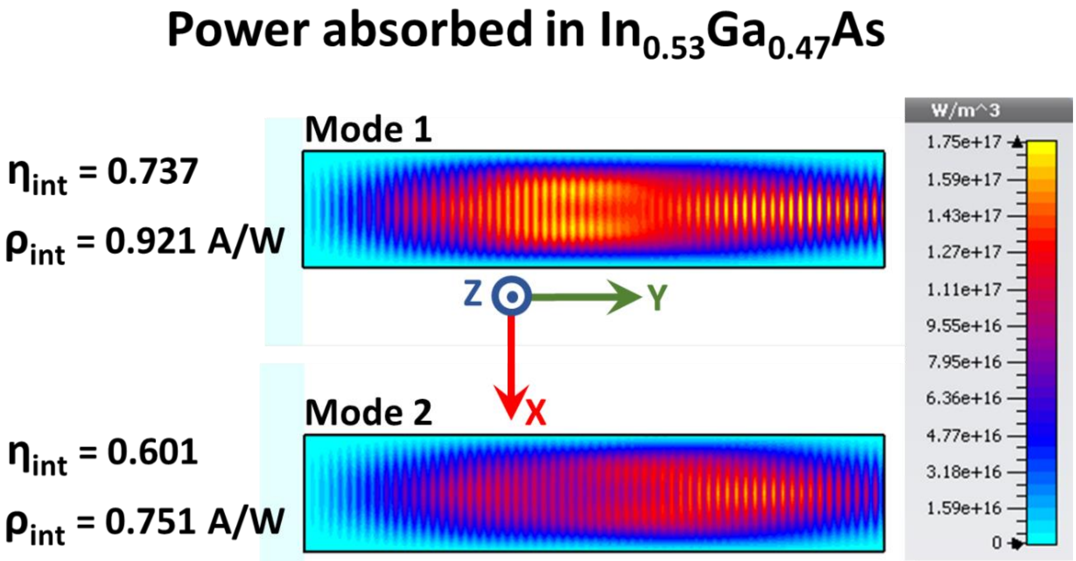

Figure 4.18: Horizontal cross section cutting through the absorber showing details of the power absorbed in the $In_{0.53}Ga_{0.47}As$ layer for mode 1 and mode.

To assess the importance of the waveguide length, the simulation for mode 1 was repeated for a number of longer waveguides and no significant difference was observed. The waveguide length is measured from the facet to the UTC ridge and includes the waveguide tapered section; a 15 µm long waveguide corresponds, for instance, to the case shown in Figure 4.14. The results relative to a 50 µm long waveguide are shown in Figure 4.19. The power coupled in the waveguide is well confined and propagates with negligible losses. Furthermore, because of the single mode propagation, the power flow along the propagation direction remains constant and the intensity pattern arriving at the ridge is always the same, regardless of the waveguide length; as a consequence the power coupling between the waveguide and the absorption layer always occurs in the same fashion. The results in Figure 4.19 show that, not only the internal quantum efficiency is virtually unchanged (+ 0.1 %) with respect to the 15 µm long waveguide case, but also the pattern of the power absorbed throughout the $In_{0.53}Ga_{0.47}As$ is the same.

For real devices the waveguide geometry is not as perfect as in our model, due to inevitable fabrication imperfections, therefore some power can be scattered and lost along the optical waveguide; also, as already mentioned, single mode propagation is hard to achieve in real optical waveguides.

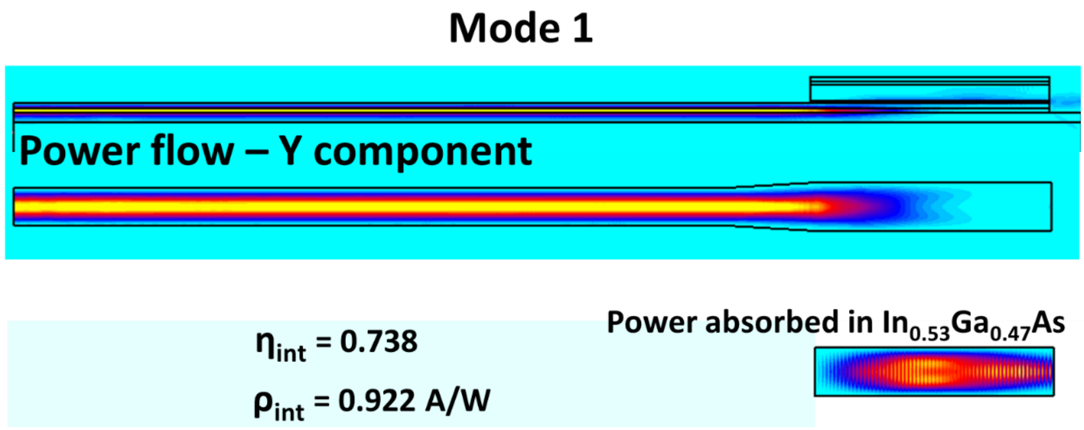

Figure 4.19: Power flow along the input waveguide and power absorption in the absorber, for the case of a 50 µm long input waveguide. The internal quantum efficiency is virtually the same (+ 0.1 %) as in the 15 µm long waveguide case; the pattern of the power absorbed throughout the $In_{0.53}Ga_{0.47}As$ is also unchanged. The waveguide length is measured from the facet to the UTC ridge and includes the waveguide tapered section; a 15 µm long waveguide corresponds, for instance, to the case shown in Figure 4.14.

In the next section a more realistic scenario is analysed, in which a Gaussian beam is the source of the optical power.

4.3.2 Gaussian beam source

Two linearly polarised (X and Z) Gaussian beams, with nominal electric field amplitude of 1 V/m and spot size of 4 µm, were used to couple light into the UTC optical waveguide. The X polarised beam was intended to excite the propagation of mode 1, whose dominant component is the electric field X component, while the Z polarised beam was intended to excite mode 2, for which the magnetic field X component is dominant and the electric field is principally in the Z direction. Details of the beam for the X polarisation case are given in Figure 4.20. The figure shows the propagating electric field in free space, though the device structure is outlined in order to discuss the alignment between beam and waveguide. The Gaussian beam wave-front is planar at the waist, therefore, for perfect alignment, the facet of the cleaved waveguide needs to lie within the same plane; also, the beam optical axis must pass through the centre of the waveguide layer cleaved facet. The incident optical power was 8.2563 x 10^{-15} W for the X polarised beam and 8.4285 x 10^{-15} W for the Z polarised beam.

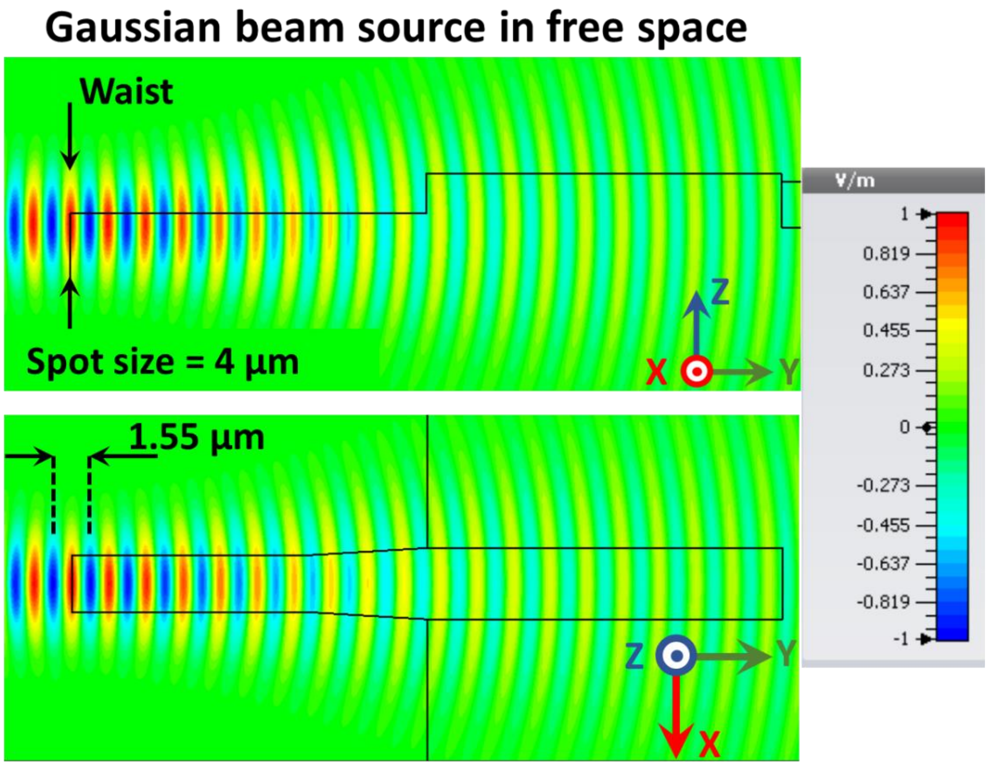

Figure 4.20: Gaussian beam details for the X polarisation case. The figure shows the propagating electric field in free space, though the device structure is outlined in order to highlight the alignment between beam and waveguide.

4.3.2.1 Gaussian beams with different polarisation

A still image of the propagating electric field magnitude, in the presence of the device structure, is shown in Figure 4.21 for both X and Z polarisations. The way in which part of the incident field is coupled down in the InP substrate is similar for the two cases, while the propagation above the device is quite different; in neither case does a significant amount of field appear to reach the absorber directly through free space, nevertheless the Z polarisation case seems to be more susceptible to this type of unintentional coupling.

It is interesting to notice that, if the field amplitude (e.g. the modulus maximum at all locations) had been shown instead of a still image of the modulus of the propagating electric field, the periodic-like pattern along the Y direction in front of the waveguide facet, visible in Figure 4.21, would have remained similar. This is due to the interference between the incident field and the field reflected from the waveguide facet. In real experiments, if no reflection coating is applied to the waveguide facet, the reflected optical signal can couple back into the lensed fibre; if no isolators are used in the fibres, such optical signal can be reflected back and forth and appear, in the measured device frequency photo-response, as periodic ripples.

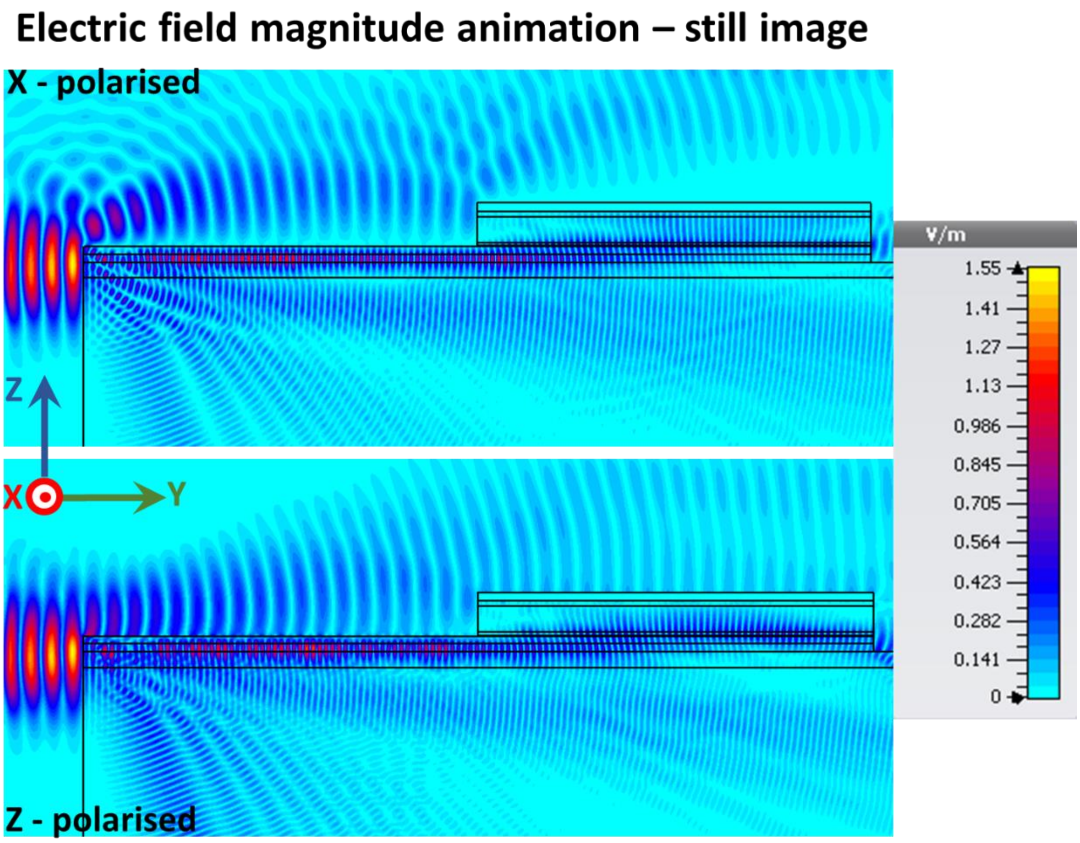

Figure 4.21: Still image of the electric field magnitude animation, in the presence of the device.

A side cross section view and a horizontal cross section view (through the waveguide layer) of the power flow along the Y direction, are shown in Figure 4.22 and Figure 4.23 respectively, for both X and Z polarisation. The propagation excited in the waveguide from the X polarised and Z polarised Gaussian beam is different, however it is clearly multimode in both cases.

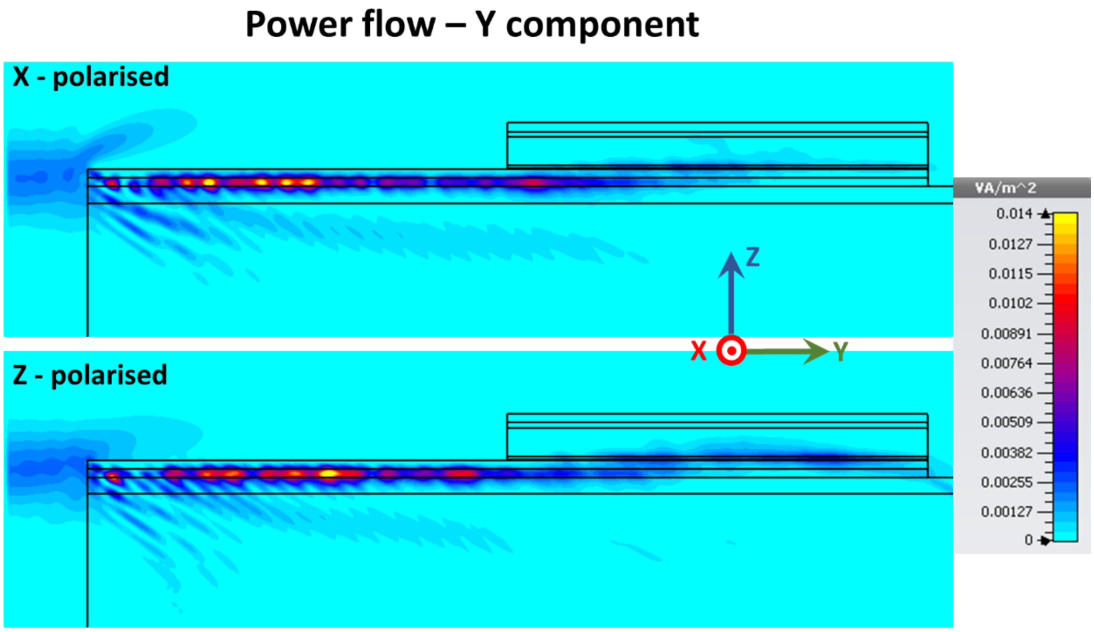

Figure 4.22: Side cross section view of the power flow along the Y direction.

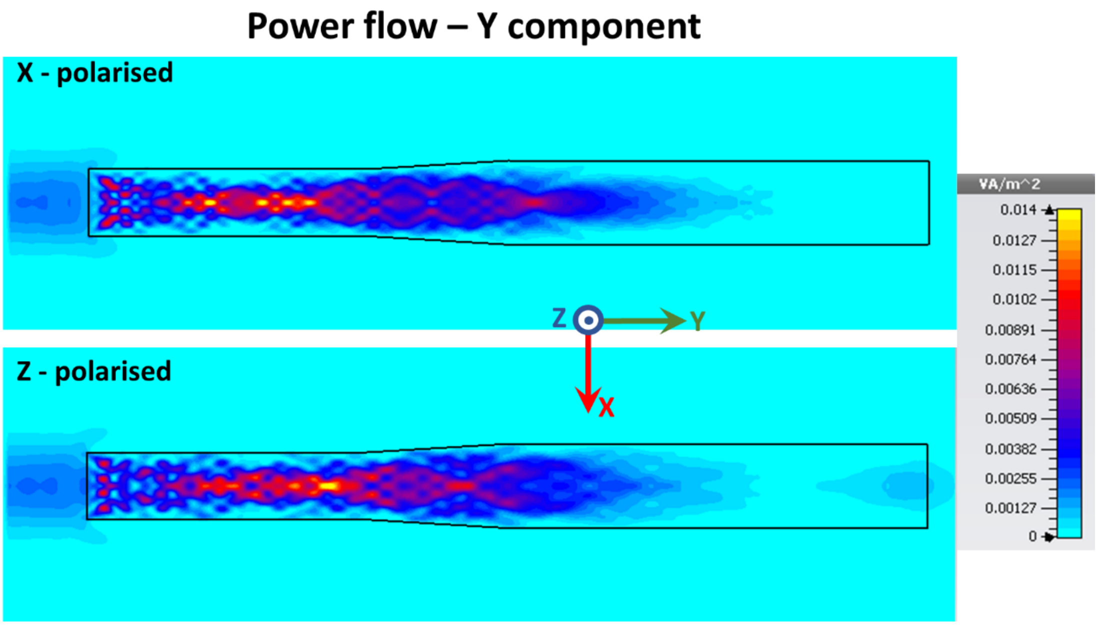

Figure 4.23: Horizontal cross section view (through the waveguide layer) of the power flow along the Y direction.

The incident optical power of the Gaussian beam in our model represents well the optical power measured with the power meter, at the output of the lensed fibre in the real laboratory experiment. As discussed previously, the power lost in the absorption layer is also provided as part of the simulation results. It is then possible to calculate the external quantum efficiency and particularly the external responsivity, which is the quantity actually measured experimentally. The external quantum efficiency and responsivity are given in Figure 4.24 for the X and Z polarisation, together with a horizontal cross section of the absorption layer showing the power absorption pattern. The Z polarised beam provides a slightly higher quantum efficiency despite mode 1 (whose main electric field component is along the X direction) having exhibited a superior performance in the single mode analysis; this may be due to the fact that the results shown in Figure 4.24 actually originate from a multimode propagation and/or to the fact that the fraction of incident power coupled into the waveguide may be higher for the Z polarised beam.

The highest experimental values of responsivity, measured on same area III-V Lab UTCs at UCL (i.e. 0.20 A/W, 0.21 A/W and 0.22 A/W) were remarkably close to numerical values of responsivity shown in Figure 4.24, which corroborates the accuracy of the numerical results. The perfect alignment between beam and waveguide, which was implemented numerically, is difficult to achieve in a measurement and therefore, the numerical values should in fact be the upper limit of the values obtainable experimentally.

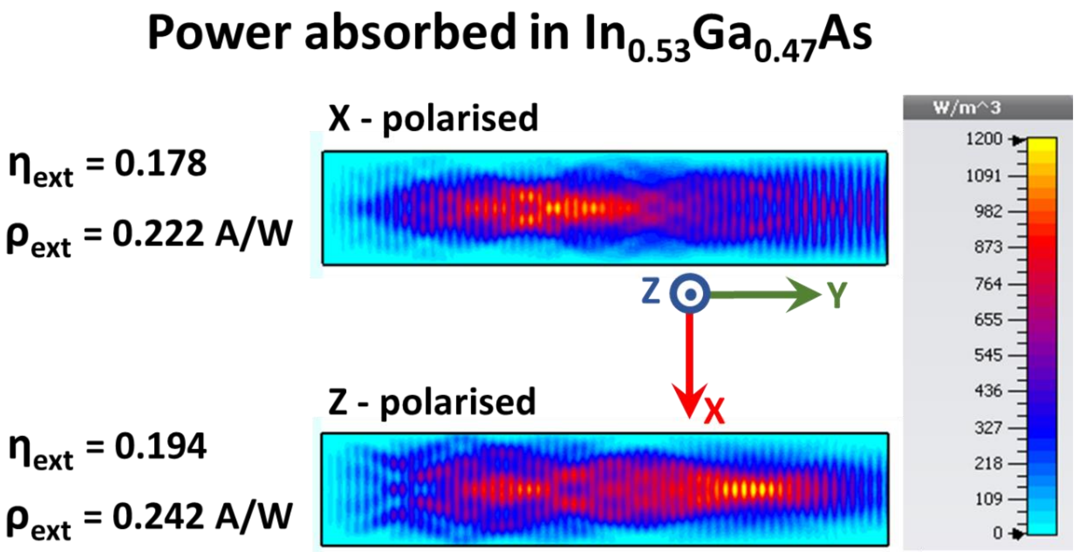

Figure 4.24: Horizontal cross section, cutting through the absorber, showing details of the power absorbed in the $In_{0.53}Ga_{0.47}As$ layer for both the X and Z polarised input Gaussian beams. The external quantum efficiency and responsivity are also given.

4.3.2.2 Optical waveguides of different length

As in the simulations using the waveguide ports, discussed in section 4.3.1, the influence of the waveguide length was investigated. The waveguide length is measured from the facet to the UTC ridge and includes the waveguide tapered section; the 15 µm long waveguide case corresponds, for instance, to the structure shown in Figure 4.14. For this analysis only the X polarised Gaussian beam was employed. Figure 4.25 shows the power flow on a horizontal cross section through the waveguide layer, for three different values of waveguide length, i.e. 15 µm, 35 µm and 50 µm. In real waveguides, due to fabrication imperfections, some power is scattered and lost as the light travels along the waveguide and therefore UTCs with longer waveguides will exhibit lower optical responsivity. The waveguides discussed in this section are ideal and have no losses, therefore longer waveguides show a self-imaging effect, as can be seen in Figure 4.25. Nevertheless, unlike the single mode propagation case, the intensity pattern in the multimode case is not constant over the propagation direction, because each mode travels with a different velocity and the way the modes combine varies along Y. For this reason the intensity pattern arriving at the UTC ridge changes with the input waveguide length and it is interesting to see how this affects the device responsivity.

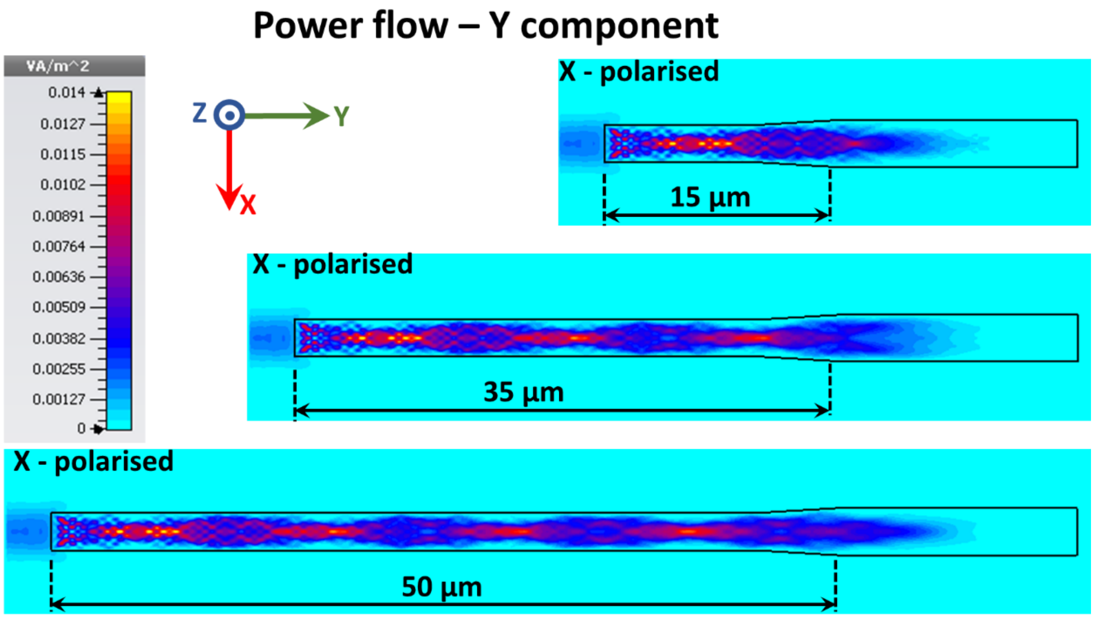

Figure 4.25: Power flow on a horizontal cross section through the waveguide layer, for three different values of waveguide length, i.e. 15 µm, 35 µm and 50 µm. The waveguide length is measured from the facet to the UTC ridge and includes the waveguide tapered section. The 15 µm long waveguide case corresponds, for instance, to the structure shown in Figure 4.14.

The external quantum efficiency, the external responsivity and the power absorption pattern in the $In_{0.53}Ga_{0.47}As$ layer, are given in Figure 4.26, for the three different waveguide lengths. The power absorption patterns in the three different cases are all different, unlike the single mode case in which the pattern was not dependent on the waveguide length. Unlike the single mode case, the external quantum efficiency varies in a perceptible way, e.g. + 5 % for the 35 µm waveguide case with respect to the 15 µm long waveguide. The fact that the quantum efficiency variation with respect to the waveguide length is not monotonic, supports the conclusion that such variations are not due to power escaping the waveguide during the propagation, but rather to the varying intensity profile.

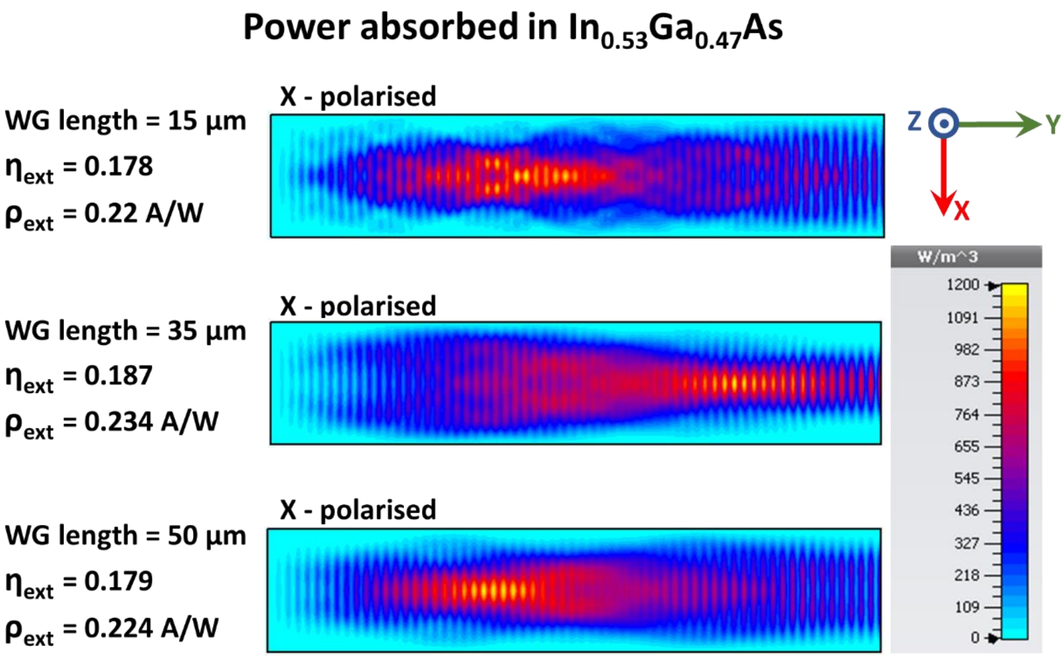

Figure 4.26: Quantum efficiency, external responsivity and power absorption pattern in the $In_{0.53}Ga_{0.47}As$ layer, for the three different waveguide lengths.

4.3.2.3 Gaussian beam misalignment

An additional essential aspect of the fibre to chip coupling, which can be investigated by means of the 3D full-wave modelling, is the effect of misalignment between Gaussian beam and optical waveguide.

Here we discuss the misalignment for the case of the X polarised Gaussian beam described in Figure 4.20 and the waveguide UTC structure in Figure 4.14.

Misalignments along all the three axes are considered and indicated as ΔX, ΔY and ΔZ. The misalignments are considered with respect to the perfect alignment, realised when the beam optical axis is perpendicular to waveguide facet, passes through the centre of the waveguide layer facet and the beam waist is located at the same Y coordinate as the waveguide facet. The beam position is fixed and the UTC waveguide structure is translated by ΔX, ΔY or ΔZ; for instance ΔX = -750 nm means that the chip is moved by 750 nm along the X axis in the negative direction. A cross section view of the modulus of the propagating electric field is shown in Figure 4.27, for the case of ΔZ = 1500 nm and ΔZ = -1500 nm. In comparison with the perfect alignment case in Figure 4.21, the field coupled into the waveguide is clearly weaker, especially for ΔZ = -1500 nm; in the 1500 nm misalignment case, a larger fraction of the incident field is coupled into the substrate as expected.

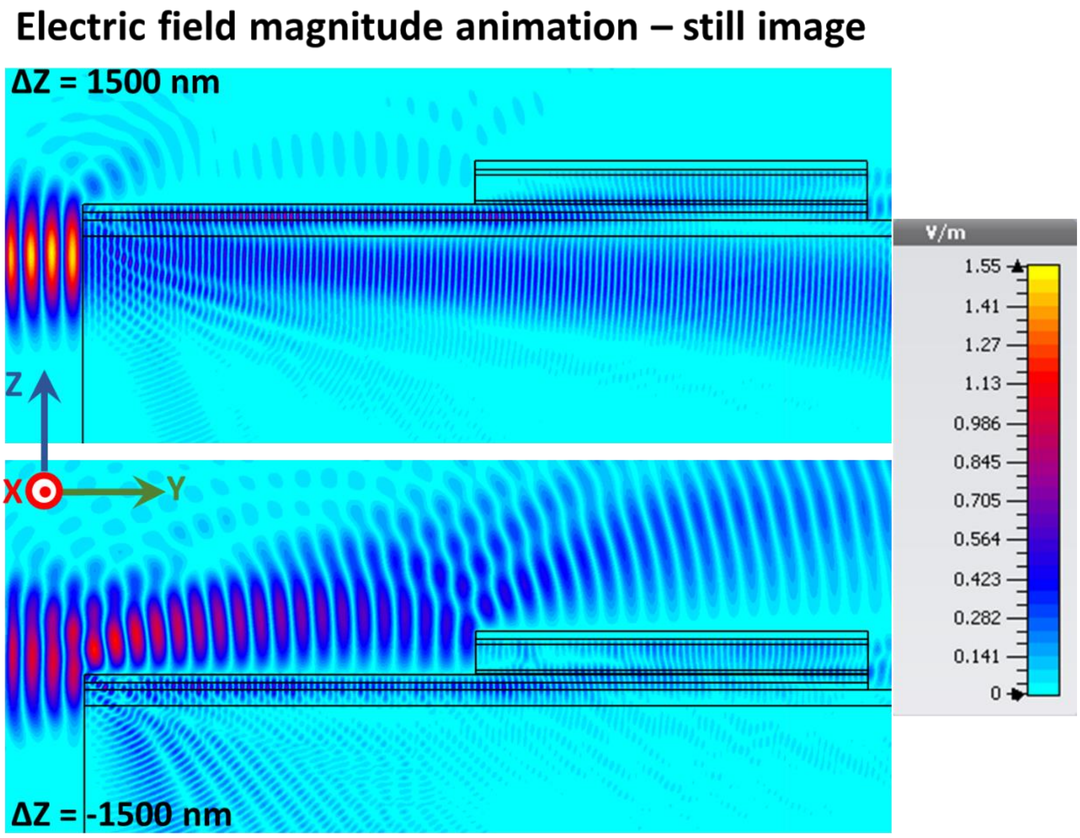

Figure 4.27: Still image of the electric field magnitude animation, for two different vertical misalignments, namely ΔZ = 1500 nm and ΔZ = -1500 nm.

The external quantum efficiency and responsivity, for a number of misalignment scenarios, are given in Table 4.4 and the responsivity versus the misalignment is plotted in Figure 4.28. A maximum misalignment of 1.5 µm was considered in all directions, which can very easily be present in a real experiment. Within this range of misalignment values, the displacement along Y does not appear to affect the responsivity significantly. The misalignment along Z seems to be the most sensitive, as expected, since the waveguide layer is 2.4 µm wide (X direction) but only 300 nm thick (Z direction); a thicker waveguide layer would be desirable, also because it would lessen the chance of exciting substrate modes while coupling the light from the lensed fibre, however it is challenging to grow InGaAsP layers thicker than 300 nm by solid source molecular beam epitaxy.

As can be noticed in Table 4.4 and in Figure 4.28, additional steps (Δz = -300 nm and Δz = -540 nm) were included for the Z misalignment between 0 nm and -750 nm, where the case Δz = -540 nm corresponds with the Gaussian beam optical axis passing through the centre of the absorber facet. In this way it is possible to check whether any local responsivity maximum is observed due to additional coupling between beam and absorber directly through free space; the results suggest that the amount of optical power coupled directly through free space is not relevant and the optical responsivity decreases monotonically as the negative displacement along Z increases.

Table 4.4: Dependence of the external quantum efficiency on the misalignment between optical waveguide and Gaussian beam (X polarisation).

Misalignment (nm)			External quantum efficiency	External responsivity (A/W)
Δx	Δy	Δz		
0	0	0	0.178	0.222
750	0	0	0.150	0.187
1500	0	0	0.090	0.112
0	0	-300	0.163	0.204
0	0	-540	0.143	0.179
0	0	-750	0.123	0.154
0	0	-1500	0.057	0.071
0	0	750	0.154	0.192
0	0	1500	0.083	0.104
0	-750	0	0.176	0.220
0	-1500	0	0.171	0.214
0	750	0	0.177	0.221
0	1500	0	0.173	0.216

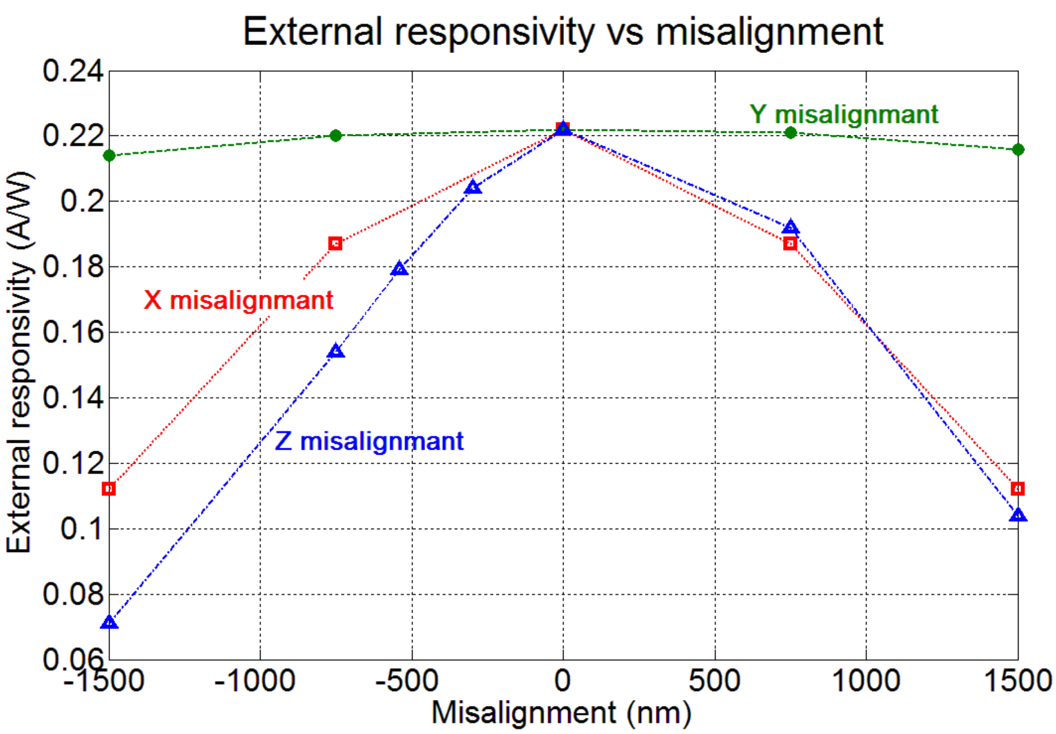

Figure 4.28: External responsivity vs misalignment.

In practical experiments, achieving a good alignment between the lensed fibre and the waveguide is difficult and requires an appropriate experimental arrangement as well as a great deal of expertise and patience. Ideally a very narrow waveguide, for single mode propagation, and a small beam spot, to increase the fraction of incident power coupled in the waveguide, are desirable; on the other hand the smaller the waveguide and the beam spot, the more challenging and sensitive the alignment. For these reasons in the future work, we will pursue further the solution employing a large diluted tapered mode converting waveguide, discussed in Chapter 8.

4.4 Conclusions

In this chapter the UTC structure has been studied for the first time by means of 3D full-wave modelling, which enabled the device parasitic inductive component to be corrected and the impedance and frequency response to be calculated up to 400 GHz. Full-wave modelling was also performed at optical frequencies to analyse the UTC optical waveguide and the power absorption in the $In_{0.53}Ga_{0.47}As$ layer. The optical full-wave modelling also allowed us to investigate the coupling between an incident Gaussian beam and the UTC optical waveguide and assess, among other things, the effect of waveguide length, beam misalignment and beam polarisation on the external responsivity as well as the type of propagation excited by the incident beam in the waveguide.

The achieved knowledge of the UTC impedance will be used, in the next chapter, to calculate and improve the efficiency of energy coupling between photodetectors and antennas. The full-wave optical analysis will serve, in the future work, to improve the UTC optical responsivity and refine the accuracy of the excitation modelling for travelling wave devices.

4.5 References

[4.1] E. D. Palik, *Handbook of optical constants of solids*, vol. 3. New York: Academic Press, 1998.

[4.2] C. Kopf, G. Kaiblinger-Grujin, H. Kosina, and S. Selberherr, “Influence of dopant species on electron mobility in InP,” *Conf. Proceedings. 1997 Int. Conf. Indium Phosphide Relat. Mater.*, pp. 280 – 283, 1997.

[4.3] T. Pearsall and J. Hirtz, “The carrier mobilities in Ga0.47In0.53As grown by organo-metalic CVD and liquid-phase epitaxy,” *J. Cryst. Growth*, vol. 54, no. 1, pp. 127–131, 1981.

[4.4] A. Rumiantsev, P. Sakalas, N. Derrier, D. Celi, and M. Schroter, “Influence of probe tip calibration on measurement accuracy of small-signal parameters of advanced BiCMOS HBTs,” *Bipolar/BiCMOS Circuits Technol. Meet. (BCTM), 2011 IEEE*, pp. 203–206, 2011.

[4.5] Anritsu, “Understanding VNA Calibration,” 2012. [Online]. Available: http://anlage.umd.edu/Anritsu_understanding-vna-calibration.pdf. [Accessed: 10-Mar-2015].

[4.6] A. J. Lord, “Comparing the accuracy and repeatability of on-wafer calibration techniques to 110GHz,” *Microw. Conf. 1999. 29th Eur.*, vol. 3, pp. 28–31, 1999.

[4.7] Cascade Microtech Application Note, “On-wafer vector network analyzer calibration and measurements,” *Publication Name PYRPROBE-0597*, 1997. [Online]. Available: http://www.cmicro.com/files/ONWAFER.pdf. [Accessed: 10-Mar-2015].

[4.8] T. Ishibashi, S. Kodama, N. Shimizu, and T. Furuta, “High-speed response of uni-traveling-carrier photodiodes,” *Japanese J. Appl. Physics, Part 1 Regul. Pap. Short Notes Rev. Pap.*, vol. 36, no. 10, pp. 6263–6268, 1997.

[4.9] T. Ishibashi, N. Shimizu, and S. Kodama, “Uni-traveling-carrier photodiodes,” *Tech. Dig. Ultrafast Electron. Optoelectron.*, vol. 13, pp. 83–87, 1997.

[4.10] T. Ishibashi, T. Furuta, H. Fushimi, and H. Ito, “Photo-response characteristics of uni-traveling-carrier photodiodes,” *Proc. SPIE 4283, Phys. Simul. Optoelectron. Devices IX*, vol. 4283, pp. 469–479, 2001.

[4.11] D. Gallagher, “Photonic CAD Matures,” *IEEE LEOS Newsl.*, vol. 22, no. 1, pp. 8–14, 2008.

[4.12] P. B. Johnson and R. W. Christy, “Optical constants of the noble metals,” *Phys. Rev. B*, vol. 6, no. 12, pp. 4370–4379, 1972.

Chapter 5 - Antenna integrated UTCs with ground planes and silicon lenses

In this chapter new THz antenna designs, obtained by means of full-wave electromagnetic modelling, are presented and shown to be suitable for integration with both standard silicon lenses and a novel solution employing a ground plane. The novel ground plane solution can offer advantages in terms of heat dissipation, as it is more suitable for the realisation of efficient heat sinks. A further consideration is that, realising accurate alignment between silicon lens and antenna chip is essential to optimise the radiation pattern and yet is a challenging task to accomplish; antennas integrated with ground planes do not require such alignment.

Substrate lenses integrated with antennas at sub-millimetre wave and THz frequencies are electrically very large and hence were typically analysed by means of geometrical optics (GO) or at best physical optics (PO), since full-wave electromagnetic modelling was computationally prohibitive and is still challenging to this day. GO can however provide sufficiently accurate results only when all geometrical features are significantly larger than the wavelength and furthermore, although PO allows diffraction and interference effects to be analysed, it is not a precise theory, unlike full-wave electromagnetism, and cannot provide information such as the effect of the lens on the antenna impedance, field polarisation or possible standing waves and resonances within the lens. In this chapter we present the full-wave modelling of a THz antenna integrated with a 4 mm diameter silicon lens; to the best of the author's knowledge, full-wave modelling of THz antennas integrated with substrate lenses have been discussed previously only in [5.1] and [5.2]. On the other hand, the effect of the misalignment between substrate lens and antenna chip will be calculated here, for the first time, by means of full-wave modelling. In Chapter 7 we will discuss a computationally even more challenging full-wave simulation of a 2 x 2 antenna array on a 5 mm diameter silicon lens; to the best of the author's knowledge a full-wave modelling of a THz antenna array on a substrate lens has never been reported in the literature.

By comparing numerical and experimental results it will be shown how the accurate antenna design, along with the results of the UTC impedance investigation, can enable the prediction of the power radiated by antenna integrated UTCs, not only in terms of trend over the frequency range but also of absolute level of emitted power.

5.1 THz planar antennas – a brief review

Millimetre-wave receivers and transmitters were traditionally waveguide-based [5.3]. The standard antennas for millimetre-wave radiometric receivers used to be machined antennas such as conical horn antennas [5.4]; corrugated horns were built up to 300 GHz and dual-mode horns up to 500 GHz [5.5], [5.6]. Another machined antenna is the travelling wave corner-cube antenna [5.7], [5.8] which is an open structure compatible with whisker contacted Schottky diodes and was used at frequencies above 600 GHz because of its relatively simple construction; the corner-cube Schottky diode receiver was for a long time the only available receiver at frequencies above 1000 GHz and increasingly optimised versions of this antenna were realised [5.9]-[5.12]. Machined antennas are, however, not ideal for sub-millimetre-wave and THz frequencies as they are difficult to realise and expensive.

Conversely, monolithic receivers, comprising a planar antenna integrated with a matching network and a mixer, soon proved to be an attractive solution for the millimetre and sub-millimetre-wave region [5.4]. Microstrip antennas are simple to fabricate, low cost, lighter and low profile and hence ideal candidates for integration with photo-mixers; besides, the planar structure of microstrip antennas enables easy fabrication of large antenna arrays. On the other hand microstrip antennas suffer from significant ohmic losses at sub-millimetre-wave and THz frequencies and exhibit reduced performance in terms of bandwidth and directivity in comparison with standard waveguide horns. Elementary antennas on planar dielectric substrates also tend to suffer from power loss to substrate modes. Elementary antennas comprise the family of electrically short dipoles, short slots, and small loops (magnetic dipoles), where the current can be accurately approximated as a constant or a linear distribution [5.4]. Detailed analyses of the surface wave losses were carried out by Pozar [5.13], Alexopoulos and co-workers [5.14]-[5.17] and Rutledge et al. [5.18]. They found that elementary antennas couple power to successively higher-order substrate modes as the thickness of the substrate increases, and in some cases, more than 90% of the radiated power is trapped in the dielectric. Therefore, the gain of elementary slot and dipole antennas on a dielectric substrate drops very quickly as the thickness of the substrate increases. The higher order modes go beyond cut off as the substrate gets thinner. To reduce the loss significantly, the substrate thickness should be much smaller than the wavelength in free space λ_0, e. g. less than 4 % for slot antennas and 1 % for dipole antennas, which basically corresponds to the standard guidelines for a patch antenna design, where the substrate thickness is usually around one hundredth of the wavelength in free space [5.19]. This translates into impractically thin substrates at sub-millimetre wave and THz frequencies.

A great deal of research was done on integrated circuit antennas since the beginning of the 1980s to tackle the main problems associated with electrically thick dielectric substrates. Several new concepts, such as the integrated horn antenna, the dielectric-filled parabola, the Fresnel plate antenna, the dual-slot antenna, and the log-periodic and spiral antennas on extended-hemispherical dielectric lenses, were developed in the millimetre and sub-millimetre wave range [5.4].

The substrate mode problem would be eliminated if the antenna was placed on a semi-infinite dielectric substrate. In this case, the dipole and slot antennas radiate most of their power into the dielectric [5.18], [5.20] with a factor of ε_r and $\varepsilon_r^{3/2}$ respectively, over the power radiated into air, where ε_r is the substrate relative electrical permittivity. For slot antennas, the power into the dielectric completely dominates the power into the air even at moderate dielectric constants. A widely accepted assumption suggests that infinite dielectric can be synthesised using a lens of the same dielectric constant, attached to the antenna substrate, hence the name substrate lens. The use of the dielectric lens, to avoid substrate modes, is based on an idea from the optical domain, and was introduced by Rutledge and Muha in 1981 [5.21]. The planar antenna presumably on a thick substrate is placed directly on the back of a dielectric lens. If the dielectric constant of the lens is close to that of the antenna substrate, then substrate modes will not exist. This approach eliminates substrate mode losses and can be designed with virtually no spherical aberration or coma [5.4]. It should be noted that these conclusions made about large substrate lens properties resulted from simplified analyses and full-wave modelling work is needed to validate them. The substrate lens can be hemispherical, hyper-hemispherical or elliptical as shown in Figure 5.1 [5.22].

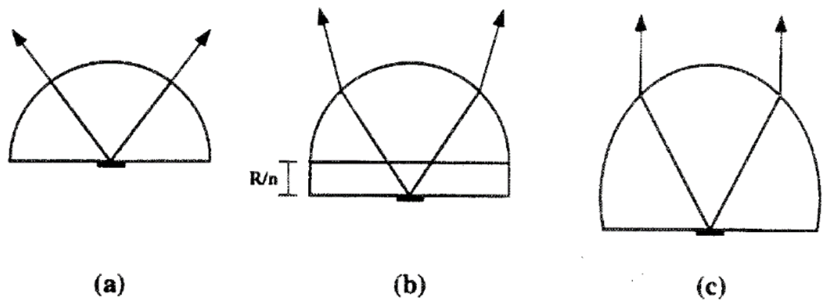

Figure 5.1: Different types of dielectric lens configurations: (a) hemispherical, (b) hyper-hemispherical , (c) elliptical [5.22]. R is the radius and n is the dielectric refractive index.

Results obtained by means of modified physical optics (PO) [5.23] and geometric optics-physical optics (GO-PO) also suggested that the directivity of an antenna integrated with substrate lenses increases with the increase in the extension length and the size of the lens and that the directivity also depends on the relative dielectric permittivity of the material used in the lens, however, with the increase in the extension length, the compactness of the antenna is reduced. The focusing properties of small substrate lenses were investigated in [5.24] and it was found that the minimum radius for acceptable operation is $0.5\,\lambda_0$ and $1\,\lambda_0$ for quartz and silicon lenses respectively, where λ_0 is the free space wavelength.

Filipovic et al. [5.25] analysed the performance of double-slot antennas on hyper-hemispherical , illustrated in Figure 5.2, and elliptical silicon lenses; the radiation pattern was evaluated employing a ray-optics/field-integration approach inside the dielectric lens, and electric and magnetic field integration on the spherical dielectric surface. The authors concluded that the elliptical lens results in diffraction-limited patterns and couples well to a plane wave with an aperture efficiency of 70%-75% and that the hyper-hemispherical lens results in a lower gain pattern. As mentioned previously, these conclusions ought to be validated with full-wave electromagnetic analysis.

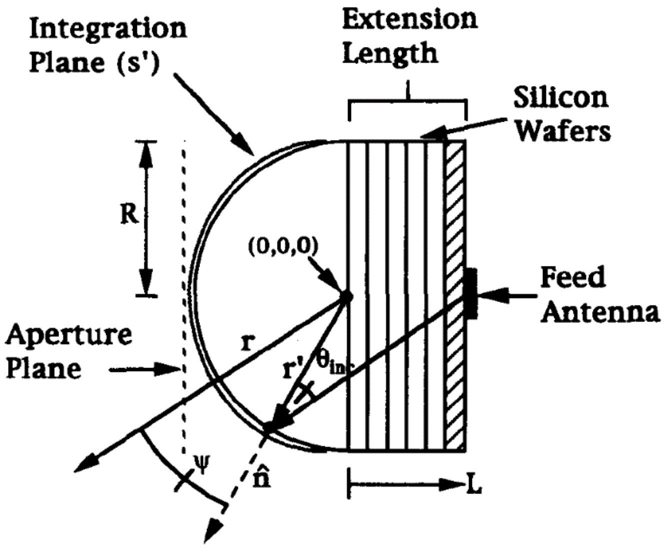

Figure 5.2: The extended hemispherical lens and the ray-tracing/field-integration [5.25].

Planar spiral and log-periodic antennas, shown in Figure 5.3 a) and Figure 5.3 b) respectively, offer an alternative to bow-tie antennas on dielectric lenses for wideband applications [5.26]-[5.28].

The lower cut-off frequency of the logarithmic spiral is approximately where the overall arm length $L \approx \left(r_{2,max} + r_{1,max}\right)/2\cos\Psi$ reaches one wavelength $\lambda_0/\sqrt{\varepsilon_{eff}}$ [5.28], [5.29] with the radii as indicated in Figure 5.3 a); the upper cut-off frequency strongly depends on the device geometry. To enhance the output power, resonantly enhanced broad band antennas can be used, such as the logarithmic-periodic antenna which consists of a bow-tie antenna with attached resonant arms; the arm is resonant at $f_n = (2c)/\left[\pi(R_n + r_n)\sqrt{\varepsilon_{eff}}\right]$, enhancing the power output at this frequency [5.30]. The operation bandwidth is determined by the smallest and the largest arm. The spiral antennas yield circularly polarised patterns with very low cross-polarization levels [5.4]. The log-periodic antennas yield linearly polarised patterns with -20 dB cross-polarized component if suspended in free space [5.31]. Also, the polarization direction of a log-periodic antenna is periodic with frequency and sweeps an angle of 45 degree.

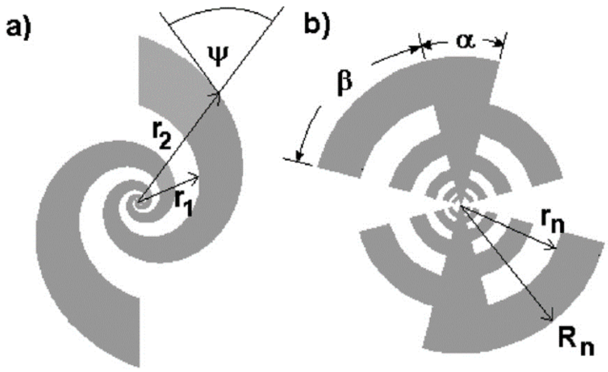

Figure 5.3: Two variations of broad band planar antennas [5.26]: (a) Logarithmic spiral antenna. (b) Logarithmic-periodic antenna.

The substrate mode problem was solved in a radically different way in [5.11], [5.32]-[5.34], by removing the substrate altogether and integrating the antenna on a thin dielectric membrane. The membrane is so thin compared with a free-space wavelength that the antenna effectively radiates in free space. The dielectric losses are eliminated and the design can be easily scaled for different wavelengths. Since the membrane is fabricated on silicon (or GaAs), the detectors and electronics can be integrated on the surrounding semiconductor substrate. The first antenna fabricated using this method was a log-periodic antenna backed by an absorbing cavity for wideband applications or a reflecting mirror for narrowband applications. This design produced very good patterns with -20 dB cross-polarization from 100 GHz to 700 GHz [5.31].

5.1.1 Some considerations about the broad band concept for antennas

The author considers that the broad band concept for antennas has often been used in an ambiguous fashion and should be better clarified. Antenna bandwidth has to be defined in terms of both gain (i.e. directivity and radiation efficiency) and efficiency of energy coupling from the source. If an antenna is efficiently coupled to its source over a wide frequency range but its directivity does not maintain a useful radiation pattern all across the same frequency range, then such an antenna should not be described as broad band. Also, regarding the coupling efficiency between antenna and source, some careful consideration should be made. Classically antennas have been fed by sources with a purely resistive (real impedance) source, in which case the antenna performs as broad band if its reactance is close to zero over a broad frequency range and its resistance is comparable to the source resistance across the same frequency range. As explained previously, when the source impedance is real, reflection-less matching with the antenna is equivalent to maximum transfer of power matching and hence, reducing the reflection coefficient automatically leads to maximising the transfer of power from the source to the antenna. For these reasons, on the assumption of driving antennas with a real impedance source, the antenna bandwidth has been traditionally defined in terms of reflection coefficient ρ, or S_{11} in dB or $VSWR$ (Voltage Standing Wave Ratio) with typical specifications requiring $\rho < 0.2 \;<=>\; S_{11,dB} < -14\,dB \;<=>\; VSWR < 1.5$. It is on the basis of such bandwidth definition that antennas like the logarithmic spiral and periodic, shown in Figure 5.3, are claimed to be broad band; however, this cannot be justified, regardless of what source is used to drive the antennas. The fact that antennas like the logarithmic spiral and periodic are broad band as defined with respect to a real impedance source, does not ensure that they will still perform as broad band antennas when driven by a source with unknown impedance, as has been the case for antennas integrated with UTCs. Based on the results discussed in Chapter 3 and 4, we know that the UTC reactance becomes increasingly capacitive with decreasing frequency, below about 400 GHz, and is expected to become noticeably inductive above 400 GHz. This means that an antenna with zero reactance would be efficiently coupled with the UTC only around 400 GHz, assuming the impedance real parts are comparable. An antenna perfectly coupled with the UTC should instead ideally have a reactance equal to the additive inverse of the UTC reactance, i.e. strongly inductive at lower frequencies and then switching to capacitive above about 400 GHz. In such a scenario the UTC would transfer the highest possible power to the antenna at all frequencies, again assuming the impedance real parts are comparable.

As a quantitative example let us consider the frequency 100 GHz, where the impedance of the 3 x 15 μm^2 UTC at -2 V bias is $Z_{UTC}(100\;GHz) = (18 - j57)\Omega$; at this frequency the power coupled to an antenna with a purely resistive impedance of $18\;\Omega$ would be smaller, by a factor of 5.5 dB, than the power coupled to an antenna having impedance $Z_{ANT}(100GHz) = (18 + j57)\Omega$ also containing an inductive reactance.

Even around 400 GHz, where the UTC reactance crosses zero, the impedance matching between the logarithmic spiral/periodic antennas and the UTCs will not be good, due to a noticeable difference in the impedance real part. The UTC impedance real part becomes very small at such high frequencies, i.e. about 15 Ω for the 3 x 15 μm^2 III-V Lab UTCs and 12.7 Ω for the 4 x 15 μm^2 III-V Lab UTCs and is expected to be less than 10 Ω for UTCs without the additional InP ridge layer. Conversely, logarithmic spiral and periodic antennas have a large input resistance, especially when considered in free space. Babinet's principle for antennas [5.29], [5.19] states that the impedance of a planar antenna Z_{PA} and the impedance of its dual surface antenna $Z_{PA,dual}$ are related to the impedance of free space $Z_0 = 377\,\Omega$ as $Z_{PA}Z_{PA,dual} = (Z_0/2)^2$. The Log-Periodic Spiral Antenna and its dual surface are identical and hence have the same impedance, therefore the theoretical impedance for a logarithmic spiral antenna in free space is about 188 Ω. Considering an effective relative electrical permittivity $\varepsilon_r = (12.5 + 1)/2 = 6.75$ when the spiral antenna is placed on a semi-infinite InP substrate, the theoretical resistance scales down by a factor $\sqrt{\varepsilon_r}$ with respect to the free space case an hence equals 73 Ω, i.e. still several times greater than the UTC impedance real part at high frequency. For efficient energy coupling with the UTC at high frequencies, antennas with a small impedance real part should be preferred; in order to achieve high radiation efficiency, such impedance real part should be attributable to radiation resistance rather than ohmic losses.

5.2 Ground plane

5.2.1 Case study - modelling and measurement of the radiated power from a bow-tie antenna integrated UTC with a ground plane

III-V Lab have provided a 3 x 15 μm^2 area UTC integrated with a bow-tie antenna with a gold screen deposited underneath the 150 μm thick InP substrate, shown in Figure 5.4 a) prior to packaging. The gold screen was not intended to operate as a ground plane for the antenna emission, therefore the whole antenna chip did not represent an optimum design for radiation with a ground plane. Nevertheless, regardless of the emission performance, the antenna was employed to verify whether the knowledge of the UTC impedance, in conjunction with the antenna full-wave modelling, could provide a good prediction of the radiated power, not only in terms of power trend over the frequency range but also in terms of absolute level of emitted power.

The antenna chip was hence modelled in CST, as shown in Figure 5.4 b), and analysed between 50 GHz and 300 GHz. Exact dimensions and geometrical details of the antenna chip were not available, therefore the values shown in Figure 5.4 are approximate. The material properties used for gold and indium phosphide were the same as in the UTC impedance modelling.

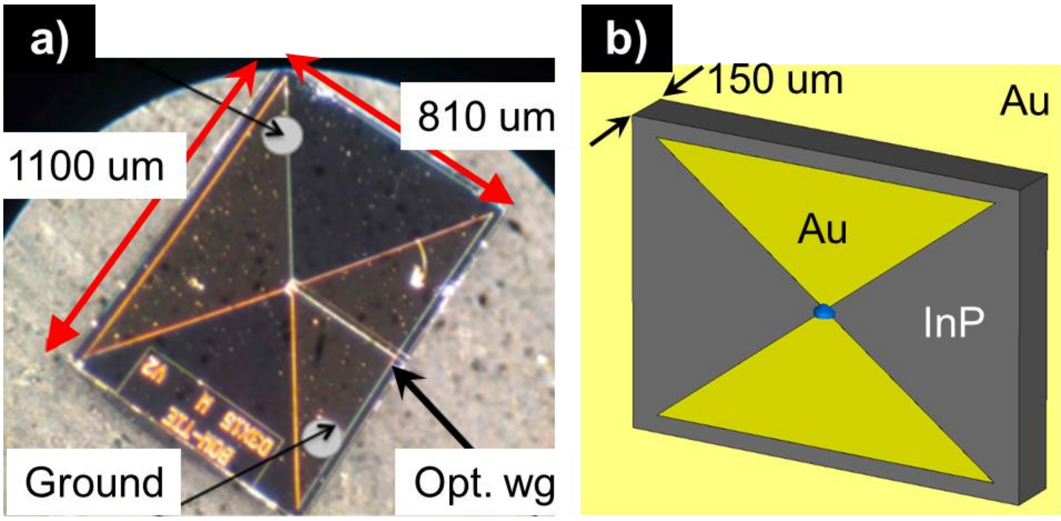

Figure 5.4: a) Bow-tie antenna integrated UTC with a ground plane, provided by III-V Lab. The photodetector area is 3 x 15 µm^2 and the antenna-chip approximate geometrical details are shown in the picture; b) CST model of the bow-tie antenna with a gold ground plane.

The total power emitted by an antenna depends on the efficiency of energy coupling with the driving source and on the radiation efficiency. The former defines the fraction of power made available by the source that is accepted by the antenna, while the latter determines the fraction of power accepted by the antenna that is coupled into free space; the antenna directivity, on the other hand, describes the angular distribution of the radiated power.

The bow-tie Antenna 3D radiation pattern (directivity in dBi) calculated in CST, is shown in Figure 5.5 for four frequencies of interest, i.e. 66 GHz, 111 GHz, 153 GHz and 200 GHz. The antenna radiation efficiency from 50 GHz to 300 GHz is given in Figure 5.6. The radiation patterns show how part of the emitted power, especially at 111 GHz, is radiated almost along the XY plane, or at least at very shallow angles, and would not be captured by a power meter positioned in front of the antenna in a real measurement. For this reason the power radiated within different solid angles along the Z direction has also been calculated, to enable a more realistic comparison with the experimental results. It is noted how a planar antenna on a thick substrate with a ground plane, can still exhibit a good radiation pattern if metal patch shape and chip size are properly designed for the frequency range of interest; as the concerned bow-tie antenna was not optimised to emit with a ground plane, the good radiation pattern shown at 200 GHz in particular, is the result of a fortunate combination of such factors.

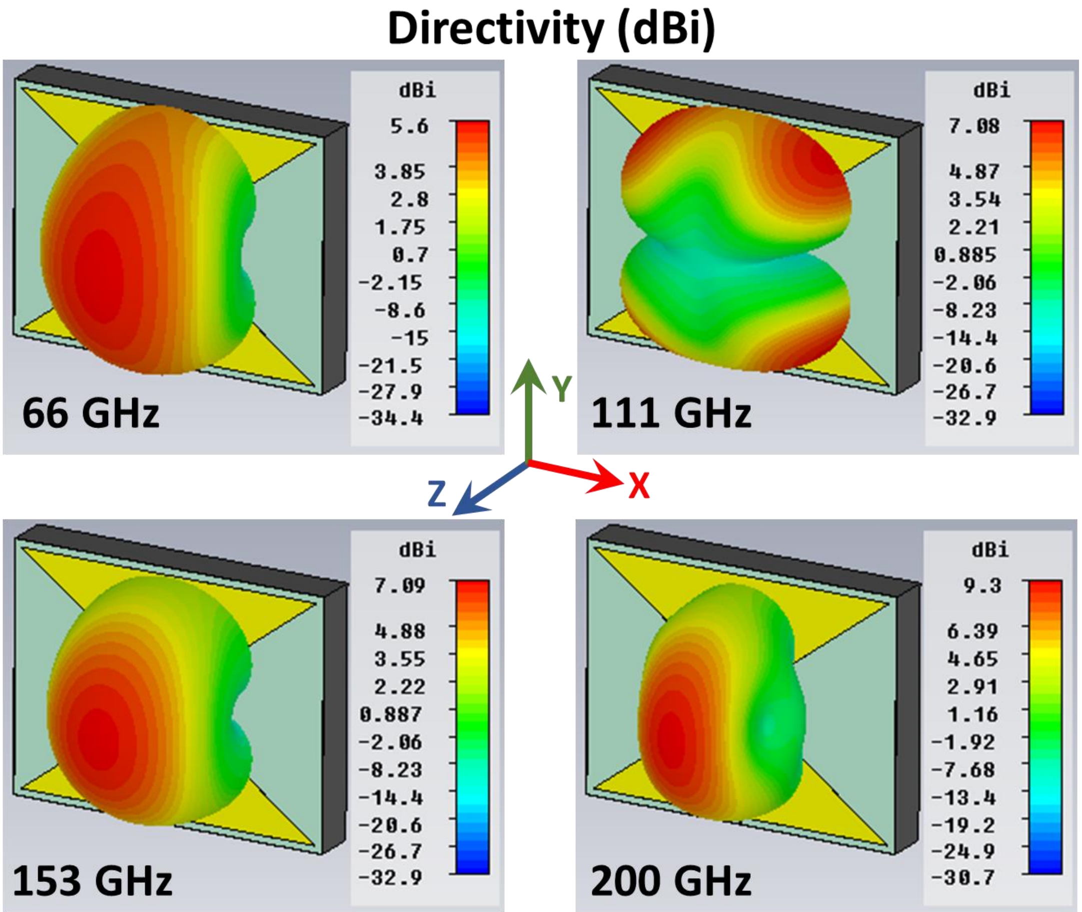

Figure 5.5: Bow-tie antenna 3D polar radiation pattern calculated in CST.

The dips in the radiation efficiency shown in Figure 5.6 are due to losses in the antenna and ground plane metal (gold).

To perform a thorough calculation of the absolute power emitted by the antenna, the coupling efficiency between the antenna and the UTC needs to be taken into account; this depends on the impedance of both antenna and photodetector and can now be evaluated using the results of the experimental and numerical analysis of UTC impedance, discussed in Chapter 3 and Chapter 4. The real and imaginary part of the bow-tie antenna impedance are plotted in Figure 5.7 and compared with those measured and calculated for the 3 x 15 μm^2 area UTC at -2 V bias.

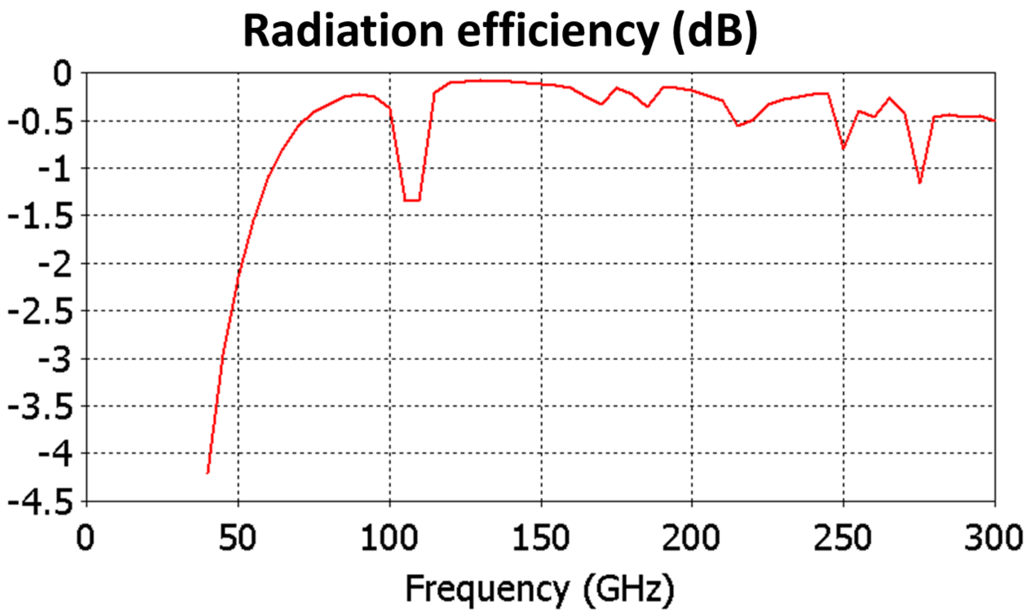

Figure 5.6: Bow-tie antenna radiation efficiency in dB calculated in CST.

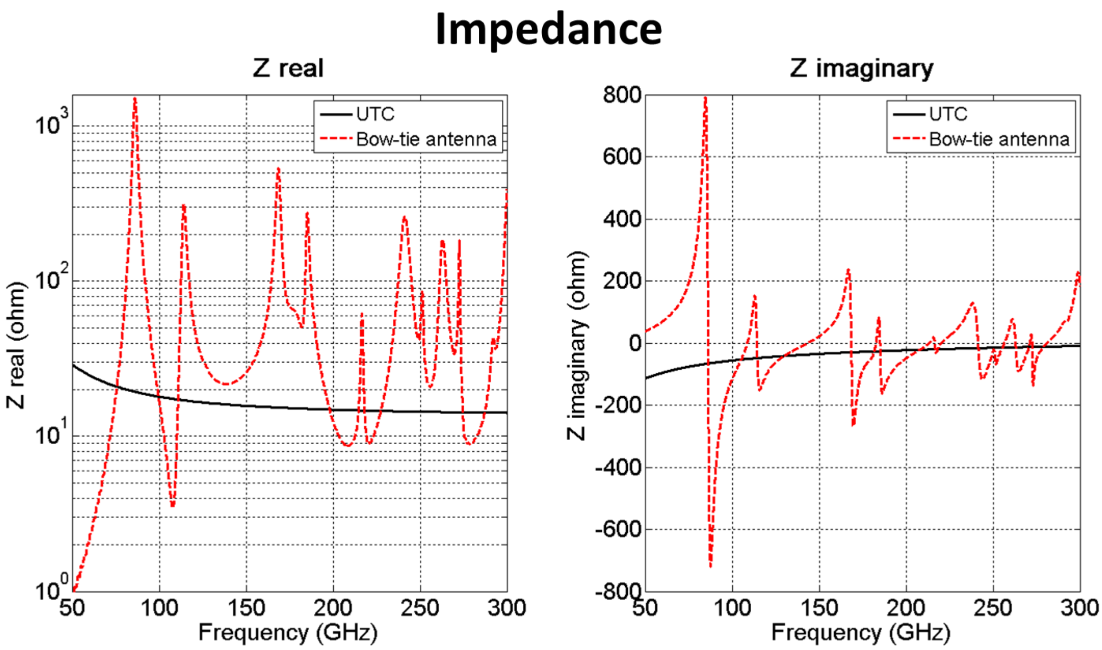

Figure 5.7: Comparison between real and imaginary part of the bow-tie antenna impedance and those measured and calculated for the 3 x 15 μm² area UTC at -2 V bias.

As discussed in Chapter 3 and Chapter 4, the maximum transfer of power between the source (UTC) and the antenna occurs at the frequencies for which the antenna impedance is equal to the UTC impedance complex conjugate. Therefore local maxima of radiated power should be expected at the frequencies where the UTC and antenna reactance have the same absolute value and opposite sign; the magnitude of such local maxima is determined by how close the impedance real parts are and by other factors like radiation efficiency, solid angle considered for the radiated power calculation and transit-time limited response of the UTC.

The power emitted by the antenna integrated UTC in Figure 5.4 a), after packaging, was measured with a basic heterodyne experimental arrangement using two free running lasers, as shown in Figure 5.8. The first polarisation controller is needed to align the field polarisation of the two tuneable lasers. The second polarisation controller, located after the erbium-doped fibre amplifier (EDFA), is employed to optimise the coupling efficiency between the lensed fibre and the optical waveguide on the UTC chip.

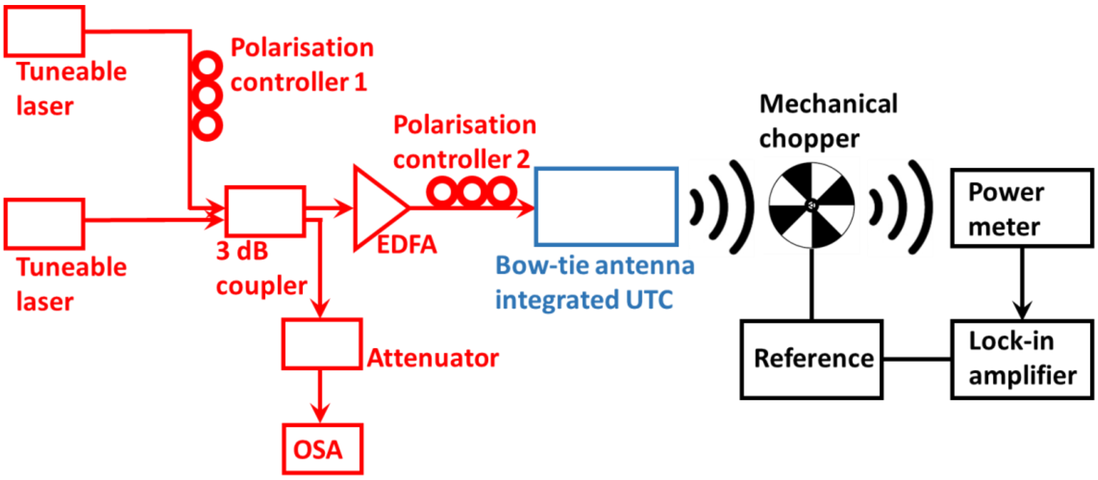

Figure 5.8: Experimental arrangement used to measure the power emitted by the antenna integrated UTC after packaging. The first polarisation controller is needed to align the field polarisation of the two tuneable lasers. The second polarisation controller, located after the erbium-doped fibre amplifier (EDFA), is employed to optimise the coupling efficiency between the lensed fibre and the optical waveguide on the UTC chip.

The optical power coupled into the UTC was measured with a power meter at the output of the fibre connecting the second polarisation controller with the UTC, and was 50 mW. The UTC was biased at -2 V and exhibited a DC photocurrent of 7.2 mA, corresponding to a 0.144 A/W responsivity. A Thomas Keating (TK) power meter system [5.35] was used to measure the radiated power. The TK measures power in a beam directed into the head window, which comprises a closed air-filled cell formed by two closely spaced parallel windows with a thin metal film in the gap between them. The beam must be 100% amplitude-modulated either at its source or by a chopper placed in the path of the beam. The modulation frequency is to be in the range 10 Hz to 50 Hz, and the lowest noise equivalent power (NEP) is found in the middle of this range. The absorption of the power in the film produces modulated variations in the temperature of the film and the layers of air in contact with it. In turn this produces a modulation of the pressure in the cell, which is detected by a pressure-transducer and measured by the lock-in amplifier. The modulated pressure change is closely proportional to the total absorbed power. As can be seen in Figure 5.8, a mechanical chopper was used in our experimental arrangement to modulate the beam, with a modulation frequency of 20 Hz.

The power radiated at each frequency by an antenna is proportional to the squared amplitude of the current flowing into the antenna at that frequency; on the other hand the current flowing into the antenna depends on the match/mismatch between antenna impedance and source impedance. An accurate calculation of the current driven by the UTC into the bow-tie antenna, over the frequency range, can be carried out using the optimised version of Circuit 3 discussed in Chapter 3, including the corrected value of parasitic inductance L_P (6.5 pH) found in Chapter 4, by replacing R_L with the antenna impedance plotted in Figure 5.7. The measured 7.2 mA DC photocurrent can be used as reference level for the current source in Circuit 3 and the transit-time limited response 2 in Figure 3.20 can be considered to take the transit-time effect into account. The power radiated by the bow-tie antenna driven by the UTC was hence calculated in CST for different conical solid angles and is plotted in Figure 5.9 along with the experimental data; the conical angles are defined with respect to the Z axis and a 90 degree conical solid angle is, for instance, identified by a 45 degree angle with respect to the Z axis. Unlike the power emitted within solid angles, the power radiated in the whole space does not depend on the radiation pattern, but only on the radiation efficiency, the UTC transit-time response and the impedance match/mismatch between UTC and antenna. It is interesting to note how all the maxima of the calculated emitted power in Figure 5.9 occur at frequencies where the imaginary parts of UTC and antenna impedance have about same absolute value and opposite sign and the real parts are comparable (i.e. 66 GHz, 111 GHz, 153 GHz, 183 GHz, 215 GHz, 225 GHz, etc.). On the other hand there are frequencies where, despite the impedance imaginary parts having similar absolute value and opposite sign, there is no peak of radiated power because the impedance real parts are greatly different; this situation is verified at 86 GHz, where the impedance real part is 20 Ω for the UTC and over 1.5 kΩ for the antenna, and at 241 GHz where the impedance real part is 15 Ω for the UTC and over 262 Ω for the antenna.

The importance of the coupling efficiency between source and antenna can be seen around 200 GHz where the power emitted within an increasingly narrow solid angle does not show any local maximum although, as shown in Figure 5.5, the directivity pattern is favourable; the reason is that the UTC and antenna reactance are both capacitive at 200 GHz, therefore little power is accepted by the antenna.

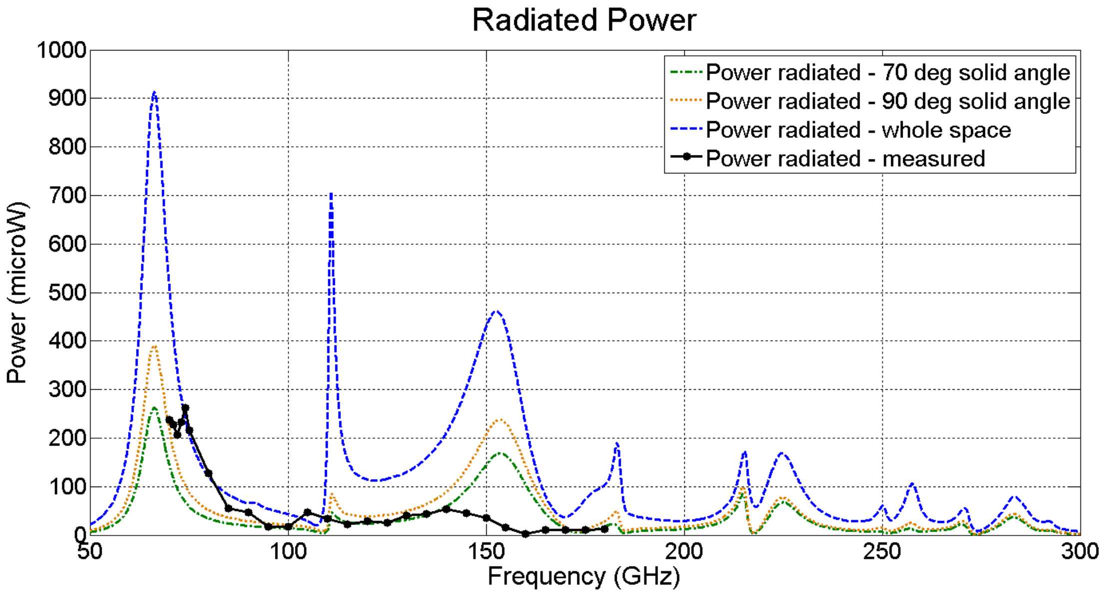

Figure 5.9: Comparison between measured radiated power and radiated power calculated within different conical solid angles.

It is also important to remark how the value of the sharp maximum of radiated power calculated at 111 GHz, is dramatically reduced as an increasingly narrow solid angle is considered; the reason is that at this frequency the power is mostly radiated at very shallow angles with respect to the antenna plane, as can be seen in Figure 5.5.

It should be noted that the real bow-tie antenna also contains thin layers of platinum and titanium, deposited prior to the gold deposition, with the titanium layer likely contributing to the power dissipation and hence radiation efficiency reduction. Like the exact antenna chip geometrical details, the thickness of the platinum and titanium layers were not available. The results of some test simulations performed in CST suggested that the losses in the titanium layer depend, in a non-negligible way, on the layer thickness; the titanium and platinum layers were hence not included in the model of the bow-tie antenna and the other antennas which will be discussed in this chapter.

The conical solid angles we have defined in the CST model equal, in steradian, $2\pi(1-\cos\theta)$, where θ is the angle identified with respect to the Z axis (e.g. 45 degree for the 90 degree conical solid angle); the 90 degree conical solid angle is equal to 1.8 steradian and the 70 degree conical solid angle is equal to 1.1 steradian. The distance between the Thomas Keating 40 mm window aperture [5.35] and the emitter in the experimental arrangement was about 33 mm, which corresponds to a solid angle almost equal to the 1.1 steradian found for the 70 degree conical solid angle. It follows that the radiated power calculated within the 70 degree conical solid angle in the CST model represents well the power measured experimentally. A direct comparison between the radiated power calculated in CST within the 70 degree solid angle and the measured radiated power, is shown in Figure 5.10 with a reduced range on the ordinate axis which enables a clearer assessment.

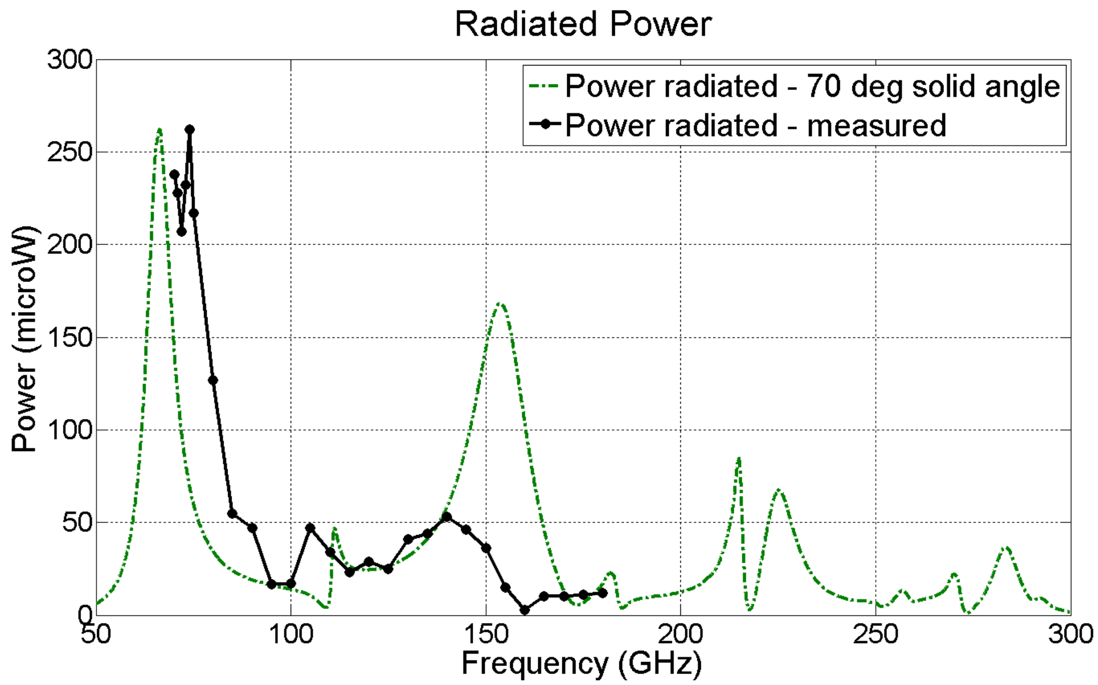

Figure 5.10: Comparison between measured radiated power and radiated power calculated within a 70 degree conical solid angle.

The trends of measured and calculated power over the frequency range are clearly correlated. The three peaks of measured power at 74 GHz, 105 GHz and 140 GHz seem to correspond to the peaks of calculated power at 66.5 GHz, 111 GHz and 153.5 GHz. The zigzag feature visible around the measured peak at 74 GHz is probably just an artefact of the measurements. The measured peak at 74 GHz and the calculated peak at 66.5 GHz have same magnitude (262 μW) and are shifted by 7.5 GHz. The measured peak at 105 GHz and the calculated peak at 111 GHz have also the same magnitude (47 μW) and are shifted by 6 GHz. The measured peak at 140 GHz and the calculated peak at 153.5 GHz show a relevant disagreement as they are shifted by 13.5 GHz and differ in magnitude by 5 dB (53 μW vs 168 μW).

The 7.5 GHz and 6 GHz frequency shifts between experimental and numerical results, regarding the first two pairs of peaks (measured at 74 GHz and 105 GHz and calculated at 66.5 GHz and 111 GHz) occur in opposite directions which could be explained by some dispersion in the semiconductor material or, most probably, by a calibration error of the frequency scale in the measurement. Other possible factors are the lack of exact information available about the antenna chip, such as exact antenna size, chip size and thickness, thickness of Ti and Pt layers, or thickness of the BCB layer deposited on top of the chip.

Based on the estimated InP substrate thickness (150 µm) and the known InP relative electrical permittivity (12.5), at 141 GHz the wave reflected from the ground plane will recombine in phase with the wave generated at the antenna source. This mechanism is likely to play an important role in the generation of the measured and calculated power peaks at 140 GHz and 153.5 GHz which will be sensitive to the exact substrate thickness, both in terms of magnitude and frequency location. An additional factor that could contribute to the smaller value of measured power (-5 dB) is that the ohmic losses in the titanium have not been included in the calculation and may present a peak at this frequency.

Following these considerations and bearing in mind the level of difficulty involved in measuring and predicting the absolute power radiated by a system involving so many variables in the equation, the agreement between experimental and numerical results shown in Figure 5.10 can be deemed satisfactory. More so if we consider that an accurate analysis of the power emitted from an antenna integrated photodetector has not been reported before, including 3D full-wave modelling of photodetector and antenna and taking into account the effect of the actual match/mismatch between photodetector and antenna.

In Figure 5.11 we re-plot the power radiated by the bow-tie antenna calculated when the UTC impedance is taken into account using the classical simplified circuit discussed in Chapter 3 and shown in Figure 3.7 b); in this case the reactive components related to the photodiode ridge are attributed to a single capacitance of 17 fF, which is the theoretical junction capacitance based on the device geometry and material properties. Figure 5.12 shows the same comparison as in Figure 5.11 with a reduced range on the ordinate axis, which enables a clearer assessment. As can be seen in Figure 5.11 and Figure 5.12, the disagreement between experimental and numerical results calculated within the 70 degree solid angle is in this case very significant; the three peaks of calculated radiated power are in this case located at 69 GHz, 111.5 GHz and 156.5 GHz and their magnitudes are 1578 µW, 135 µW and 341 µW which correspond to discrepancies with the measured peaks equal to 7.8 dB, 4.6 dB and 8 dB. A design based on the classical junction-capacitance/series-resistance assumption would have led to a substantial overestimation of the radiated power obtainable.

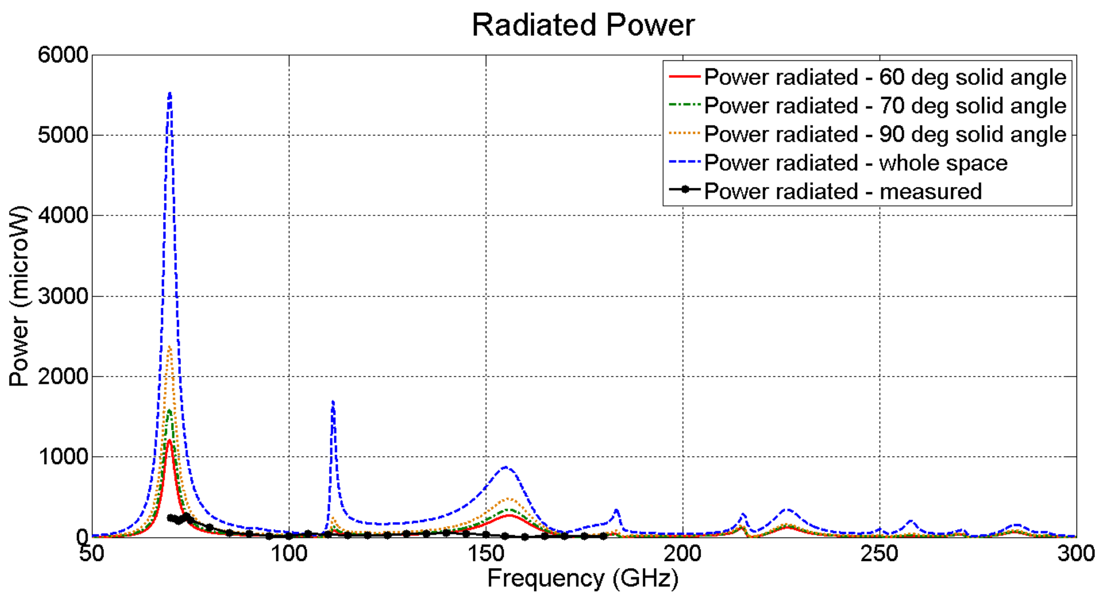

Figure 5.11: Comparison between measured radiated power and radiated power calculated when the UTC impedance is taken into account using the classical simplified circuit discussed in Chapter 3 and shown in Figure 3.7 b); in this case the reactive components related to the photodiode ridge are attributed to a single capacitance of 17 fF, which is the theoretical junction capacitance based on the device geometry and material properties.

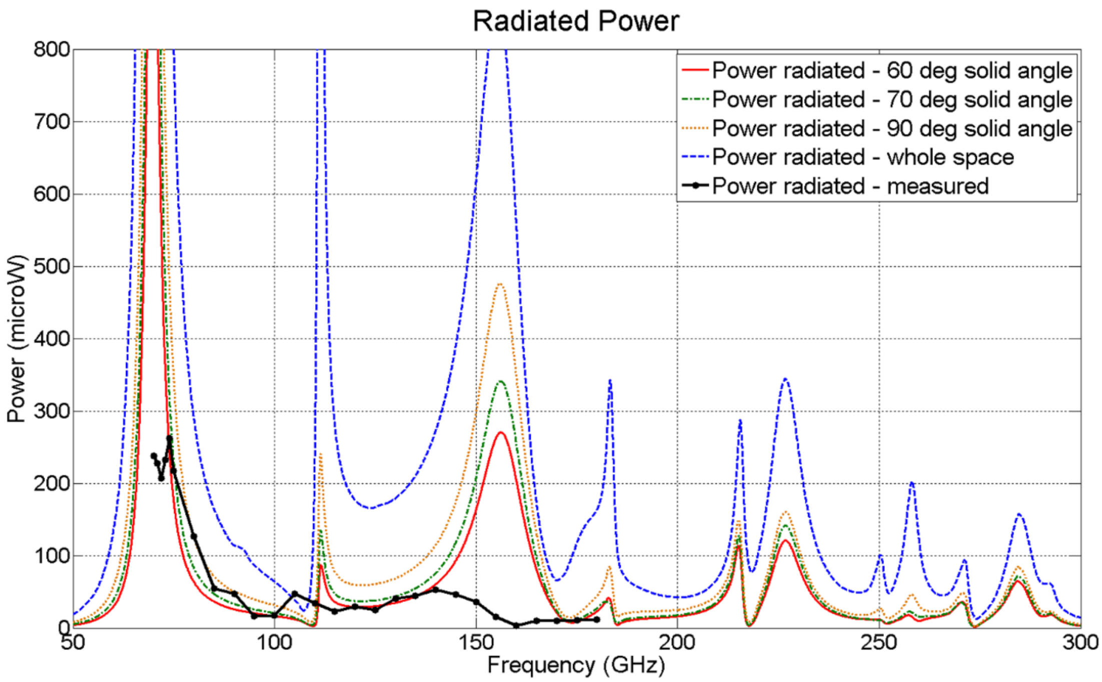

Figure 5.12: Same plot as in Figure 5.11, shown with a reduced range on the ordinate axis to enable a clearer assessment.

5.2.2 Modified bow-tie antenna designs with high radiation efficiency and directivity

In this section the design of planar THz antennas on electrically thick substrates with a ground plane is presented. The large thickness of the substrate, in terms of wavelength, complicates the optimisation of the radiation pattern over a wide frequency range. Substrate modes tend to be excited, as extensively shown in the literature by detailed analyses carried out by Pozar [5.13], Alexopoulos and co-workers [5.14]-[5.17] and Rutledge et al. [5.18]., therefore the radiation efficiency can be reduced if a significant amount of power remains trapped within the substrate and is eventually lost as ohmic or dielectric losses.

As shown in [5.19] for the case of a half-lambda dipole facing a parallel metallic plane, the optimum distance between antenna and ground plane should be less than a one quarter wavelength in order to obtain the maximum of directivity aligned with the direction perpendicular to the plane. The behaviour of a planar dipole on a semiconductor substrate with a ground plane is not as straightforward. Consider the case of a planar dipole of length $L = 165\ \mu m$, on a semi-infinite InP (relative electrical permittivity 12.5) substrate; such a dipole resonates at a frequency of about 320 GHz (e.g. the reactance is equal to zero), at which the wavelength inside InP is $\lambda_{InP} = 265\ \mu m$ and in the free space $\lambda_0 = 937\ \mu m$. If an infinite metallic plane parallel to the InP/air interface is introduced on the semi-infinite InP side it is found that the distance between this ground plane and the antenna (i.e. the substrate thickness t_s) influences the radiation pattern in a way which is substantially different from the case of a half-lambda dipole facing a parallel metallic plane in free space. Figure 5.13 illustrates the radiation pattern of the planar dipole on InP substrate with a ground plane at 320 GHz, for a sequence of 6 different values of substrate thickness t_s; the maximum value of thickness below which the main lobe is always orthogonal to the ground plane is much smaller than $2L/4$ and even than $\lambda_{InP}/4$ and seems rather to agree with the standard guidelines for a patch antenna design, where the substrate thickness is usually around $\lambda_0/100$ (one hundredth of the wavelength in free space) [5.19]. When the substrate thickness is equal to 8 µm, e. g. just below $\lambda_0/100$, the main lobe is still perpendicular to the ground plane, as shown in Figure 1 (a); when $t_s = 15\ \mu m$, e. g. just above $\lambda_0/100$ but still smaller than $\lambda_{InP}/4$, the main lobe breaks up and the maximum of directivity is into the substrate, as illustrated in Figure 5.13 (b); for $t_s = 40\ \mu m$ (e. g. still smaller than $\lambda_{InP}/4$), as in Figure 5.13 (c), there is basically no radiation along the direction orthogonal to the ground plane and the main lobe is in the substrate; for greater thickness values, such as 75 µm, 100 µm and 165 µm as shown in Figure 5.13 (d), (e) and (f) respectively, the beam is unstable and the radiation pattern deteriorates significantly. These results seem to suggest that meeting the condition $t_s \approx \lambda_0/100$ is the only way to realise planar antennas with ground planes endowed with good radiation properties; on the other hand it is clear that achieving such a condition at THz frequencies is not possible in practice. Indium Phosphide is a fragile material and even thickness values around 100 µm are not easy to obtain by substrate thinning. At 320 GHz, as discussed above, $\lambda_0/100$ is approximately 9 µm and this value would become gradually smaller as the frequency goes up, therefore it is reasonable to conclude that substrate thinning is not a viable solution.

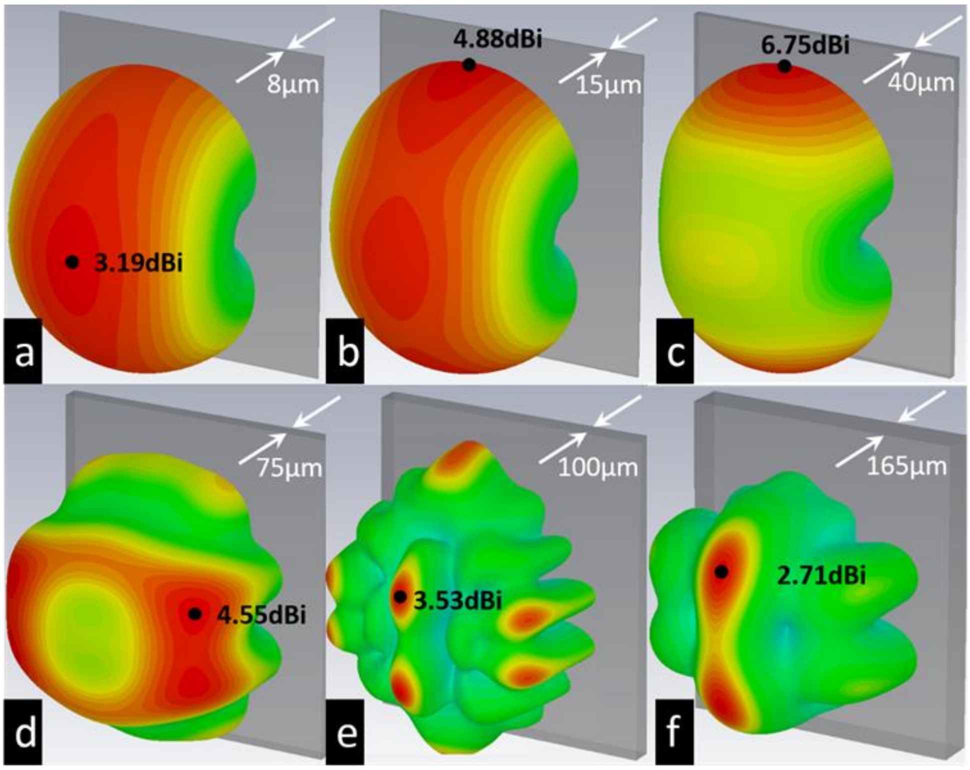

Figure 5.13: Radiation pattern of a 165 µm long planar dipole on InP substrate with a ground plane at 320GHz, for a sequence of 6 different values of substrate thickness.

An exhaustive numerical analysis, guided by basic theoretical considerations, has shown, that the realisation of planar THz antennas on electrically thick substrates with ground planes, exhibiting good radiation properties, is indeed possible by simultaneously optimising the metallic pattern and the substrate horizontal dimensions; the latter become an important parameter to be optimised, since the reflections from the sides of the InP substrate influence the antenna performance, unlike, allegedly, antenna chips on substrate lenses.

Figure 5.14 shows design geometrical details of two planar antennas with ground planes, integrated with 3 x 15 μm^2 area UTCs, optimised to radiate within a frequency range centred at 345 GHz, where a minimum in the water absorption is present. The ground plane is not displayed explicitly, however the boundary condition underneath the chip consists of an infinite metallic plane and the Z axis identifies the intended radiation direction.

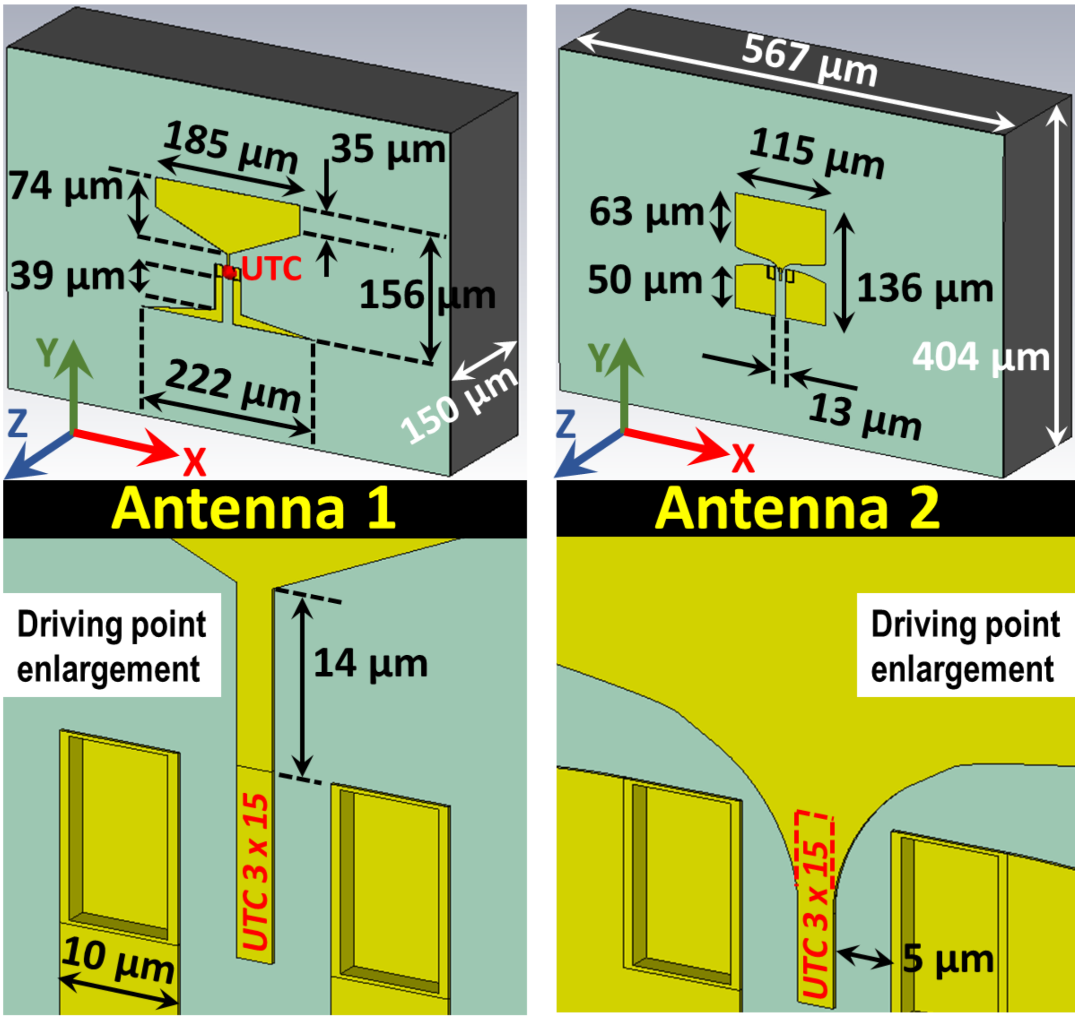

Figure 5.14: Geometrical details of two planar antennas with ground planes, integrated with 3 x 15 µm^2 area UTCs, optimised to radiate within a frequency range centred at 345 GHz.

The chip material properties are the same as shown in Figure 4.2 for the chip model employed to analyse the UTC impedance; the geometry underneath antenna metal and polymer layer have also been kept the same as shown in Figure 4.2, in order to take the UTC ridge, mesa and waveguide shapes into account, although they have a marginal effect on the antenna radiation properties. The thin layers of titanium and platinum, which were included in the model shown in Figure 4.2, have been ignored in the antenna models in Figure 5.14 where only a 300 nm layer of gold makes up the antennas. Since the two antennas are not symmetrical along the Y axis direction, the UTC position in the optimised designs shown in Figure 5.14, is not equidistant from the chip upper and lower edges, being 215 µm from the upper edge and 189 µm from the lower edge.

Antenna 1 and Antenna 2 exhibit almost identical radiation properties (i.e. radiation efficiency and directivity pattern), particularly around 345 GHz, but they have different input impedance. Antenna 1 was the first to be designed and was optimised in terms of radiation properties only, since the UTC impedance study had not yet been completed and hence a target value for the antenna impedance optimisation was not available. Once the UTC impedance study was complete and its impedance known, an additional antenna modelling study was undertaken, aiming to modify Antenna 1's impedance and achieve a better coupling efficiency with the UTC around 345 GHz, while maintaining the good radiation efficiency and directivity already attained with Antenna 1; Antenna 2 is the result of such additional modelling work. Figure 5.15 shows the radiation efficiency and the directivity along the Z axis direction, of Antenna 1 and Antenna 2, from 150 GHz to 400 GHz; as anticipated, the radiation performance of the two antennas is very similar and virtually identical around 345 GHz. The directivity along the Z axis of both antennas presents a very deep dip at about 275 GHz, where the wavelength in InP is 308.6 µm; considering that the InP substrate in the model is 150 µm thick, the displayed dips are likely associated to a destructive interference between the waves reflected from the ground plane and the waves emitted from the antenna directly in the air. Examples of the 3D-radiation pattern, at six frequencies near 345 GHz, are shown in Figure 5.16 for Antenna 1; as described earlier Antenna 2 has identical radiation properties at these frequencies.

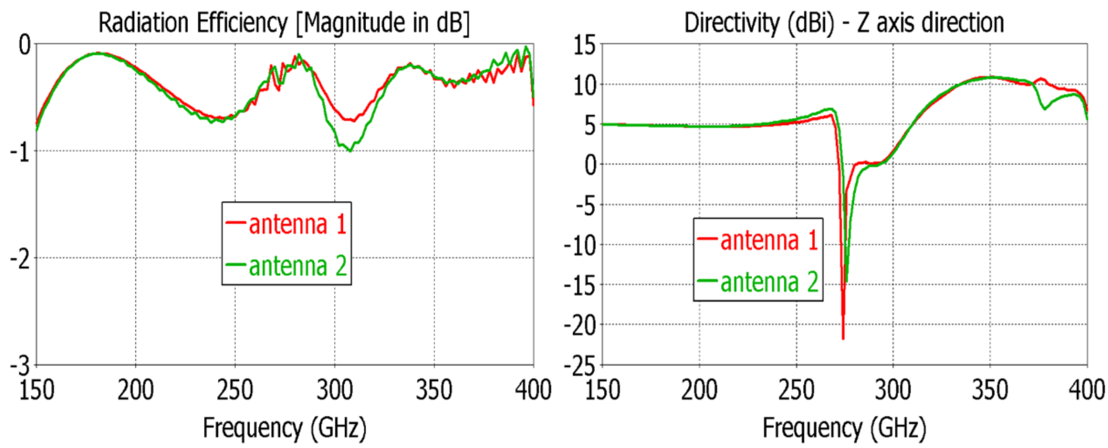

Figure 5.15: Radiation efficiency and directivity of Antenna 1 and Antenna 2.

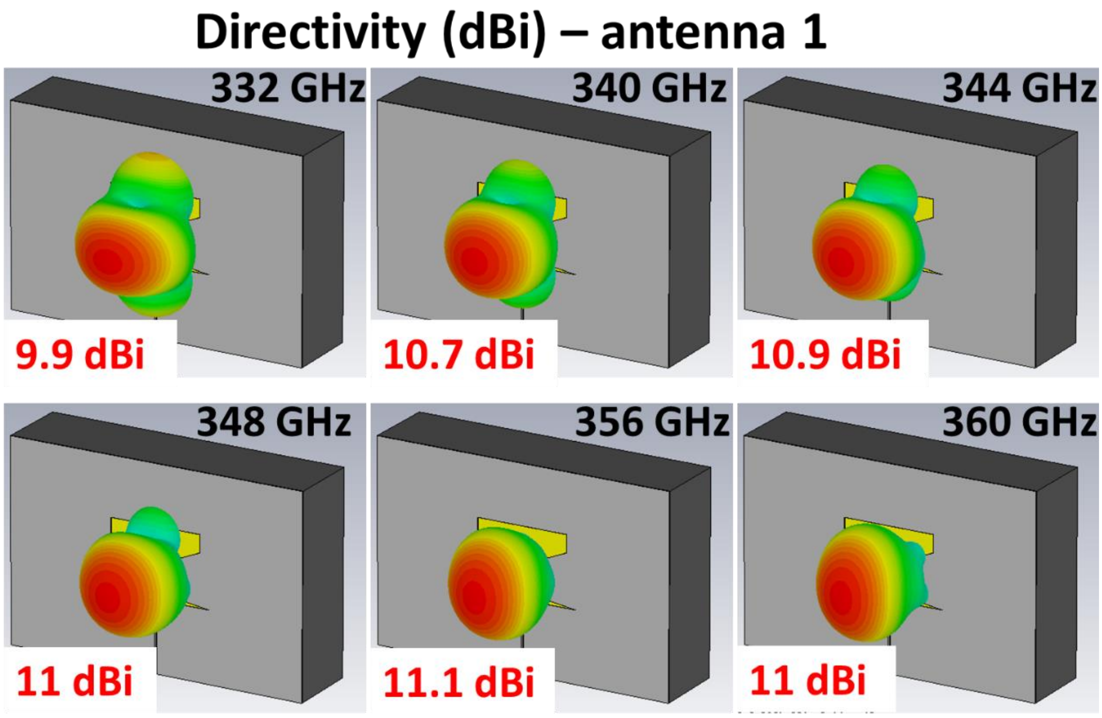

Figure 5.16: Antenna 1 radiation pattern at six frequencies of interest. The specified values in dBi (in red) are the maximum directivity values of the main lobe.

The impedance of Antenna 1 and Antenna 2 is given in Figure 5.17 and compared with the impedance of the 3 x 15 μm^2 III-V Lab UTC at -2 V bias. At 345 GHz the UTC resistance (impedance real part) is about 15 Ω, while the reactance is slightly capacitive, e.g. -5 Ω. Between 330 GHz and 360 GHz Antenna 1 resistance ranges from 125 Ω to 400 Ω and its reactance is strongly inductive, e.g. between about 80 Ω and 240 Ω, therefore the coupling efficiency between UTC and antenna is rather poor. Antenna 2 was designed to approach the complex and conjugate matching with the UTC and as a result its resistance was reduced to values between 10 Ω and 18 Ω, while its reactance is between 10 Ω and 25 Ω, across the frequency range 330 GHz to 360 GHz.

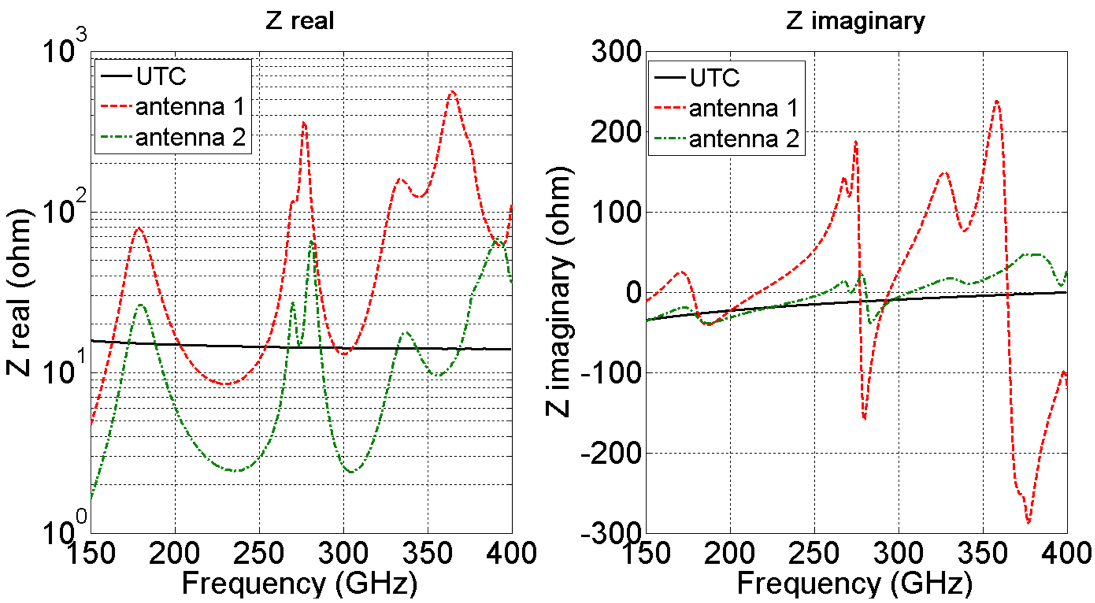

Figure 5.17: Impedance real and imaginary part of Antenna 1 and Antenna 2; the impedance of the 3 x 15 μm^2 III-V Lab UTC at -2 V bias (continuous black line) is also shown for comparison.

The power radiated by Antenna 1 and Antenna 2 is plotted in Figure 5.18 for a DC photocurrent of 10 mA. The power emitted within the frequency range of interest, e.g. 330 GHz to 360 GHz, by Antenna 2 (up to 87 μW) is up to 3.5 times greater than the power emitted by Antenna 1 (up to 25 μW), which highlights the importance of realising efficient energy coupling between the antenna and the driving source (i.e. UTC). The power radiated within a 60 degree conical solid angle, identified by a 30 degree angle with respect to the Z axis, is also plotted in Figure 5.18; this shows that the peaks of power radiated in the whole space by Antenna 1 around 230 GHz and 295 GHz, and by Antenna 2 around 270 GHz, are not emitted along the Z axis direction and go down by at least 6 dB when calculated within the solid angle.

The emitted power would go up by 6 dB for every 3 dB increase of the photocurrent amplitude; for instance, Antenna 2 would radiate up to 348 μW around 345 GHz for a 20 mA DC photocurrent. Indeed the UTC transit-time limited response also limits the power that can be emitted at high frequencies.

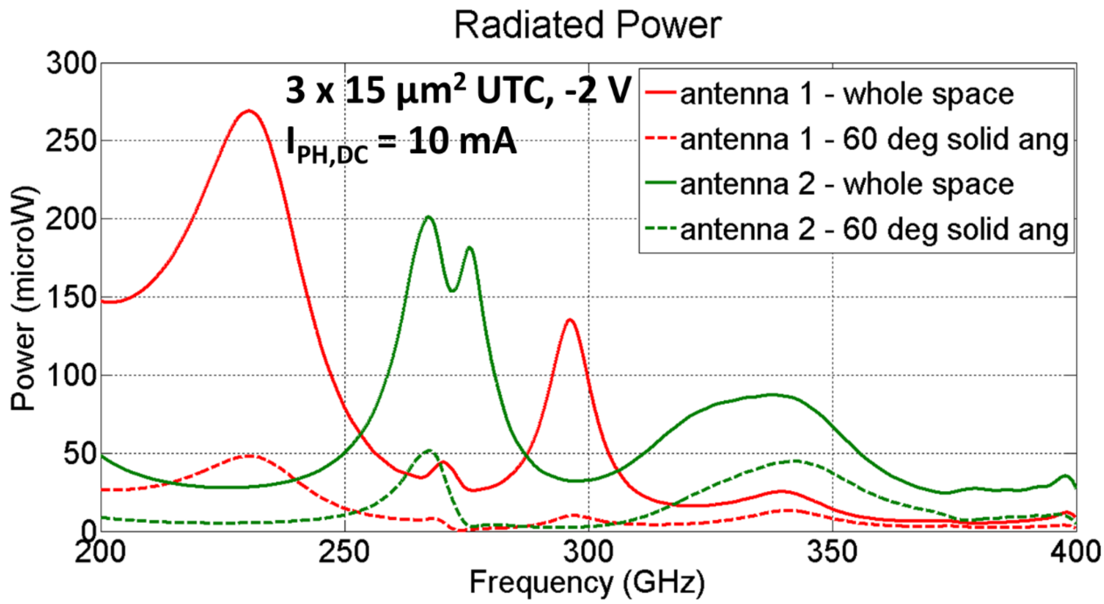

Figure 5.18: Power radiated by Antenna 1 and Antenna 2, for a DC photocurrent of 10 mA. The power emitted within the frequency range of interest, e.g. 330 GHz to 360 GHz, by Antenna 2 (up to 87 μW) is up to 3.5 times greater than the power emitted by Antenna 1 (up to 25 μW). The power radiated within a 60 degree conical solid angle, identified by a 30 degree angle with respect to the Z axis, is also plotted.

To understand how the emitted level of power can be increased, one has to consider that, the ideal case would consist of an antenna with a large impedance real part (due to radiation resistance, not ohmic losses) driven by an ideal current source which has, by definition, an infinite output impedance; in such a scenario the current source could inject a large current into the antenna endowed with a high radiation resistance, resulting in a very large radiated power. If an antenna with a high radiation resistance, such as Antenna 1 near 345 GHz, is driven by a low output impedance source, such as the UTC, the current injected into the antenna is very low and so is the emitted power. That is why, the best that can be achieved at these frequencies, using such a UTC as source, is to employ a low impedance antenna, approaching the complex conjugate matching with the UTC, having radiation efficiency and directivity as high as possible.

Following these consideration it is possible to understand, from an alternative perspective, why low device capacitance and series resistance are highly desirable in a UTC to be integrated with antennas. If the UTC Circuit 3 model, discussed in Chapter 3, is converted into its Norton equivalent circuit (current source), it can be seen that the output impedance real part of the Norton equivalent can be increased either increasing the series resistance R_1 or decreasing the capacitances; however if we do increase R_1 we cause the Norton equivalent current (which depends on the circuit elements) to decrease. Therefore if R_1 is kept low while the capacitances are decreased, we obtained a Norton equivalent (our current source) which has a high real part of the output impedance without a reduction of the Norton equivalent current; in short we would have a current source able to couple high power into a high radiation resistance antenna realising the complex-conjugate matching.

5.2.2.1 Effect of the bias lines on the radiation performance

In this section some initial investigations are made, concerning the effect that bias lines can have on the radiation properties of Antenna 1 and Antenna 2 and a preliminary design is presented.

Figure 5.19 shows, on the left hand side, the surface current distribution on the metal of Antenna 1 and the electric field amplitude on the surface of the chip at 345 GHz, without any bias line; areas of low current amplitude on the metal and low field amplitude on the chip surface are highlighted as suitable for the realisation of high inductance lines connecting the antenna to small metal pads for wire bonding.

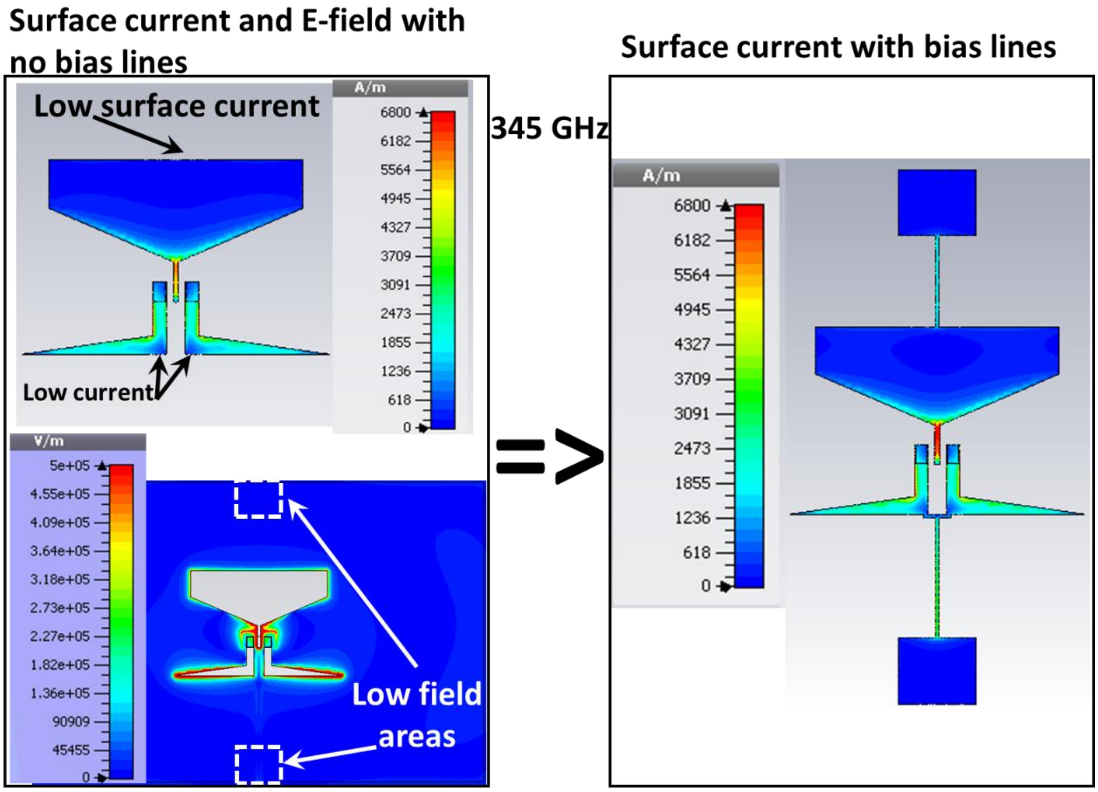

Figure 5.19: Bias line design. The current distribution on the metal of the antenna has not changed following the introduction of the bias lines and the metal pads. It is noted that when the same bias line design was modelled for the case of Antenna 1 on a substrate silicon lens instead of a ground plane, the effect on the radiation pattern was found to be significant. The main radiation beam tended to split up along the antenna length direction (Y axis direction in Figure 5.14) suggesting that the bias lines and the pads were in fact acting as an extension of the antenna length.

On the right hand side of Figure 5.19 the design of bias lines and metal pads is given and it is shown that the current distribution on the metal of the antenna has not changed. As a confirmation of the suggested design validity the radiation pattern of Antenna 1 including bias lines and metal pads, is shown Figure 4.19 and no significant changes are noted compared with the radiation pattern without bias lines and pads, previously shown in Figure 5.16.

It is noted that when the same bias line design was modelled for the case of Antenna 1 on a substrate silicon lens instead of a ground plane, the effect on the radiation pattern was found to be significant. The main radiation beam tended to split up along the antenna length direction (Y axis direction in Figure 5.14) suggesting that the bias lines and the pads were in fact acting as an extension of the antenna length.

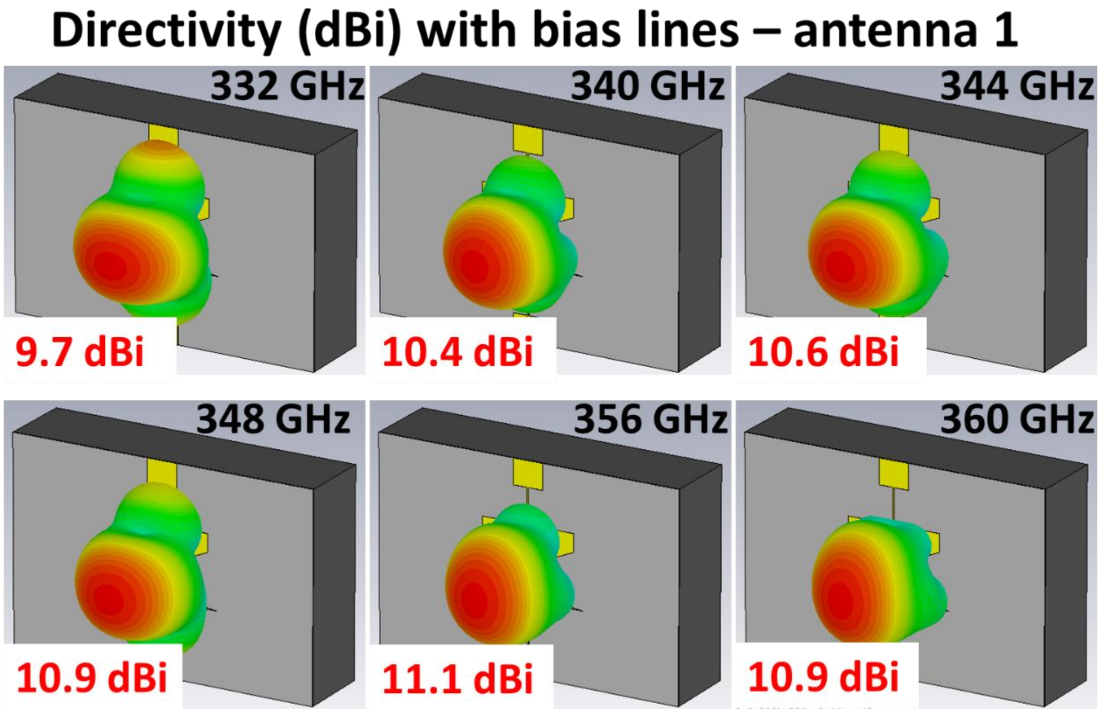

Figure 5.20: Radiation pattern of Antenna 1 including the effect of bias lines and metal pads. No significant changes are noted compared with the radiation pattern without bias lines and pads.

5.2.3 Novel design of THz planar antennas with a closer ground plane for easy array fabrication

In realising antenna arrays with ground planes, a potential issue associated with Antenna 1 and Antenna 2 design arises from the fact that the chip dimensions are part of the optimised parameters and should not be altered. While the optimised chip dimensions of a single antenna element can be achieved by accurate cleaving, the only way to create an array made up of Antenna 1 or Antenna 2 as elements, would be to realise the array on a large chip and then separate the antennas with deep trenches; this will require a challenging fabrication. If the antenna elements were left unseparated on a whole large chip, the optimised performance of the single element Antenna 1 (Antenna 2) would be lost and mutual coupling between the array elements would further cause the radiation performance to deteriorate.

In this section we present a third antenna design with a ground plane (Antenna 3) which, despite a lower radiation efficiency, has the advantage of being independent from the chip horizontal dimensions and a large array could easily be fabricated on a whole large substrate chip with virtually no mutual coupling among the antenna elements. An overview of the antenna geometry and the radiation efficiency are given in Figure 5.21

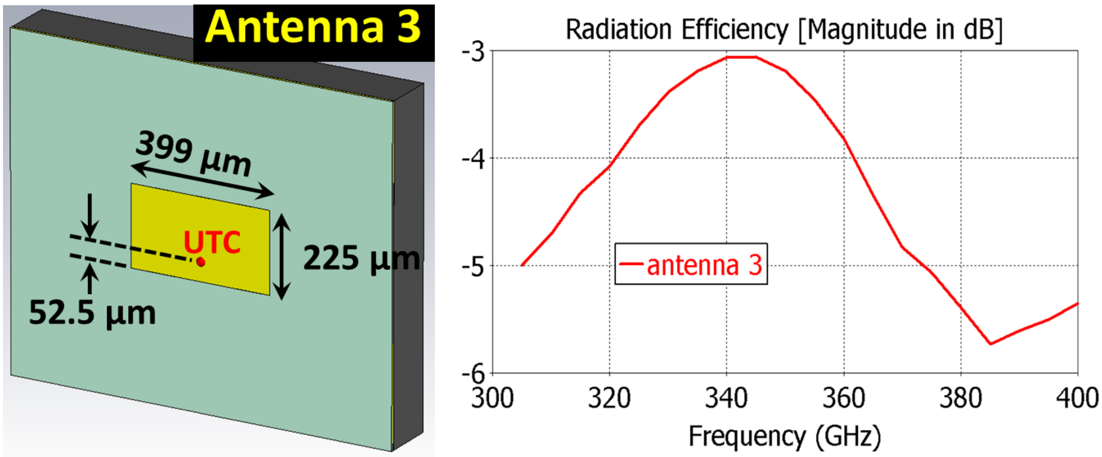

Figure 5.21: Overview of Antenna 3 geometry and radiation efficiency.

Antenna 3 is essentially a rectangular patch antenna. As mentioned previously such an antenna needs a ground plane very close to the patch. In this design the close ground plane is realised by depositing a layer of gold all around the UTC p-contact ridge, prior to deposition of the passivation layer (i.e. BCB or SiO_xN_y) on top of which the rectangular patch will be in turn deposited. The UTC position is highlighted in red in Figure 5.21. While the patch size affect both antenna impedance and radiation, the UTC position with respect to the rectangle influences the antenna impedance; the UTC near the patch centre would see a very low impedance while near the edges the impedance would increase. Since for this design the passivation layer should be thicker than usual (say up to 8 µm) the only fabrication difficulty could be realising the contact between the rectangular gold pad and the underlying UTC p-contact through a relatively deep via. Low electromagnetic energy would couple down in the InP substrate and no horizontal propagation within the electrically thin passivation layer could occur; as a consequence the chip horizontal dimensions are not relevant and no mutual coupling would occur within an array using Antenna 3 as the element. Antenna 3 has also been optimised to emit around 345 GHz when driven by the III-V UTC. The radiation efficiency, plotted in Figure 5.21, is modest because of ohmic losses. The 3-D radiation pattern (directivity in dBi) from 335 GHz to 360 GHz is shown in Figure 5.1. The impedance is shown in Figure 5.23 and compared with that of the UTC.

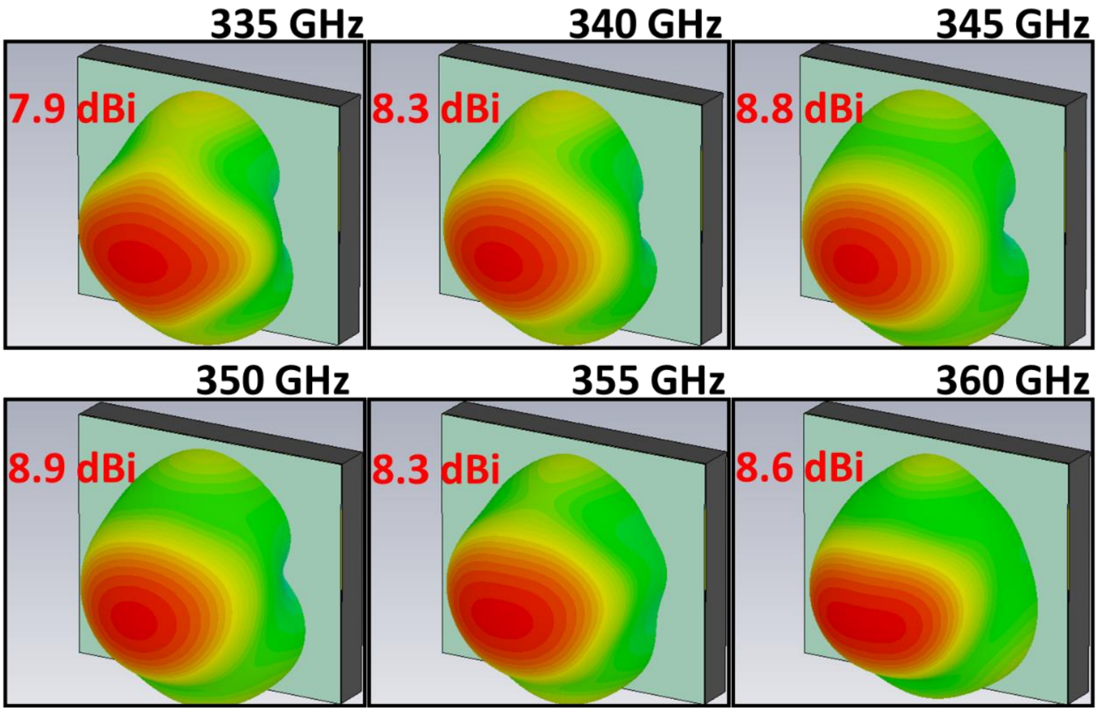

Figure 5.22: 3-D radiation pattern (directivity in dBi) of Antenna 3, from 335 GHz to 360 GHz.

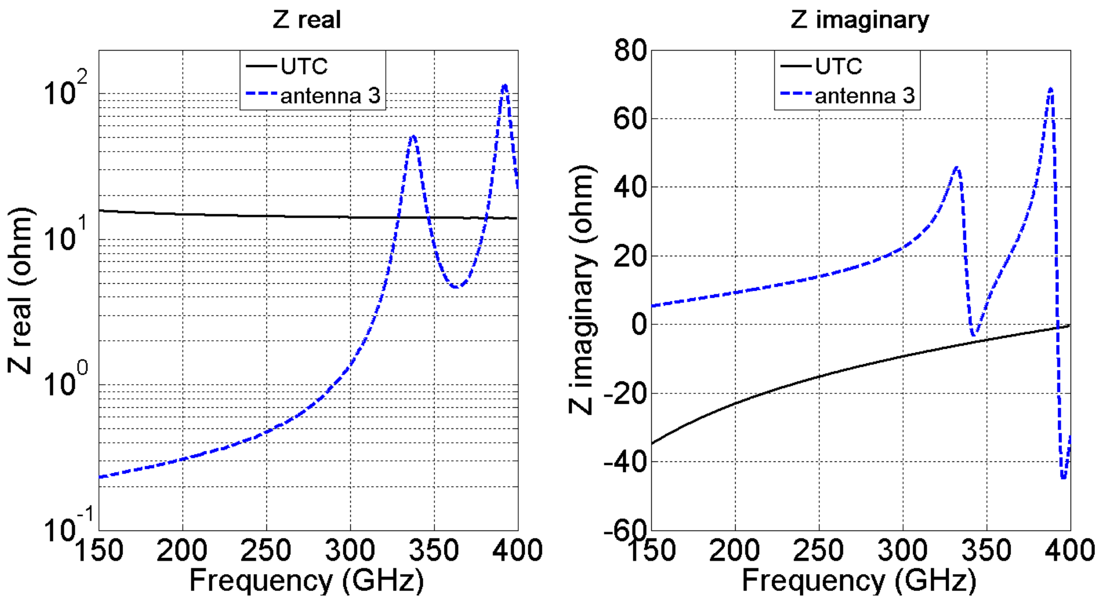

Figure 5.23: Comparison between Antenna 3 impedance and the impedance of the 3 x 15 μm^2 III-V Lab UTC at -2 V bias (continuous black line)

Figure 5.24 shows the power radiated by Antenna 3 from 300 GHz to 400 GHz, in the whole space and within the 60 degree solid angle. Although the level of radiated power is rather low, the design of this antenna concept is still at its infancy and substantial improvements are possible. As mentioned above, this antenna is suited to large array fabrication.

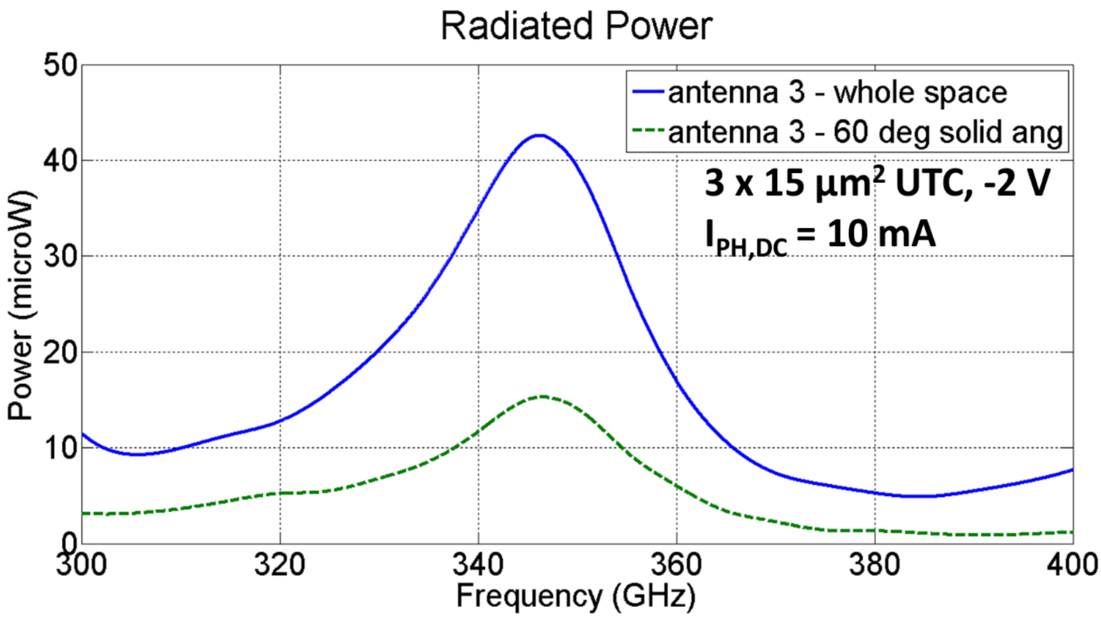

Figure 5.24: power radiated by Antenna 3 from 300 GHz to 400 GHz, in the whole space and within the 60 degree solid angle.

5.3 Lens

5.3.1 Modified bow-tie antenna on a silicon lens

The use of silicon lenses combined with antenna integrated uni-travelling carrier photodiodes is an established solution to couple THz power into free space as radiation [5.36].

The response (in terms of S parameters and impedance) of planar antennas on InP chips integrated with a silicon lens, is typically assumed to be equivalent to the response of the same antenna on a semi-infinite InP substrate. In this section the performance of Antenna 2 will be investigated by means of 3D full-wave modelling, when the antenna is integrated with a 4 mm diameter collimating Si lens instead of the ground plane. When the alignment between antenna chip and lens is perfect, the lens enables efficient radiation and good radiation pattern, and the antenna impedance is similar to the impedance of the same antenna on a semi-infinite InP substrate. The lens-integrated antenna radiation is, however, rather sensitive to the alignment between chip and lens, and in general the lens focusing properties are not as neat and even as often depicted on the basis of geometrical optics analyses. Resonances and standing waves tend to take place inside the lens, part of the energy coupled into the lens remains trapped inside and the ongoing reflections cause it to be emitted along undesired directions. Reservations about THz substrate lenses were expressed by the authors in [5.37], where an extended hemielliptic lens for a sub-millimetre-wave receiver was analysed.

Antenna 2 has been modelled on a 4 mm diameter Si lens in a collimating configuration, realised, for an InP chip on a silicon lens, when the source and the lens tip are about 1.41 times the lens radius apart [5.38]. An overview of the CST model and the radiation efficiency between 150 GHz and 400 GHz are given in Figure 5.25.

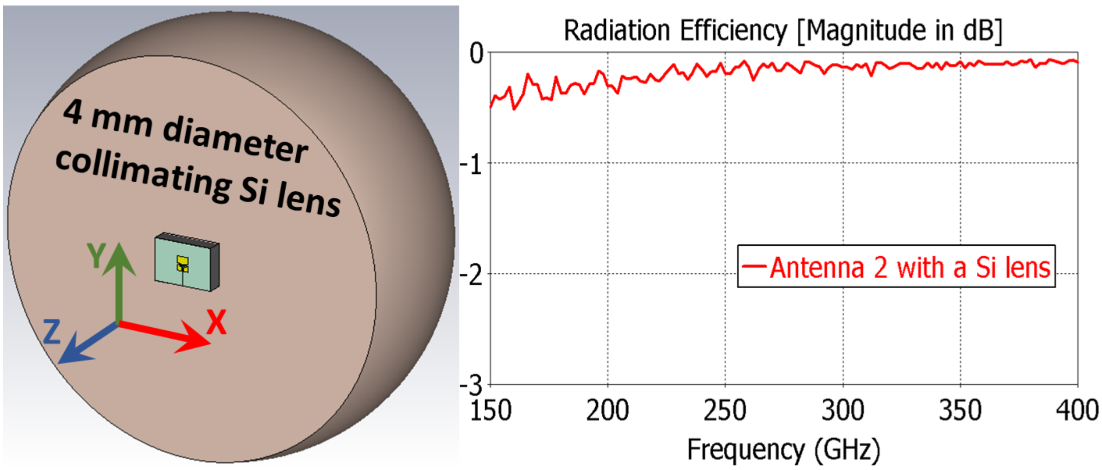

Figure 5.25: Model overview of Antenna 2 on a 4 mm diameter collimating Si lens and radiation efficiency.

The 3D directivity pattern in dBi is shown in Figure 5.26. The lens antenna exhibits a good radiation pattern along the intended direction of radiation (i.e. Z axis negative direction) with directivity up to 20.2 dBi at 344 GHz. Nevertheless, despite the perfect alignment between lens and chip realised in the model, the whole radiation pattern is not as even as expected and some rather noticeable side lobes tend to appear. This might be favoured by the fact that Antenna 2 was mainly optimised to work on a ground plane but is mainly the effect of the inevitable ongoing internal reflections that, as will be shown, get worse as the alignment accuracy decreases.

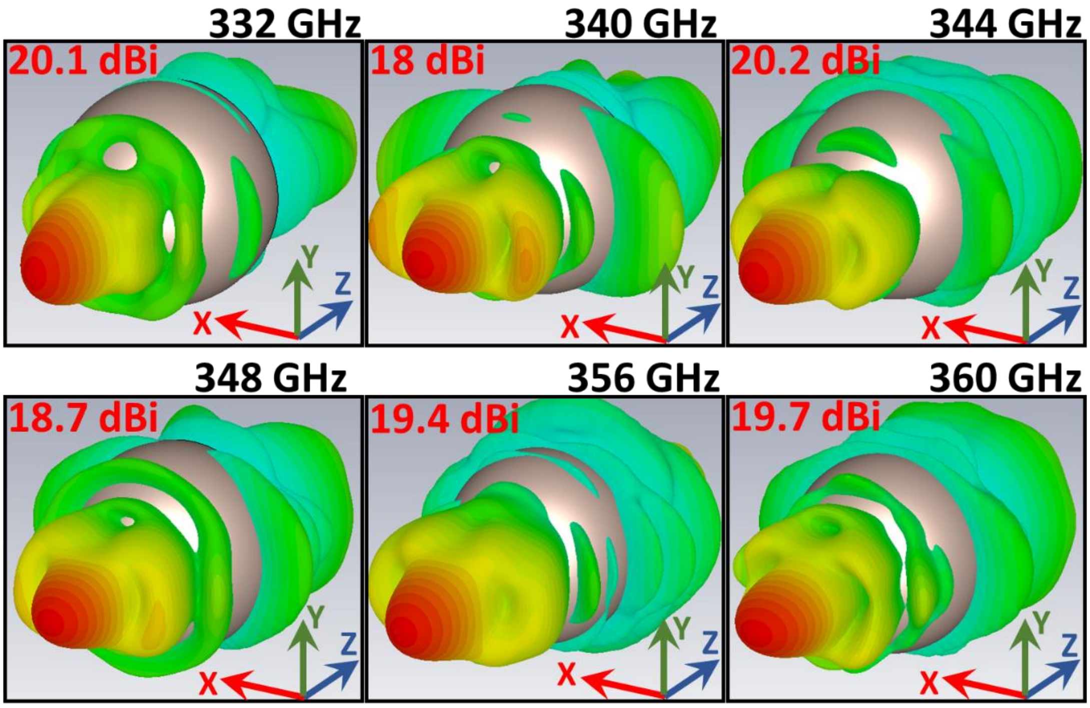

Figure 5.26: 3D directivity pattern in dBi. The lens antenna exhibits a good radiation pattern along the intended direction of radiation (i.e. Z axis negative direction) with directivity up to 20.2 dBi at 344 GHz.

In Figure 5.27 the impedance of Antenna 2 on the Si lens is compared with the UTC impedance and with the impedance of Antenna 2 on a semi-infinite InP substrate. The latter impedance appears to be a moving average of the lens antenna impedance; therefore if it is acceptable to say that they are similar it is not accurate to say that they are equivalent since the oscillations of the lens antenna impedance around the value of the semi-infinite impedance case are large and can affect the coupling with the driving source.

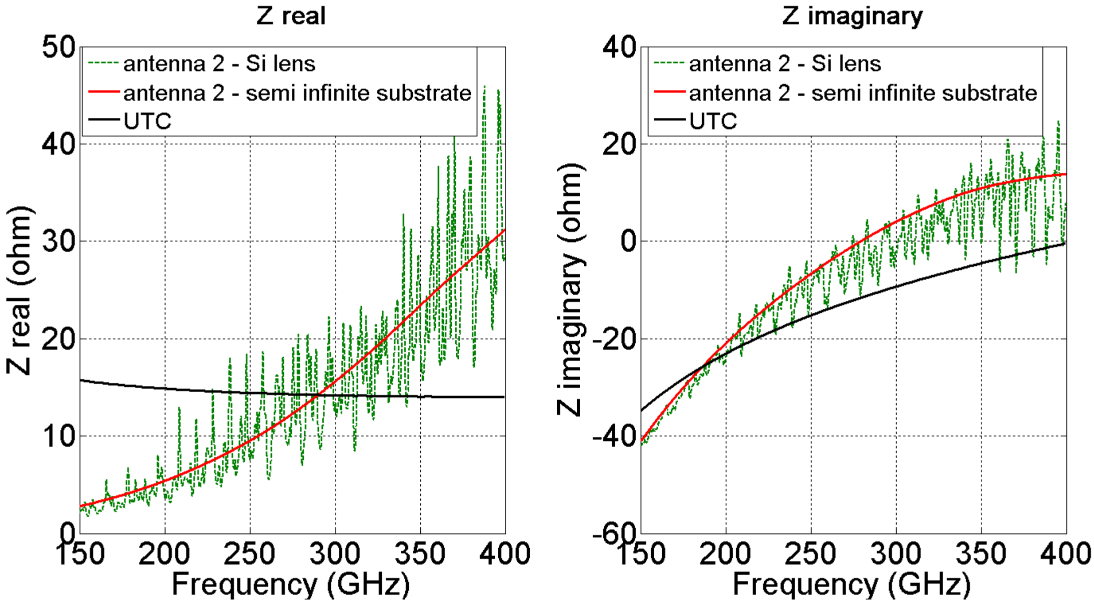

Figure 5.27: Comparison between the impedance of Antenna 2 integrated with Si lens and the impedance of the 3 x 15 μm² III-V Lab UTC at -2 V bias (continuous black line). The impedance of Antenna 2 on a semi-infinite InP substrate is also plotted.

The highly oscillating trend of the lens antenna impedance is caused by the mentioned ongoing reflections inside the lens, caused by the trapped energy. Such oscillating trend is, as expected, reproduced in the radiated power, plotted in Figure 5.28.

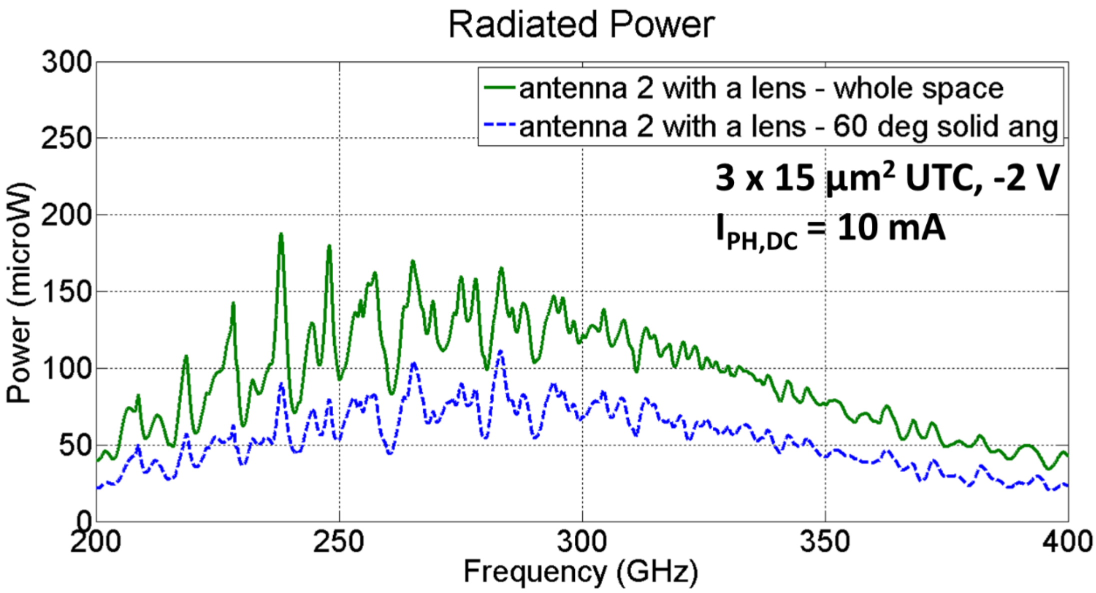

Figure 5.28: Power radiated by Antenna 2 integrated with a silicon lens in the whole space and within a 60 degree conical solid angle.

By performing a moving average of the radiated power in Figure 5.28, it is found that a maximum of almost 140 μW is emitted at about 280 GHz, while a power of approximately 85 μW is radiated at 345 GHz.

5.3.2 Performance sensitivity to the lens alignment

In this section we carry out a brief investigation about the effect of the alignment between the substrate lens and the antenna chip on antenna performance. For instance, with reference to the structure overview in Figure 5.25, a misalignment ΔY is defined as a displacement of the antenna chip along the Y axis direction, with respect to the perfect alignment position. For this model, the perfect alignment is achieved when the centre of the InP substrate chip has the same X, Y coordinates as the centre of the lens flat face. A positive value of ΔY means that the chip has been translated along the Y axis positive direction by a distance ΔY. Figure 5.29 shows how the radiation pattern calculated at 344 GHz, changes with respect to the perfect alignment case (i.e. ΔY = 0) when three increasing misalignments of ΔY = 100 μm, ΔY = 200 μm and ΔY = 300 μm are considered.

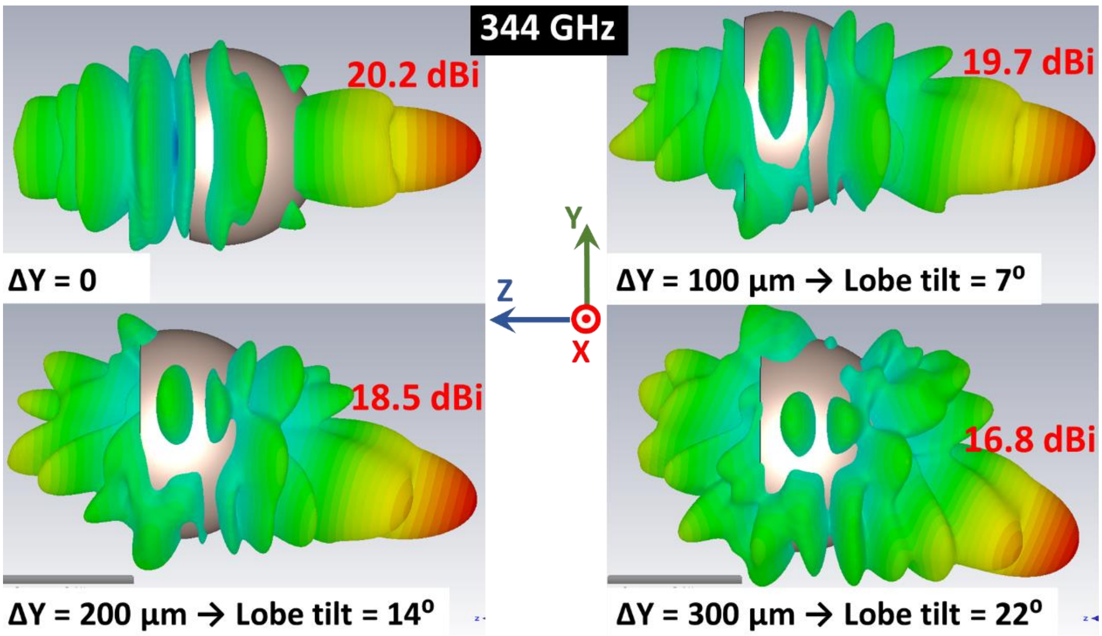

Figure 5.29: Changes, of the radiation pattern calculated at 344 GHz, with respect to the perfect alignment case (i.e. ΔY = 0) when three increasing misalignments of ΔY = 100 μm, ΔY = 200 μm and ΔY = 300 μm are applied.

The effect introduced by the misalignment is quite significant as the main lobe of the radiation pattern tilts downwards by an increasing angle. To show clearly the effect of the misalignment, large misalignment values have been modelled, i.e. 100 µm, 200 µm and 300 µm. The 100 µm misalignment produces a tilt of 7 degrees, while the 300 µm misalignment generates a tilt as large as 22 degrees. Furthermore, because of the misalignment, the main lobe decreases in magnitude, by up to 3.4 dB, while the side lobes become increasingly prominent. As a consequence of these changes in the radiation pattern, the directivity along the intended direction, e.g. the negative Z axis, falls dramatically, as shown in Figure 5.30.

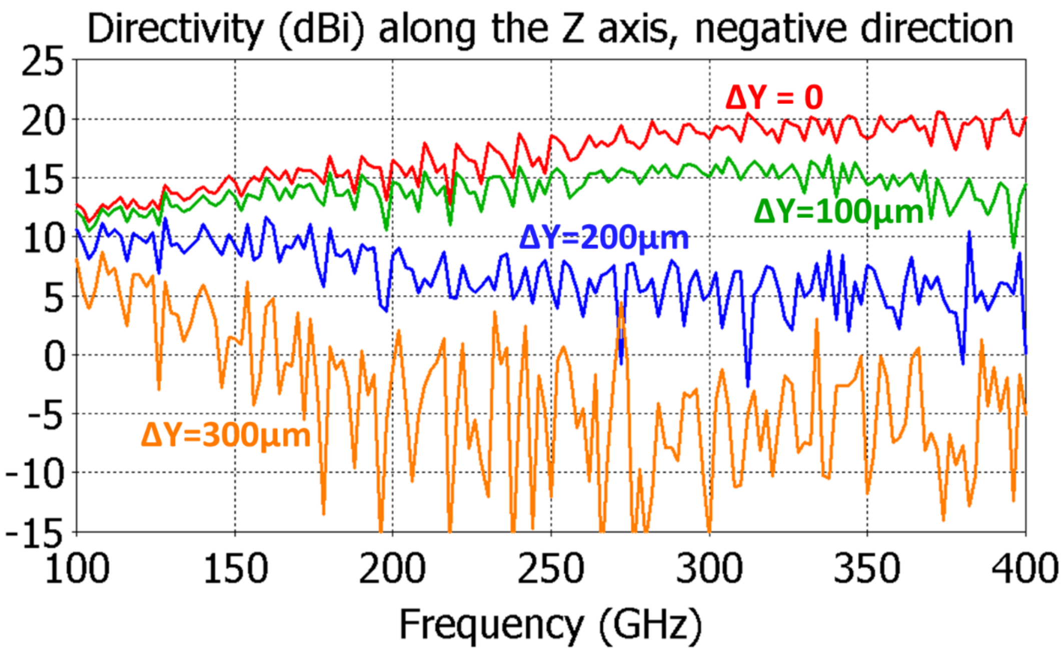

Figure 5.30: Effect of the misalignments on the directivity along the intended direction, e.g. the negative Z axis.

An additional concern regarding the operation of substrate lenses is, as mentioned previously, the fact that they may perform more as a resonator than an actual focusing lens, as also suggested in [5.37]. Figure 5.31 is a cross section view of the lens antenna structure, through the cutting plane [XZ], and shows the amplitude of the electric field at 350 GHz for the perfect alignment case (ΔY = 0). As suspected, the amount of energy trapped inside the lens is relevant and the pattern of the electric field amplitude clearly shows resonances and standing waves, with nodes and antinodes.

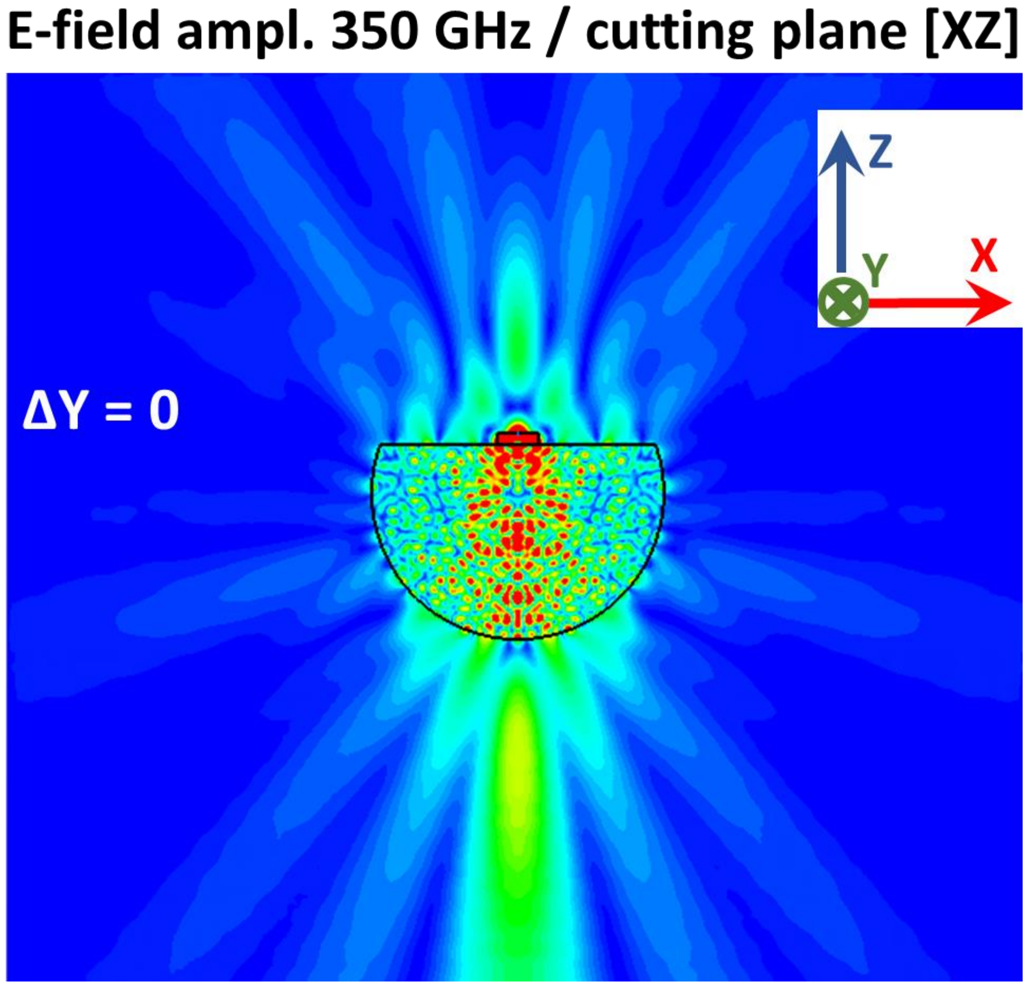

Figure 5.31: Cross section view of the lens antenna structure, through the cutting plane [XZ], showing the amplitude of the electric field at 350 GHz for the perfect alignment case (ΔY = 0)

Perhaps even more interesting is the [YZ] plane cross section through the lens, showing, Figure 5.32, the electric field amplitude in the four cases of different misalignment, i.e. ΔY = 0, ΔY = 100 µm, ΔY = 200 µm and ΔY = 300 µm. It appears that the general amplitude of the field inside the lens tends to increase with increasing misalignment, which is consistent with the fact that the lens focusing properties deteriorates.

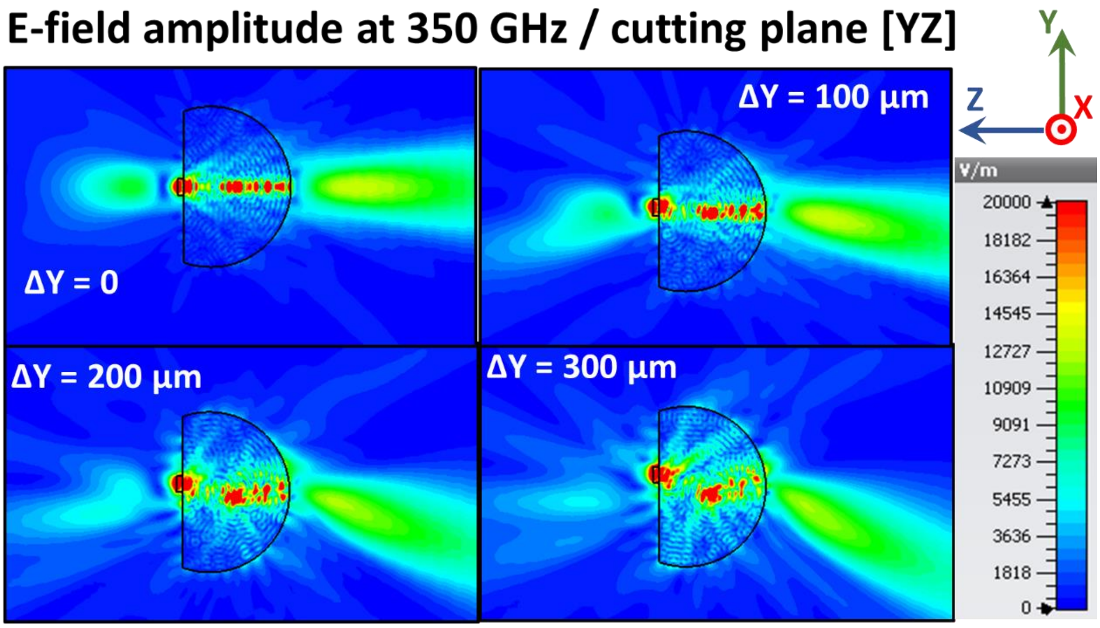

Figure 5.32: [YZ] plane cross section views through the lens, showing the electric field amplitude in the four cases of different misalignment, i.e. ΔY = 0, ΔY = 100 µm, ΔY = 200 µm and ΔY = 300 µm.

Substrate lenses are hence theoretically capable of realising high directivity radiation patterns when integrated with ad-hoc antennas and when an ideal perfect alignment between lens and antenna chip is achieved. The radiation pattern though is sensitive to the alignment accuracy and in reality, a relevant amount of energy remains trapped inside the lens as ongoing internal reflections which cause the radiation pattern to be rather unpredictable. The internal reflections also cause large and thick ripples in the trend of radiated power and impedance over the frequency range. For all these reasons, as will be shown in Chapter 7, substrate lenses are not suited to antenna arrays because of the inevitable and significant misalignment between the lens and all the array antenna elements.

5.4 Thermal considerations

Successful realisation of effective heat sinks is central to the successful maximisation of the RF power extracted from high power UTCs since these can suffer from overheating failure before reaching saturation [5.39]. While in the future research work an in-depth thermal analysis of UTC-PD structures will be performed, supported by the thermal solver of CST Studio suite, here some basic thermal considerations are presented.

The use of a gold ground plane, instead of a silicon lens, can allow a more efficient heat dissipation to be achieved, as gold thermal conductivity is more than twice that of silicon (318 $Wm^{-1}K^{-1}$ vs. 149 $Wm^{-1}K^{-1}$). Peytavit et al [5.40] have demonstrated a continuous wave output power, from a low-temperature-grown GaAs photoconductor, reaching 1.8 mW at 252 GHz for 270 mW input optical power, 24 mA DC photocurrent and 3 V bias voltage; such a high level of output power was made possible by the use of a metallic mirror-based Fabry-Pérot cavity and an impedance matching circuit. An essential merit of the device discussed in [5.40] is its remarkable capability to handle such a high thermal power, which the authors attribute to the thermal management built on the thinness of the LT-GaAs layer and the high thermal conductivities of the buried gold layer and the silicon substrate.

Although silicon is a fairly good thermal conductor, the thermal management of an antenna chip sitting directly on metal (ground plane), rather than on silicon (lens), can in principle be superior.

In Figure 5.33 an example is shown of an InP antenna chip placed directly on metal (left hand side) or on a small 1 mm diameter silicon lens; the extra Si slab placed between the lens and InP chip serves to realise a collimating configuration [5.38].

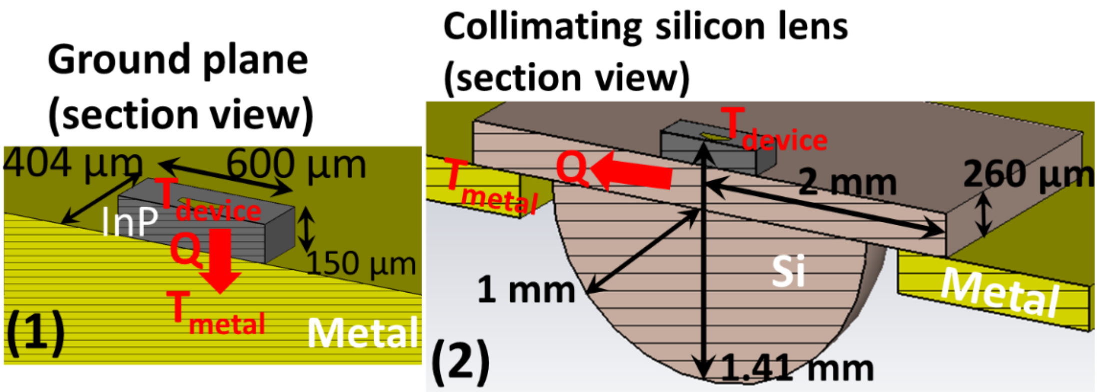

Figure 5.33: Schematic diagram of a chip on a ground plane (left hand side) and on a silicon lens (right hand side), for thermal management considerations.

The thermal conductivity of indium phosphide, $\sigma_{th,InP} = 68\ [W/(m \cdot K)]$, is lower than that of silicon, $\sigma_{th,Si} = 149\ [W/(m \cdot K)]$; however, although the InP chip is present in both scenarios and the heat flow Q has to pass through it, what really defines the efficiency of a system in getting rid of the heat, is the system total thermal resistance R_{th}. For a given device temperature T_{device} and a given metal heat sink temperature T_{metal}, the heat flow Q increases as the total thermal resistance decreases, as in (5.1):

$$Q = (T_{device} - T_{metal})/R_{th} \tag{5.1}$$

We have named $R_{th,(1)}$ for the ground plane configuration and $R_{th,(2)}$ for the silicon lens configuration. The total thermal resistance of the ground plane configuration coincides with the thermal resistance of the InP substrate $R_{th,InP-sub}$, which can be calculated based on the substrate geometry and thermal conductivity, and hence $R_{th,(1)} = R_{th,InP-sub} \approx 9[K/W]$. The total resistance of the silicon lens configuration contains an additional contribution in series with $R_{th,InP-sub}$, that is the resistance $R_{th,Si-slab}$ offered by the slab of silicon that separates the InP chip and the metal heat sink. For the geometry shown in Figure 5.33, $R_{th,Si-slab}$ can be estimated to be about $R_{th,Si-slab} \approx 8.5\ (K/W)$ and therefore the total thermal resistance for the silicon lens configuration is $R_{th,(2)} = R_{th,InP-sub} + R_{th,Si-slab} \approx 17.5\ (K/W)$ which is almost double that for the ground plane configuration. For larger lenses and if the additional Si slab is thin, the total resistance of the configuration with the silicon lens should increase further.

5.5 Conclusions

In this chapter the design of new THz antennas, obtained by means of full-wave electromagnetic modelling, has been described. The new antennas have shown to be suitable for integration with both standard silicon lenses and a novel solution employing a ground plane. Realising accurate alignment between silicon lens and antenna chip is essential to optimise the radiation pattern and yet is a challenging task to accomplish; antennas integrated with ground planes do not require such alignment. The influence of the misalignment between antenna chip and substrate lens on the radiation pattern, has been shown, and found to be significant. The ground plane solution can offer advantages in terms of heat dissipation, as it is more suitable for the realisation of efficient heat sinks. In this chapter the case study of a large bow-tie antenna has also been presented and the comparison between modelled and measured radiated power has been discussed; it is shown that the knowledge about the UTC impedance achieved in Chapter 3 and 4 enables the radiated power to be predicted with satisfactory accuracy while the radiated power calculated based on the classical junction-capacitance/series-resistance concept is in substantial disagreement with the measurements.

5.6 References

[5.1] T. K. Nguyen, T. A. Ho, H. Han, and I. Park, “Numerical Study of Self-Complementary Antenna Characteristics on Substrate Lenses at Terahertz Frequency,” *J. Infrared, Millimeter, Terahertz Waves*, vol. 33, no. 11, pp. 1123–1137, Jul. 2012.

[5.2] T. K. Nguyen, F. Rotermund, and I. Park, “A traveling-wave stripline dipole antenna on a substrate lens at terahertz frequency,” *Curr. Appl. Phys.*, vol. 14, no. 8, pp. 998–1004, Aug. 2014.

[5.3] R. S. Tahim, G. M. Hayashibara, and Kai Chang, “Design and performance of W-band broad band integrated circuit mixers,” *IEEE Trans. Microw. Theory Tech.*, vol. 31, no. 3, pp. 277–283, 1983.

[5.4] G. M. Rebeiz, “Millimeter-wave and terahertz integrated circuit antennas,” *Proc. IEEE*, vol. 80, no. 11, pp. 1748–1770, 1992.

[5.5] G. A. Ediss, S. J. Wang, and N. J. Keen, “Quasioptical components for 230 GHz and 460 GHz,” *IEE Proc. H Microwaves, Antennas Propag.*, vol. 132, no. 2, pp. 99–106, 1985.

[5.6] G. A. Ediss, “Technical memorandum. Dual-mode horns at millimetre and sub-millimetre wavelengths,” *IEE Proc. H Microwaves, Antennas Propag.*, vol. 132, no. 3, pp. 215–218, 1985.

[5.7] H. R. Fetterman, P. E. Tannenwald, B. J. Clifton, C. D. Parker, W. D. Fitzgerald, and N. R. Erickson, “Far-ir heterodyne radiometric measurements with quasioptical Schottky diode mixers,” *Appl. Phys. Lett.*, vol. 33, no. 2, pp. 151–154, 1978.

[5.8] E. Sauter, G. V. Schultz, and R. Wohlleben, “Antenna patterns of an open structure mixer at a submillimeter wavelength and of its scaled model,” *Int. J. Infrared Millimeter Waves*, vol. 5, no. 4, pp. 451–463, 1984.

[5.9] E. N. Grossman, “The coupling of submillimeter corner-cube antennas to Gaussian beams,” *Infrared Phys.*, vol. 29, no. 5, pp. 875–885, 1989.

[5.10] J. Zmuidzinas, A. L. Betz, and R. T. Boreiko, “A corner-reflector mixer mount for far infrared wavelengths.,” *Infrared Phys.*, vol. 29, no. 1, pp. 119–131, 1989.

[5.11] S. S. Gearhart, C. C. Ling, and G. M. Rebeiz, “Integrated millimeter-wave corner-cube antennas,” *IEEE Trans. Antennas Propag.*, vol. 39, pp. 1000–1006, 1991.

[5.12] S. S. Gearhart, C. C. Ling, G. M. Rebeiz, H. Davee, and G. Chin, “Integrated 119-µm linear corner-cube array,” *IEEE Microw. Guid. Wave Lett.*, vol. 1, no. 7, pp. 155–157, 1991.

[5.13] D. Pozar, “Considerations for millimeter wave printed antennas,” *Antennas Propagation, IEEE Trans.*, vol. 31, no. 5, pp. 740–747, 1983.

[5.14] N. Alexopoulos, P. B. Katehi, and D. B. Rutledge, “Substrate Optimization for Integrated Circuit Antennas,” *Microw. Symp. Dig. 1982 IEEE MTT-S Int.*, pp. 190–192, 1982.

[5.15] P. Katehi and N. Alexopoulos, “On the effect of substrate thickness and permittivity on printed circuit dipole properties,” *Antennas Propagation, IEEE Trans.*, vol. 31, no. 1, pp. 34–39, 1983.

[5.16] H. Yang and N. Alexopoulos, “Gain enhancement methods for printed circuit antennas through multiple superstrates,” *IEEE Trans. Antennas Propag.*, vol. 35, no. 7, pp. 860–863, 1987.

[5.17] D. R. Jackson and N. G. Alexopoulos, “Microstrip dipoles on electrically thick substrates,” *Int. J. Infrared Millimeter Waves*, vol. 7, no. 1, pp. 1–26, 1986.

[5.18] D. B. Rutledge, D. P. Neikirk, and D. P. Kasilingam, “Integrated circuit antennas,” in *IInfrared and millimeter waves*, vol. 10, New York: Academic, 1983.

[5.19] J. D. Kraus and R. J. Marhefka, *Antenna for all applications*, 3rd ed. Boston: Tata McGraw-Hill, 2002.

[5.20] D. B. Rutledge and M. S. Muha, “Imaging antenna arrays,” *Antennas Propagation, IEEE Trans.*, vol. 30, no. 4, pp. 535–540, 1982.

[5.21] D. P. Neikirk, D. B. Rutledge, D. B. Rutledge, M. S. Muha, H. Park, and C.-X. Yu, “Far-infrared imaging antenna arrays,” *Appl. Phys. Lett.*, vol. 40, no. 3, pp. 203–205, 1982.

[5.22] D. F. Filpovic, “Analysis and design of dielectric-lens antennas and planar multiplier cuircuits for millimeter-wave applications,” University of Michigan, 1995.

[5.23] D. Pasqualini and S. Maci, “High-frequency analysis of integrated dielectric lens antennas,” *IEEE Trans. Antennas Propag.*, vol. 52, no. 3, pp. 840–847, 2004.

[5.24] D. Kasilingam and D. Rutledge, “Focusing properties of small lenses,” *Int. J. Infrared Millimeter Waves*, vol. 7, no. 10, pp. 1631–1647, 1986.

[5.25] D. F. Filipovic, S. S. Gearhart, and G. M. Rebeiz, “Double-slot antennas on extended hemispherical and elliptical silicon dielectric lenses,” *IEEE Trans. Microw. Theory Tech.*, vol. 41, no. 10, pp. 1738–1749, 1993.

[5.26] S. Preu, G. H. Döhler, S. Malzer, L. J. Wang, and A. C. Gossard, “Tunable, continuous-wave Terahertz photomixer sources and applications,” *J. Appl. Phys.*, vol. 109, no. 6, pp. 061301 1 – 061301 56, 2011.

[5.27] R. DuHamel and D. Isbell, “Broad band logarithmically periodic antenna structures,” *IRE Int. Conv. Rec.*, vol. 5, pp. 119–128, 1957.

[5.28] J. Dyson, “The equiangular spiral antenna,” *IRE Trans. Antennas Propag.*, vol. 7, no. 2, pp. 181–187, 1959.

[5.29] C. A. Balanis, *Antenna theory: analysis and design*, 3rd ed. New York: Wiley, 2012.

[5.30] Y. Huo, G. W. Taylor, and R. Bansal, “Planar log-periodic antennas on extended hemishperical silicon lenses for millimeter/submillimeter wave detection applications,” *Int. J. Infrared Millimeter Waves*, vol. 23, no. 6, pp. 819–839, 2002.

[5.31] G. M. Rebeiz, W. G. Regehr, D. B. Rutledge, R. L. Savage, and N. C. Luhmann, “Submillimeter-wave antennas on thin membranes,” *Int. J. Infrared Millimeter Waves*, vol. 8, no. 10, pp. 1249–1255, 1987.

[5.32] G. M. Rebeiz, D. P. Kasilingam, Y. Guo, P. A. Stimson, and D. B. Rutledge, “Monolithic millimeter-wave two-dimensional horn imaging arrays,” *IEEE Trans. Antennas Propag.*, vol. 38, no. 9, pp. 1473–1482, 1990.

[5.33] G. M. Rebeiz and D. B. Rutledge, “Millimeter and submillimeter wave antenna structure,” US4888597 A, 1989.

[5.34] W. Y. Ali-Ahmad, W. L. B. Bishop, T. W. Crowe, and G. M. Rebeiz, “86-106 GHz quasi-integrated low noise Schottky receiver,” *IEEE Trans. Microw. Theory Tech.*, vol. 41, no. 4, pp. 558–564, 1993.

[5.35] “TK Absolute Power / Energy Meter System,” 2010. [Online]. Available: http://www.terahertz.co.uk/images/tki/PMETER/manual321.pdf. [Accessed: 10-Mar-2015].

[5.36] E. Rouvalis, C. C. Renaud, D. G. Moodie, M. J. Robertson, and A. J. Seeds, “Traveling-wave Uni-Traveling Carrier photodiodes for continuous wave THz generation,” *Opt. Express*, vol. 18, no. 11, pp. 11105–11110, 2010.

[5.37] A. V. Boriskin, A. I. Nosich, S. V. Boriskina, T. M. Benson, P. Sewell, and A. Altintas, “Lens or resonator? Electromagnetic behavior of an extended hemielliptic lens for a sub-millimeter-wave receiver," *Microw. Opt. Technol. Lett.*, vol. 43, no. 6, pp. 515–518, Dec. 2004.

[5.38] J. Van Rudd and D. M. Mittleman, "Influence of substrate-lens design in terahertz time-domain spectroscopy," *JOSA B*, vol. 19, no. 2, pp. 319–329, 2002.

[5.39] X. W. X. Wang, N. D. N. Duan, H. C. H. Chen, and J. C. Campbell, "InGaAs–InP photodiodes with high responsivity and high saturation power," *IEEE Photonics Technol. Lett.*, vol. 19, no. 16, pp. 1272–1274, 2007.

[5.40] E. Peytavit, P. Latzel, F. Pavanello, G. Ducournau, and J. F. Lampin, "Milliwatt output power generated in the J-Band by a GaAs photomixer," *Int. Conf. Infrared, Millimeter, Terahertz Waves, IRMMW-THz*, pp. 8–10, 2013.

Chapter 6 - Study of THz emission by means of a sub-wavelength aperture probe

In this chapter an extensive analysis is presented, regarding the use of a sub-wavelength aperture probe to investigate THz emission, particularly in antenna near- and far-fields. The probe exhibits properties enabling accurate detection of far fields and the experimental system incorporating the probe is suited to map antenna far-field radiation patterns.

Furthermore, thanks to its excellent properties as a near-field detector, the probe enables the reconstruction of the electric field in the vicinity of antennas. In future work the sub-wavelength aperture probe will be employed as a tool to assist the realisation of the optimum terahertz antenna via experimental analysis of the antennas designed numerically. The probe allows, with little invasiveness [6.1] and with increasing space resolution [6.2], [6.3], the reconstruction of the electric field distribution and hence surface current distribution, providing important information about the antennas.

6.1 Modelling of surface waves on a THz antenna detected by a near-field probe

In this section a detailed report about the modelling of the experimental system based on the sub-wavelength aperture probe employed to detect THz emission in the near-field of a planar bow-tie antenna is presented. For the first time the accuracy of the proposed interpretation of the images mapped by the probe is demonstrated [6.1]; the very good agreement between numerical and experimental results proves that the physical quantity detected by the probe over metallic surfaces is the spatial derivative of the electric field normal component. The achieved understanding of the probe response allows a correct interpretation of the images and the distribution of the electric field to be extracted. A first assessment of the probe invasiveness has also been carried out, finding that the pattern of the surface waves on the antenna is not modified significantly by the proximity of the probe. This makes the experimental system an effective tool for near-field imaging of THz antennas and other metallic structures.

6.1.1 Introduction

Application of the near-field scanning probe microscopy method at terahertz (THz) frequencies (λ = 30-1000 µm) has enabled studies of a range of scientific questions [6.4]. The method allows spatial resolution to be improved beyond the diffraction limit, as well as detecting evanescent components of the THz field [6.4]-[6.11]. This capability is particularly suitable for studies of electromagnetic fields in the near-field region of antennas. Several investigations of THz and optical antennas have been performed recently [6.11]-[6.16]. Antennas provide the possibility to concentrate the electric field in a sub-wavelength region and application of optical antennas enabled challenging studies, such as spectroscopic investigation of individual molecules. The concentrated field in the antenna gap however depends sensitively on the antenna geometry and experimental images of the field distribution in the near-field zone of the antenna are essential for evaluating the antenna performance.

Understanding of the near-field probe interaction with objects is central to the correct interpretation of images. In general, near-field images represent a convolution of the optical field with the near-field probe spatial response, which is often a complex function of the electric field vector and its derivatives, especially if probe modulation techniques are used to improve the method sensitivity. Near-field probes also disturb the optical field and it is important to understand the probe invasiveness.

One of the probes developed for THz near-field microscopy, the integrated sub-wavelength aperture probe [6.17], was recently shown to be sensitive to THz surface plasmon waves [6.8], [6.11]. The probe provides the possibility of mapping THz surface waves with spatial resolution better than 10 microns [6.2], [6.3] and to track the wave propagation in time [6.8], [6.11]. To enable precise analysis of the surface wave phenomena, an understanding of the probe response is essential.

Experimental results discussed in [6.11] suggested that the near-field images represent the in-plane spatial derivative of the surface plasmon field distribution. The spatial derivative nature implies that near-field images may show patterns that are different from the surface plasmon field distribution. For example, a uniform travelling wave is displayed with a phase shift and a standing surface wave confined on small metallic objects, such as an antenna, may show a change in the detected pattern symmetry. The detected field amplitude may also depend on the direction of the surface wave propagation. Analysis of near-field images of test objects suggested that these effects are present and a simplified coupling mechanism was introduced to explain the near-field probe response [6.11].

In order to verify the model of the near-field probe response, the response has been evaluated numerically; the computational approach also allows a preliminary assessment of the question of probe invasiveness. The near-field response is analysed by considering surface plasmon waves on the surface of a bow-tie antenna and comparing the results with experimental images collected by the near-field probe. The numerical results confirm that the experimental images display the spatial derivative of the surface plasmon field formed on metallic surfaces and show similar field patterns on the surface of the bow-tie antenna with and without the near-field probe present. The invasiveness of the probe only becomes evident near the edges of the antenna. The results show that the integrated sub-wavelength aperture probe can be applied to imaging of surface plasmon waves on patterned metallic surfaces, such as antennas and metamaterials.

6.1.2 Integrated sub-wavelength aperture near-field probe

In the experimental system, the integrated sub-wavelength aperture probe is positioned within a few microns of the sample surface (Figure 6.1 a)). The sample is illuminated from the substrate side by an unfocused THz beam formed by a cylindrical waveguide [6.11]. The probe contains a GaAs photoconductive antenna detector attached to a transparent substrate (the antenna and the low temperature grown GaAs layer facing the substrate), and a flat thin metallic screen (gold, 600 nm) deposited on the back side of the thinned GaAs layer [6.17]. The screen has a 20 μm × 20 μm aperture in the centre of the antenna region (Figure 6.1 a), inset). Details of the probe design, fabrication and its performance with a THz time-domain system are described in [6.17], [6.18]. The probe detects only a local value of the THz field in the region of the aperture. A field distribution near the sample surface therefore can be mapped by scanning the sample with respect to the probe. In order to keep the illumination field constant during the scan, the sample is attached rigidly to a waveguide.

The effect of the probe on the sample is equivalent to the effect of an infinite metallic plane positioned parallel to the sample surface, because the screen is large in size (≈ 2 mm × 6 mm) compared with the bow-tie antenna and the illuminating beam. It can also be assumed that the aperture in the screen does not perturb the field distribution because the aperture is significantly smaller than the wavelength and the sample.

The metallic screen can support surface waves excited within the sample. Consider a sample that contains a planar bow-tie antenna on a dielectric substrate and plasmon waves excited on the antenna surface by a THz wave incident from the substrate side. The incident wave forms an electric field pattern, which represents travelling and standing surface waves on the antenna surface (Figure 6.1 b)). The electric field vector is oriented perpendicular to the surface in the close proximity to the surface and it decays exponentially away from the surface. It is important to consider the effect of the metallic plane of the probe positioned parallel to the antenna surface. Although the field distribution near the antenna is in general affected by the metallic surface, the pattern of the surface plasmon wave is expected to remain similar to the original pattern because the original surface plasmon field satisfies the boundary conditions imposed by the metallic plane.

The choice of the bow-tie antenna as a sample to analyse in the experiment is justified by its size and shape. The bow-tie antenna employed in this work is 600 μm long and offers a large enough area for correct detection of surface waves; the spectral content of the THz pulse that is used to excite the antenna (1.4 to 2.1 THz) contains frequencies significantly higher than the half-lambda resonance of the bow-tie antenna and can therefore produce identifiable patterns. The shape of the antenna enables formation of interference patterns due to reflections travelling from multiple directions. The antenna is also much bigger than the probe aperture, which defines the spatial resolution. It is noted that detection of surface waves on metallic structures with features comparable in size to the aperture can be ambiguous because, near the edges, the incident field is also detected by the probe.

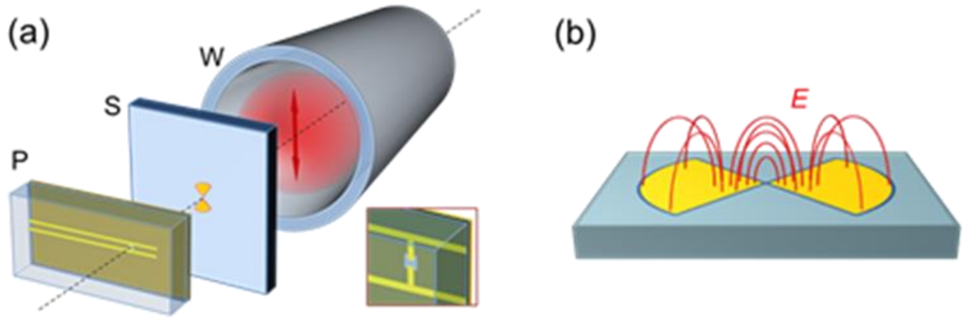

Figure 6.1: a) Schematic diagram of the experimental arrangement [6.1] showing the integrated near-field probe (P), the bow-tie antenna sample (S), and the THz waveguide (W). The inset shows an enlarged antenna section of the probe. b) Schematic diagram of the bow-tie antenna sample showing the electric field lines forming on the antenna surface when it is illuminated by the THz beam from the substrate side.

The sub-wavelength aperture allows a small amount of the surface plasmon wave to couple through it as an evanescent field. This field is measured by the THz photoconductive antenna detector, however the relationship between the detected field and the surface plasmon wave field in the vicinity of the aperture is not direct. According to the coupling mechanism proposed in [6.11], the in-plane variation of the surface plasmon field causes a potential difference on the opposite edges of the aperture. The corresponding electric field is in the plane of the aperture and it is proportional to the in-plane gradient of the surface plasmon wave distribution. The THz photoconductive antenna is also oriented in the plane of the aperture and therefore the field coupled through the aperture can be detected by the antenna as a projection of the gradient vector on the antenna axis. The mapping of the field distribution therefore results in an image that combines the surface plasmon wave pattern on the antenna and the incident field distribution.

The next section discusses the results of numerical simulations to model the integrated near-field probe by a metallic plane positioned at distance of 3 μm away from the bow-tie antenna sample. The surface plasmon field formed by a modelled THz pulse between the antenna surface and the probe surface is compared to the surface field formed without the metallic plane present. The results of the simulations allow verification of the coupling mechanism and an initial evaluation of the invasiveness of the near-field probe.

6.1.3 Numerical modelling and simulation

Previous work proposed a hypothesis, supported only by a simplified explanation of the coupling mechanism and experimental clues, suggesting that the physical quantity detected by the probe on metallic surfaces is in fact the spatial derivative of the electric field normal (z in the experiment) component with respect to the direction parallel to the dipole inside the probe (which in the experiment coincides with the y axis). This simulation intends to provide, for the first time, conclusive evidence of the accuracy of the proposed hypothesis. For this purpose the experimental system based on the sub-wavelength aperture probe is modelled and the windowed time domain experiment described in [6.11] is replicated numerically. All numerical simulations are performed using CST Studio Suite and all data pre- and post-processing is carried out in MATLAB.

An overview of the model structure is shown in Figure 6.2 a), while Figure 6.2 b) illustrates the plane wave employed as excitation source. The bow-tie antenna chip has been modelled following the system employed in the laboratory experiment [6.11], with the following geometrical parameters: 1) angle α = 90°; 2) radius r = 300 µm; 3) gap in the midpoint g = 10 µm; 4) lossy gold thickness t_m = 300 nm; 5) loss free GaAs substrate height, width and thickness h_s = 1460 µm, w_s = 1290 µm and t_s = 150 µm respectively. The properties of gold [6.19], [6.20] and GaAs [6.21], [6.22] used for the simulation are shown in Table 6.1 and the geometrical parameters are listed in Table 6.2 together with their values.

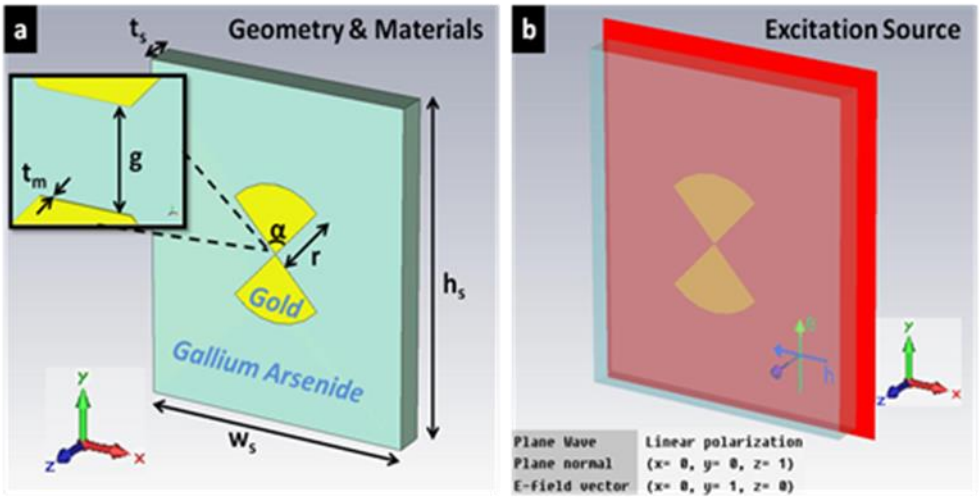

Figure 6.2: (a) Model structure and materials. (b) Plane wave employed as excitation source. [6.1]

The modelled probe response must not be affected by reflections inside the substrate or border effects originating at the edges of the substrate. However the perfect boundary absorption could not be applied right at the faces of the GaAs substrate because, when using a plane wave as excitation, the material at the absorbing boundaries must be homogeneous; this is not the case for our model where GaAs and air would both be present at the boundaries. The modelled antenna chip was then completely surrounded by air and reflections within the GaAs substrate would take place. The size of the substrate was therefore modelled large enough to allow the waveform coming from the excitation source to pass over the antenna undisturbed, before any reflection from the substrate sides could affect the probe within the time window in which its response was analysed.

The presence of the probe over the bow-tie antenna is taken into account by placing an infinite gold plane that acts as z_{max} boundary condition, 3 µm above the substrate. All the other boundary conditions are set to “open (add space)” meaning that some space between the faces of the substrate and the boundary box is filled with background material, air in this case.

Table 6.1: Physical properties of the materials used in the model.

Material Properties				
Material	**Type**	**Dielectric Permittivity**	**Magnetic Permeability**	**Electrical Conductivity**
Gold	Lossy Metal	--	1	4.561×10^7 [S/m] [6.19],[6.20]
Gallium Arsenide	Loss Free Isotropic Dielectric	12.94 [6.21],[6.22]	1	--

Table 6.2: List of the geometrical parameters

Geometrical Parameters		
Name	**Value**	**Unit Measure**
r	300	μm
α	90	deg
t_m	300	nm
g	10	μm
t_s	150	μm
h_s	1460	μm
w_s	1290	μm

As shown in Figure 6.2 b) the excitation source is modelled as a plane wave propagating forward along the z axis and linearly polarised in the y axis. In order to match the modelling as closely as possible to reality, the waveform employed for the numerical simulation was calculated from the actual signal detected in the laboratory experiment performed by Dr. Raimund Mueckstein [6.11], whose samples are shown in Figure 6.3 with black circles, and was imported into the model as an ASCII file. A pre-processing of the detected samples was necessary to make the signal compatible with the software requirements, and consisting of four steps: 1) up-sampling to adapt the coarse detected signal to the much finer time step used in the CST default waveforms; 2) removing the abrupt truncations at the start and end points of the function as they would introduce ripples in the frequency domain; this is done by fitting the signal extremities to appropriate sinusoidal signals rapidly decaying to zero; 3) scaling to give the function an amplitude compatible with the typical values employed in the CST default waveforms; 4) removing a small DC component present in the waveform detected in the lab experiment. The experimental samples of the original waveform were detected on the same face of the substrate where the bow-tie antenna lies, but far enough from the antenna and the borders of the substrate to avoid any interference from the antenna response, the reflections inside the substrate or the border effects; the same detection has also been performed numerically to make sure that the signal time of flight and the temporal derivative effect introduced by the probe on the incident field tangent component [6.11] were properly taken into account. The waveform depicted as a continuous line in Figure 6.3 represents the signal detected in the simulation on the same plane containing the antenna but far away from any interference.

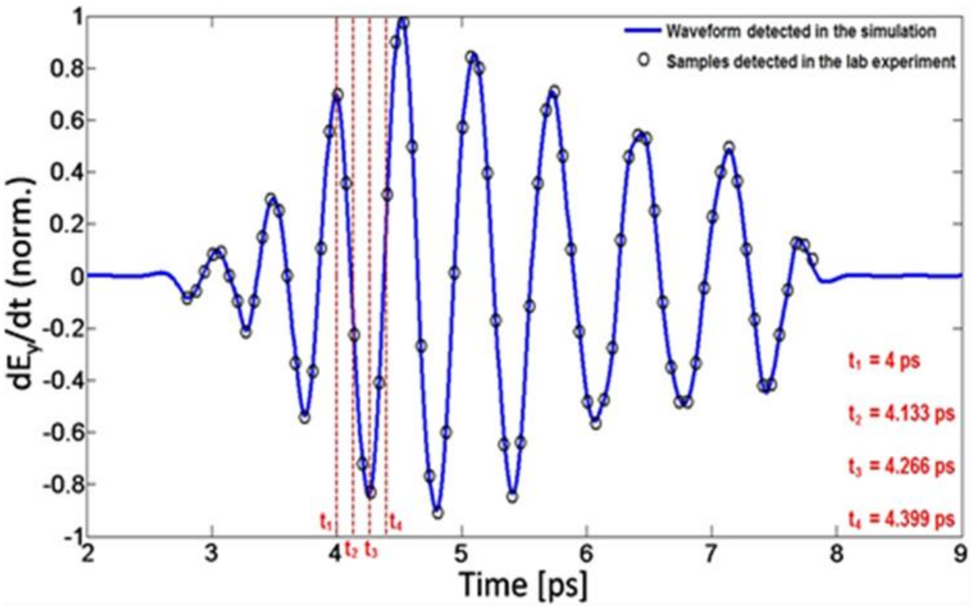

Figure 6.3: Excitation waveform. The black circles are the samples of the actual signal detected in the laboratory experiment performed by Dr. Raimund Mueckstein [6.11]. The waveform depicted as a continuous line represents the signal in the simulation arriving at the same detection point. As explained in [6.11], far away from any interference, the probe detects the time derivative of the transverse incident field (E_y in this work). The instants t_1, t_2, t_3, t_4 are the times at which the field was mapped in the laboratory experiment.

The instants t_1, t_2, t_3, t_4 highlighted in Figure 6.3 are the times at which the field was mapped in the laboratory experiment. Thus, in order to compare the experimental and the numerical results, the simulation has to calculate the electric field on the surface of the antenna over a lapse of time containing the instants t_1, t_2, t_3, t_4. The values of the z component of the electric field calculated 3 µm over the substrate in the instants t_1, t_2, t_3, t_4 were then exported in ASCII files with x step and y step of 1 µm. These ASCII files were then imported in MATLAB to calculate the spatial derivative. The goal is to demonstrate that the physical quantity detected by the probe on the metal of the antenna is the spatial derivative of the electric field z component on the surface of the antenna. Finally, in order to carry out a comparison with the measurement results, the matrices containing the electric field derivative values were mapped and saved as images.

6.1.4 Results and Discussion

The comparison between the measurement and the numerical calculation results is shown in Figure 6.4. The images in the first row represent the patterns mapped with the data collected in the laboratory experiment performed by Dr. Raimund Mueckstein [6.11]; in these images the current detected at the output of the photoconductive antenna inside the sub-wavelength aperture probe is plotted. The images in the second row are the results of the CST simulation followed by the MATLAB post-processing and display the spatial derivative of the electric field z component. Since the probe in general detects the combination of the normal and the tangent components, the comparison is valid only on the metallic surface of the bow-tie antenna, where no incident field is present.

The good agreement between numerical calculation and experimental results demonstrates that the physical quantity detected by the probe is indeed the spatial derivative of the electric field of the surface wave. It is important to note that the experimental images obtained with the sub-wavelength aperture probe are not expected to depend on the aperture size as long as the aperture is significantly smaller than the wavelength and smaller than the sample features. It was shown previously that an incident THz pulse (E_x) detected by the sub-wavelength aperture probes with different aperture sizes, shows the same waveform shape [6.23], i.e. the probe frequency response scales by a constant if the aperture size is varied. Based on the coupling model proposed in [6.11], it is expected that the frequency response to the E_z component, similarly to the response to E_x component, maintains its functional frequency dependence if the aperture size is varied. As a consequence, the detected images and time-domain waveforms are not expected to depend on the probe aperture size. This conclusion is consistent with the result of the modelling in which no assumption is made about the aperture size except that it is substantially smaller than the wavelength. Smaller apertures, of course, improve the spatial resolution, whereas the patterns themselves are not affected; it is noted that the amplitude of the detected signal decreases with the aperture size.

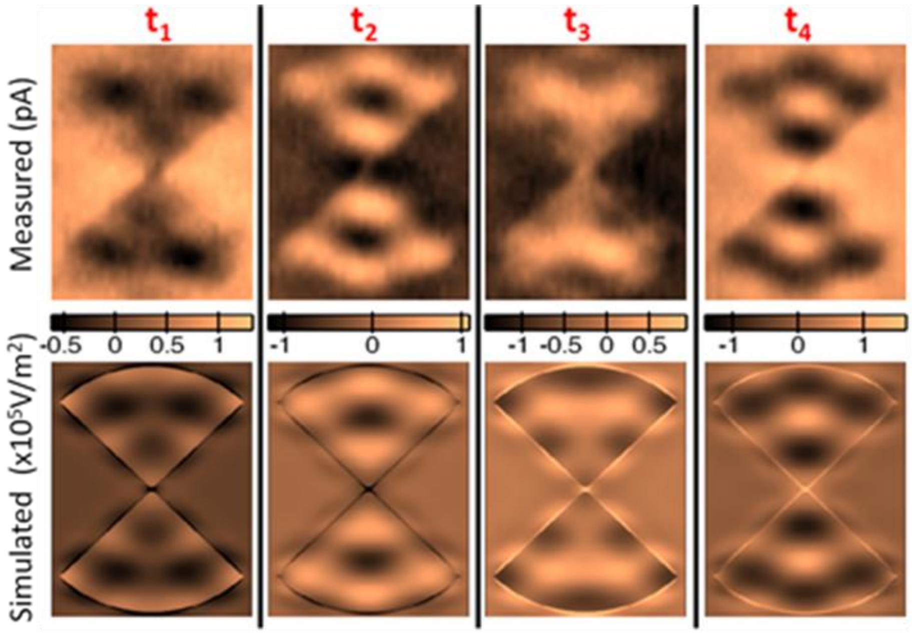

Figure 6.4: Comparison between the patterns mapped in the laboratory experiment performed by Dr. Raimund Mueckstein [6.11] and the patterns obtained through CST simulation and MATLAB post-processing. The experimental images depict the current detected at the output of the photoconductive antenna inside the probe. The numerical images depict the spatial derivative dEz/dy of the electric field z component. Each image covers an area of 460 x 620 μm^2.

Figure 6.5 also shows the good agreement between the time-domain waveform detected in the laboratory experiment (black circles) on the metal of the antenna at a distance of 175 µm from the centre of the gap and the time-domain waveform of the electric field z component spatial derivative $dE_z(t)/dy$ obtained in the simulation (continuous line) at the same location. The comparison is only valid before the instant 7 ps indicated by the dashed line because, after this instant, the reflections originating from the faces of the substrate reach the antenna and cause interference in the simulation. As explained previously, the substrate in the numerical model has been designed to be significantly smaller than the real substrate employed in the laboratory experiment, in order to reduce the computational load; as a consequence the reflections are detected earlier in the simulation than in the real experiment. It should be noted the powerful hardware employed to perform the simulation discussed in Chapter 4, 5 and 7 was not available when the work presented in this section was carried out.

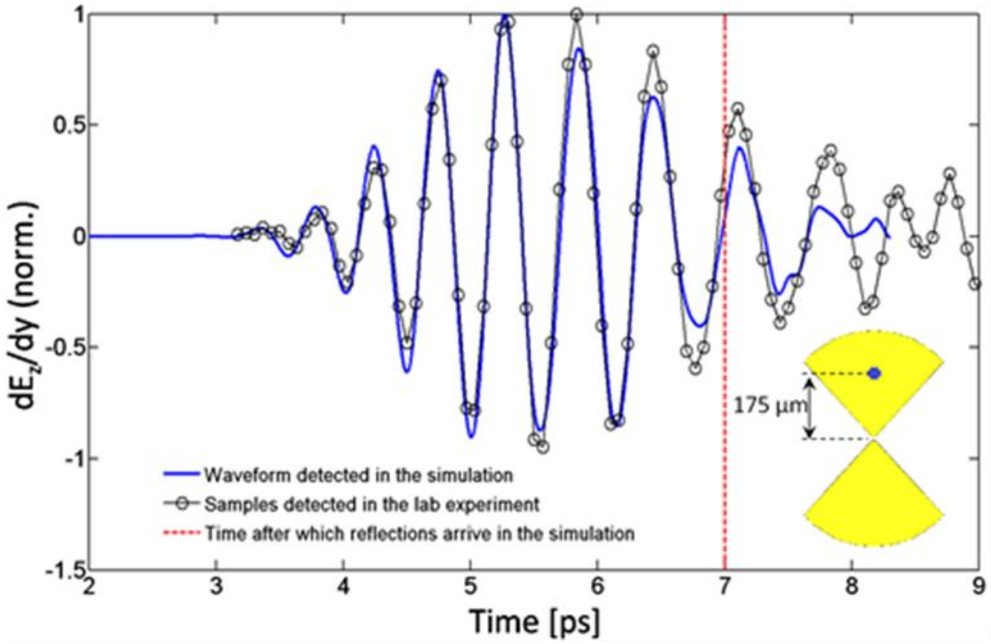

Figure 6.5: Comparison between the time-domain waveform detected in the laboratory experiment (black circles) on the metal of the antenna at a distance of 175 µm from the centre of the gap and the time-domain waveform of the electric field z component spatial derivative $dE_z(t)/dy$ obtained in the simulation (continuous line) at the same location (shown in the inset). The comparison is only valid before the instant 7 ps, indicated by the dashed line; after this instant the reflections from the faces of the substrate reach the antenna and cause interference in the simulation.

The mapping of the field distribution on THz antennas allows application of near-field imaging in further studies of antenna analysis and design. In order to carry out a first assessment of the invasiveness of the probe on the surface wave during the considered window of time, a second simulation was run to calculate the distribution of the electric field over the antenna when the probe is not present. The z_{max} boundary condition over the antenna is therefore changed to “open (add space)”.

The comparison between the electric field z component on the antenna at the time t_1, t_2, t_3, t_4 with and without the probe is illustrated in Figure 6.6. The presence of the metallic plane 3 µm over the antenna seems to support the normal component of the electric field resulting in larger values of the field, as is evident from the scale on the colour bars in Figure 6.6. The difference in amplitude is, though, not important as long as the pattern of the electric field distribution is not affected significantly by the probe. The colours in the case without probe have been saturated to highlight the distribution pattern and allow a comparison. Apart from a border effect, that is worth further investigation, the distribution of the electric field within this early window of time has not changed significantly, with maxima and minima still present in the same locations.

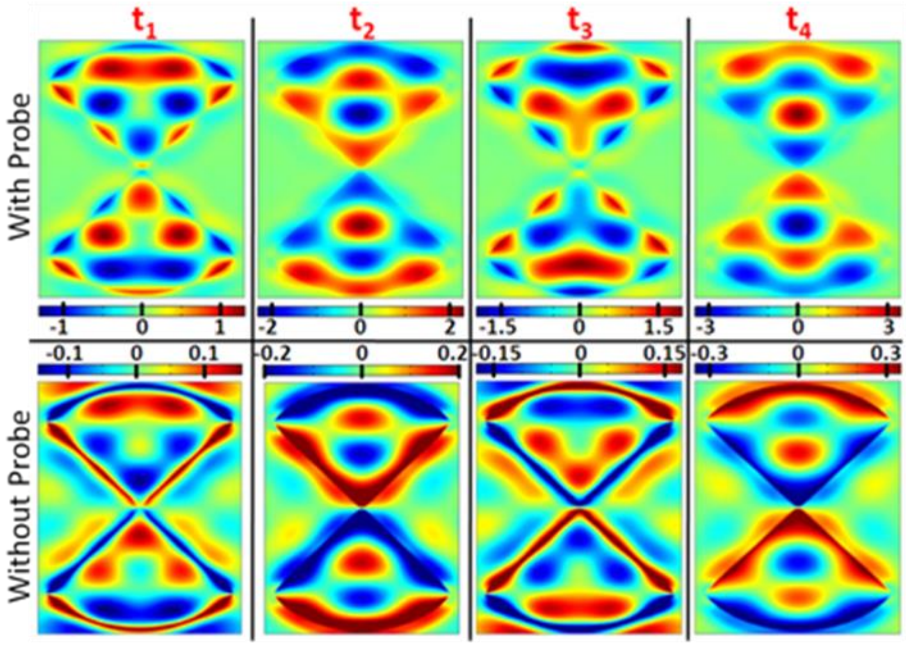

Figure 6.6: Comparison between the simulated E_z component on the antenna at the times t_1, t_2, t_3, t_4 with and without the probe. The scale in the case without the probe has been saturated to highlight the distribution pattern and allow a comparison.

6.2 Probe far-field properties and applications

An essential step in the realisation and optimisation of antennas is the experimental characterisation of the far-field radiation pattern. At sub-millimetre wave and THz frequencies this type of measurement is challenging and no standard experimental arrangement exists. Part of the challenge can be attributed to the available power-meters, i.e. Thomas Keating and Golay Cell. Both these power-meters are very sensitive to vibrations, require the detected signal to be 100 % amplitude modulated (which may entail the presence of a mechanical chopper in front of the detector) and need an infra-red (IR) filter since they are very broad band detectors and would also pick up any background IR power; the idea of mounting either power-meters on any mechanical system scanning the hemisphere in front of the antenna source appears really impractical. Furthermore the Thomas Keating 40 mm window aperture [6.24] is too large to provide a good angular resolution, unless the distance between source and power-meter is increased accordingly. On the other hand, the option of measuring the antenna radiation pattern by changing the antenna orientation while maintaining the power-meter in a fixed position and at a fixed distance, is equally impractical when characterising unpackaged antenna integrated photodiodes. Rotating the device would almost certainly influence the fibre to optical waveguide alignment; any change of radiated power with respect to the angular position could be due to either the antenna directivity or simply to a fibre to chip coupling efficiency deterioration.

The experimental system based on the sub-wavelength aperture probe, whose details can be found in [6.17] and [6.18], has been extensively employed to map near-fields across planar surfaces [6.11], [6.17], [6.25], [6.26] proving to provide repeatable and accurate results. The spatial resolution is defined by the aperture size and can be as good as 3 μm [6.2], while the step by which the planar scanning is performed can be of several μm. In a recent paper [6.27] the probe has been employed to provide a detailed analysis of the THz emission generated by photo-excited charge density gradients on GaAs and Fe-doped InGaAs surfaces; as well as mapping the near-field in the vicinity of the surfaces, the probe was also employed to detect the THz emission in the far-field region.

The radiation emitted by a finite size source is equivalent, far away from the source, to spherical wave-fronts centred at the source; at each location on the wave-front the electrical and magnetic field are orthogonal to one another and are both orthogonal to the propagation direction, which coincides with the radial direction. The propagation direction also coincides with the Poynting vector which defines the power flow. The ideal characterisation of a source radiation pattern would hence be realised by scanning a large enough hemispherical surface centred at the source, and detecting, at each point, the power delivered by the Poyinting vector to the elementary surface orthogonal to the Poynting vector. This seems to suggest that if the sub-wavelength aperture probe is to be used to measure antenna far-fields, the probe aperture plane should be orthogonal to the incident Poynting vector (radial direction) at all locations and the distance between probe aperture and antenna source should be maintained constant. It is going to be shown that the antenna far-field radiation pattern, within a solid angle subtended by a planar surface in the antenna far-field region, can instead be obtained by simply mapping the incident field across the same planar surface by means of the sub-wavelength aperture probe system. Every point scanned across the plane will be at a different distance from the source, which can be taken into account knowing that the field amplitude in the far-field region is inversely proportional to the distance. The fact that the incident Poynting vector will have a different orientation with respect to the aperture and its normal, can be accounted for thanks to a property of the probe verified by means of full-wave modelling. The probe 3D model is described in Figure 6.7.

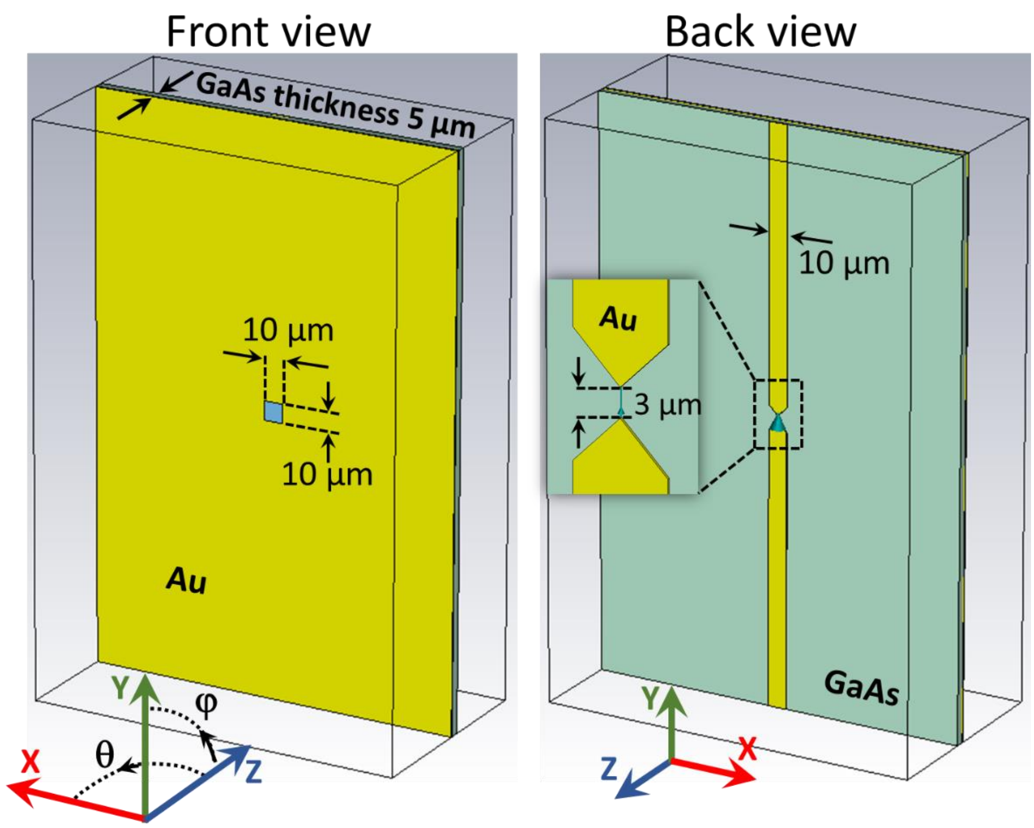

Figure 6.7: Probe complete model. The front view shows the gold screen and the 10 x 10 μm^2 aperture, where the incident field is received. The back view shows the 10 μm wide metal strips making up the photoconductive antenna; the metal strips have been extended as far as the perfectly absorbing boundaries in order to avoid any reflection. The back view inset gives details of the 3 μm antenna gap, where the voltage induced by the incident wave is recorded.

The front view shows the gold screen and the aperture (10 x 10 μm^2 size chosen for this analysis) where the incident field is received. The back view shows the 10 μm wide metal strips making up the photoconductive antenna; the metal strips have been extended as far as the perfectly absorbing boundaries in order to avoid any reflection. The back view inset gives details of the 3 μm antenna gap, where the voltage induced by the incident wave is recorded.

The default excitation source employed for this simulation consists of a plane wave linearly polarised along the Y axis and propagating along the positive orientation of the Z axis; this situation corresponds to the angles φ and θ, shown in Figure 6.7, being both equal to zero. Starting from this scenario, Figure 6.8 shows how the detected voltage changes as the plane wave propagation direction (i.e. Poynting vector) is rotated within the plane YZ by an angle φ ranging from 0^{o} to 85^{o}, while the angle θ is maintained constant at zero degrees.

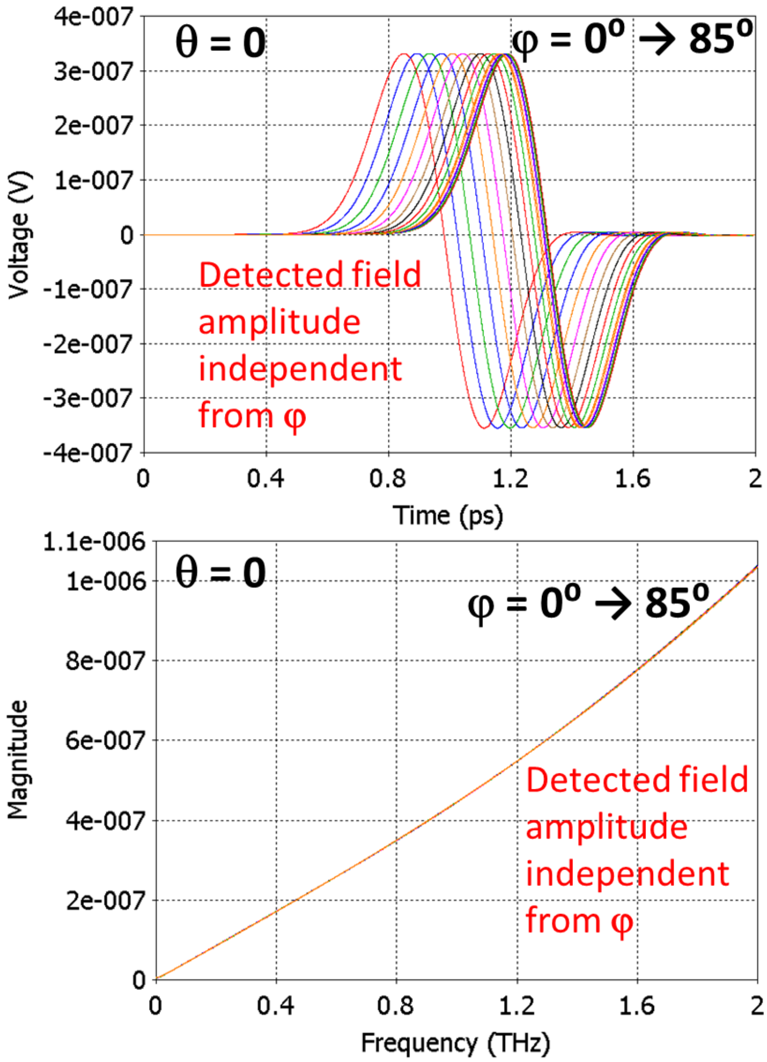

Figure 6.8: Detected voltage for different orientations of the Poynting vector within the plane YZ.

Remarkably the detected voltage is completely independent of the angle φ and the probe can be considered as an omnidirectional detector with respect to such angle. The spectra of the signals detected for different values of φ, plotted in Figure 6.8, cannot be told apart as they are practically identical, while the time shifts among the waveforms are only due to slightly different arrival times.

Figure 6.9 shows how the detected voltage changes as the plane wave propagation direction (i.e. Poynting vector) is rotated within the plane XZ by an angle θ ranging from 0^{o} to 85^{o}, while the angle φ is maintained constant at zero degree.

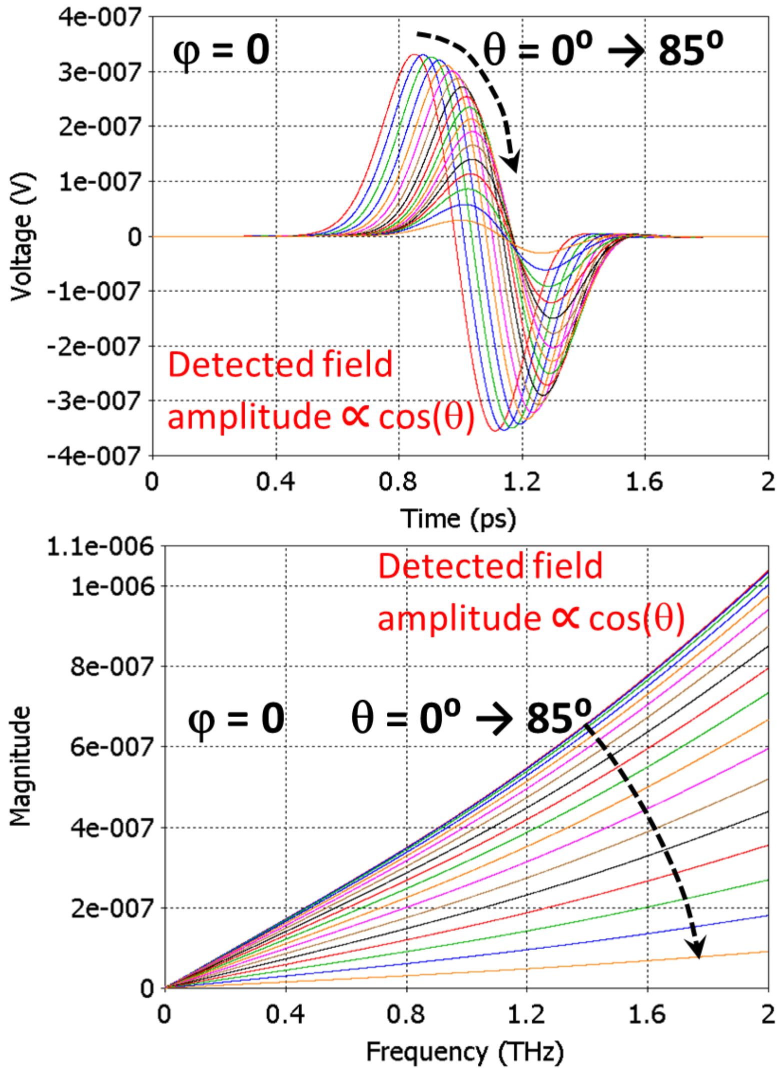

Figure 6.9: Detected voltage for different orientations of the Poynting vector within the plane XZ.

In this case the amplitude of the detected voltage changes with respect to the angle θ. However, although the detected signal does depend on the angle θ, the relation follows an exact law and is therefore easy to take into account; in fact, as shown in Figure 6.10, the amplitude of the detected voltage decreases exactly as cos(θ), with respect to the angle θ, at all frequencies. Figure 6.10 shows the amplitude of the voltage versus the angle θ, at five different frequencies (0.2 THz, 0.6 THz, 1.0 THz, 1.4 THz and 1.8 THz). The circular marks in Figure 6.10 represent the voltage spectrum amplitude values calculated in CST and are extracted from the curves in Figure 6.9, while the continuous black lines are precise mathematical cosine functions with different amplitudes; as can be seen the cos(θ) functions fit the CST results perfectly.

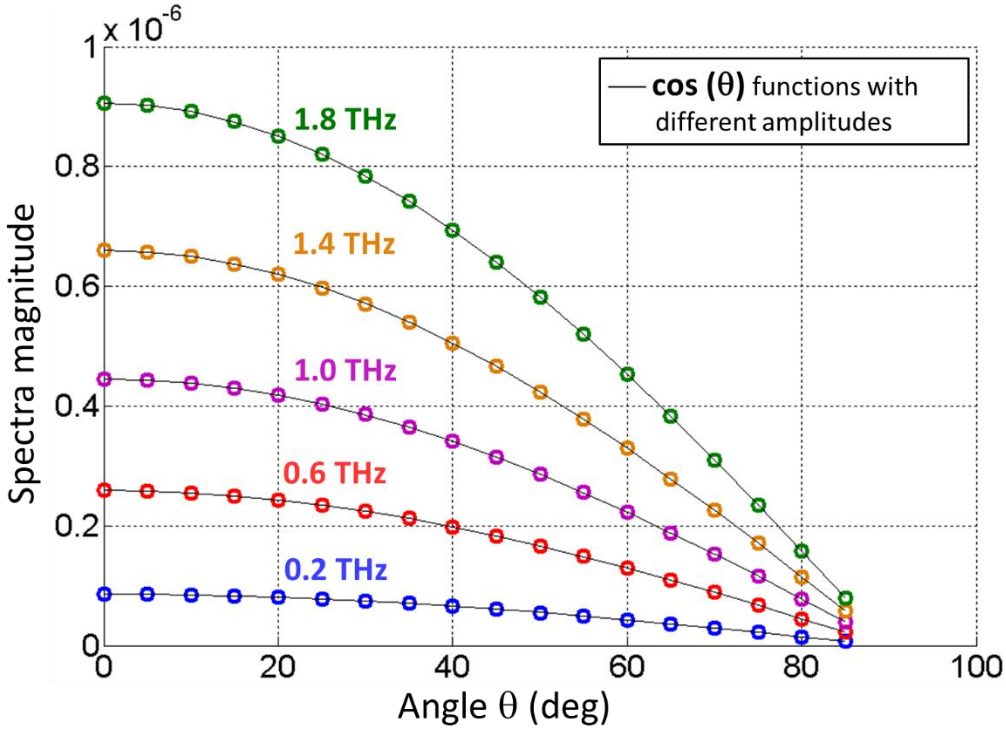

Figure 6.10: Amplitude of the voltage versus the angle θ, at five different frequencies (0.2 THz, 0.6 THz, 1.0 THz, 1.4 THz and 1.8 THz). The circular marks represent the values of voltage amplitude calculated in CST and are extracted from the curves in Figure 6.9, while the continuous black lines are precise mathematical cosine functions.

It is noted that the frequency domain results shown in Figure 6.8 and Figure 6.9 are normalised with respect to the excitation signal spectrum and hence represent the response to a Dirac delta signal (i.e. constant spectrum). It is then clear how the frequency domain functions plotted in Figure 6.8 and Figure 6.9, approximate very well the response of an ideal time-differentiator, up to a scale factor; this confirms further, that the sub-wavelength aperture probe detects the time derivative of incident fields, as already discussed in [6.1] and [6.11]. The results presented in this section, bear out that the field mapped by the sub-wavelength aperture probe across a planar surface located in the far-field of an antenna source, can be employed to obtain an accurate measurement of the antenna radiation pattern within the solid angle subtended by the planar surface.

6.3 Conclusions

The response of the integrated sub-wavelength aperture probe has been modelled and measured for the case of a bow-tie THz antenna on a dielectric substrate. The simulation results have provided conclusive demonstration that the physical quantity detected by the probe over metallic surfaces is the spatial derivative of the electric field normal component. A preliminary assessment of the invasiveness of the probe has also been carried out, showing that the probe did not modify significantly the field distribution on the surface of the antenna. The achieved full understanding of the near-field probe response and its limited invasiveness allow a correct interpretation of the images and the distribution of the electric field, and hence surface currents, to be extracted, providing important information about THz antenna operation. The sub-wavelength aperture probe has also been shown to be a valid tool to measure the far-field radiation pattern of antenna integrated photodetectors at sub-millimetre wave and THz frequencies, where this type of measurement is challenging and no standard experimental arrangements are available.

6.4 References

[6.1] M. Natrella, O. Mitrofanov, R. Mueckstein, C. Graham, C. C. Renaud, and A. J. Seeds, "Modelling of surface waves on a THz antenna detected by a near-field probe," *Opt. Express*, vol. 20, no. 14, pp. 16023–16032, Jul. 2012.

[6.2] A. J. Macfaden, J. L. Reno, I. Brener, and O. Mitrofanov, "3 µm Aperture Probes for Near-Field Terahertz Transmission Microscopy," *Appl. Phys. Lett.*, vol. 104, no. 1, pp. 011110 1 – 011110 5, Jan. 2014.

[6.3] A. J. Macfaden, J. L. Reno, I. Brener, and O. Mitrofanov, "Transmission of THz pulses through 3µm apertures: applications for near-field microscopy," *Lasers Electro-Optics (CLEO), 2014 Conf.*, pp. 1–2, 2014.

[6.4] A. J. L. Adam, "Review of Near-Field Terahertz Measurement Methods and Their Applications," *J. Infrared, Millimeter, Terahertz Waves*, vol. 32, no. 8–9, pp. 976–1019, Jul. 2011.

[6.5] K. Yang, G. David, J. G. Yook, I. Papapolymerou, L. P. B. Katehi, and J. F. Whitaker, "Electrooptic mapping and finite-element modeling of the near-field pattern of a microstrip patch antenna," *Microw. Theory Tech. IEEE Trans.*, vol. 48, no. 2, pp. 288–294, 2000.

[6.6] M. A. Seo, A. J. L. Adam, J. H. Kang, J. W. Lee, S. C. Jeoung, Q. H. Park, P. C. M. Planken, and D. S. Kim, "Fourier-transform terahertz near-field imaging of one-dimensional slit arrays: mapping of electric-field-, magnetic-field-, and Poynting vectors," *Opt. Express*, vol. 15, no. 19, pp. 11781–11789, 2007.

[6.7] A. J. Huber, F. Keilmann, J. Wittborn, J. Aizpurua, and R. Hillenbrand, "Terahertz near-field nanoscopy of mobile carriers in single semiconductor nanodevices," *Nano Lett.*, vol. 8, no. 11, pp. 3766–3770, 2008.

[6.8] R. Mueckstein and O. Mitrofanov, "Imaging of terahertz surface plasmon waves excited on a gold surface by a focused beam," *Opt. Express*, vol. 19, no. 4, pp. 3212–3217, Feb. 2011.

[6.9] K. Ishihara, K. Ohashi, T. Ikari, H. Minamide, H. Yokoyama, J. Shikata, and H. Ito, "Terahertz-wave near-field imaging with subwavelength resolution using surface-wave-assisted bow-tie aperture," *Appl. Phys. Lett.*, vol. 89, no. 20, pp. 201120 1 – 201120 3, 2006.

[6.10] M. Walther and A. Bitzer, "Electromagnetic wave propagation close to microstructures studied by time and phase-resolved THz near-field imaging," *J. Infrared, Millimeter, Terahertz Waves*, vol. 32, no. 8–9, pp. 1020–1030, Mar. 2011.

[6.11] R. Mueckstein, C. Graham, C. C. Renaud, A. J. Seeds, J. A. Harrington, and O. Mitrofanov, “Imaging and analysis of THz surface plasmon polariton waves with the integrated sub-wavelength aperture probe,” *J. Infrared, Millimeter, Terahertz Waves*, vol. 32, no. 8–9, pp. 1031–1042, Aug. 2011.

[6.12] Q.-H. Park, “Optical antennas and plasmonics,” *Contemp. Phys.*, vol. 50, no. 2, pp. 407–423, Mar. 2009.

[6.13] E. Cubukcu, N. Yu, E. J. Smythe, L. Diehl, K. B. Crozier, and F. Capasso, “Plasmonic laser antennas and related devices,” *Sel. Top. Quantum Electron. IEEE J.*, vol. 14, no. 6, pp. 1448–1461, 2008.

[6.14] P. Ghenuche, S. Cherukulappurath, T. H. Taminiau, N. F. van Hulst, and R. Quidant, “Spectroscopic mode mapping of resonant plasmon nanoantennas,” *Phys. Rev. Lett.*, vol. 101, no. 11, pp. 116805 1 – 116805 4, Sep. 2008.

[6.15] E. S. Barnard, R. A. Pala, and M. L. Brongersma, “Photocurrent mapping of near-field optical antenna resonances,” *Nat. Nanotechnol.*, vol. 6, no. 9, pp. 588–593, Sep. 2011.

[6.16] A. Kinkhabwala, Z. Yu, S. Fan, Y. Avlasevich, K. Müllen, and W. E. Moerner, “Large single-molecule fluorescence enhancements produced by a bowtie nanoantenna,” *Nat. Photonics*, vol. 3, no. 11, pp. 654–657, Oct. 2009.

[6.17] O. Mitrofanov, M. Lee, J. W. P. Hsu, I. Brener, R. Harel, J. F. Federici, J. D. Wynn, L. N. Pfeiffer, and K. W. West, “Collection-mode near-field imaging with 0.5-THz pulses,” *Sel. Top. Quantum Electron. IEEE J.*, vol. 7, no. 4, pp. 600–607, 2001.

[6.18] O. Mitrofanov, R. Harel, M. Lee, L. N. Pfeiffer, K. West, J. D. Wynn, and J. Federici, “Study of single-cycle pulse propagation inside a terahertz near-field probe,” *Appl. Phys. Lett.*, vol. 78, no. 2, pp. 252–254, 2001.

[6.19] M. A. Ordal, L. L. Long, R. J. Bell, S. E. Bell, R. R. Bell, R. W. Alexander, and C. A. Ward, “Optical properties of the metals Al, Co, Cu, Au, Fe, Pb, Ni, Pd, Pt, Ag, Ti, and W in the infrared and far infrared,” *Appl. Opt.*, vol. 22, no. 7, pp. 1099–1120, Apr. 1983.

[6.20] F. Garet, L. Duvillaret, and J.-L. Coutaz, “THz time-domain spectroscopy of nanometric-thick gold layers,” *Infrared Millim. Waves, 2004 12th Int. Conf. Terahertz Electron. 2004. Conf. Dig. 2004 Jt. 29th Int. Conf.*, pp. 467– 468, 2004.

[6.21] D. Grischkowsky, S. Keiding, M. van Exter, and C. Fattinger, “Far-infrared time-domain spectroscopy with terahertz beams of dielectrics and semiconductors,” *J. Opt. Soc. Am. B*, vol. 7, no. 10, pp. 2006–2015, 1990.

[6.22] M. Nagai, K. Tanaka, H. Ohtake, T. Bessho, T. Sugiura, T. Hirosumi, and M. Yoshida, “Generation and detection of terahertz radiation by electro-optical process in GaAs using 1.56 μm fiber laser pulses,” *Appl. Phys. Lett.*, vol. 85, no. 18, pp. 3974–3976, 2004.

[6.23] O. Mitrofanov, L. N. Pfeiffer, and K. W. West, “Generation of low-frequency components due to phase-amplitude modulation of subcycle far-infrared pulses in near-field diffraction,” *Appl. Phys. Lett.*, vol. 81, no. 9, pp. 1579–1581, 2002.

[6.24] “TK Absolute Power / Energy Meter System,” 2010. [Online]. Available: http://www.terahertz.co.uk/images/tki/PMETER/manual321.pdf. [Accessed: 10-Mar-2015].

[6.25] M. Navarro-Cía, M. S. Vitiello, C. M. Bledt, J. E. Melzer, J. A. Harrington, and O. Mitrofanov, “Terahertz wave transmission in flexible polystyrene-lined hollow metallic waveguides for the 2.5-5 THz band,” *Opt. Express*, vol. 21, no. 20, pp. 23748–23755, Oct. 2013.

[6.26] O. Mitrofanov, W. Yu, R. J. Thompson, Y. Jiang, I. Brener, W. Pan, C. Berger, W. A. de Heer, and Z. Jiang, “Probing terahertz surface plasmon waves in graphene structures,” *Appl. Phys. Lett.*, vol. 103, no. 11, pp. 111105 1 – 111105 4, 2013.

[6.27] R. Mueckstein, M. Natrella, O. Hatem, J. R. Freeman, C. S. Graham, C. C. Renaud, A. J. Seeds, E. H. Linfield, A. G. Davies, P. J. Cannard, M. J. Robertson, D. G. Moodie, and O. Mitrofanov, “Near-field analysis of terahertz pulse generation from photo-excited charge density gradients,” *Terahertz Sci. Technol. IEEE Trans.*, vol. 5, no. 2, pp. 260 – 267, 2015.

Chapter 7 - UTC PDs monolithically integrated with THz antenna arrays

In this chapter the radiation performance of three 2 x 2 antenna arrays, employing the antennas presented in Chapter 5 as single elements, is studied in CST Studio. The full-wave electromagnetic modelling of antenna arrays on substrate lenses is computationally demanding and, to the best of the author's knowledge, has not been reported to date; on the other hand it can reveal important aspects of the array-lens system performance, which could not be picked up with simplified approaches. Recently, a planar Yagi-Uda array, without any lens, has been analysed at 590 GHz [7.1]. In general though, many antenna systems were built on the substrate-lens principle, such as imaging antenna arrays [7.2], far infrared imaging antenna arrays[7.2], a 36-element imaging array for plasma diagnostics at 300 GHz [7.3], a linear polarimetric array [7.4], a two-dimensional tracking array at 240 GHz [7.5], a 119 µm imaging array [7.6]. Nevertheless, the full-wave electromagnetic modelling has revealed that substrate lenses are not suitable for integration with arrays, as their focusing properties, which have been shown to be sensitive to the alignment with the source, deteriorate dramatically due to the inevitable misalignment with the single antenna elements. Conversely, antenna arrays on a ground plane exhibit good directivity patterns, provided the mutual coupling and the substrate modes occurring through the electrically thick substrate are eliminated; this can require a challenging fabrication process.

In general mutual coupling is a natural effect in antenna array operation and can also be desirable if properly managed. It is possible to achieve array superdirectivity, in the sense that the directivity of an array of "N" elements is greater than "N" times the single antenna directivity [7.7], [7.8]; however, in this case, the total efficiency of the system deteriorates as the mutual coupling and passive reflection produce an active reflection coefficient that results in a reduced total efficiency [7.7], [7.9].

It has to be stressed that the array results shown in this chapter have been obtained by actually simulating the simultaneous excitation of all the single elements, as this allows a thorough and realistic evaluation of the mutual coupling effects. The software also provides a post-processing option which can calculate the results of an arbitrary array geometry simply by combining the result of the single antenna element; this option, though enabling a reduction of both computational load and time, has not been deemed appropriate inasmuch as the effects of the mutual coupling are ignored and the results are therefore unrealistic.

The use of antenna arrays integrated with UTC photodiodes offers advantages not only related to the increase of directivity but also in terms of maximum input power that can be fed into the system. When a single antenna is employed, the maximum current amplitude that can be driven into the antenna is limited by the saturation of the UTC, therefore, no matter how much optical power is available, there is a limit on how much RF power can be coupled into the antenna. If an array with N UTC-integrated antenna elements is employed, it is in principle possible to couple into the array N times the maximum power that was possible to feed into the single antenna integrated UTC; this will be ideally reflected in an increase of the total radiated power by a factor N, e.g. 6 dB for the case $N = 4$. In a real antenna array, mutual coupling among the antenna elements is present and influences the energy coupling between each antenna and its driving source; the impedance that each element of an array presents to its source, while influenced by the coupling with the other antennas of the array, is different from the impedance of the single antenna operating alone. In fact, the current that flows into an antenna of the array generates a voltage across the feeding point of other antennas which is described using the concept of mutual impedance. For these reasons, the mentioned 6 dB increase in total emitted power, for the case of a 2 x 2 array, occurs only if the mutual coupling among the antennas is negligible.

The first array presented here, which operates with a ground plane, employs Antenna 2, discussed in Chapter 5, as the antenna element; an overview of the optimised configuration for this array is shown in Figure 7.1, together with the 3D directivity pattern in dBi, at five frequencies from 335 GHz to 355 GHz. As discussed previously, the chip dimensions are part of the optimised parameters for Antenna 2 and should not be altered. While the optimised chip dimensions of a single Antenna 2 chip can be achieved by accurate cleaving, the only way to create an array using Antenna 2 as the element, is to fabricate the array on a large chip and then separate the antennas with deep trenches; this requires a challenging fabrication process. If the antenna elements were left unseparated on a whole large chip, the optimised performance of the single antenna element (Antenna 2) would be lost and strong mutual coupling among the array elements and substrate modes would further cause the array performance to deteriorate.

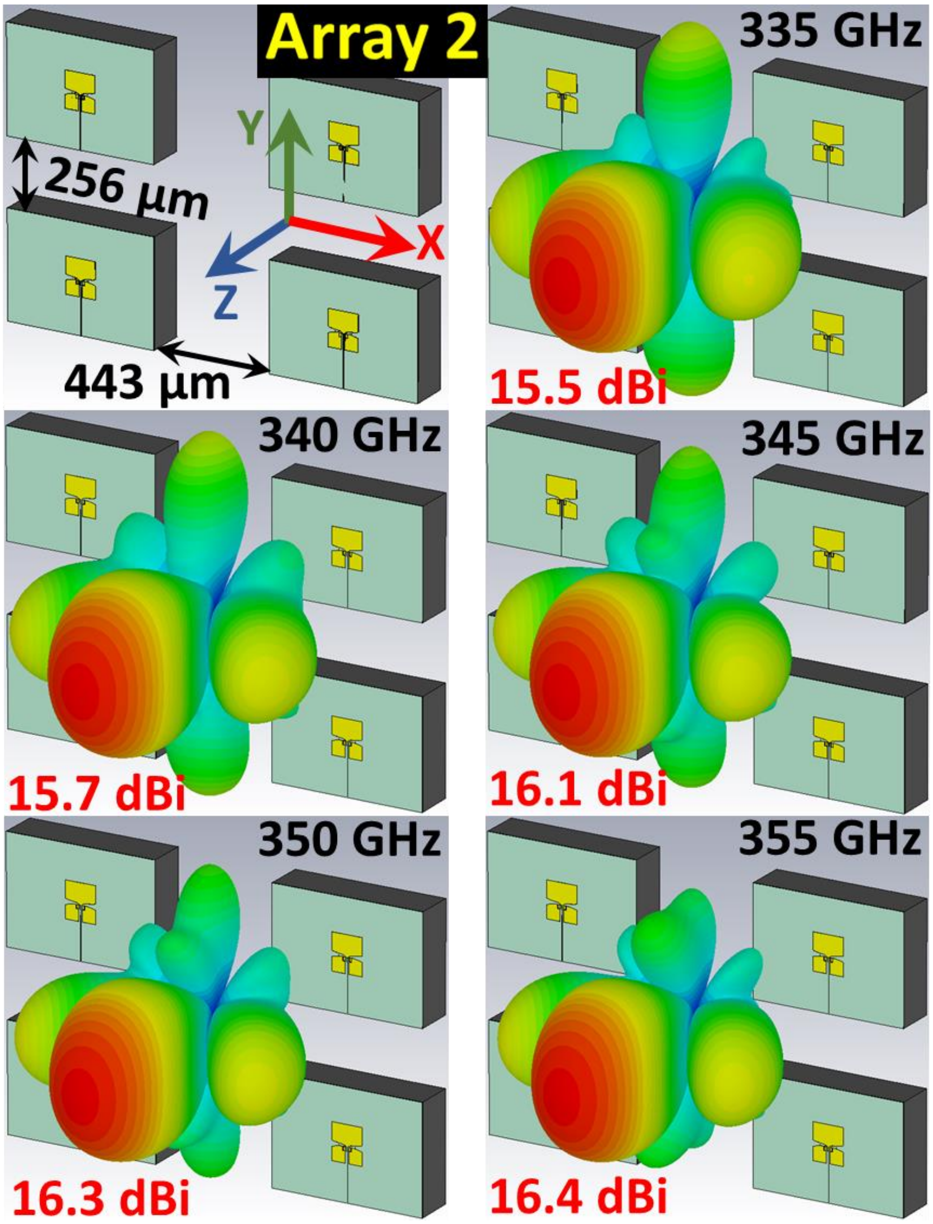

Figure 7.1: Array 2 structure overview and 3D directivity pattern in dBi from 335 GHz to 355 GHz. Array 2 employs Antenna 2 as antenna element.

For Array 2, the mutual coupling among the antenna elements is really modest and hence each antenna operates almost independently and is driven by the same current as the case of the single antenna integrated UTC. This means that the 6 dB increase of the RF power coupled into the array system is approachable for this case. Array 2 directivity along the Z axis direction, is between 5 dB and 6 dB greater than the directivity of Antenna 2. Consequently the power density radiated by Array 2 along the Z axis can be between 11 dB and 12 dB greater than that radiated by Antenna 2 alone.

The second array, also with a ground plane, employs Antenna 3 as the element, which was defined in Chapter 5. An overview of the optimised configuration for this array is shown in Figure 7.2, together with the 3D directivity pattern in dBi, at five frequencies from 335 GHz to 355 GHz.

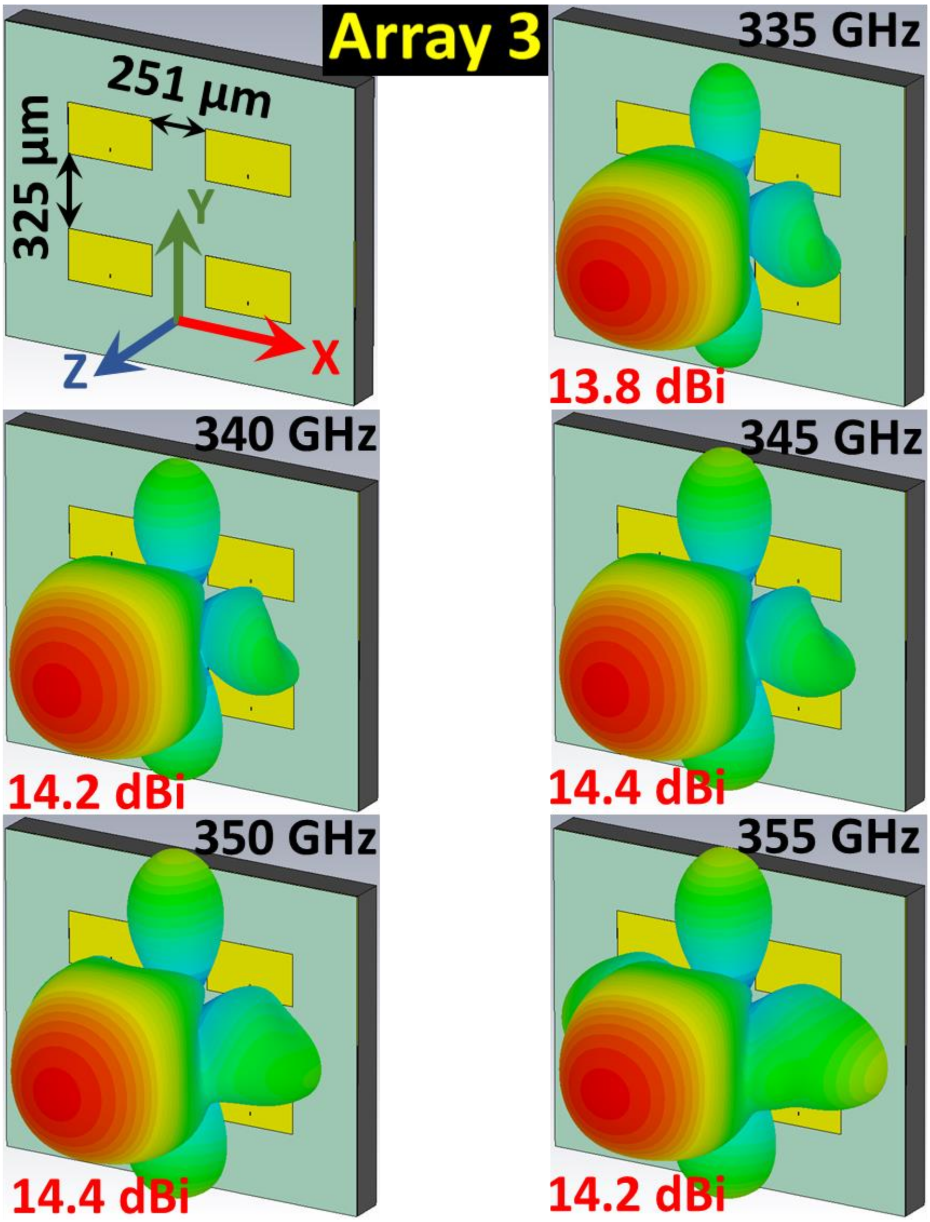

Figure 7.2: Array 3 structure overview and 3D directivity pattern in dBi from 335 GHz to 355 GHz. Array 3 employs Antenna 3 as antenna element. Antenna 3 was defined in Chapter 5.

Since Antenna 3 performance does not depend on the chip horizontal dimensions, the array can be fabricated on a whole large chip without affecting the optimised performance of the single antenna element (Antenna 3). Thanks to the presence of the gold layer deposited just below the passivation layer (SiO_xN_y or BCB), which acts as a ground plane close to the rectangular patch, low electromagnetic energy couples down in the InP substrate and no horizontal propagation within the electrically thin passivation layer occurs; consequently the mutual coupling among the array antenna elements is weak. Similarly to Array 2, the directivity of Array 3 along the Z axis direction is increased by at least 5 dB, with respect to the directivity of Antenna 3 alone. Consequently, thanks to the reduced mutual coupling and the directivity enhancement, the power density radiated by Array 3 along the Z axis can also be between 11 dB and 12 dB greater than that radiated by Antenna 3 alone. Although Antenna 3 was shown to have a lower radiation efficiency than Antenna 2 and be able to radiate less power when driven by the III-V Lab UTC, the easier fabrication of Array 3, which does not need the antenna elements to be separate by deep trenches, makes it feasible to realise larger arrays with a further increase of the power radiated along the Z axis direction.

The third array is shown in Figure 7.3; an overview of the optimised configuration is given, together with the 3D directivity pattern in dBi, at five frequencies from 335 GHz to 355 GHz. This lens-array essentially consists of Array 2 on a 5 mm diameter Si lens instead of the ground plane. As can be seen, the radiation pattern is very irregular and changes noticeably over the frequency range while remaining very poor. As shown in Chapter 5, ongoing internal reflections do occur in substrate lenses and tend to become even more significant when the misalignment between chip and lens is not perfectly realised. Thus, when a lens is integrated with an array, its focusing properties are lost entirely, because of the inevitable and substantial misalignment with each antenna element; the energy trapped inside the lens in the form of ongoing internal reflections, is progressively and unevenly transferred into free space, following unpredictable radiation patterns that change sharply over the frequency range. A cross section view of the lens-array structure, through the plane [XZ], is given in Figure 7.4 and shows the amplitude of the electric field at 350 GHz. Such a system would not be useful for any sub-millimetre wave application.

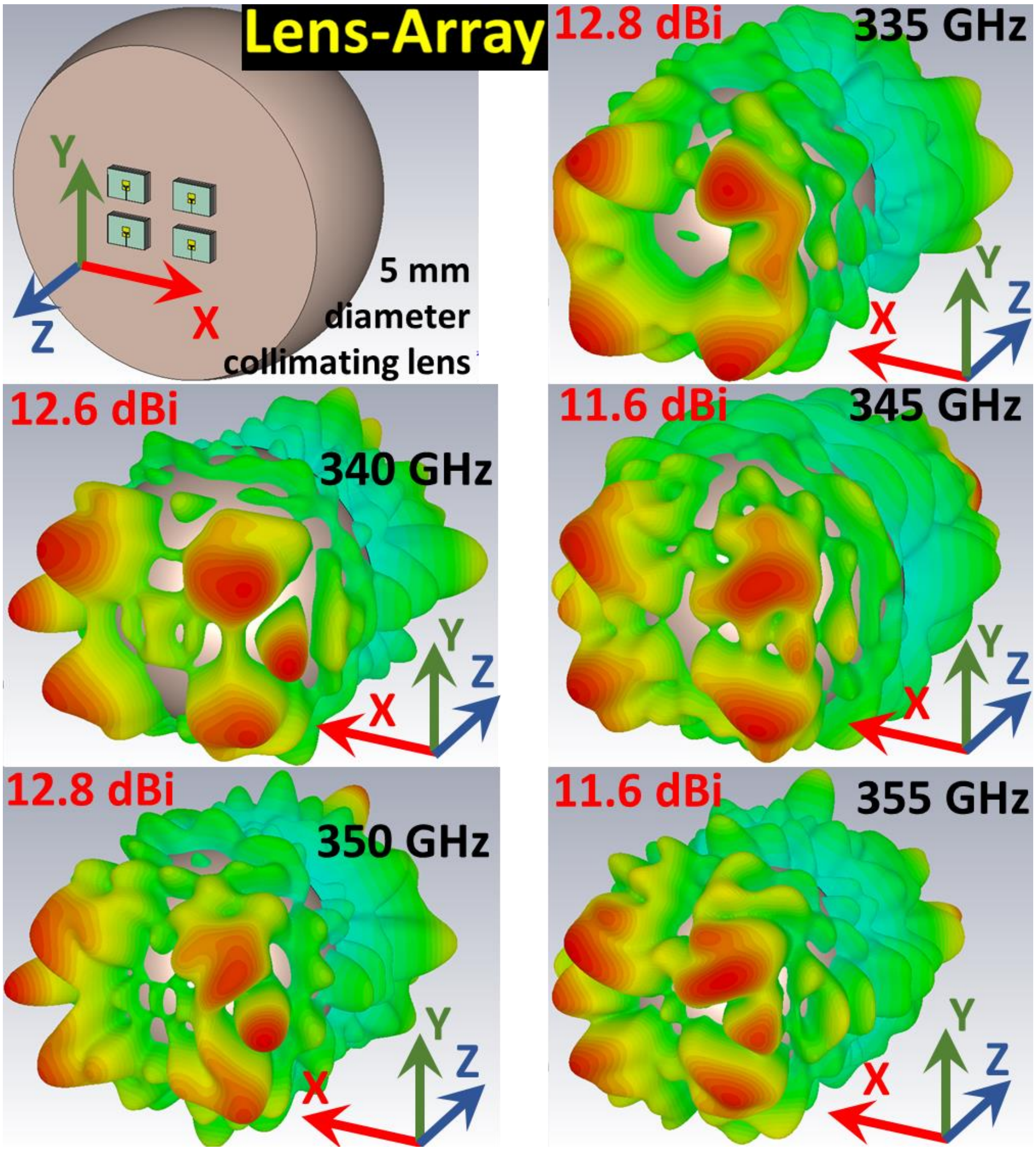

Figure 7.3: Overview of lens-array and 3D directivity pattern in dBi from 335 GHz to 355 GHz. Lens-array essentially consists of Array 2 on a 5 mm diameter Si lens instead of the ground plane.

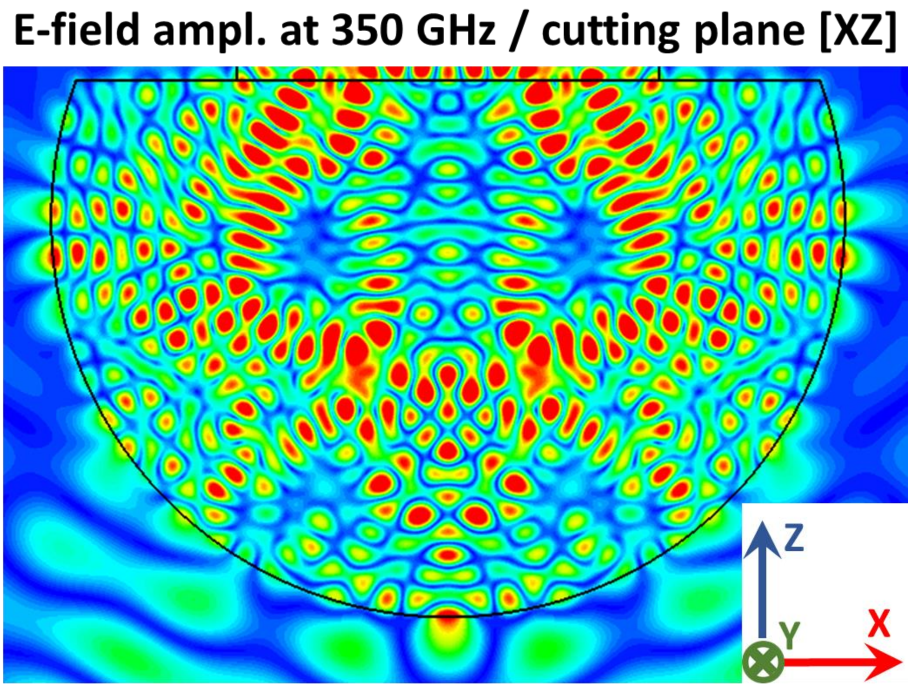

Figure 7.4: Cross section view of the lens-array structure, through the plane [XZ], showing the amplitude of the electric field at 350 GHz.

7.1 Conclusions

In this chapter three different 2 x 2 array designs, to be monolithically integrated with UTC-PDs, have been discussed. The first array (Array 2) operates with a ground plane and employs Antenna 2, discussed in Chapter 5, as antenna element; Array 2 exhibits good performance in terms of radiation pattern and shows reduced mutual coupling among its elements, although requiring a challenging fabrication process to separate the antenna elements.

The second array (Array 3) also operates with a ground plane and employs Antenna 3, discussed in Chapter 5, as antenna element. Array 3 overcomes the mutual coupling problem without requiring difficult fabrication, and is suitable for easy fabrication of large arrays.

The third array (lens-array) essentially consists of Array 2 on a 5 mm diameter Si lens instead of the ground plane; it was found that substrate lenses are not suitable to antenna array designs, due to the inevitable and substantial misalignment between the lens and the antenna elements. The energy trapped inside the lens in the form of ongoing internal reflections, is unevenly transferred into free space, with very irregular directivity patterns that change dramatically over the frequency range. For this reasons, such a system would not be useful for any sub-millimetre wave application. By using Array 2 or Array 3, an increase of the power density radiated along the target direction, greater than 11 dB, is in principle possible.

7.2 References

[7.1] K. Han, T. K. Nguyen, I. Park, and H. Han, “Terahertz Yagi-Uda antenna for high input resistance,” *J. Infrared, Millimeter, Terahertz Waves*, vol. 31, no. 4, pp. 441–454, 2010.

[7.2] D. B. Rutledge and M. S. Muha, “Imaging antenna arrays,” *Antennas Propagation, IEEE Trans.*, vol. 30, no. 4, pp. 535–540, 1982.

[7.3] P. E. Young, D. P. Neikirk, P. P. Tong, D. B. Rutledge, and N. C. Luhmann, “Multichannel far-infrared phase imaging for fusion plasmas,” *Rev. Sci. Instrum.*, vol. 56, no. 1, pp. 81–89, 1985.

[7.4] P. P. Tong, D. P. Neikirk, P. E. Young, W. A. Peebles, N. C. Luhmann, and D. B. Rutledge, “Imaging polarimeter arrays for near-millimeter waves,” *Microw. Theory Tech. IEEE Trans.*, vol. 32, no. 5, pp. 507–512, 1984.

[7.5] P. P. Tong, D. P. Neikirk, D. Psaltis, D. B. Rutledge, K. Wagner, and P. E. Young, “Tracking antenna arrays for near-millimeter waves,” *Antennas Propagation, IEEE Trans.*, vol. 31, no. 3, pp. 512–515, 1983.

[7.6] D. P. Neikirk, P. P. Tong, D. B. Rutledge, H. Park, and P. E. Young, “Imaging antenna array at 119 µm,” *Appl. Phys. Lett.*, vol. 41, no. 4, pp. 329–331, 1982.

[7.7] A. Ludwig, “Mutual coupling, gain and directivity of an array of two identical antennas,” *Antennas Propagation, IEEE Trans.*, vol. 24, no. 6, pp. 837–841, 1976.

[7.8] M. Wang, W. Wu, and Z. Shen, “Bandwidth Enhancement of Antenna Arrays Utilizing Mutual Coupling between Antenna Elements,” *Int. J. Antennas Propag.*, vol. 2010, no. Article ID 690713, pp. 1–9, 2010.

[7.9] R. E. Collin and F. J. Zucker, *Antenna theory*. New York: McGraw-Hill, 1969.

Chapter 8 - Conclusions and future work

The results and discussions presented in this thesis aim to contribute to advances in the realisation of Continuous Wave (CW) Photonic Terahertz (THz) Emitters based on InP Uni-Travelling-Carrier Photodiodes (UTC-PDs) integrated with THz antennas or arrays of THz antennas. The portion of the electromagnetic spectrum comprised between microwave and infrared radiation (i.e. THz gap) has been subject to intense study during the last 20-30 years due to the number of exciting potential applications in this frequency range. Although significant progress has been achieved, the THz gap is certainly the least tapped region of the electromagnetic spectrum and our capability to generate, manipulate and detect THz and sub-millimetre waves is still at its early stages compared to other frequency ranges. The results and discussions in this thesis can contribute to filling in the THz gap, since the solution employing photonic techniques for the generation of sub-millimetre and THz waves, via photomixing of lasers operating at 1550 nm, is a major candidate for the realisation of tuneable, power efficient, compact and cost effective sources operating at room-temperature; indeed, the availability of sources endowed with such properties would make many important applications possible in this frequency range, such as ultra-broad band wireless communications, spectroscopic sensing and THz imaging.

An overview of the THz gap has been given in the thesis introduction. The advantageous properties of this type of radiation have been explained and the technological solutions needed to fully exploit the potential of this frequency range and make many applications possible have been discussed. A detailed review and comparison of state of the art sources for continuous wave (CW) THz generation has also been provided.

All the UTC-PDs exhibiting record breaking performance in terms of bandwidth and output power, for operation at 1.55 µm wavelength, have been fabricated on Al-free InGaAsP-based materials. It has been shown in this thesis for the first time, how InGaAsP-based UTC-PDs can be realised from materials grown by Solid Source Molecular Beam Epitaxy. By using Solid Source MBE it is possible to solve the major problem associated with the diffusion of zinc in Metal Organic Vapour Phase Epitaxy (MOVPE) and exploit the superior control provided by MBE growth techniques without the costs and the risks of handling toxic gases in Gas Source MBE. This achievement is a milestone towards the development of a simple, repeatable and high yield fabrication process enabling the realisation of high performance UTCs at UCL, from material growth to device fabrication.

The maximisation of the power extracted from a UTC is central to the successful realisation of a photonic THz emitter. When the UTCs are integrated with antennas, such maximisation entails the optimisation of the energy coupling between UTC and antenna, which in turns requires knowledge of the UTC impedance; this aspect of photonic emitters has not received much attention in the literature, having often been underestimated in favour of the physics of the device employed as a source. In this thesis a semi analytical study of the impedance of waveguide UTCs has been carried out, supported with experimental data taken up to 110 GHz, circuit analysis and 3D full-wave electromagnetic modelling of waveguide UTC structures. This study has enabled a deeper understanding of the UTC to antenna coupling efficiency question and has pointed out that the antenna design should take the complex (i.e. not real) nature of the source (UTC) impedance into account in order to realise broad band performance. A significant potential improvement in this way is then envisaged.

The coupling efficiency between the optical power source and the photodetector is another key factor in the realisation of high performance photonic emitters; for the case of edge-coupled waveguide UTCs this requires the coupling optimisation between lensed optical fibre and UTC optical waveguide. This coupling mechanism has been investigated in this thesis by means of 3D full-wave modelling. This has allowed, among other things, the optical source to be realistically modelled as a Gaussian beam incident on the waveguide facet, enabling the assessment of the external responsivity (very good agreement with the measurements was obtained), the effect of the fibre misalignment, the type of propagation excited in the UTC waveguide by the incident beam, and the way the light propagates throughout the structure; this approach will support the future design of UTC structures with increased external responsivity. Besides, the 3D full-wave analysis enables the visualisation and a better understanding of the light absorption pattern through the absorption layer which represent truly valuable information for the future coupling optimisation between long travelling wave devices and antennas up to very high frequencies.

It has been shown that the knowledge of the UTC impedance enables the calculation, by means of full-wave modelling, of the power radiated by an antenna integrated with the UTC, not only in terms of trend over the frequency range but even in terms of absolute level of emitted power. Good agreement with the experimental results has been attained.

Given a high performance UTC efficiently coupled to an antenna, the additional requirement is to obtain high performance from the antenna in terms of radiation efficiency and radiation pattern. In this thesis the design of high radiation efficiency and high directivity antennas with ground planes on electrically thick substrates, has been demonstrated at sub-millimetre wave frequencies. The ground plane solution can also offer some advantage in terms of heat dissipation. The same antennas have also been shown to work well when integrated with substrate Si lenses, however the 3D full-wave analysis has highlighted that substrate lenses only radiated efficiently and evenly if accurately aligned with the antenna chip; for these reason substrate lenses are not suitable to be used with antenna arrays. On the other hand two antenna array designs with a ground plane have been successfully modelled, although one requires a challenging fabrication to suppress the deleterious effect of mutual coupling among the antenna elements and the other, which uses a novel antenna concept with a close ground plane, exhibits narrow band operation. Significant room for improvements is envisaged in this context.

This thesis also reports an in-depth study of the response of a sub-wavelength aperture probe and its use as an additional experimental tool for the analysis of antenna near- and far-field properties, which in turn can provide valuable information for the design improvement. The probe enables the reconstruction of the electric field in the vicinity of antennas and hence the surface current distribution, providing important information about the antennas. The sub-wavelength aperture probe has also been shown to be a valid tool for the measurement of the far-field radiation pattern from antenna integrated photodetectors at sub-millimetre wave and THz frequencies, where this type of measurement is challenging and no standard experimental arrangements are available.

8.1 Suggestions for future work

In this final section a list of suggestions for future research work is given.

1) UTC-to-antenna coupling optimisation for long travelling wave photodiodes: Following from the approach developed to evaluate the UTC impedance and from the knowledge attained about the UTC-to-antenna coupling efficiency question, it is of great interest to extend this analysis to long travelling wave devices, for which the lumped element assumption no longer stands. The 3D-full-wave modelling at optical frequencies can help understand better how the light is absorbed and hence the RF current is generated across a long absorption layer. DC optical responsivity and RF power delivered to the integrated antenna over the frequency range, can both be noticeably improved.

2) Fabrication and characterisation of antenna integrated emitters with ground planes and lenses: Once the fabrication of CPW-integrated edge-coupled waveguide UTCs is optimised, the same photodetectors will be integrated with the antenna designs presented in this thesis and with further antenna designs that will be investigated. The results of the characterisation of such antenna integrated UTCs will suggest the way for further developments.

3) Fabrication and characterisation of antenna integrated emitter arrays with ground planes and lenses: The fabrication of UTCs integrated with arrays of THz antennas will follow the fabrication of single antenna integrated UTCs. Before the latter fabrication can be started, the performance and reliability of the single element antenna will be verified experimentally.

4) Further design and modelling of antenna array solutions: As mentioned previously, significant room for improvements is envisaged for the design of THz antenna arrays. Besides seeking further improvement in the array directivity and radiation efficiency, the future modelling work will aim to devise array concepts that overcome the mutual coupling issue without requiring a challenging fabrication process.

5) Fabrication of edge-coupled UTCs with tapered mode converting waveguide: A solution to improve the fibre-to-chip coupling efficiency is the use of a diluted tapered mode converting waveguide. A schematic diagram of a UTC integrated with such a waveguide designed within the Photonics group at UCL [8.1] is illustrated in Figure 26 (a), while Figure 26 (b) shows the actual device fabricated by CIP Technologies Ltd. This design can substantially increase the device responsivity and is also compatible with a Travelling Wave (TW) design, which reduces the total high frequency roll-off [8.1]. For high speed operation the width of the UTC p-contact ridge (equal to the absorber width) needs to be small while efficient light coupling from an optical fibre needs wide devices. To overcome this problem the tapered mode converting waveguide was proposed [8.2]; in this way the additional large diluted waveguide enables the Mode Field Diameter (MFD) from a lensed fibre to be matched. In the tapered section, light is coupled into the intermediate waveguide that is optimized to match the modes of the absorber.

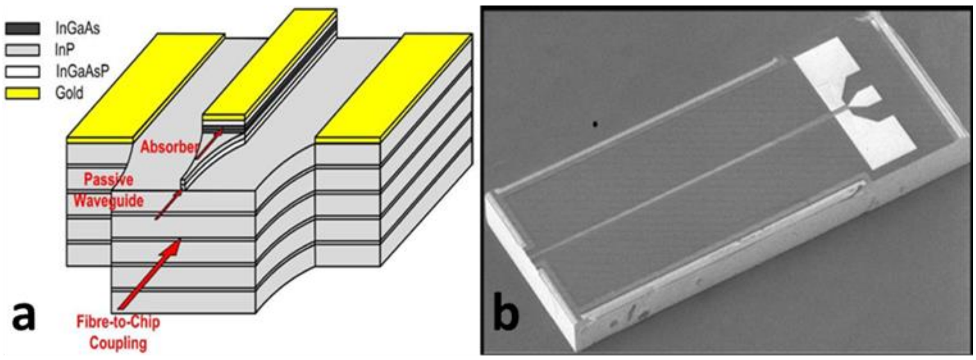

Figure 8.1: (a) Schematic diagram of an edge-couple UTC with a diluted mode converting waveguide for high efficiency lens-to-chip coupling. (b) Photograph of the device fabricated by CIP Technologies Ltd.

In the future work the fabrication of mode converting waveguide integrated UTCs will be undertaken. The fabrication of such devices is challenging due to the very narrow width of the passive waveguide at the coupling point and the high level of precision required for the alignment between diluted and passive waveguide and between passive waveguide and p-contact ridge. Moreover the growth of new materials by solid source MBE will be necessary as the diluted tapered mode converting waveguide needs additional epitaxy layers.

6) In-depth thermal analysis of UTC-PD structures: an in-depth thermal analysis of UTC-PD structures will be performed by means of the CST studio suite thermal solver.

7) Theoretical study and modelling of new UTC designs, aiming at improved and easier coupling of the optical power into the chip: A fundamental and theoretical revision and re-thinking up of the UTC concept will be considered, with the ultimate objective to mitigate the trade-off imposed by the current designs for the simultaneous optimisation of DC responsivity, RC-limited response and transit-time limited response.

8) Modelling and simulation of systems employing the near-field sub-wavelength aperture probe for THz spectroscopy applications: Spectroscopy is one of the most attractive applications within the THz frequency range. The sub-wavelength aperture probe, discussed in detail in Chapter 6, has already been shown to be a valuable system for THz spectroscopy applications. In [8.3] the probe was successfully employed to detect and investigate the magnetic dipole and electric dipole resonances in single high-permittivity TiO_2 microspheres. In [8.4] and [8.5] the probe was employed to investigate, at THz frequencies, the impact of sub-wavelength-size dielectric particles on Zenneck surface waves on planar metallic antennas, enabling the detection of perturbations of the surface waves as a signature of the particle presence despite its sub-wavelength size. Further study on spectroscopy applications using the probe are envisaged for future research work.

The sub-wavelength aperture probe system is a consolidated experimental arrangement to detect THz waves in the form of pulsed radiation and as such has so far been employed within THz time-domain spectroscopy techniques. The use of the probe to detect CW THz radiation is being investigated and will be part of future research work.

8.2 General Conclusions

In this work, design procedures, analysis and measurement of UTC-PDs as THz sources, have been undertaken. This has shown the way forward for UTC-PD based THz source design. With the completion of the future work described above, these sources should be excellent options for communications and spectroscopy.

8.3 References

[8.1] E. Rouvalis, C. C. Renaud, D. G. Moodie, M. J. Robertson, and A. J. Seeds, "Continuous wave Terahertz generation from ultra-fast InP-based photodiodes," *IEEE Trans. Microw. Theory Tech.*, vol. 60, no. 3 part 1, pp. 509–517, 2012.

[8.2] F. Xia, J. K. Thomson, M. R. Gokhale, P. V. Studenkov, J. Wei, W. Lin, and S. R. Forrest, "An asymmetric twin-waveguide high-bandwidth photodiode using a lateral taper coupler," *IEEE Photonics Technol. Lett.*, vol. 13, no. 8, pp. 845–847, 2001.

[8.3] O. Mitrofanov, F. Dominec, P. Kužel, J. L. Reno, I. Brener, U.-C. Chung, C. Elissalde, M. Maglione, and P. Mounaix, "Near-field probing of Mie resonances in single TiO_2 microspheres at terahertz frequencies," *Opt. Express*, vol. 22, no. 19, pp. 23034–23042, Sep. 2014.

[8.4] M. Navarro-Cía, M. Natrella, F. Dominec, J. C. Delagnes, P. Kužel, P. Mounaix, C. Graham, C. C. Renaud, A. J. Seeds, and O. Mitrofanov, "Terahertz imaging of sub-wavelength particles with Zenneck surface waves," *Appl. Phys. Lett.*, vol. 103, no. 22, pp. 221103 1 – 221103 5, 2013.

[8.5] M. Navarro-Cía, M. Natrella, F. Dominec, J.-C. Delagnes, P. Kuzel, P. Mounaix, C. Graham, C. C. Renaud, A. J. Seeds, and O. Mitrofanov, "Zenneck THz surface waves-assisted imaging of subwavelength dielectric particles," *Lasers Electro-Optics (CLEO), 2014 Conf.*, pp. 1–2, 2014.